



III° Workshop

Plasmi Sorgenti Biofisica ed Applicazioni

Lecce, 19 Ottobre 2012

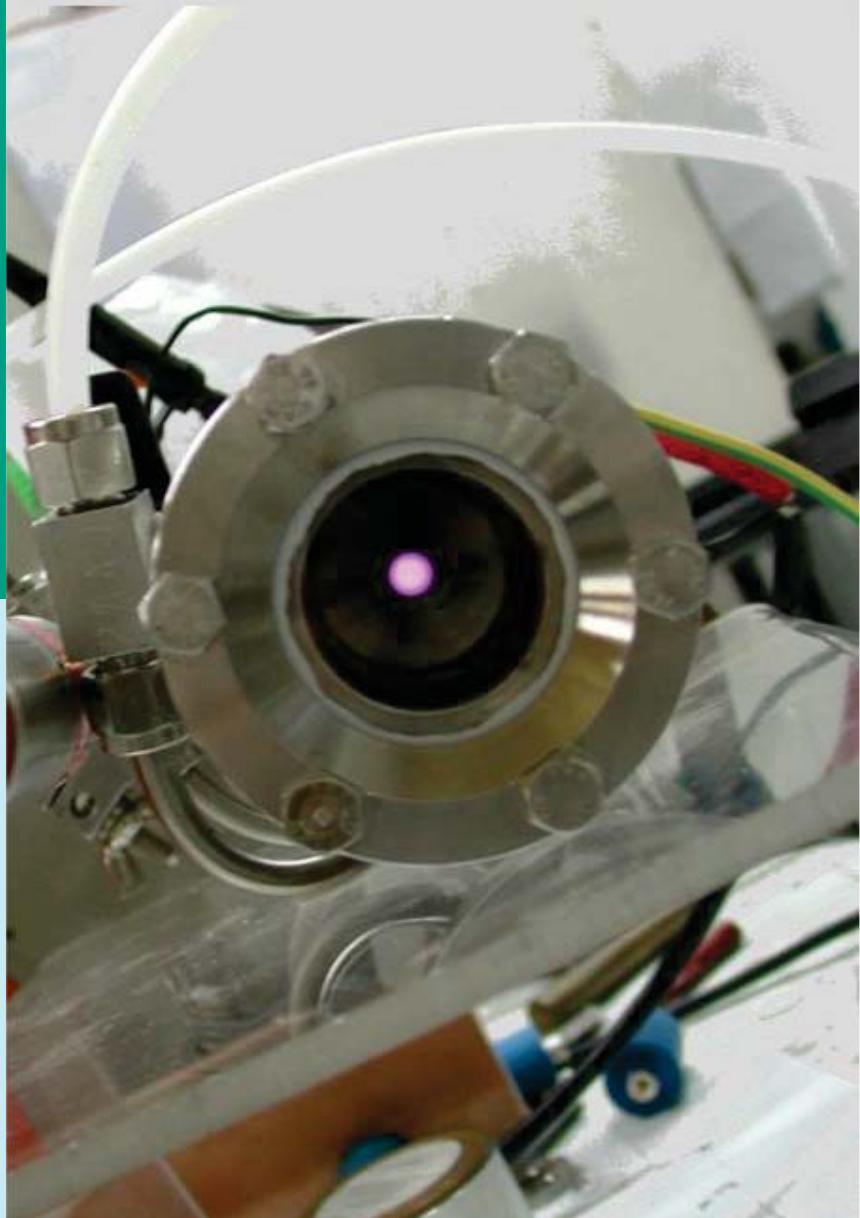
Dipartimento di Matematica e Fisica "Ennio De Giorgi"
Università del Salento – Lecce

<http://psba2012.dmf.unisalento.it/>

A cura di
Vincenzo Nassisi
Domenico Delle Side
Luciano Velardi

TEMATICHE

Sorgenti di particelle e radiazioni
Nuove tecniche di accelerazione
Applicazioni biologiche e microbiche
Biomateriali
Applicazioni ai beni culturali
Materiali per protesi ed ortesi
Diagnostica di impulsi ed Imaging
Sorgenti di radiofrequenza ed interazioni biologiche



III Workshop

Plasmi Sorgenti Biofisica ed Applicazioni

**Lecce, 19 ottobre 2012
Università del Salento**

**Aula “Benvenuti”
Dipartimento di Matematica e Fisica “Ennio De Giorgi”**

a cura di

**prof. Vincenzo Nassisi
dott. Domenico Delle Side
dott. Luciano Velardi**



**UNIVERSITÀ
DEL SALENTO**

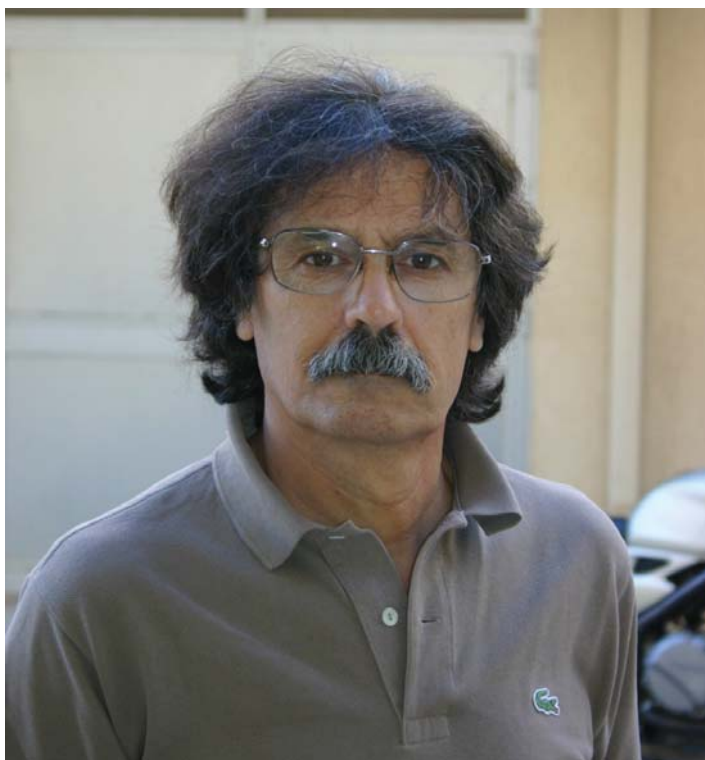
© 2013 Università del Salento – Coordinamento SIBA
ISBN 978-88-8305-101-2 (print version)



<http://siba2.unisalento.it>

eISBN 978-88-8305-102-9 (electronic version)
<http://siba-ese.unisalento.it>

III WORKSHOP “PLASMI, SORGENTI, BIOFISICA ed APPLICAZIONI”



Il 19 ottobre 2012 si è tenuto in Lecce il III workshop “Plasmi, Sorgenti, Biofisica ed Applicazioni”, presso l’aula conferenze “Ennio De Giorgi” del Dipartimento di Matematica e Fisica organizzato con la partecipazione del Dipartimento di Scienze Biologiche e con il supporto della locale sezione INFN.

Lo scopo del workshop è stato sempre quello di confrontare le proprie esperienze scientifiche e tecnologiche nelle differenti discipline allo scopo di concentrare i vari sforzi e raggiungere quel risultato che la comunità intera è in attesa di ricevere.

Le tematiche trattate sono state argomenti di Fisica, Biologia, Medicina, Biotecnologia, Chimica ed Ingegneria.

La ricerca scientifica continua produrre interessanti risultati in varie discipline nonostante le pesanti difficoltà presenti nel nostro paese. I risultati devono essere messi a disposizione dell’uomo, inteso come individuo soggetto ad invecchiamento e come individuo strettamente dipendente dall’ecosistema. Quindi, la ricerca di base è importante e lo è sempre di più se alla fine della scoperta è possibile ricevere le giuste considerazioni tali da poter operare applicazioni immediate per scoprire nuove conoscenze e per migliorare la qualità della vita. In questa fase applicativa, ma anche in quella di ricerca di base, le istituzioni dovrebbero essere sensibili ad individuare gli sforzi che molti ricercatori ed altrettanti giovani aspiranti ricercatori dedicano alla ricerca, spesso senza nessuna prospettiva per il futuro.

È vero, il mondo sta cambiando e perciò dovremmo allungare lo sguardo e progettare/realizzare il futuro, dico progettare/realizzare e non programmare. Oggi, si sente sempre di più parlare di *incarico a progetto*. Tutto ciò è poco male, ma i progetti presentati agli enti committenti dovrebbero essere valutati con il giusto metro affinché i nostri giovani cervelli non siano costretti ad emigrare laddove giuste considerazioni sono ricevute senza troppe umiliazioni.

La partecipazione al workshop è stata numerosa, oltre 70 persone. Hanno partecipato Fisici, Biologi, Medici, Ingegneri e privati, provenienti da tutta Italia e dall’estero, Bari, Catania, L’Aquila, Legnaro, Lecce, Milano, Messina, Praga, ecc. Si sono registrati ben 30 contributi con la partecipazione di oltre 140 autori.

Sarà proposta la IV edizione per il 2014 sfidandoci sui nuovi risultati sempre più entusiasmanti.

In attesa di ripetere l'esperienza colgo l'occasione per ringraziare quanti hanno contribuito al successo del workshop: la dott.ssa Daniela Dell'Anna, il dott. Giovanni Buccolieri, il dott. Fabio Paladini, il dott. Domenico Zito e il sig. Salvatore Mega per la disponibilità a curare la parte logistica, il dott. Luciano Velardi e il dott. Domenico Delle Side per l'impegno e la cura del presente volume.

Un sentito riconoscimento va a tutti i relatori, a tutti gli autori dei lavori, al Dipartimento di Matematica e Fisica per il sostegno finanziario, alla locale sezione INFN per aver agevolato la realizzazione del presente volume e al SIBA dell'Università del Salento per aver collaborato alla pubblicazione degli atti.

Prof. Vincenzo Nassisi

Responsabile del Laboratorio di Elettronica Applicata e
Strumentazione - LEAS

Dipartimento di Matematica e Fisica "Ennio De Giorgi"
Lecce

III° Workshop Plasmi, Sorgenti, Biofisica ed Applicazioni

Indice dei contributi

Autori	Titolo	Pagina
Nassisi V, Delle Side D, Velardi L, Buccolieri G, Accoto G, De Benedittis A, Giuffreda E, Gerardi R, Krasa J	Preliminary study of novel Faraday cup for fast ion beams generated from a LIS source	1
Cutroneo M, Torrisi L, Visco AM, Brancato V	Optical absorption coefficient measurements in nanostructures embedded in UHMWPE	5
Velardi L, Delle Side D, De Marco M, Nassisi V	Emissione characterization of ion beams provided by Platone accelerator	11
Buccolieri G, Castellano A, Congedo A, Buccolieri A, Nassisi V, Cataldo R, Gorgoglione MA, Ciccarese N, Delle Side D, Velardi L	Misure di radioattività naturale nel sito preistorico di <i>Grotta dei Cervi</i> in Porto Badisco (LE)	17
Italiano A, Torrisi L, Cutroneo M, Gentile C, Torrisi A	A comparative analysis of old and recent Ag coins by XRF methodology	23
Alemanno E, Martino M, Caricato AP, Corrado M, Pinto P, Spagnolo S, Chiodini G, Perrino R, Fiore G	Laser Induced Nano-Graphite Electrical Contacts on Synthetic Polycrystalline CVD Diamond for Nuclear Radiation Detection	29
Palladino L, Festuccia R, Di Paolo Emilio M, Limongi T	Project and realization of a microbeam at 2.48 nm	34
Scolaro C, Torrisi L, Cutroneo M, Caridi F, Roszkowska AM, Pedullà E	A Liquid contact angles on biocompatible surfaces	38
Cicala G, Magaletti V	Deposition of thick and thin nanocrystalline diamond films by microwave plasma enhanced chemical vapor deposition	43
Imperio E, Giancane G, Valli L	Fourier transform infrared spectroscopy (FTIR) investigation focused on Italian postage stamps in the course of time	49
Donativi M, De Nunzio G, Cataldo R, De Mitri I, Pastore G, Rucco M, Carlà A, Peccarisi M, Massafra A, Demitri R, Di Sabatino S, Buccolieri R, Quarta R, Grimaldi M, Manca AD, Torsello M, Zecca I, Falini A, Castellano A, Bello L, Soffietti R, Galluccio G, Batzella S	Sistemi di Computer-Assisted Detection di Analisi di Dati Bio-medici	53
Krasa J, Margarone D, Velyhan A, Pfeifer M, Ullschmied J, Klir D, Rezac K	Multi MeV protons, deuterons and carbon ions produced by the PALS laser system	60
Vitale S	Dispositivi acustici impiantabili	64
Piscitelli P, Argentiero A, Neglia C, Peluso A, Di Rosa S, Ferrarese A, Caiaffa V, Agnello N, Chitano G, Gaudino G, Bortone I, Benvenuto M, Distante A	La fragilità ossea svelata dagli ultrasuoni può consentire la "produzione di salute" su larga scala: studio pilota in pazienti talassemici	68
Russo D, Cavalera E, Papaleo A, Leone A, Ricci FP, Di Paola G, Capomolla C, Natali M, Pastore G, Santantonio M	Intensity Modulated Radiation Therapy with volumetric modulation (VMAT)	73
Natali M, Capomolla C, Russo D, Pastore G, Cavalera E, Leone A, Zagari A, Santantonio M	Controlli dosimetrici pretrattamento in IMRT (Intensity Modulated Radiation Therapy) con tecnica VMAT (Volumetric Modulated Arc Therapy)	80

Papaleo A, Cavallera E, Russo D, Leone A, Di Paola G, Ricci FP, Capomolla C, Natali M, Santantonio M	Dynamic-arc-IMRT with Serial Tomotherapy	84
Capomolla C, Quarta S, Ciccarese G, Natali M, Cazzato M, Papaleo A, Russo D, Zagari A	Analisi dell'indeterminazione della distribuzione di dose nella tomoterapia seriale	91
Pennetta C, Palatella A	Analysis of Time Statistics of Extreme Variations of Heart Beat Fluctuations	96
Specchia V, Friscini A, Dell'Isola D, Delle Side D, Velardi L, Nassisi V, Pimpinelli S, Bozzetti MP	Stress da radiazione RF a 900 MHz ed attivazione di elementi trasponibili in tessuti germinali di <i>Drosophila melanogaster</i>	101
Blus C, Giannelli G, Szmukler-Moncler S	Bactericide effect of a powerful Ultrasonic Bone Surgery device (piezo-surgery): Oral surgery application to BRONJ treatment	106
Della Patria A, Oleari C, Fermi F, Piegari A, Sytchkova A	A compact spectral camera for VIS-NIR imaging	113
Troisi L, Bona F, Citti C, Giancane G, Granito C, Liu T, Troisi A	Alternative acceptor materials for organic photovoltaic cells	119
Delle Side D, Velardi L, De Marco, Nassisi V	Protons production by solid hydrogenated targets via excimer laser ablation	123
Visco AM, Brancato V, Primerano P, Milazzo MF, Cutroneo M, Scolaro C, Caridi F, Torrisi L	Chemical and physical modifications of polyethylene containing nanostructures	128
Visco AM, Brancato V, Cutroneo M, Scolaro C, Caridi F, Torrisi L	Applications of laser welding for the joint of plastic materials	133
Caridi F, Cutroneo M, Scolaro C, Torrisi L	Proton emission by laser ablation at different wavelengths	138
Delle Side D, Alifano P, Nassisi V, Talà A, Tredici SM, Velardi L	Enhancing UHMWPE Antibacterial Properties Through Ion Implantation	143
Agosteo S, Anania MP, Caresana N, Cirrone GP, De Martinis C, Delle Side D, Fazzi A, Gatti G, Giove D, Giulietti D, Gizzi L, Labate L, Londrillo P, Maggiore M, Nassisi V, Pola A, Sinigardi S, Tramontana A, Schillaci F, Turchetti G, Varoli V, Velardi L	LILIA project: ion beams for hadron therapy	149
Nassisi V, Delle Side D, Velardi L, Buccolieri G, Paladini F, Giove D, De Martinis C, Fazzi A	High voltage pulse of short duration to feed a solenoid for intense ion beam transport	158
Scarpa D, Manzolaro M, Vasquez J, Biasetto L, Cavazza A, Corradetti S, Montano J, Manente M, Curreli D, Meneghetti G, Pavarin D, Tomaselli A, Grassi D, Benetti P, Andrighetto A, Prete G	Advances in the SPES Project and its ion source systems	160

Preliminary study of novel Faraday cup for fast ion beams generated from a LIS source

Nassisi V^{1,2}, Delle Side D^{1,2}, Velardi L^{1,2}, Buccolieri G^{1,2}, Accoto G¹, De Benedittis A¹, Giuffreda E¹, Gerardi R¹, Krása J³

¹ Department Mathematics and Physics, University of Salento, LEAS Laboratory, Via per Arnesano, Lecce, Italy

² INFN Section of Lecce, Via per Arnesano, Lecce, Italy

³ Institute of Physics, ASCR Prague Czech Republic

Abstract

In this work we present a study on Faraday cups. These devices are utilized to perform time of flight measurements in order to characterize charged beams in different situations particularly for accelerator by double stage configuration. The secondary electron emission during the beam interaction with ion collector modifies the true current because the read values are strongly dependent on the beam incident angle. To eliminate the suppressing grid, we tested new cup collector surfaces and we compared the results to the ones performed using the flat collector. For this purpose, we performed experiments utilizing simple tilted collectors at 30°, 45° and 55° determining the gamma factor of the secondary electron emission. Tests were performed utilizing Cu ion beams at energy up to 40 kV

Introduction

The characterization of ion beams by conventional Faraday cups[1] can induce wrong measurements owing to the secondary electron emission (SEE). All this is mainly due to high beam energy and to generation of soft X rays. To overcome this problem a polarized transparent electrode is placed near the cup collector at negative voltage with respect to the collector one to capture the generated electrons[2]. We want to study a new configuration in order to avoid the application of the suppressing electrode because we want to utilize the Faraday cup also as a third electrode[3, 4], a useful improvement in multiple stages accelerator devices. In fact applying a high voltage on this electrode we can further accelerate the beam particles.

The theory behind a Faraday cup is very simple. It becomes complex when diagnosing fast pulses where the resulting signal due to

ion beams must be transmitted to the oscilloscope by a transmission line.

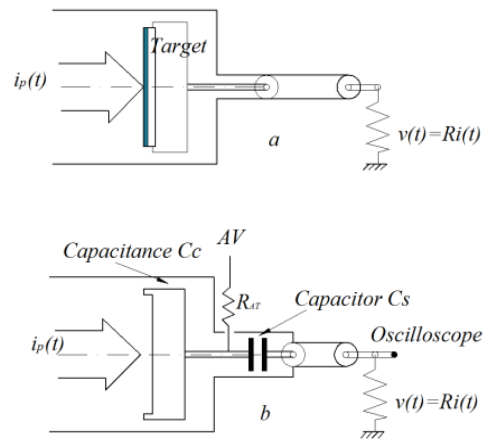


Fig.1: Faraday cup: a) for electron and ion beam; b) for plasma.

The transmission line utilized in laboratory has a characteristic impedance of 50 Ω and in order to ensure a good transmission also the Faraday cup structure must present the same impedance.

Very simple Faraday cup configurations are sketched in Fig. 1, suitable for electron and ion beams (a) and for plasma beam (b), both without the suppression electrode. Generally, Faraday cups are composed of an ion collector where the beam particles impinge inducing a current proportional to the incoming signal if the cup is preventively connected to ground by a resistor equal to characteristic impedance. In fact, Faraday law for variable currents due to charge density cannot be applied. Just after the beam interaction with the cup collector, the system must be considered like a transmission line. Generally, the output signal of the cup is transferred to oscilloscope or resistor divider by the diffuse 50 Ω transmission line. When the beam energy is sufficient to provoke SEE the cup generally is modified inserting the suppression electrode or changing the collector configuration with a cone as showed in Fig. 2.

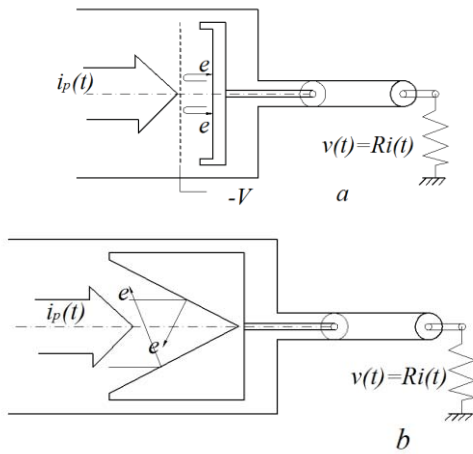


Fig. 2: Faraday cup: a) with suppression electrode; b) with cone collector.

The electric scheme of the cup suitable for charged beams or plasma is illustrated in Fig. 3.

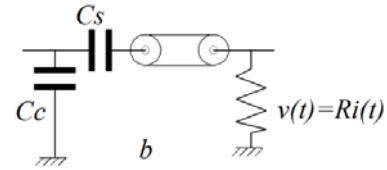
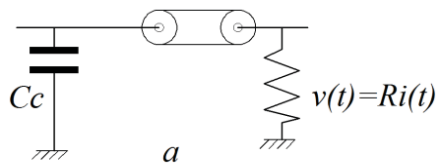


Fig. 3: Faraday cup schemes suitable for: a) charged beams; b) plasma beams.

The current $i(t)$ provides the beam current by the following relation:

$$i_p(t) = \frac{i(t)}{\beta(1-\gamma)} \quad \text{per} \quad \text{elettroni} \quad (1)$$

$$i_p(t) = \frac{i(t)}{\beta(1+\gamma)} \quad \text{per} \quad \text{ioni}$$

Where β is the optical transmission of the grid (if absent it is equal to 1) and γ is SEE parameter.

Materials and methods

The device used in these experiments is the accelerator Platone at the LEAS laboratory. The accelerator consists on a vacuum chamber and an excimer laser (a Compex 205 operating in the UV range). Its output beam has 600 mJ maximum output energy, 248 nm wavelength, 25 ns pulse duration and maximum repetition rate 50 Hz. The laser beam streaks the solid targets to generate plasma in the vacuum chamber. Particularly, inside the vacuum vessel an expansion chamber was placed tightly closed around the target support. The plasma expands inside the expansion chamber but, being no electric fields breakdowns are absent. The length of expansion chamber (18 cm) was sufficient to decrease the plasma density. The target, together with the expansion chamber, is connected to a power supply of positive bias voltage. Four capacitors of 1 nF stabilized the accelerating voltage during the fast ion extraction. Owing to the plasma expansion the charges reach the extremity of the expansion chamber. This extremity was drilled by a 1.5 cm hole to allow the ion extraction.

A pierce ground electrode was placed at 3 cm distance from the expansion chamber. After this electrode, another electrode, placed at 2 cm from the ground electrode and connected to a power supply of negative bias voltage, was utilized as third electrode and also as Faraday cup collector. The laser beam direction impressed the target at an angle of 70° with respect to the normal to the target surface. During our measurements the laser spot area onto the target surface was fixed at 0.005 cm^2 for all experimental conditions. In this experiment all measurements were performed with the only first accelerating gap. In front the ground electrode the Faraday cup was placed.

The preliminary experiments were performed with three cups of different conformation: we call DZ the collector by double zig-zag Fig. 4, 90° the collector with surface by single tilted of 45° with respect to main axis, Fig.5, and 45° the collector with single surface tilted of 22.5° with respect the main axis, Fig. 6.

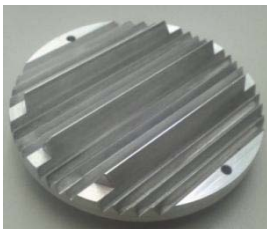


Fig. 4: Faraday cup collector double zig zag.



Fig. 5: Faraday cup collector 90° .



Fig. 6: Faraday cup collector 45° .

Results

The target used in this experiment was pure Cu disks and the laser energy 25 mJ.

The total charge collected with the three cups and the one obtained with the plane one is shown in Fig. 7.

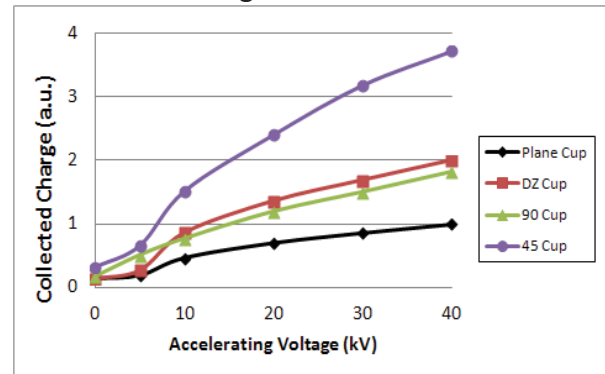


Fig. 7: Output charge with the plane collector and with DZ, 90° and 45° collectors.

It is well evident that the recorded current increases with the collector having the shortest angle. Nevertheless although the angle might reduce SEE electrons, it seems not sufficient and the reason could depend on the high intensity of SEE electrons. For this purpose we analyzed other three different cups composed by a simply tilted plane with respect to the ion beam axis. They were tilted of 30° , 45° and 55° , Fig. 8 a,b and c.

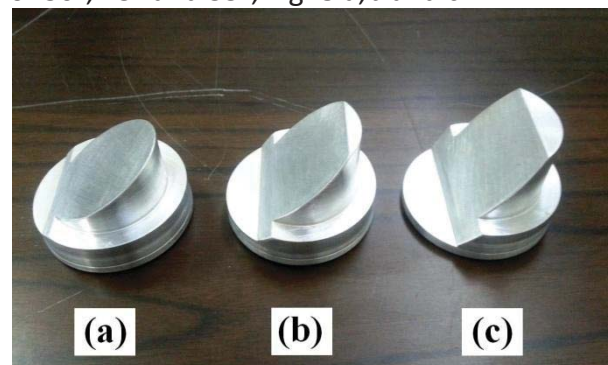


Fig. 8: Photos of cup collectors. a) collector tilted at 30° ; b) collector tilted at 45° ; c) collector tilted at 55° .

The measurements, performed with and without the suppression grid, were compared with the one obtained with the plane collector, Fig. 9.

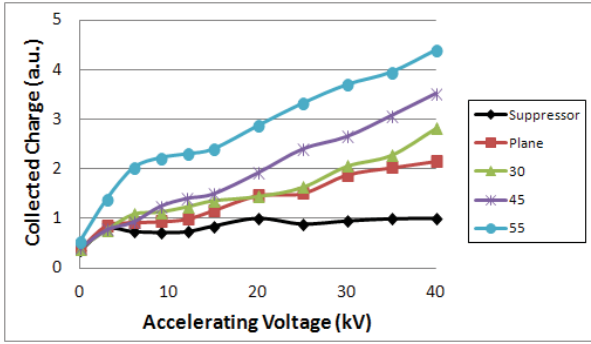


Fig. 9: Output results by a cup with the collector; plane, tilted at 30°, 45° and 55°, and with the suppressor grid.

These results confirm that the SSE increases on tilted angle, as pointed out in [5]. Indeed, it is known that SEE should increase as a function of the tilt angle following a law of the type

$$\gamma(\theta) = \gamma_0 \sec(\theta)$$

where θ is the tilt angle and γ_0 is the SEE coefficient at normal incidence. This behavior depends on the fact that a variation in the angle induces an increase in the path of the ions inside the metal plate where the escape of electrons is easier. It is worth noticing that our results show a dependence on the tilt angle that is nearly exponential due to the energy spread of the beam. Therefore, to get correct results it is necessary to apply the suppression grid. In fact in Fig. 9 are reported the collected charge obtained with the suppression electrode applied to the tilted cups. The results are very similar with the three cups for a free plasma expansion (ion energy up to 1 keV), and we can conclude that, without the suppressor grid, real values cannot be read in post acceleration mode. This configuration cannot be used as third accelerating electrode because it is impossible to apply the suppressing electrode to an electrode placed at high voltage.

By means of the experimental data we computed the γ parameter of SEE (see equation (1)) as a function of the tilt angle, for various accelerating voltages, Fig. 10.

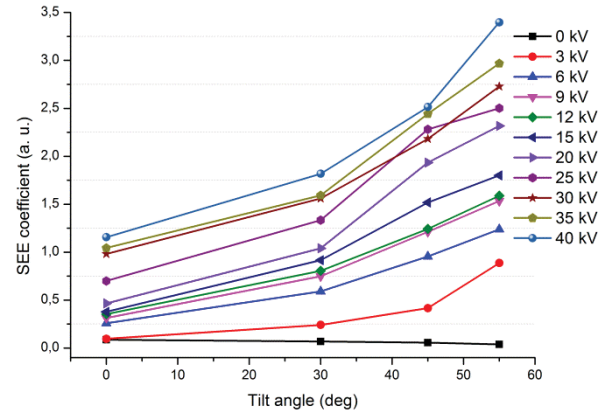


Fig. 10: SEE Gamma parameter for various accelerating voltages as a function of the tilt angle.

Conclusions

We have studied the behavior of different Faraday cups utilized to perform time of flight measurements. The secondary electron emission during the beam interaction with ion collector modifies the real current because the read values are strongly dependent on the beam incident angle. So, a suppressing grid is indispensable.

References

- [1] A. Luches, V. Nassisi and M.R. Perrone, Rev. Sci. Instrum. 56, 759-760 (1985)
- [2] J. S. Pearlman, Rev. Sci. Instrum. 48, 1064-1067 (1977)
- [3] V. Nassisi, M.V. Siciliano, "Cu and Y ion beams by a new LIS generator", Nucl. Instrum. Meth. B 269, 2919-23 (2011)
- [4] L. Velardi, M.V. Siciliano, D. Delle Side and V. Nassisi, Production and Acceleration of Ion beams by Laser Ablation, Rev. Sci. Instrum. 83, 02B717 (2012)
- [5] E. J. Sternglass, Phys. Rev., 108, p. 1-12 (1957).

Optical absorption coefficient measurements in nanostructures embedded in UHMWPE

M. Cutroneo^{1,2}, L. Torrisi^{1,3}, A.M. Visco⁴, V. Brancato⁴

¹ *Dip.to di Fisica e Sci. d. Terra, Univ. di Messina, V.le F.S. D'Alcontres 31, 98166 S. Agata (ME), Italy*

² *INFN-Sez. CT, Gruppo Coll. Messina, V.le F.S. D'Alcontres 31, 98166 S. Agata (ME), Italy*

³ *INFN-Laboratori Nazionali del Sud, V. S. Sofia 64, 95124 Catania, Italy*

⁴ *Dip.to di Chimica Ind. e Ing. dei Materiali, Univ. di Messina, Ctr. Di Dio, 98166 S. Agata (ME), Italy*

Abstract

Light absorption coefficients in Ultra High Molecular Weight Polyethylene have been determined in the range between 200 nm and 1200 nm wavelength by means of optical spectroscopy. The absorption investigations have been carried out by evaluating the absorption of characteristic peaks emitted from a Hg-Ar lamp and detected by at high sensitivity optical spectrometer. Measurements have been performed in pure and doped polyethylene. As doping agent at different concentrations, have been employed nanostructures of carbon-nanotubes, iron oxide and methylene-blue. The aim of these analyses is to modify the absorption coefficients of polyethylene-based polymers in a large range of wavelength in order to obtain special polymers for optical applications in different scientific fields, such as physics, medicine, chemistry and engineering.

Introduction

The interest on modified specimens such as nanocomposites or nanotubes has increased in several branch of science as a result of their numerous applications: medical, thermoplastical material, electric insulator, lens,... By using microstructures embedded in polymeric materials it is possible to improve the optical absorbing properties [1]. As an example, it is well-known as the Through Transmission Visible Laser Welding (TTVLW) method, requires two plastic materials which will be joined by localized heating at this two interfaces. This process needs an optically transparent plastic layer and another absorbent [2]. The localized heating at these two interfaces, produces a strong weld. Another interesting application is related to the employing of modified polymers in order to be irradiated by high intense lasers

to generate plasmas in vacuum [3]. Moreover, special polymers characterized by roughness or containing nanostructures with dimensions comparable with the laser wavelength, enhances strongly their energy absorption through mechanisms of resonant absorption of the laser light [4]. For these reasons, it is very interesting the study of absorbing materials or combinations of materials such as nanofibers and nanostructures embedded in polymers which have high absorption coefficient at particular wavelengths. Additives such as carbon nanotubes (CNTs), nanostructures of Fe₂O₃, and a pigment of C₁₆H₁₈N₃SCI (Methylene Blue), can be utilized to color black, red or blue, respectively, because the polymer's absorbance is sensitive to the presence of colorant (chromophores) pigments [5]. In order to study physical properties of nanostructures embedded in UHMWPE (Ultra High Molecular Weight Polyethylene), the

interactions with modified samples, optical parameters, such as the absorption coefficient and the attenuation length have been investigated

Materials and methods

Several kind of targets have been employed, all with a common matrix of Ultra High Molecular Weight Polyethylene, 3×10^6 g/mol molecular weight, 50% crystalline and 50% amorphous. Targets contain Fe_2O_3 , $\text{C}_{16}\text{H}_{18}\text{N}_3\text{SCl}$ and CNT nanostructures in different concentrations, ranging between 0.01 wt% and 10 wt%, were used for experiments. As can be seen in Fig. 1, these fillers color the polymer red, blue, and black, respectively.

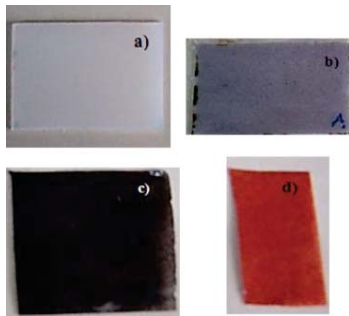


Fig.1 Pure polyethylene (a), Polyethylene + $\text{C}_{16}\text{H}_{18}\text{N}_3\text{SCl}$ (b), Polyethylene + CNT (c), Polyethylene + Fe_2O_3 , (d)

The particles size for iron oxide and the diameter of carbon nanotubes is about 100 nm, instead Methylene Blue is entrapped in a silica matrix with particles size lower than 50 μm .

Plastic samples with thickness ranging between 10 μm and 1mm have been used for the optical measurements.

The optical properties of polymers have been analyzed considering the effects of thickness of these films on their physical, electric and mechanical properties. An incident radiation produced by a Hg-Ar lamp impinges a sample placed into a holder-target with a tilt angle of 90° , and a fraction of the wave is absorbed when a radiation passes through the infinitesimal thickness dx .

The difference in intensity dI , due to the slice of absorbing material dx is given by:

$$dI = I \mu dx \quad (1)$$

where μ is the absorption coefficient.

The Beer-Lambert's law [6] has the form:

$$I = I_0 e^{-\mu x} \quad (2)$$

from which :

$$\mu = (1/x) \ln(I_0/I) \quad (\text{cm}^{-1}) \quad (3)$$

Where the absorbance μ of electromagnetic wave, is expressed in terms of incident light I_0 , transmitted light I and thickness x of the sample used. Fig. 2 shows the sketch for the optical spectroscopy configuration.

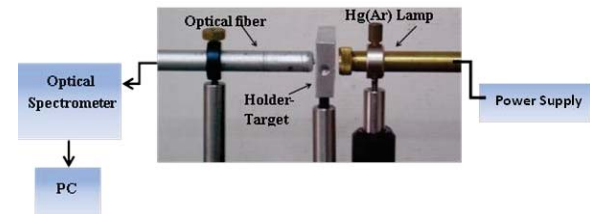


Fig.2 Optical Spectroscopy set-up

The beam of light is captured by an optical Fiber interfaced to Horiba Jobin Yvon Spectrograph instrument covering the 220-1100 nm wavelength range. A Lynear spectroscopy software acquires up to 160 full spectra per second, those are stored on a PC. Subsequently, a sample is placed on a holder target, the wave impinges perpendicularly into a target and then, emerges across the sample with an intensity lower than the entered light. The Hg(Ar) lamp contains a small amount of mercury which dominates the output spectrum as showed in Fig.3 and argon as a started gas.

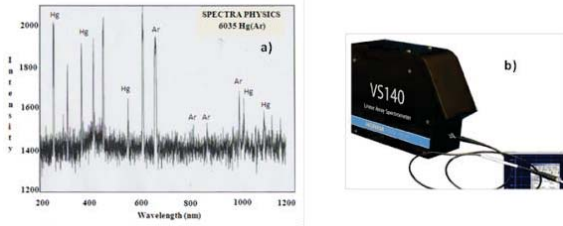


Fig.3 Hg(Ar) lamp spectrum (a) measured by Horiba Jobin Yvon Spectrograph (b)

It is well-known that after a beam light impinges on a target a fraction of it is reflected, part of it undergoes absorption and scattering processes and part of it is transmitted. In order to reduce the absorption and the scattering effects, the thickness of samples employed were ranged between 10 μm and 1 mm. The optical response of the specimens, is given by the Beer-Lambert law, which describes in general the exponential decrease of light intensity $E(z)$ as a function of the material depth z due to the absorption. The transmission yield was investigated at different operation wavelengths, by evaluating different characteristic peaks of the lamp, particularly the lines at 240 nm, 600 nm and 1080 nm wavelength that have been chosen to calculate the absorption in the doped materials having concentrations of 0.1%, 0.3%, 0.5% and 1%, for different thickness, 10 μm , 100 μm , 600 μm , and 1000 μm employed for these measurements. It has been useful to consider the penetration depth of the radiation defined as the depth at which the intensity of collimated beam is attenuated by a factor $1/e$. The attenuation length or to be more exact, penetration depth of the beam radiation can be expressed as:

$$L=1/\mu \text{ (cm)} \quad (4)$$

where μ is the absorption coefficient for the treated material.

Results

Fig. 4 indicates the fraction of transmitted intensity of the incident light on UHMWPE 1mm in thickness and in the regions of near UV, Visible and near IR.

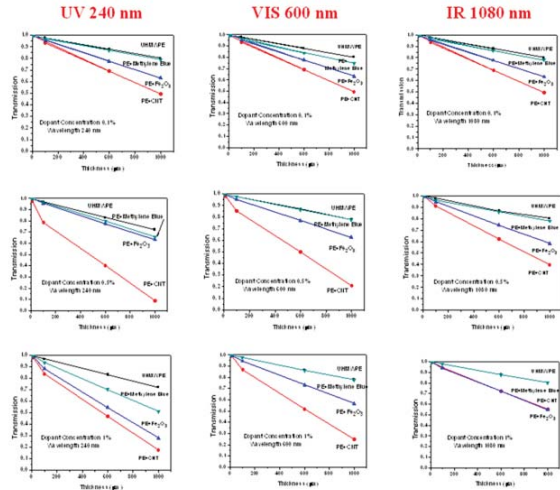


Fig. 4 Spectra comparison showing transmission as a function of thickness, concentration of dopants and wavelengths

Pure UHMWPE has high transmittivity at UV, VIS, and IR, which is about 85% for 1mm in thickness. UHMWPE + CNT (1%) presents the minor transmittivity at UV,VIS and IR which is 15%, 25%, and 55% respectively, for the three used wavelengths (240 nm, 600 nm and 1080 nm). UHMWPE +Methylene Blue has higher transmittivity of the doped polymer and it shows values comparable to pure UHMWPE for VIS and IR, while values of about 60% for 1% in concentration. Higher percentage of filler, of the order from 5% to 10%, show lowest transmittance than other for blue polymers. UHMWPE+ Fe₂O₃ (1%) has a significant transmittance that is roughly 30%, 60% and 55% for UV, VIS and IR respectively. In general, in the UV region the transmission decreases as a consequence of an increment of the absorption coefficient. By way of polyethylene with CNTs embedded at the same conditions considered

previously, and at 240 nm view as for concentration of 0.1wt% and 1 wt%, the percentage of transmitted light goes from 60% to 15% respectively. Moreover, evaluating different wavelengths, it has been observed the increase of transmitted light, from 25% at 600nm, up to 70% at 1080 nm. It is common knowledge that molecules absorb specific frequencies that are characteristics of its own structure. These absorptions are resonant frequencies, i.e. the frequency of the absorbed radiation matches the frequency of the bond or group that vibrates. However at the employed wavelengths region, in the near IR and visible, the absorption peaks are due mainly to de-excitation of molecules of the chromophores embedded in the UHMWPE. The interpretation of the absorption coefficient vs. wavelength spectrum for polyethylene it is possible by knowing the molecular structure. Although to a first approximation, polyethylene may be considered as an infinite chain of CH₂ groups, the chains are found in the planar zig-zag configuration. By the comparison between experimental data and literature, Fig. 5 (a), (b), presents high absorption with the peak position near 290nm, 510nm, 550nm, due to C-H* de-excitation modes. Fig.5 (c) (d) show absorption peaks at 246nm, 292 nm, 664nm [7]. The absorption bands with maxima at 610nm and 664nm are assigned to C-C* transition de-excitation of dimmers (C₂H₄) and monomers(CH₂), respectively [8].

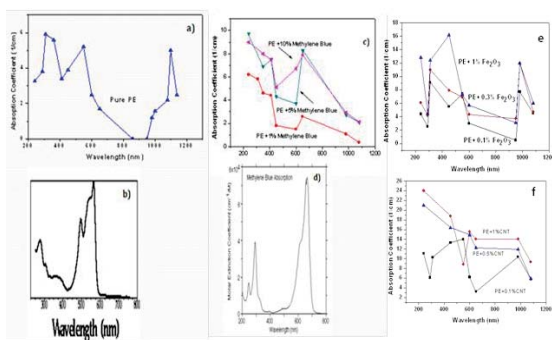


Fig. 5 Absorption coefficient vs Wavelength for a)UHMWPE, c) PE+Methylene Blue, e) PE+Iron Oxide

The absorption spectra of polyethylene with Fe₂O₃, C₁₆H₁₈N₃SCI and CNTs, at concentration of 0.01, 0.1, 0.5, 1 wt% embedded showed in Fig. 5 indicate the increase of the absorption coefficient with the concentration of dopants and its decreasing with the wavelength.

In Fig. 6 are presented the values of measured absorption coefficients, μ achieved by using the expression (4) for targets manufactured by using UHMWPE as matrix for samples where micro and nano structures have been embedded.

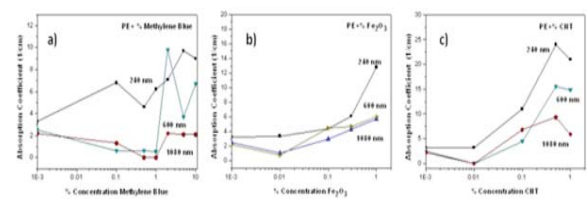


Fig. 6 Graphics relating absorption coefficient as a function of dopant concentration

The absorption coefficient increased linearly with increasing of concentration of nanostructures.

In Fig.7 reporting the attenuation length vs. the wavelength and doping concentration.

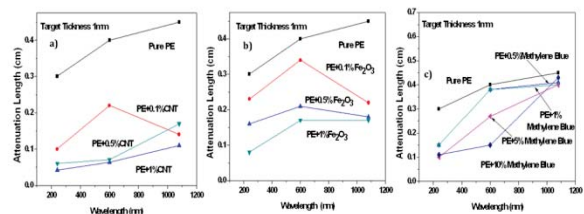


Fig. 7 Graphics regarding attenuation coefficient as a function of the wavelength for samples with same thickness

The attenuation length for 1mm PE from 0.1% to 1% CNT is of about 500 μ m at 240 nm and increments to about 0.15 cm for 1080 nm. For comparison, in pure PE the attenuation length assumes the value of 0.3 cm, 0.4 cm and 0.46 cm for 240 nm, 600 nm and 1080 nm respectively (a). The attenuation length for visible radiation generally is intermediate with respect to near UV and IR regions.

The length of extinction is 400 μm for polyethylene with CNTs filler embedded in concentration of 1%, and 0.1 cm for Methylene Blue in concentration of 10%. The reason of this difference is due to the carbon nanotubes that are highly absorbent, and have a size of the order of 100 nm. On the contrary, Methylene Blue is entrapped in a silica matrix with about 50 μm particles of size. The measurements performed, have been repeated with different concentrations, thickness and confirm, as presented in Fig.8, that the absorption in UV range is higher than VIS and near IR regions, and that pure polymers transmit light more than plastic materials doped with Methylene Blue, Iron oxide and carbon nanotubes respectively.

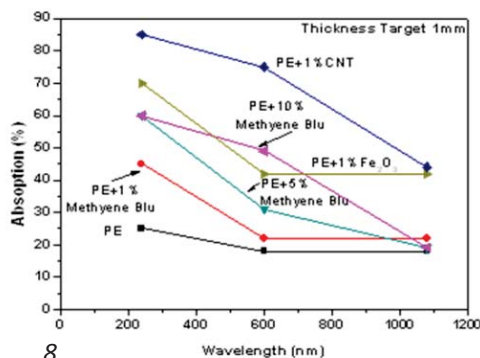


Fig. 8 Absorption percentage as a function of wavelength and dopant concentration

Discussion and conclusions

The absorbance measurements of nanostructures embedded in UHMWPE, were obtained by using a single and simple set up consisting in an optical spectrometer and the characteristic lines of the Hg-Ar lamp. They put in evidence the relation between attenuation coefficient and concentration of embedded nanostructures.

It has been observed that the absorbance depends on the thickness of the specimens, on the radiation wavelength and on the nature of filler employed.

CNT, Fe₃O₂, Methylene Blue, are responsible for interesting effects because by changing

their concentration change important parameters of the treated samples.

In this context, in the field of polymer welding have been investigated the better conditions to produce high absorption and consequently a good joint [10] for mechanical or biomedical applications. Moreover, the prepared polymers find interesting applications in the use of special thin targets to be laser irradiated at high laser intensity in order to obtain high hydrogenated plasmas in vacuum [11].

The use of modified targets and the investigation of their optical properties have some advantages, from laser irradiations such as to treat surfaces in order to modify the roughness of the specimen and their physical and chemical properties (mechanical resistance, electric conductivity, thermal conductivity, chemical reactivity, wetting ability, etc.) and to control the absorption of laser light.

References

- [1] S.T. Amancio-Filho, J.F. dos Santos. Polymer Engineering and Science, 49 (2009) 1461-1476.
- [2] J.P. Coelho, M.A. Abreu, M.C. Pires, Opt. Laser. Eng. 34 (2000) 385–395.
- [3] L. Torrisi, S. Cavallaro, M. Cutroneo, D. Margarone, and S. Gammino Review of Scientific Instruments 83, 02B310 (2012)
- [4] M. Cutroneo, L. Torrisi, Activity Report ISSN 2038-5889 pag. 71-76
- [5] V.V. Semak, R.J. Steele, P.W. Fuerschbach and B.K. Damkroger, Journal of Physics D: Applied Physics, 33 (2000), 1179-1185.
- [6] F.A Jenkins, H.E White, Fundamental of Optics, Mc Graw-Hill, 1981, p.231
- [7] T. Maehara, K. Nishiyama, S. Onishi, S. Mukasa, H. Toyota, M. Kuramoto, S. Nomura, A. Kawashima, Journal of Hazardous Materials 174 (2010) 473-476
- [8] S.H.A. Nicolai, J.C. Rubim, Langmuir 19 (2003) 4291-4294
- [9] Dr. Najat .J.saleh & Zanaib.Y.shnean, Eng. & Tech. Vol. 26, No.9, 2008

- [10] A.M. Visco, N. Campo, V. Brancato, L. Torrisi, F. Caridi, M. Cutroneo, APSUSC 23023(2012)
- [11] Torrisi L, Giuffrida L, Cutroneo M, Cirrone P, Picciotto A, Krasa J, Margarone D, Velyhan A, Laska L, Ullschmied J, Wolowski J, Badziak J, Rosinski M, Rev Sci Instrum. 2012 Feb, 83(2):02B315S.

Emittance characterization of ion beams provided by PLATONE accelerator

Velardi L^{1,2}, Delle Side D^{1,2}, De Marco M¹, Nassisi V^{1,2}

¹*Laboratorio di Elettronica Applicata e Strumentazione (LEAS), Dipartimento di Matematica e Fisica, University of Salento, Lecce, Italy*

²*Istituto Nazionale di Fisica Nucleare (INFN) Section of Lecce, Lecce, Italy
E-mail: luciano.velardi@le.infn.it*

Abstract

Laser ion sources offer the possibility to have ion beams that can be useful as injector for particle accelerators. In this work, we studied the geometric quality of ion beams produced by the PLATONE accelerator. It is a LIS source and an electrostatic accelerator. It consists of ns pulsed KrF laser which works at the intensity of 10^8 - 10^{10} W/cm² and a vacuum chamber where the ions are extracted from the plasma plume and accelerate by a double gap accelerating system. The accelerating voltage applied in DC mode was 60 kV. The beam characterization was performed by the Pepper Pot method with the use of radio-chromic films as sensible target. The measurements were performed by varying the geometric configuration of the anode (the extracting electrode) for the accelerating system. The lowest value found for the normalized emittance was 0.20π mm mrad.

Introduction

In the last decade, new techniques to produce particle beams make use of the interaction between high power femtosecond laser pulses and thin foils [1]. In contrast with other techniques, these give the advantage to obtain highly collimated and energetic particle beams from the rear of the target surface. Depending on the laser parameters, two mechanisms seems to be responsible of the ion acceleration: target normal sheath acceleration (TNSA) [2] and radiation pressure acceleration (RPA) [3]. Despite of the high quality beams obtained through TNSA and RPA systems, older and well known techniques, such as pulsed laser ablation (PLA), still play a fundamental role

for applications, since the former have extremely high total costs of ownership and require large space for its working.

It is well known that the use of the PLA technique allows to easily obtain ions from solid targets, whose energy can be easily increased by applying post acceleration [4, 5]. Today it is possible to easily arrange laser beams at intensities of the order of 10^8 - 10^{10} W/cm² and ns pulse duration that, interacting with solid matter in vacuum, produces hot plasmas [6] at high temperature and densities, of the order of tens of eV.

Thermal interactions, adiabatic expansion in vacuum and Coulomb interactions are responsible for the primary ions acceleration in plasma. By applying post acceleration, it is

possible to extract from the plasma plume specific charged particles. This idea can be applied to plasmas of moderate density owing to their low electric conductivity.

Nowadays, ion beams of moderate energy have a wide range of applications, from scientific to industrial ones [7-9].

So many laboratories, as well as the LEAS, are involved to develop accelerators of very contained dimensions, easy to be installed in little laboratories and hospitals. The use of ion sources facilitates the improvement of ion beams of moderate energy and good geometric qualities.

There are many methods to obtain particle beams; the application of pulsed laser ablation (PLA) technique (the one that we adopt in this work) allows to get ions from solid targets, without any previous preparation, whose energy can be easily increased by post acceleration systems [4-5]. In this way, plasma can be generated from many materials, also from refractory ones.

In this work, we characterize the ion beams provided by a laser ion source (LIS) accelerator composed by two independent accelerating sectors, using an excimer KrF laser to get PLA from pure Cu target. Using a Faraday cup and a pepper pot system, we studied the extracted charges and the geometric quality of the beams.

Materials and methods

The Platone accelerator is a LIS source with an electrostatic system to extract and accelerate the ions. It consists of a KrF excimer laser operating in the UV range (λ : 248 nm, τ : 25 ns) to get PLA from solid targets and a vacuum chamber device for the expansion of the plasma plume, the extraction and acceleration of its ion component. The maximum output energy of the laser is 600 mJ. The angle formed by the laser beam with respect to the normal to the target surface is 70° . Focalizing the laser beam by a thin lens of 15 cm length, the spot area onto the target surface was fixed at 0.005 cm^2 , obtaining an irradiance of the order of 10^8 W/cm^2 .

The accelerating system consist of three parts[X]: an expansion chamber (EC), closed around to the target support (T) at a positive high voltage (HV) of +40 kV, a pierce ground electrode (GE) placed at 3 cm distance from EC and a third electrode (TE) placed at 2 cm from GE connected to a power supply of negative bias voltage of 20 kV. In this way it is possible to generate an intense accelerating electric field in two gaps, between EC-GE and GE-TE. Four capacitors of 1 nF, between EC and ground, stabilize the accelerating voltage during the fast ion extraction.

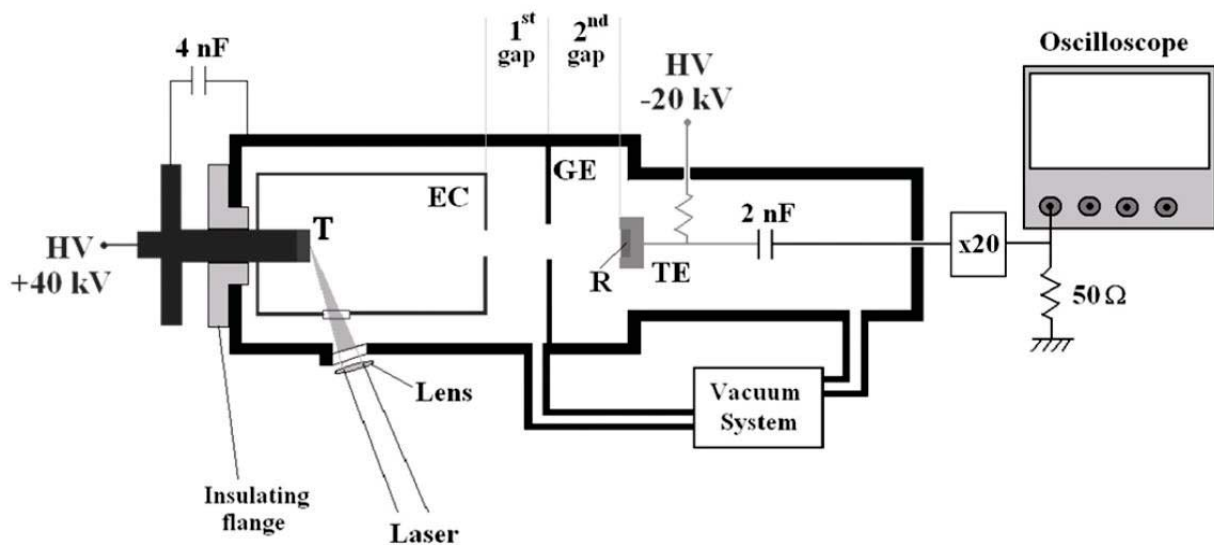


Figure 1: Schematic drawing of the LIS accelerator (T: Target support, EC: Expansion Chamber, GE: Ground Electrode, R: Radiochromic, TE: Third Electrode)

The TE is also utilized as Faraday cup collector; in fact it is connected to the oscilloscope by a HV capacitor (2 nF) and a voltage attenuator, x20, in order to separate the oscilloscope from the HV and to suit the electric signal to oscilloscope input voltage. The value of the capacitors (4 nF) applied to stabilize the accelerating voltage and the one of the capacitors (2 nF) used to separate the oscilloscope from the HV are calculated assuming a storage charge higher than the extracted one. Under this condition, the accelerating voltages during the charge extraction is constant as well as the oscilloscope is able to record the real signal. TE is not able to support the suppressing electrode on the cup collector and therefore secondary electron emission, caused by high ion energy, is present.

In order to compare the efficiency of the extraction and the geometric quality of the beams we varied the configuration of the EC (the extracting electrode) by modifying the hole. We mounted a grid and so we obtained three configurations (see Fig. 2):

- extraction hole without grid **(a)**,
- extraction hole with a plane grid **(b)**,
- extraction hole with a curved grid, radius 0.8 cm **(c)**.

The attenuation factor of the grid is 20%. Using TE as Faraday cup and a pepper pot system (see Fig. 4), we studied the extracted charges and the geometric quality of the beams.



Figure 2: Photos of the extraction hole without a grid (a), with a plane grid (b) and with a curved grid (c).

Results

The value of the laser irradiance used to produce ion beams was $1.0 \times 10^8 \text{ W/cm}^2$ and the ablated target was pure (99.99 %) disk of Cu. Figure 3 shows the extracted charge for different accelerating voltage values for the three configurations. The Faraday cup was placed at 25 cm from the target.

A measure of the beam quality could be the product of the beam's width and divergence, where the divergence relates to the random or thermal velocity spread. So, for the geometric characterization of the beam we performed emittance measurements by the pepper pot technique [10].

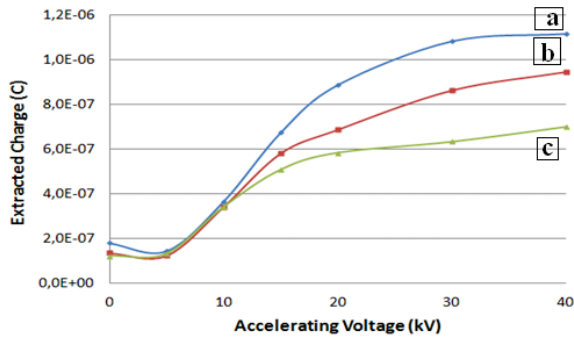


Figure 3: Extracted charge for different anode configurations.

use, led to adopt these detectors as simple ion beam transverse properties diagnostic tools. So, the ion beam after the mask imprinted the radiochromic film and then it was possible to measure the divergence of all beamlets. The divergence values allowed to determinate the beam area in the trace plane TPx. For a z-axis beam propagation, the x-plane emittance ϵ_x is $1/\pi$ times the area Ax in the TPx occupied by the points representing the beam particles at a given value of z.

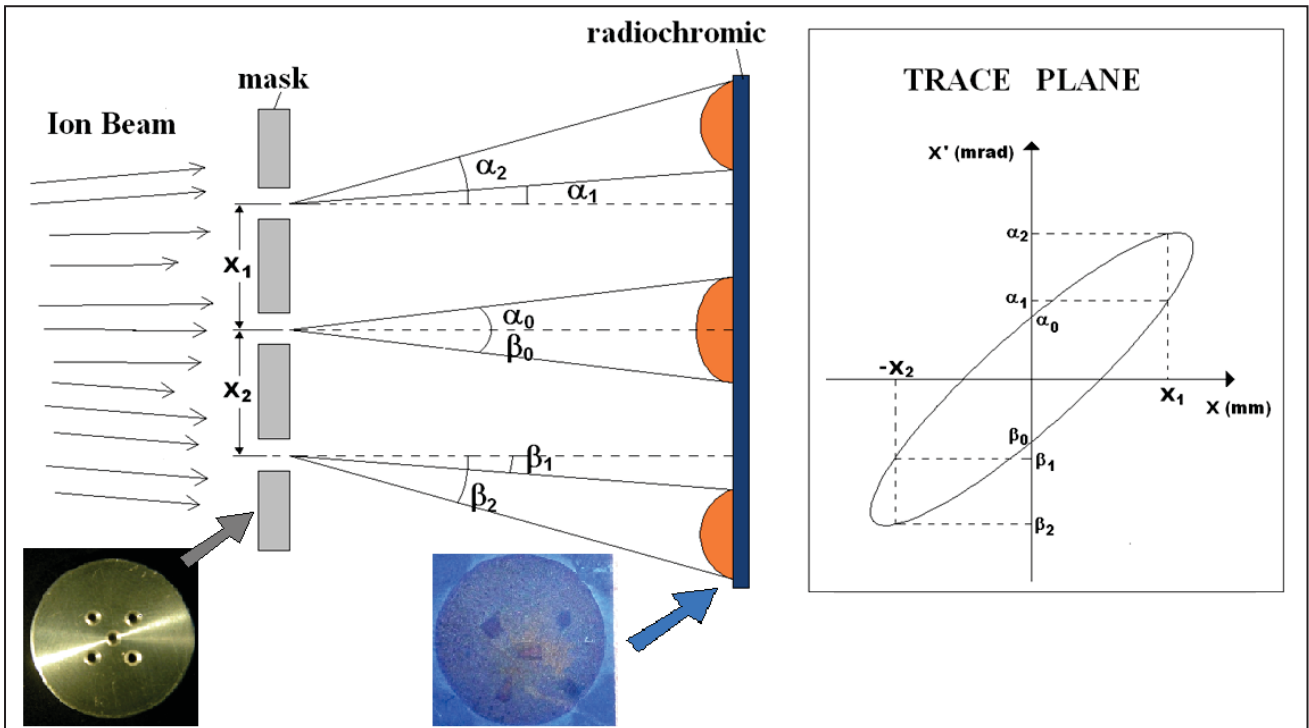


Figure 4: sketch of the system used to measure the emittance value by pepper pot technique.

Figure 4 shows a sketch of the system used to measure the emittance value by pepper pot technique. The mask we used has 5 holes of 1mm in diameter and it was fixed on the GE. One hole is in the centre of the mask and 4 holes are at 3.5mm from the centre. We used as photo-sensitive screen radiochromic films (R) Gafchromic EBT, placed on the TE. Radiochromic detectors involve the direct impression of a material by the absorption of energetic radiation, without requiring latent chemical, optical, or thermal development or amplification. A radiochromic film changes its optical density as a function of the absorbed dose. This property and the relative ease of

So, we applied 250 laser shots to imprint the radio-chromic films. We measured the emittance for the three different anode configurations.

Discussion

By the radiochromic images we draw the ellipses in the trace plane and we calculated the area. The results are shown in Fig. 5 were it is inserted a table of the emittance values found. The obtained results show that the best configuration to have a low emittance value is the hole without the grid.

Therefore, by Liouville's theorem it is known that the area occupied by the particle beam in PPx is an invariant quantity and the normalized emittance is:

$$\epsilon_{nx} = \beta\gamma \epsilon_x \quad (1)$$

where $\beta=v/c$ and γ is the Lorentz factor.

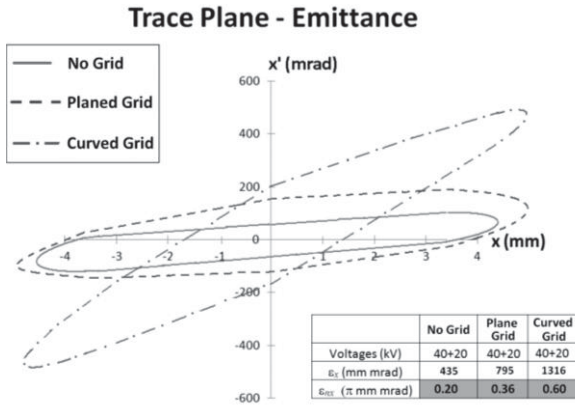


Figure 4: Emittance diagram in the trace plane for different anode configurations.

We perform measurements of emittance in the “no grid” configuration for different accelerating voltages. The obtained values of the area in the TPx resulted of 613, 545 and 435 mm mrad for 30, 40 and 60 kV of total accelerating field, respectively (Fig. 5).

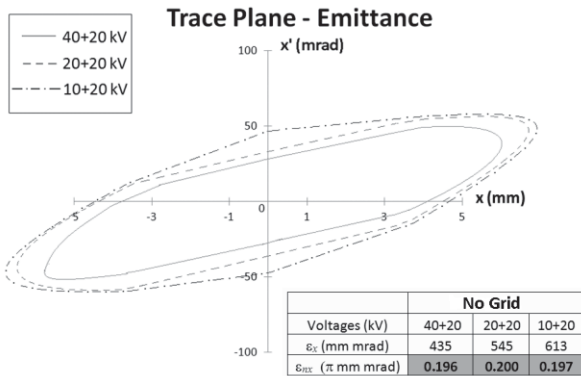


Figure 5: Emittance diagram in the trace plane for different accelerating voltage values, in “no grid” configuration.

Considering equation (1) we found the normalized emittance values. For all the applied voltage values, the normalized emittance resulted constant:

$$\epsilon_{nx} = 0.2 \pi \text{ mm mrad.}$$

By these results, PLATONE is very promising to be used to feed large accelerators. The

challenge of the moment is to get accelerators of dimensions so small that can be easily deployed in little laboratories and hospitals.

Conclusions

The post-acceleration of ions emitted from laser-generated plasma can be developed to obtain small and compact accelerating machines. The output current can easily increase on accelerating voltage. We have also demonstrated that by two gap of acceleration it is possible to increase the ion energy avoiding to apply only one acceleration voltage of high value. Increasing the voltage of the first accelerating gap, we increased substantially the efficiency of the extracted current due to the rise of the electric field and extracting volume inside the EC. We measured the geometric characteristics of the beam by means the pepper pot technique. We found a low value for the normalized emittance of our beams, $\epsilon_{nx} = 0.2 \pi$ mm mrad.

So this study have demonstrated that our apparatus can be produce ion beam with good quality, such as low emittance. For this reason it is very promising to be used to feed large accelerators.

References

- [1] M. Hegelich, S. Karsch et al, Phys. Rev. Lett., **89** (2002) 085002.
- [2] S. C. Wilks, A. B. Langdon et al, Phys. Plasmas, **8** (2001) 542.
- [3] T. V. Liseykina, M. Borghesi et al, Plasma Phys. Control. Fusion, **50** (2008)124033.
- [4] L. Torrioni, S. Cavallaro et al, Rad. Eff. and Def. in Solids, **165** (6-10) (2010) 509-520.
- [5] V. Nassisi and A. Pedone, Rev. Sci. Instrum., **74** (2003) 68.
- [6] F. Belloni, D. Doria, A. Lorusso, and V. Nassisi, Rev. Sci. Instrum., **75** (2004) 4763.

- [7] A. Lorusso, L. Velardi et al, Nucl. Inst. and Meth. in Phys. Res. B, **266** (2008) 2490-2493.
- [8] F. Noli, A. Lagoyannis and P. Misaelides, Nucl. Inst. and Meth. in Phys. Res. B, **266** (2008) 2437–2440.
- [9] M. Rosinska, B. Badziak, P. Parys, J. Wołowski and M. Pisarek, Appl. Surf. Sci., **255** (2009) 5418–5420.
- [10] J.G. Wang, D.X. Wang and M. Reiser, Nucl. Inst. and Meth. in Phys. Res. A, **307** (1991) 190-194.

Misure di radioattività naturale nel sito preistorico di *Grotta dei Cervi* in Porto Badisco (LE)

Buccolieri G¹, Castellano A¹, Congedo A¹, Buccolieri A², Nassisi V¹, Cataldo R¹, Gorgoglione MA³, Ciccarese N⁴, Delle Side D¹, Velardi L¹

¹ Dipartimento di Matematica e Fisica, Università del Salento, via per Monteroni, 73100, Lecce, giovanni.buccolieri@unisalento.it

² Dipartimento di Scienze e Tecnologie Biologiche e Ambientali, Università del Salento, via per Monteroni, 73100, Lecce

³ Soprintendenza per i Beni Archeologici della Puglia, via Duomo 33, 74100, Taranto

⁴ Gruppo Speleologico Salentino, Maglie (LE)

Abstract

Nel presente lavoro sono riportati I risultati di una campagna di misure finalizzata alle determinazioni della concentrazione di radon all'interno di Grotta dei Cervi di Porto Badisco (LE). Grotta dei Cervi è una cavità carsica caratterizzata da un complesso pittorico neolitico imponente.

Introduzione

Recentemente, e con maggior frequenza rispetto a qualche anno fa, capita che i mezzi di comunicazione si occupino di radon. Il gas nobile radon è un elemento presente in natura, con cui dobbiamo convivere, ma da cui dobbiamo anche proteggerci, poiché, essendo un gas radioattivo, durante il suo processo di decadimento emette radiazioni ionizzanti.

Le concentrazioni di radon nell'aria sono variabili in funzione, oltre che della presenza di uranio nel sottosuolo, anche di numerosi parametri fisici o meteorologici come la geomorfologia del sito, la pressione atmosferica, la temperatura, l'umidità, la stagione dell'anno. Il radon, liberandosi dal suolo in forma gassosa e attraversando il terreno, raggiunge la superficie e si mescola rapidamente con l'atmosfera ottenendo una concentrazione tipicamente inferiore a 10 Bq/m³.

Ben diversa è invece la situazione per i luoghi chiusi dove si raggiungono normalmente valori molto superiori (anche di 2-3 ordini di grandezza).

In Italia esiste una normativa che offre un quadro di riferimento sulla problematica del radon negli ambienti di lavoro, in particolare si rammenta il D.Lgs. n° 241 del 26 maggio 2000 [1], in attuazione della direttiva 96/29/EURATOM in materia di protezione sanitaria della popolazione e dei lavoratori contro i rischi derivanti dalle radiazioni ionizzanti. Il livello di azione fissato dal decreto, per gli ambienti di lavoro, è pari a 500 Bq/m³. La normativa fornisce inoltre informazioni relative al calcolo della dose ammissibile per anno.

Nel presente lavoro sono riportati i risultati sperimentali di una campagna di misure atte alla determinazione della concentrazione di radon nella Grotta dei Cervi in località Porto Badisco (Le) al fine di valutare i tempi di permanenza in grotta per gli operatori.

La Grotta dei Cervi di Porto Badisco (LE), già candidata a patrimonio mondiale UNESCO, è uno dei siti archeologici più significativi del territorio salentino per la presenza di uno straordinario repertorio di pittogrammi di epoca neolitica e di altre evidenze archeologiche che attestano una lunga frequentazione della grotta dal paleolitico superiore all'età dei metalli.

Il sito si estende lungo 3 corridoi principali, le cui pareti sono decorate con pittogrammi di epoca neolitica realizzati in ocre rosse e, in numero maggiore, con un impasto a base di guano di pipistrello (Graziosi).

La Grotta dei Cervi

La Grotta dei Cervi in località Porto Badisco (Le) è un notevole complesso sotterraneo, di antica frequentazione a scopo di culto del periodo neolitico. Essa è situata in località "Montagnola"; carta I.G.M. 215 III S=, long. Est Monte Mario 6°02'0", latid. Nord 40°04'54", quota m 26 s.l.m; sviluppo spaziale di m 1550 (rilievo di Franco Orofino, 1970); temperatura interna medi 16-20° C; infine, umidità relativa media 92-99%.

La Grotta è stata scoperta il 1° febbraio del 1970 da cinque membri del Gruppo Speleologico Salentino "P. de Lorentiis" di Maglie - Lecce-(I.Mattioli, S.Albertini, R.Mazzotta, E.Evangelisti e D.Rizzo) ed è il complesso pittorico neolitico più imponente d'Europa. In un primo momento le si diede il nome di "Antro di Enea", per via della leggenda secondo la quale Enea sbarcò in Italia proprio a Porto Badisco. Il nome attuale deriva dalle successive scoperte dei pittogrammi. La grotta non è accessibile al pubblico. Reperti ceramici rinvenuti alla base dei pannelli pittorici hanno conferito una datazione di circa 3.900 anni A.C., che colloca i riti di Badisco in equilibrio nella fase di poderosa trasformazione dei cacciatori-raccoglitori, in allevatori-coltivatori. La grotta è ricca di pitture parietali, brune e nere, schematiche, figurative, essenziali, tracciate sulle umide pareti rocciose della grotta,

usando del guano di pipistrello mescolato con argilla bruna. Sono circa tremila i segni pittorici, compresi anche i pochissimi di colore rosso racchiusi in un ristretto spazio e schizzati usando della ocre rossa. Questi segni sono giunti a noi probabilmente grazie al regolare microclima che ha "governato" la grotta. Luogo di culto preistorico, unico nel suo genere in tutta Europa, la Grotta dei Cervi è difficilmente accessibile ed è chiusa non solo al grande pubblico ma anche agli studiosi per non alterare il delicato microclima che ha permesso sinora la conservazione delle pitture. Il sistema naturale di climatizzazione non deve essere assolutamente modificato, ad esempio per un eventuale sfruttamento turistico a diretto contatto con il complesso, altrimenti è certa e incontrovertibile la distruzione totale delle pitture parietali della Grotta dei Cervi di Porto Badisco, riconosciuta come il più importante complesso pittorico neolitico in Europa.

La Grotta dei Cervi di Porto Badisco non tutela solo le pitture parietali, ma conserva un inestimabile lascito, costituito da resti di armi e utensili in selce, ossidiana ed osso, cocci di ceramica ed un numero considerevole di misteriosi ideali segreti che raccontano il nostro passato e quello di questa nostra terra.

Materiali e Metodi

Il presente lavoro, svolto nell'ambito di una collaborazione tra l'Università del Salento e Soprintendenza per i Beni Archeologici della Puglia, ha avuto come finalità la determinazione della concentrazione del gas radon all'interno della Grotta dei Cervi, in località Porto Badisco, ai fini sia di una valutazione del rischio per la sicurezza e la salute del personale scientifico presente che per studi microclimatici.

Per portare a termine tale studio, è stata indispensabile disporre di una strumentazione adeguata: in grado di eseguire misure in tempi contenuti, non

richiedente alimentazioni esterne, facile da trasportare, resistente ad elevati valori di umidità relativa sono le principali richieste.

A tale scopo, si è utilizzato un rilevatore a stato solido, il RAD07, prodotto dalla DURRIGE Company. Al fine di ottimizzare i parametri strumentali sono state realizzate una serie di misure preliminari prima in laboratorio e poi in situ.

In Fig. 1 si riporta la planimetria della grotta.

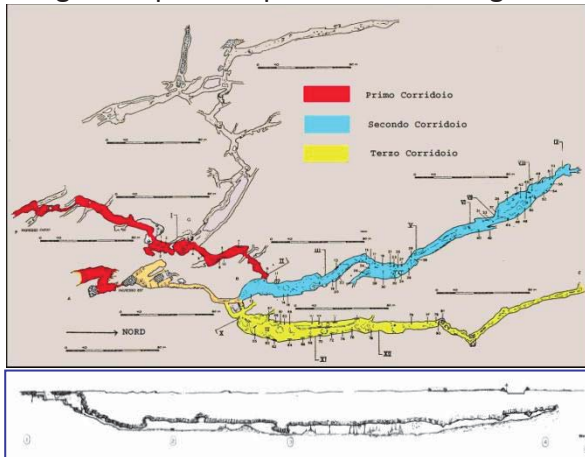


Fig. 1: Planimetria della grotta

L'interno della grotta offre un suggestivo spettacolo di dipinti rupestri, centinaia di pitture realizzate dagli antichi abitanti della grotta ed a cui deve il suo nome per la ricorrente rappresentazione e disegno di cervi (Fig. 2).



Fig. 2: Pittogramma rupestre raffigurante scene di caccia

Come si evince dalla figura 1, la grotta si sviluppa seguendo tre corridoi. Il secondo corridoio, oggetto delle misure del presente

lavoro, è ricco di iscrizioni pittoriche, tra le quali scene di caccia, con uomini che tendono l'arco e circondano le prede, rappresentazioni di vita quotidiana e di oggetti, figure di donne di uomini e di bambini, cervi cani ed altri animali, ed altre di contenuto magico e religioso (fig. 4), non ancora del tutto identificate nel loro significato. Una lettura accurata dei pittogrammi conferma la presenza di animali domestici e coltivazioni in atto a riprova del fatto che l'uomo di Badisco oltre a cacciare allevava e coltivava (Fig. 3).



Fig. 3: Dettaglio di un pittogramma. I punti in rosso rappresentano un campo di grano mentre, oltre alle scene di caccia, si evidenzia la presenza di animali "allevati"



Fig. 4: Dettaglio di un pittogramma.

Probabilmente la vita nella grotta dava ai vari spazi interni diverse funzioni, l'area più vicina all'ingresso era quella in cui si svolgeva la vita quotidiana, mentre le parti più all'interno della caverna erano utilizzate per i culti sacri.

La parte della grotta forse più affascinante, ed anche un po' misteriosa è rappresentata dalla stanza che si trova al fondo della grotta, probabilmente uno dei principali accessi in passato, chiamata "stanza delle manine" (Fig. 5) la cui volta è completamente decorata da numerose impronte di mani, lasciate lì dagli antichi piccoli abitanti della caverna probabilmente nell'esecuzione di riti di iniziazione: nel silenzio totale che domina qui, l'immagine delle impronte sulle pareti è particolarmente evocativa ed anche un po' inquietante.



Fig. 5: Ambiente della Grotta: la "stanza delle manine"

La grotta alterna nel suo complessivo sviluppo zone di difficile accesso con "stanze" di vaste dimensioni Fig. 6.

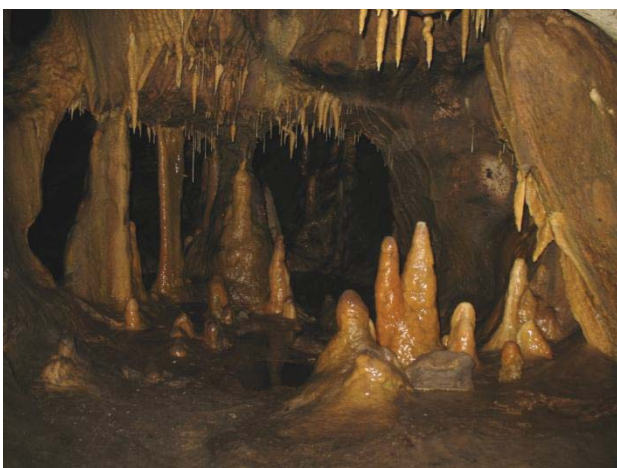


Fig. 6: Particolare della grotta

Per decidere in quali ambienti sotterranei della Grotta effettuare le misure di concentrazione di radon, sono state considerate le regioni di maggiore interesse

dal punto di vista storico e quindi maggiormente frequentate dagli studiosi. Numerosi studi hanno messo in evidenza la variabilità della concentrazione di radon anche fra ambienti contigui: tenendo conto che, nel caso specifico della Grotta, si tratta di un unico ambiente interconnesso, le misure sono state effettuate in ogni ambiente "funzionalmente" separato. Lo strumento utilizzato per la misura del Radon in aria è composto dal rivelatore RAD7: rivelatore a stato solido costituito da materiale semiconduttore (silicio) che converte la radiazione alfa direttamente in segnale elettrico. La procedura per la misura dell'emanazione di gas radon mediante il RAD7 è suddivisa nelle seguenti tre fasi: epurazione del RAD7; esecuzione della misura e lettura del RAD7. Nella fase di epurazione lo strumento è connesso ad un filtro per polveri ed al filtro contenente il gel di silice al fine di bloccare il particolato sospeso e di generare flussi d'aria con una umidità relativa inferiore al 10% (come raccomandato dal costruttore). L'operazione di purificazione è protratta normalmente per diversi minuti antecedentemente ad ogni operazione di misura e ovviamente in ambienti aperti (fuori dalla grotta). Le misure sono state eseguite con cicli da 30 minuti: in ogni acquisizione sono stati eseguiti 5 cicli. Le misure sono state eseguite in condizioni di equilibrio secolare Po-218/ Rn-222: dopo circa 15 minuti dall'inizio della misura, il Po-218 raggiunge la condizione di equilibrio secolare col Rn-222. In queste condizioni l'attività del Po-218 è pari al 97% dell'attività del radon. Per tale motivo i risultati del primo ciclo di misura sono stati scartati.

Risultati, discussione e conclusione

In figura 7 si riporta la planimetria della Grotta con l'indicazione dei punti di campionamento.

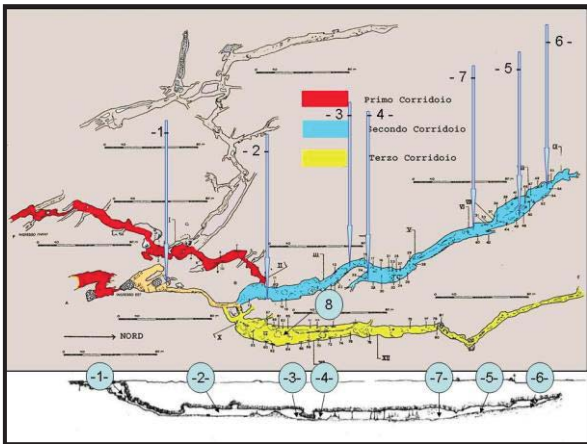


Fig. 7: Punti di misura

Nella tabella che segue (Tab. 1) sono riportati i valori di concentrazione del Radon, in Bq/m³, nelle diverse regioni analizzate: si riporta la media pesata delle 4 acquisizioni utili.

	Data	Media pesata
1	4-apr-11	300±50
2	20-apr-11	780±70
3	30-apr-11	810±80
4	18-mag-11	1210±90
5	21-mag-11	3530±150
6	28-mag-11	3860±160
7	7-giu-11	3540±150
8	16-giu-11	3420±150

Tab. 1: Risultati campionamento

La discrepanza esistente tra le varie concentrazioni di Radon misurate nei vari punti, non può essere giustificata andando ad analizzare la geologia del sottosuolo in quanto, come è noto, la concentrazione di Radon dipende sì, dalla concentrazione di uranio presente nelle rocce che lo costituiscono, ma il sito presenta una conformazione compatta ed univoca.

Come suggerito dalla letteratura relativa sull'argomento in questione, la variazione nell'andamento delle concentrazioni di radon all'interno della Grotta, si potrebbe spiegare con stati di microclima differenti.

In funzione di quanto indicato nel D. Lgs. 241/00, utilizzando il fattore di conversione, si riportano in Tab. 2, i tempi di permanenza tali da non superare il livello di azione per gli

addetti al lavoro, pari a 3 mSv/anno di dose. Il fattore convenzionale di conversione è fissato in 3x10⁻⁹ Sv di dose efficace per unità di esposizione espressa in Bq h/m³. Un ambiente a 500 Bq/m³ frequentato per 2000 h lavorative (ore lavorative annuali) produce una dose efficace pari a:

$$500 \frac{\text{Bq}}{\text{m}^3} \cdot 2000 \text{ h} \cdot 3 \cdot 10^{-9} \frac{\text{Sv}}{\text{Bq} \frac{\text{h}}{\text{m}^3}} = 3 \text{ mSv} \quad (1)$$

Fissato il livello di azione (3 mSv), stabilito dal D.Lgs. 241/00, note le concentrazioni di radon, ed il fattore di conversione, si ricavano i tempi di esposizione invertendo la formula, e risolvendo rispetto a questi.

	Concentrazione Rn [Bq/m ³]	Tempi di permanenza [h]
1	300±50	3.300±600
2	780±70	1280±120
3	810±80	1240±120
4	1210±90	830±60
5	3530±150	283±12
6	3860±160	259±10
7	3540±150	282±12
8	3420±150	292±13

Tab. 2: Risultati campionamento

Attualmente, all'interno della grotta dei Cervi, il Laboratorio di Archeometria del Dipartimento di Matematica e Fisica dell'Università del Salento, sta eseguendo delle misure di microclima e studi sui materiali. Tali lavori richiedono la presenza di operatori con frequenza bisettimanale e con tempi di permanenza in grotta, per singolo accesso, di circa tre ore per un totale di circa 80 ore per anno: dai dati ottenuti nel presente lavoro si evince che tali accessi non richiedono l'utilizzo di alcun ulteriore dispositivo di protezione.

E' interessante confrontare i valori registrati, nel presente lavoro di ricerca, con quelli registrati precedentemente dallo stesso gruppo di ricerca e relativi alla Grotta della

Zinzulusa (Castro-LE). In Fig. 8 si riportano i punti di misura e in Tab. 3 i risultati.

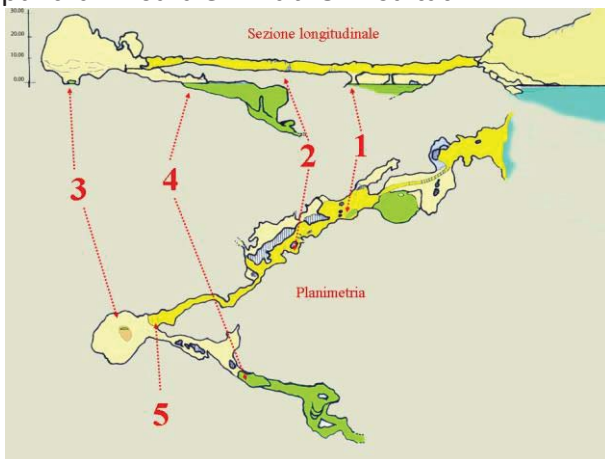


Fig. 8: Punti di misura nella Grotta della Zinzulusa

	Concentrazione Rn [Bq/m ³]
1	280 ± 50
2	540 ± 90
3	1280 ± 110
4	860 ± 90
5	830 ± 190

Tab. 3: Valori di radon misurati nella Grotta della Zinzulusa

Anche in questo caso non sono stati evidenziati rischi apprezzabili nè per i numerosi visitatori nè per gli addetti ai lavori.

References

- [1] Decreto Legislativo 26 maggio 2000, n°241, Attuazione della direttiva 96/29/Euratom in materia di protezione sanitaria della popolazione e dei lavoratori contro i rischi derivanti dalle radiazioni ionizzanti, Gazzetta Ufficiale n°153-Serie Generale, (4 luglio 2001)

A comparative analysis of old and recent Ag coins by XRF methodology

A. Italiano¹, L. Torrisi², M. Cutroneo², C. Gentile² and A. Torrisi³

¹INFN, Sez. CT, Gruppo Coll. ME, V.le F.S. D'Alcontres 31, 98166 S. Agata (ME), Italy

²Dip.to di Fisica, Università di Messina, V.le F.S. D'Alcontres 31, 98166 S. Agata (ME), Italy

³Dipartimento di Fisica, Università di Catania, V.le S. Sofia 64, 95124, Catania, Italy

Abstract

The investigation of silver coins dated since the first century B.C. up to recent times, coming from different countries in the world, has successfully generated a growing interest among numismatic researchers. The classification of these coins into originals, copies and imitations - according to their provenance and to their Ag content - has been performed by using the X-ray fluorescence (XRF) analysis. The archaeological challenge is to explain the large diversification of these coins, to determine the differences in composition, weight and physical aspects. A non-destructive physical method was employed to study the properties of silver coins (as in this case) allowing a detailed characterization of the analyzed samples. The XRF analysis was applied to the bulk, through an X-ray tube, and to the surface patina, through an electron beam.

Introduction

The growing interest in the archaeological research techniques is important to have detailed evidence of the history and culture of the past. In particular our attention has focused on XRF analysis of silver coins. The samples originate from the first century B.C. until today, coming from different countries whose study has recently gained value relatively to their origin context, allowing to get historical information. A fundamental problem deals with the classification of these coins into originals, copies and imitations, according to their provenance and to their silver content. In the last years, Greek and Roman Ag coins have been well classified by means of the X-ray fluorescence (XRF) analysis [1, 2]. The archaeological problem arises from the necessity to explain the large

diversification of these coins, as well as the differences in composition, weight and physical aspects [3]. Ancient and recent coins usually have a roughly homogeneous core and mostly thin surface layer with different composition and varying thickness. This layer can be silver enriched, oxidized, corroded or soiled. Therefore, the application of a non-destructive physical method represents a powerful tool to investigate the properties of silver coins. We adopted the XRF analysis with an X-ray tube to study deep layers, while for surface layers an electron beam was employed [4].

Materials and methods

We prepared an experimental set-up, in which each coin was examined by the XRF technique using an X-ray tube at 23 kV

voltage and 15 μA current using an Ag anode (Amptek), besides to a 20 keV electron microprobe of a SEM microscope (Fei Quanta Inspect) [5]. A Si(Li) detector, cooled by Peltier effect, was employed to detect photons between 1 and 20 keV energy with an energy resolution of 190 eV FWHM at 5.9 keV, with a typical acquisition time of 30 minutes.

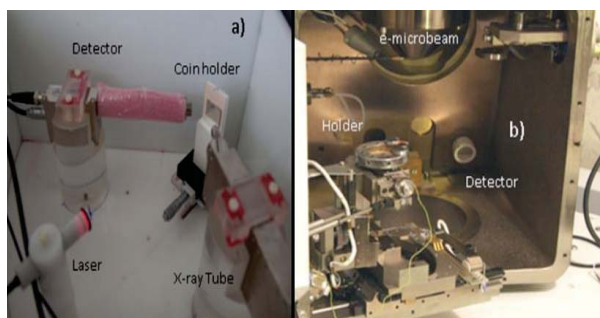


Fig. 1. Experimental set-up of the XRF systems using a) X-ray tube and b) an e-microbeam.

Fig. 1 shows a picture of the XRF systems using a) X-ray tube and b) an e-microbeam. The XRF analysis using X-ray tube was performed in air adopting a coin-detector distance of 2.5 cm, while the analysis carried out by means of an e-microbeam was conducted in high vacuum (10^{-6} mbar). Pure thick Ag sheets, supplied by Goodfellow, were used as certified reference materials, and irradiated under the same conditions as the samples investigated. All analyzed coins were chemically and, in some cases, mechanically cleaned to remove any eventual dirtiness trace.

The 23 keV photons supplied by the X-ray tube in Ag bulk have an absorption mass coefficient of about $10 \text{ cm}^2/\text{g}$; the Ag thickness at which the initial intensity I_0 decreases to 1% is about 460 μm , according to NIST database [6]. In addition, 20 keV electrons in Ag bulk have a range of about 0.5 μm , evaluated by SREM code [7], therefore the estimated composition will refer to the bulk if using the X-ray tube, while regarding

only to the surface layers if we employ the SEM electron microbeam.

We analyzed two sets of silver coins: the old Ag coins and the recent ones.

The 'ancient' group includes: #1) Greek Tetradrachms from Messana, 470–466 B.C.; #2) Greek Tetradrachms from Messana, 470–466 B.C. (counterfeit); #3) Roman Denarius, II Cen. A.C.; #4) Alexander the Great, Drachma, IV Cen. A.C.; #5) Gigliato Roberto D'Angiò, XIV sec. A.C. (counterfeit). The 'recent' group includes: #6) 1 Swiss Franc, 1934; #7) Quarter Dollar, USA, 1943; #8) 5 Lire, Vittorio Emanuele, Italy, 1945; #9) 500 Lire, Caravelle, Italy, 1960; #10) 500 Lire, Guglielmo Marconi, Italy, 1974. The photos of the ten coins are reported in Fig. 2.



Fig. 2. Picture of the ten analyzed coins.

The Ag content in the bulk composition of each coin was measured with respect to the standard calibration sample. Different thickness samples were used, namely from 0.5 mm up to 5 mm, in steps of 0.5 mm, in order to provide as a good comparison with coins having the same thickness.

Results

The geometry of the samples plays a decisive role in the quantitative XRF: Fig. 3 shows that the X-ray beam or electron beam may have a different incident angle, Φ_{inc} , penetrating in a convex surface: a) at high incident angles (with respect to the normal direction) the ionized layers are close to surface so that the self-absorption effects of the X-ray emission are negligible; b) for small incident angle the

ionized layers are depth and the self-sorption effects appear to be more consistent.

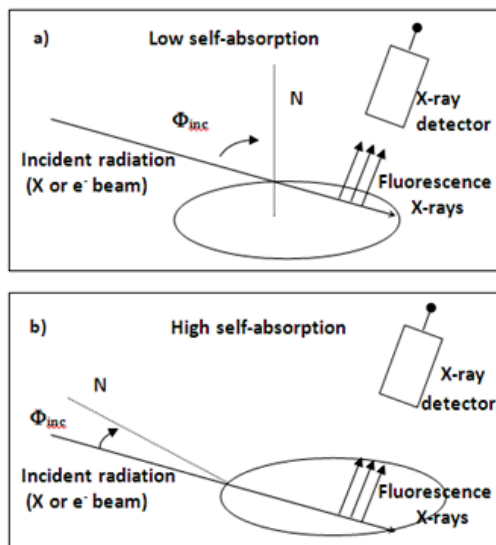


Fig. 3. Sketch of geometry for a) low self-absorption effects and for b) high self-absorption effects.

As a matter of fact, when the surface morphology has convexities, the study of geometry, concerning irradiation, X-ray detection and the region of the analyzed surface is crucial.

In order to take into account the X-ray yield vs. target irregularities, we studied the dependence of the Ag- L_{α} line X-ray yield on the incident angle for a convex surface having 1 cm curvature radius. As results show (see Fig. 4a), at large angles (glancing conditions) the yield increases, while it decreases at low incidence angles (close to the normal incidence).

A gradient of about 60% may occur due to these geometrical effects with the consequence of altering the final results of the Ag concentration measurements. So, the best choice - when possible - is to analyze the flat regions of the coins; in other cases, one needs to correct the quantitative yield for the 'corrective factor' due to the self-absorption effect. The metal thickness deserves a particular care too, since the Ag- L_{α} yield, induced by 23 keV X-rays, linearly increases with the film thickness up to about 2.5 mm

thickness (saturation value), as reported in the plot of Fig. 4b. A lower thickness of the coins can affect the total Ag-yield due to a lower X-ray fluorescent yield emitted by the sample. Thus the comparison between the standard thickness and the coin thickness must be considered in order to have a correct quantitative determination of the Ag content. As an example, Fig. 5 shows a typical XRF spectrum obtained analyzing an old silver coin: Greek Drachma, IV Cent. B.C., while Fig. 6 reports a typical XRF spectra obtained analyzing a recent silver coin: 1 Swiss Franc,

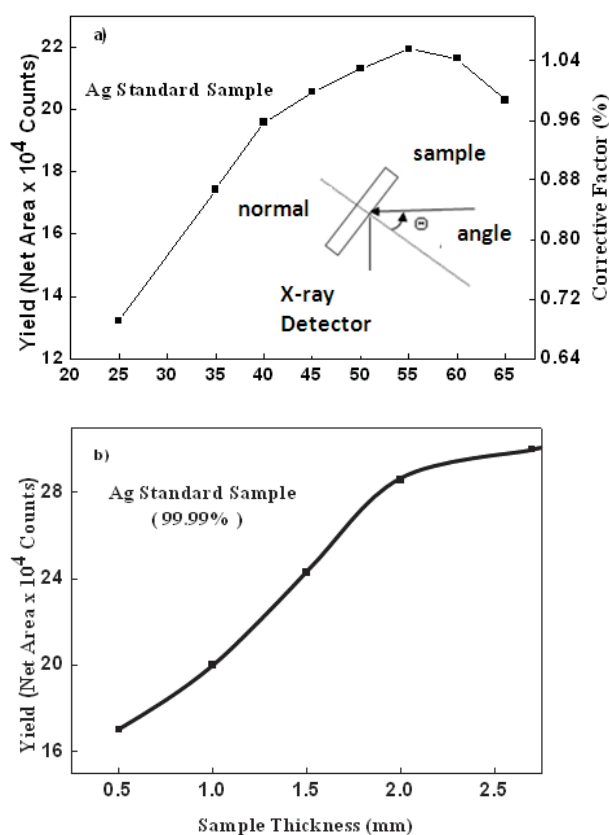


Fig.4. a) Ag- L_{α} line X-ray yield vs. the incident angle for a convex surface having 1 cm curvature radius and b) the plot of Ag- L_{α} yield vs. the film thickness.

1934. In our investigations, the quantitative analyses are based on the comparison with the standard sample as follows. The X-rays yield is described by the relation:

$$Y=C \phi \varepsilon \sigma_p \Delta t F_c \quad (1)$$

where C is the element concentration, ϕ is the radiation flux (X-rays or electrons), ε is the detection efficiency, σ_p is the X-ray production cross section for the given line, Δt is the collection time and F_c is the corrective factor with respect to the flat surface of the standard. Operating in the same experimental conditions of analysis for coin and standard, the measured concentration in the coin is given by:

$$C_c = C_s Y_c / Y_s F_c \quad (2)$$

The elemental atomic composition was measured for the bulk and for the surface patina by using the X-ray tube excitation and the electron SEM microbeam probe, respectively. The bulk analysis is reported in the upper spectrum while the surface analysis is featured in the bottom one (see Figs. 5) and 6). Taking into account the amount of Ag in the bulk of the coin, the measurements were performed with respect to the standard sample of pure Ag, with the same thickness of the analyzed sample.

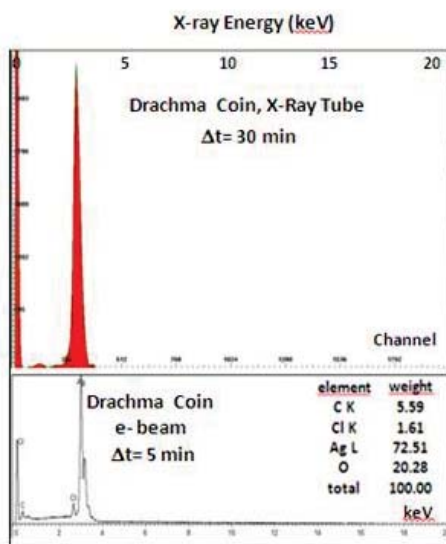


Fig.5. Set of a typical XRF spectra obtained analyzing the old silver coins: #1.

The Ag content of the bulk is always larger than the value measured in the patina layers mainly due to the presence of layers containing silver oxide. As Table I clearly

shows, the patina contains from about 5% to about 50% less than the percentage of Ag in the bulk. This result can be attributed to contamination and to oxidation processes occurring on the coin surface. The most of superficial layers are composed by Ag_2O and CuO and contain many oxidized species, such as MgO , CO_2 , SiO_2 and SO . All coins show an amount of Cu, as contaminant or as high content of the bulk composition. Cu is present as traces, as for the coin #3 and #4, where its atomic concentration is 0.33 and 0.13%, respectively. Cu is present as a bulk contribution below 10%, such as for the coins #1, #2, #6 and #8, some times at higher concentrations, such as for the coins #5, #7, #9 and #10. In coin surface the Cu content is lower with respect to its content in the bulk, again due to the presence of oxidized species at the surface, such as CuO and Cu_2O .

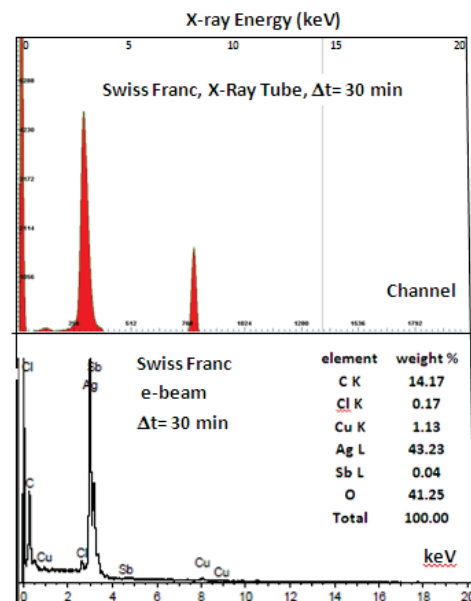


Fig.6. Set of a typical XRF spectra obtained analyzing the recent silver coins: #6 (a)

The evaluation of the thickness of patina coating in recent and old silver coins should be useful to distinguish between true and false coins, in order to find the best methodology to preserve the maintenance of coins inside museums, as well as for historical classifications and forensic

investigations. These measurements have been performed in order to improve the technique, to evaluate the correct element concentration measurement and to assure the repeatability of the analyses.

Coin	#1 Greek Tetradrachm - Messina, 470-466 B.C.	#2 Greek Tetradrachm- Messana, 470- 466 B.C., (counterfeit)	#3 Roman Denarius, II cen. B. C.	#4 Drachma, IV cen. A.C.	#5 Gigliato R. D'Angiò, XIV cen. A.C. (counterfeit)	#6 1 Swiss Franc, 1934	#7 Quarter Dollar, 1943	#8 5 Lire, V. Emanuele II, 1945	#9 500 Lire, G. Marconi, 1974	#10 500 Lire, Caravelle, 1960
Weight (g)	17.50	18.00	3.60	3.81	3.60	4.96	6.11	4.90	11.00	10.83
(E) Ag content (atm %)			73.00- -89.00	90.00			90.00	83.50	83.50	83.50
(M) Ag-bulk content (%)	74.40	83.30	89.00	73.00	35.00	82.60	82.50	75.00	69.00	83.00
(M) Ag- patina content (%)	63.70	71.25	76.38	72.51	23.35	57.44	75.29	70.33	60.00	73.32
(E) Cu content (%)						5.00	10.00	4.00	16.50	4.00
(M) Cu content (%)	1.00	2.50	0.33	0.13	33.40	6.45	13.00	5.00	13.80	13.60
Bulk Ag content errors (%)			11.00- -8.90	16.60			8.30	1.30	17.30	1.16

Table I. Percentage of silver and copper evaluated inside and on the surface of old and recent coins and their comparison with expected values; (E)=expected, (M)=measured.

Finally, XRF analysis is a useful technique to study the Ag content in bulk and patina surface. Other analyses should be considered in order of course to confirm our results and to have other characterization of the coins. Chemical investigation, X-ray diffraction, depth profiles analyses and others should be applied as comparative and complementary techniques to XRF in order to obtain more coin bulk and surface characterizations [9, 10].

Discussion and conclusions

Analyses already presented in literature [9] are in good agreement and often show that oxygen in the ratio Ag/O is low in recent coins; on the contrary, it should be higher in old coins. This trend validates that patina coating is thinner in recent coins and seems to reach tens of microns; on the other hand,

in older coins it is thicker, growing up to hundreds of microns.

References

- [1] A.S. Darling, J.F. Healy, Nature 231, 443, 1971
- [2] R. Klockenkamper, H. Bubert and K. Hasler Archeometry 41 (2), 311, 1999
- [3] L. Torrisi, G. Mondio, A.M. Mezzasalma et Al., Eur. Phys. J. D 54, 225–232, 2009
- [4] S. Sanchez Ramos, F. Bosch Reig et Al., Spectr. Acta B: At. Sp. 57 (4), 689, 2002
- [5] Amptek, Application notes 2012: <http://www.amptek.com/appnotes.html>
- [6] NIST "X-ray mass attenuation coeff", (<http://www.nist.gov/pml/data/xraycoef/index.cfm/>), 2012
- [7] E. Ziegler, SREM, The Stopping and Range of Electrons in Matter, 2012: <http://www.srim.org/SREM.htm>

- [8] F. Caridi, L. Torrasi, M. Cutroneo et Al., Appl. Surf. Sci., 2012, in press
- [9] M. Cutroneo, L. Torrasi, F. Caridi et Al., Appl. Surface Science xxx, 2012, in press
- [10] L. Torrasi, F. Caridi, L. Giuffrida et Al., Nucl. Instr. and Methods B268,1657-1664, 2010

Radiation Damage of Polycrystalline CVD Diamond with Graphite Electrical Contacts

E. Alemanno^{1,2}, M. Martino^{1,2}, A.P. Caricato^{1,2}, M. Corrado^{1,2}, C. Pinto^{1,2}, S. Spagnolo^{1,2}, G. Chiodini², R. Perrino², and G. Fiore²

¹ Istituto Nazionale di Fisica Nucleare - sezione di Lecce - via Arnesano, 73100, Lecce, Italy.

² Department of Mathematics and Physics "E. De Giorgi", University of Salento, Via Arnesano, 73100 Lecce, Italy.

E-mail address: Emanuele.Alemanno@le.infn.it

Abstract

In this work we show preliminary results of radiation damage for a polycrystalline diamond with graphite contacts in terms of time response after 62 MeV protons irradiation for a total fluence of $(2.0 \pm 0.08) \times 10^{15}$ protons/cm². In addition, we describe the realization of a new type of device made with graphite micro-strips by laser micro-writing on diamond surface. In this way we made 20 graphite micro-strips of width about 87 μm and spacing between each other of about 60 μm .

Introduction

Due to its exceptional electrical, thermal and optical properties, diamond is a very attractive material for radiation detection. Diamond can detect any kind of radiation that is more energetic than its band-gap of 5.47 eV, e.g., deep UV photons, X-rays, gamma rays, charged particles and neutrons with a dynamic range in energies spanning from 5.47 eV up to GeV of cosmic rays. Because of its radiation hardness it needs no frequent replacements, it can be operated at room temperature with no need for cooling, it has a resistivity several orders of magnitude greater than silicon, an extremely low leakage current and no need for p- type or n-type junctions as required in the fabrication of silicon radiation detectors.

In this work, we show preliminary results of a device based on detector grade polycrystalline CVD diamond film with graphite electrical contacts fabricated on

both faces of the diamond surfaces (called "Sandwich" configuration). The device was prepared by front and back irradiation of the diamond bulk by a 193 nm UV ArF excimer laser according to the experimental setup in ref. [1]. This device was characterized as a nuclear radiation detector and consequently we evaluated its response under irradiation by a ⁶⁰Co γ -ray source and 120 GeV proton beam [1].

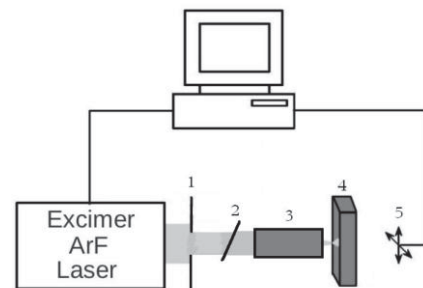


Fig. 1: Setup for micro-focusing laser beam. We used an aluminum mask with a square hole (1) and a beamsplitter (2) to divide the laser beam in two parts. One of these parts was directed onto a micro-spot focusing objective (3) to focalize the beam on diamond sample surface (4) that was kept on an automatic moving holder (5).

In this work we studied radiation damage of the diamond detector in terms of time response in order to verify radiation damage of the new type of ohmic electric contact. Finally, we made graphite micro-strips on another diamond sample surface to realize a new type of device by the experimental setup in Fig. 1.

Diamond graphitization

In this work we used ArF excimer laser (193 nm) for diamond surface graphitization because of the optical properties of high purity diamond that absorbs radiation at wavelength of about 193 nm and it is transparent at radiation having longer wavelength [2]. The absorbed laser energy is converted to lattice thermal energy making the transition diamond to graphite energetically favorite [3]. In the same time laser light power density and laser shoots are kept lower than diamond ablation thresholds [4], [5].

In literature, graphitization processes with ArF laser light on CVD diamond are reported [5]. The authors showed that a graphitic layer was created, and not another allotropic carbon structure, making use of micro-Raman scattering spectroscopy. In ref. [6] we also made use of this technique on thermal grade polycrystalline CVD diamond to confirm the graphitic nature of the fabricated layers by excimer laser. The micro-Raman measurements on the sample irradiated with ArF excimer laser showed the presence of trigonally coordinated carbon (graphite) with different degrees of structural disorder associated to the G band at about 1580 cm^{-1} , to the D (disorder) band around 1350 cm^{-1} and to the G' band at about 2720 cm^{-1} , due to the so called turbostratic t-graphite. The turbostratic t-graphite is a stacking of graphene layers which are rotationally random with respect to one another along the *c* axis. The G' band of a typical turbostratic t-graphite is a single Lorentian peak, like in a graphene monolayer, but with

a FWHM value between 50 and 75 cm^{-1} . This is a larger value than the FWHM of a graphene monolayer G' band, which is about 25 cm^{-1} [7]. From the results obtained in previous work we graphitized an high quality Chemical Vapor Deposition (CVD) diamond sample (Fig. 2) by an ArF excimer laser and we used the same experimental conditions of ref. [6].

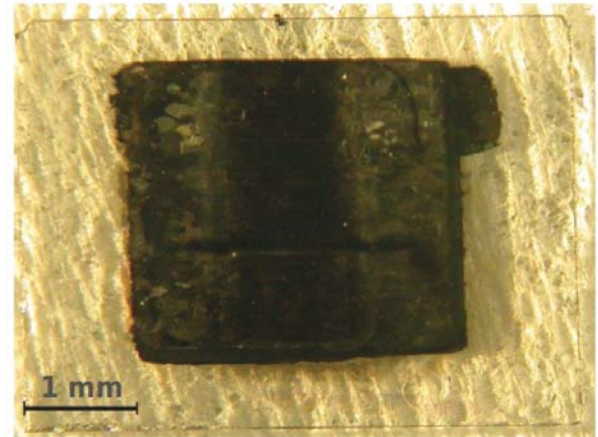


Fig. 2: Optical microscopy image of the polycrystalline CVD diamond detector grade film of $(5 \times 5 \times 0.3)\text{ mm}^3$ size after laser treatment. The black pad at the center of the device is the photo-generated graphite electrical contact created on the diamond sample surfaces taken by ref. [1].

Micro-strip graphitization

We realized graphite micro-strips on high quality Chemical Vapor Deposition (CVD) diamond sample surface by micro-focusing ArF excimer laser beam (193 nm). The sample was an un-doped synthetic detector grade polycrystalline diamond acquired from Diamond Detectors Ltd. The thickness was of $300\text{ }\mu\text{m}$ after mechanical-chemical polishing and laser cuted to a size of $0.5 \times 0.5\text{ cm}^2$. In detail we prepared 20 graphite micro-strips by irradiation of the diamond surface with a 193 nm UV ArF excimer laser (Lambda Physik LPX305i). The laser emitted 20 nsec long light pulse with an energy of about 160 mJ/pulse at 10 Hz repetition rate. The laser beam with a transverse size of about $20 \times 10\text{ mm}^2$ was directed onto an aluminum mask with a square hole to select only the central part of the beam. The mask was the object and we

focalized an image on diamond surface by a micro-spot focusing objective, 15X for 192 - 194 nm wavelengths and a numerical aperture (NA) that was 0.32. Before the objective we used a fused silica coated beamsplitter designed for a low transmission ratio of approximately 10-30 % at 193 nm at 45 degrees to reduce the laser power. The beamsplitter divides the laser beam in two parts. One of these parts was directed onto the micro-spot focusing objective to focalize the beam on diamond sample surface that was kept on an automatic moving holder. The holder was a x-y handling stage automatically controlled by a 2D step motors (see Fig. 1). The focused image was a circle of about 87 μm in diameter and the local laser fluence was about 5 J/cm^2 at the sample surface. The irradiation intensity was very uniformly distributed within the radiation spot. The device was treated in air and at room temperature. Moving diamond sample at a velocity of about 0.3 mm/s we produced 20 graphite micro-strips with width of about 87 μm and spacing between each other of about 60 μm (Fig. 3).

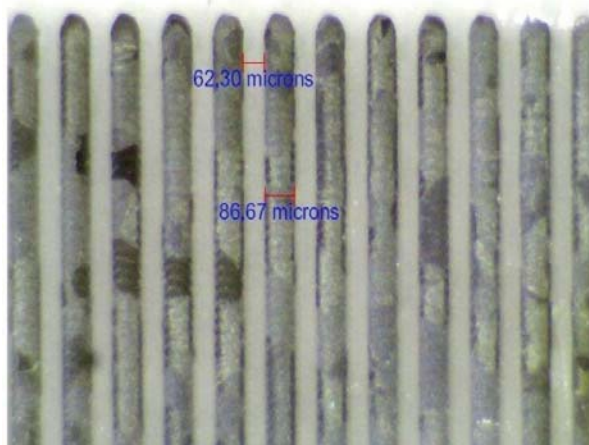


Fig. 3: Optical microscopy image of the polycrystalline CVD diamond detector grade film of $(5 \times 5 \times 0.3) \text{ mm}^3$ size after laser treatment. The black strips are graphite micro-strips on diamond sample surface.

On the other surface of diamond sample we made a scansion of the surface moving the diamond holder to a velocity of 0.3 mm/s and we created a graphite pad of 9 mm^2 like in Fig. 2 using the same experimental setup

used for micro strip focusing (see Fig. 1). The laser light power density and laser shoots are kept lower than diamond ablation thresholds [4], [5] in each case. By the sample in Fig. 3 we have demonstrated that it's possible to realize micro-strips on diamond sample. By theoretical considerations we expected this results. Graphitization process is activated from heat transfer on diamond surface by laser light absorption. Laser used by us emitted 20 nsec long light pulse, i.e. we transfer heat on diamond surface inside a time interval of 20 nsec. If we give to diamond surface heat from an epicenter (laser spot) the heat diffuses from it toward the external points. If we multiply the time duration laser pulse with thermal diffusivity for diamond given to us by Diamond Detectors Ltd company ($2.8\text{-}11.6 \text{ cm}^2/\text{s}$) we have the value of the graphitized surface by our own nanosecond laser ($0.714\text{-}23.2 \mu\text{m}^2$). This value is much less than the surface graphitized by us, because we focalized a laser spot with a diameter of 86.67 μm to create the micro-strips.

Radiation damage

In this section we complete the study about diamond detector grade [1] by studying radiation damage of polycrystalline diamond in terms of time response. For this purpose we irradiated the detector by an estimated integrated fluence of $(2.0 \pm 0.08) \times 10^{15}$ protons / cm^2 at an energy of 62 MeV on diamond sensor and evaluated the response under β source after and before protons irradiation. For protons irradiation we used the experimental setup of Fig. 4.



Fig. 4: Setup in the experimental area for the 62 MeV proton irradiation at INFN Laboratori Nazionali del Sud (Catania, Italy).

We collected protons from the zero degree beam line of the INFN Laboratori Nazionali del Sud Superconducting Cyclotron. The nominal beam current was of 10 nA and the protons bunch of about 3 nsec width and 25 ns period. While for β analysis we employed the setup in Fig. 5. A commercial diamond [8] were used as reference detector respect to graphitized detector. We lined up the devices and irradiated with the same β source to ensure a generic β electron across diamond under test (graphitized diamond) and go toward diamond to trigger (reference commercial diamond) as we can see in Fig. 5.

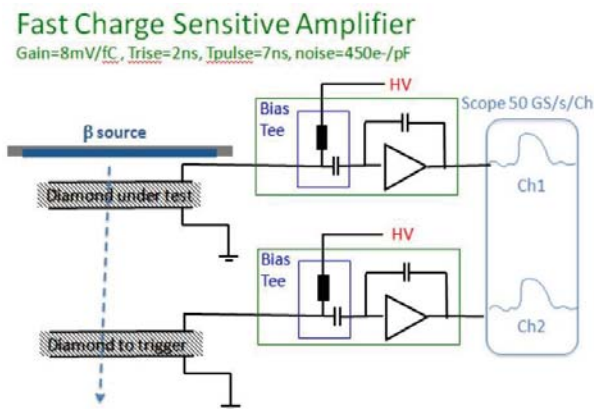


Fig. 5: β source experimental setup with fast charge amplifiers to study fast detector response.

We used two fast charge sensitive amplifiers (gain = 8 mV/fC, time rise = 2 ns, time pulse = 7 ns, noise = 450 e⁻/pF) and a digital scope to record the output signals from the devices. In Fig. 6 we report the β time responses before and after protons irradiation. The rise-time of the peaks is dominated by front-end electronics, but no change in pulse shape is observed before and after irradiation for both detectors and consequently no change in time response is evident.

Conclusions

In this work we continued the studies about a device based on detector grade polycrystalline CVD diamond film. In ref. [1] we obtained the electrode thicknesses (44 ÷ 83) nm by resistivity measurement on

graphite layers, we demonstrated the Ohmic behavior of the electrodes by dark current measurements made on the diamond device. Finally, we demonstrated that this device produce a response under irradiation by a ⁶⁰Co γ -ray source and 120 GeV proton beam. In this work we showed preliminary studies of radiation damage for polycrystalline diamond in terms of time response and realized that before and after 62 MeV protons irradiation for a total fluence of $(2.0 \pm 0.08) \times 10^{15}$ protons/cm² diamond doesn't change in time response if we test the device with a β source. The last work was the fabrication of a new type of device made with graphite micro-strips. We didn't characterize yet this detector, but we demonstrated that it's possible to do micro-writing on diamond surfaces by laser techniques. In this way we made 20 graphite micro-strips on diamond surface with width of about 87 μ m and spacing between each other of about 60 μ m.

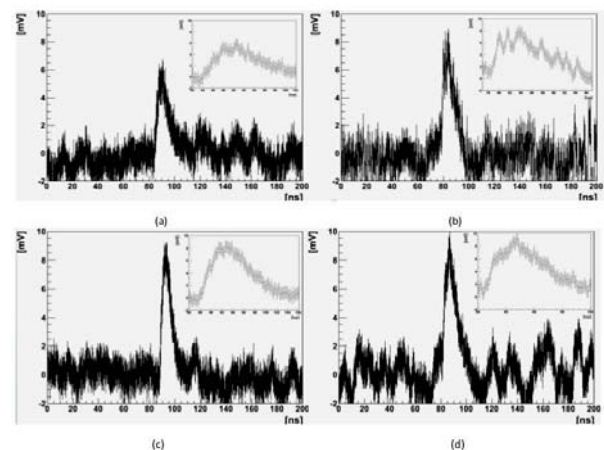


Fig. 6: Time response to a β source for a commercial diamond detector before (a) and after (b) protons irradiation and for the graphitized diamond detector before (c) and after protons (d). The insets report a zoom of the peaks.

References

- [1] E. Alemanno, M. Martino et al, In Proceeding of the International Conference on Diamond and Carbon Materials in Granada, Spain on 3-6 September (2012).

- [2] S. Sciortino, *Nuovo Cimento*, vol. **22** (1998).
- [3] V. N. Strekalov, V. I. Konov, V. V. Kononenko, and S. M. Pimenov, *Appl. Phys. A*, **76**, 603–607 (2003).
- [4] J. F. Lin, J. W. Lin, and P. J. Wei, *Diamond & Related Materials*, **15**, 1–9 (2006).
- [5] S. S. M. Chan, M. D. Whitfield, R. B. Jackman, G. Arthur, F. Goodall, and R. A. Lawes, *Semicond. Sci. Technol.*, **18**, S47–S58 (2003).
- [6] E. Alemanno, A. Caricato et al, *Proceeding of the 8th International Conference on Photo-Excited Processes and Applications (ICPEPA-8) in Rochester, NY USA on August 12-17, (2012).*
- [7] L. Malard, M. Pimenta, G. Dresselhaus, and M. Dresselhaus, *Phys. Rep.*, **473**, 51–87 (2009).
- [8] Galbiati A., Lynn S., Oliver K., Schirru F., Nowak T., Marczevska B., Dueas J.A., Berjillos R., Martel I., and Lavergne L., *IEEE Transactions on Nuclear Science*, Volume: **56** Issue: 4, 1863 – 1874 (2009).

Project and realization of a microbeam at 2.48 nm

Palladino L^{1,2}, Di Paolo Emilio M^{1,2}, Festuccia R^{1,2} and Limongi T³

¹ Dipartimento di Medicina clinica, sanità pubblica, scienze della vita e dell'ambiente - Università de L'Aquila – Italia

² INFN, Laboratorio Nazionale del Gran Sasso, Assergi (AQ) - Italia

³ Istituto Italiano di Tecnologia (IIT). Via Morego 30, 16163 Genova, Italia

Libero Palladino <libero.palladino@aquila.infn.it>

Maurizio Di Paolo Emilio <dipmaurizio@msn.com>

Tania Limongi <Tania.Limongi@iit.it>

Abstract

In this article, the geometry of the optical system, the software/hardware control system and the preliminary measures of the monochromatic beam intensity will be reported.

The high X ray conversion efficiency of the Yttrium (Y) used as target in a plasma source, will be important in the realization of an intense monochromatic X-ray beam. In particular, we collect and focus a monochromatic soft X-rays beam at the wavelength of 2.48 nm (500 eV) by multilayer spherical mirror. These mirrors reflect at an angle of incidence close to the normal of the surface.

Moreover, the improvements of the optical system are presented: from the currently with a magnification about 2 in the focal spot to have a magnification less than or equal to 1.

In this way, we obtain a monochromatic microbeam to be used in radiobiological topics and in transmission X-ray microscopy.

A new microbeam system is being implemented at the PLASMA-X laboratory in University of L'Aquila.

Introduction

The X-ray micro-beams are important experimental tools in the field of radiobiology and X ray microscopy due to two significant characteristics: (i) the micrometer size of the focal spot and (ii) the high monochromaticity of the photon energy.

The microbeams play an important role in the study of the biological effects of the ionizing radiation at low doses and low energy photons (100 eV - 1.5 keV).[1]. In particular in the study of mechanisms related to the important phenomenon of the 'bystanding effect' which seems to be linked to cellular apoptosis.[2].

The x ray source of our microbeam is a plasma-laser described in detail in the references [3].

Because of the low average x-ray emitted by the plasma-laser source on a 2π sr solid angle, we used a multilayer spherical mirror for focusing and monochroming the X-ray beam.

These mirrors have the particularity to reflect the radiation at an incidence angle close to the normal of the mirror surface.

In this mode we can obtain a large collecting area and with a reflectivity of between 30% and 1% with an $\lambda/\lambda_c \approx 200$ (depends on the x-ray wavelength). [4]

X-ray microbeam layout at 2.48 nm

a) General

The choice of the 2.48 nm wavelength is determined by the possibility of applying the microbeam in biological imaging and radiobiological themes.

At this wavelength the water (oxygen) is transparent while the biological structures (carbon) are opaque. This aspect permits to obtain: (i) a natural contrast from the water (background) and the biological structures in the x-ray image formation, (ii) to study the “first mechanisms” that connected the photoelectron emission, obtained by photoelectric absorption, with biological effects that are established in the cells.

In figure 1 we show the half intensity path of the X ray radiation at 2.48 nm (500 eV).

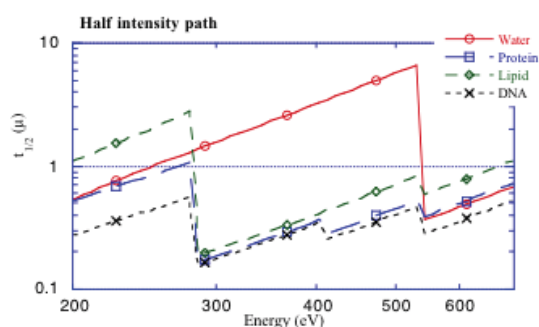


Figure 1 – Half intensity path of the X ray radiation from 200 – 600 eV for different compounds. [6]

The x ray plasma emission depends on the material: in our case the yttrium (Y 39) has a high x-ray conversion efficiency to 2.48 nm and will be used as target in the plasma source. [5]

The monochromatic microbeam at 2.48 nm is obtained using a multilayer spherical mirror, that selects the wavelength of X-rays with an incident angle of 8 degrees from the normal to the surface of the mirror. The mirror has a useful diameter $D = 30$ mm and a curvature radius $R = 265$ mm.

To protect the mirror from the debris, produced during the formation of the plasma, we used a window of protection of 50 nm thick silicon nitride.

In Figure 2 we show the pictures of the inside of the interaction chamber (C is the center) where we can see the layout of the spherical mirror (S in figure 2) respect to the target (T in figure 2), both run on rails driven by step-by-step motors controlled by computer. The sensitivity of the whole movement is $< 1 \mu\text{m}$. The optical and geometric system is very rigid. A single triangle, SCT, together the biological sample position (F in figure 2) must satisfies the optical equation of the mirrors and the constancy of the incidence angle on the mirror simultaneously.

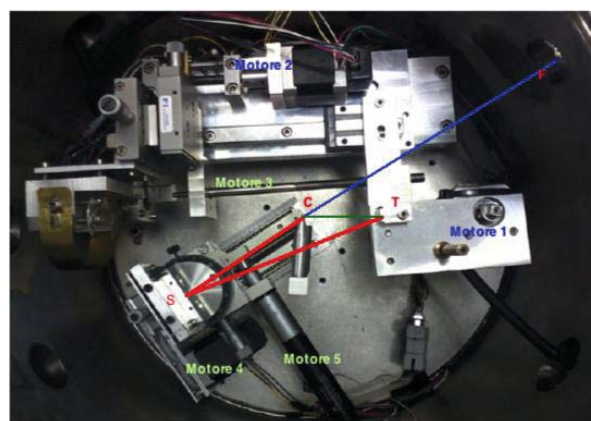


Figure 2 – The x ray interaction chamber. C is the center, S is the mirror, T is the target. The five motors are indicated.

b) Software & Hardware

The software used for management of the system is designed by high level programming language; the hardware is composed of 5 serial controllers, 4 stepper motors and 1 DC motor. The block diagram is visualized in figure 3.

The controller gives a number of features to achieve automation and handling tasks in research and industry in a very cost effective way. Programming is facilitated by the high-level mnemonic command language with macro and compound command functionality.

Macros can be stored in the non-volatile memory for later recall.

Each Motor with encoder is connected to the controller identified by physical address.

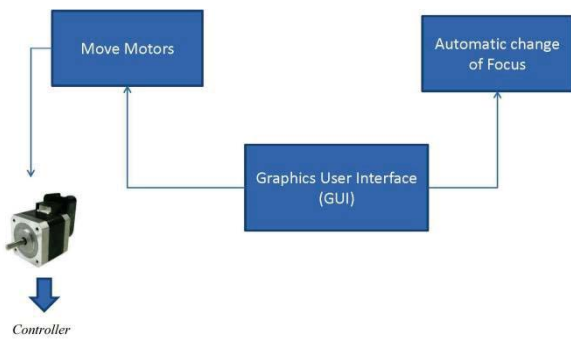


Figure 3 - General block diagram

The motors used in the configuration can be described with the following principal features:

- Accurate positioning;
- Encoder with 3 output channels;
- Stepping control.

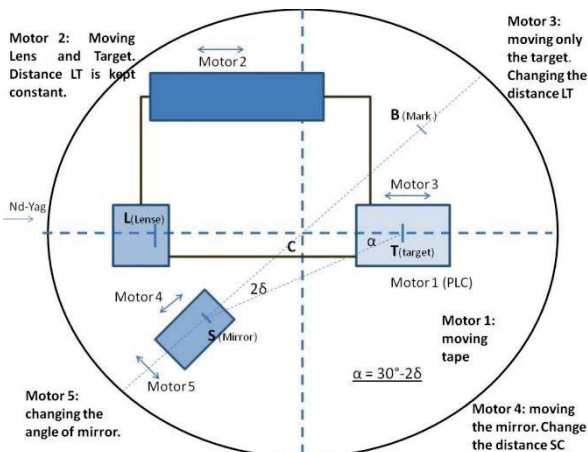


Figure 4 - General setup (hardware)

In according to the figure 4 it is possible to define the movement for each motor:

- Stepper Motor 1: used for moving the tap connected to the PLC system;
- Stepper Motor 2: used for moving lens and target together;
- Stepper Motor 3: used for moving only the lens;
- Stepper Motor 4: used for moving the mirror;
- DC Motor 5: used for rotating the mirror changing the angle.

Main features of the software design can be described as below:

1. Flexible code

2. Simple GUI to re-program
3. Possibility to manage the motors together or in singular

The process of software design (figure 5) consists of developing intermediate levels of abstraction until we reach a compromise: a set of abstractions that satisfy the needs of application programmers and are efficiently implementable (or better yet, already implemented as part of this negotiation process) on the basis of what was available in the first place.

Good design is a negotiation of a process that tries to reconcile the two points, working top-down from the client side and bottom-up from the supplier side.

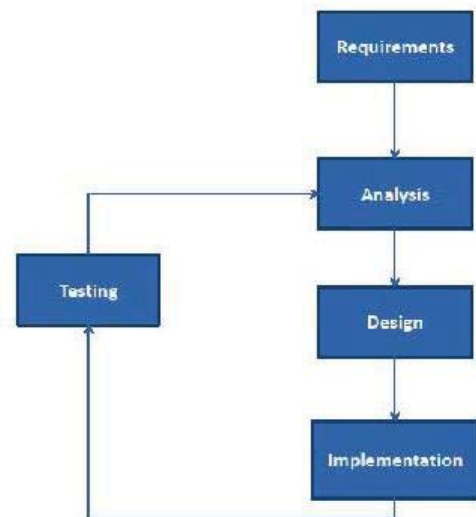


Figure 5 - Process of software design

X-ray microbeam: preliminary measures

The of the presented work is to realize a monochromatic microbeam at 2.48 nm wavelength, which is within the water window energy region. To reflect and select photons with a wavelength of 2.48 nm, a multilayer spherical mirror [4] with a resolution $\lambda \approx 200$ and a reflectivity $\approx 1\%$ was used. The multilayer structure includes two packets: 230 periods with a step of 1.256 nm and 220 periods with a step of 1.2475 nm. The material in both packets is W/B4C. The

photons were selected with a reflection angle of 8 degrees from the normal of the mirror surface. In figure 6 the reflection curve of the mirror with geometric parameters is shown. The component at 2.48 nm has been focused in the geometry shown in Fig. 7. The mirror plasma distance is 201.5 mm and the image point of the plasma was formed at a distance of 400.2 mm from the mirror. The X-ray detector was placed in the proximity of the focus point of the monochromatic beam. A vanadium microfoil 1 micron thick was placed before the input of a detector to separate the ultraviolet and visible window. The soft X-rays were generated from an yttrium target with a laser beam energy of 3.6 J. The charge collected by the detector was 4 nC which corresponding approximately to 3×10^9 photons of 500 eV energy.

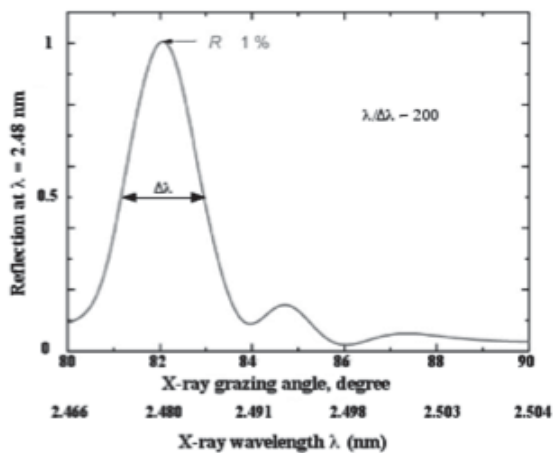


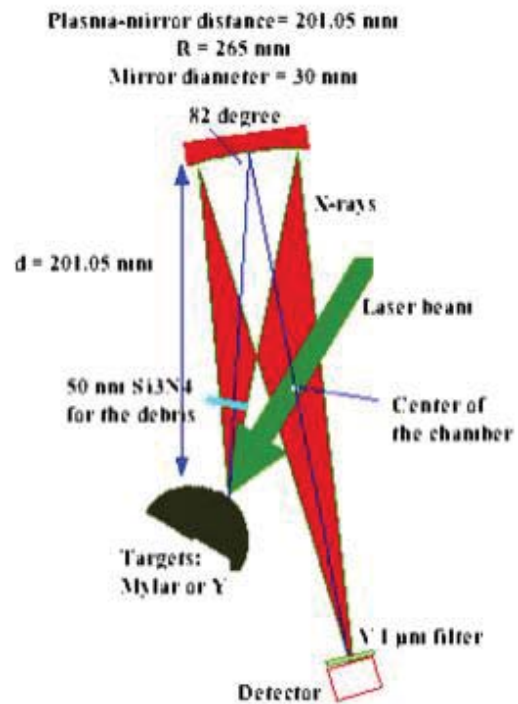
Figure 6. Curve of the reflectivity of the multilayer deposited on the substrate of the spherical mirror.

Considering the magnification 2 of the image of the source the focus of microbeam can be estimated having a density of photons equal to 2×10^5 photons/ μm^2 . considerable interest for biological applications.

Conclusions

From the microbeam measures, approximately 3×10^9 photons of 500 eV energy were obtained, which correspond to a photon density of 2×10^5 photons/ μm^2 . This results were of significant interest for

biological applications. In future we will provide an optimization of optical parameters and an improvement of the X ray



emissions using other materials such as rhenium.

Figure 7. Schematic description of the experimental microbeam arrangement for the measurement of the energy of the X-ray beam reflected from the spherical mirror. The figure shows the optical configuration of the microbeam.

References

- [1] Gerardi, S., Journal of Radiation Research **50**: A13-A20 (2009).
- [2] Prise, K. M., G. Schettino, et al., Journal of Radiation Research **50**: A1-A6 (2009).
- [3] Palladino L, Limongi T. et al, Radiation Effects And Defects In Solids, vol. **163**, p. 505-512 (2008).
- [4] Artyukov, I., Y. Bugayev, et al, Optics Letters **34**(19): 2930-2932 (2009).
- [5] Libero Palladino, Ramon Gimenez et al, Applied Surface Science 2012 (in press).
- [6] Laboratory, L. B. N. X-Ray Data Booklet Center for X-ray Optics and Advanced Light Source.

A Liquid contact angles on biocompatible surfaces

C. Scolaro¹, L. Torrisi¹, M. Cutroneo¹, F. Caridi¹, A.M. Roszkowska² and E. Pedullà³

¹ *Università di Messina, Dip.to di Fisica e Scienze della Terra, F. S. D'Alcontres, 98166 S. Agata-Messina, Italy, corresponding author, email: cscolaro@unime.it*

² *Dipartimento delle Specialità Chirurgiche, U.O.C. di Oftalmologia, Azienda Ospedaliera Universitaria, Messina*

³ *Dipartimento di Chirurgia, Università di Catania, via plebiscito, 628 – 95100 (CT)*

Abstract

Measurements of liquid contact angles on biocompatible surfaces have been performed at the Physics Department of Messina University. Biological solutions, polymers, ceramics and metals have been studied.

Surface treatments by using different laser irradiations, depending on the laser intensity and wavelength, permit to change drastically the wet-ability of many materials and to enhance their biocompatibility and functionality.

Results of our investigations put in evidence the best materials to increase or to reduce the wet-ability of the biological liquids. Results will be presented and discussed in detail with special regard to their applications in biological environment where the materials can be embedded.

Introduction

The degree of biocompatibility of a material is a function not only of the characteristics and properties of the materials and implanted devices, but also of the conditions of the host organism and of the surgical technique. It is important to know the wet-ability of the material to be implanted in order to determine whether or not it should promote the epitaxial cells growth in the body [1]. The wet-ability is a very important property of surfaces and can be defined as the ability to wet uniformly and in a stable manner from a liquid substance [2-3].

The ablation with laser pulses is a high-precision technology and spatial resolution which allows to obtain an efficient energy transfer without significantly damaging the surrounding material. A characteristic

advantage of this technique is its ability to modify the properties of wet-ability of the substrate [4].

Materials and methods

In this work were measured and compared the angles of wet-ability of polymeric substrates, metallic and ceramic biocompatible materials [5]. The main polymers used for the calculation of wet-ability in this work are: *Intraocular lens AcrySof IOL (PMMA based)*, *polyethylene (PE)*, *polytetrafluoroethylene or teflon (PTFE)*, *polylactic acid (PLA)*, *polymethylmethacrylate (PMMA)*.

At the Department of Plasma Physics of the University of Messina has been used a Q-switched Nd: YAG laser at intensity of 10^8 W/cm² operating at the fundamental

wavelength of 1064 nm, with pulse duration of 3 ns, energy of 180 mJ, which can operate in single shots and repetition rate (1 to 10 Hz).

At the University Hospital of Messina in the Department of Surgical Specialties, UOC of Ophthalmology was used the UV-ArF excimer laser (Technolas 217Z100P) operating at the fundamental wavelength of 193 nm, characterized by a beam energy of 160 mJ with pulse duration of 18 ns with a Gaussian energy profile plate, working in single mode or repetition rate of 100 Hz.

At the Dental Clinic of Catania has been used a diode laser (Lamba Scientific - D5-Doctor Smile) fundamental wavelength 810 nm, 5 W, CW.

Metallic materials from equipment used for measuring wet-ability in this work are *Gold, Silver, Palladium, Copper, Titanium, Austenitic Steels AISI 304 and AISI 316L and Titanium Alloy Ti₆Al₄V (TAV), Zinc (Zn).*

The ceramic materials of which has been calculated the angle of contact are: *Al₂O₃, Diamond, SiO₂, Glassy Carbon (CVD), Silica, TiO₂.*

The method used for the measurement of the angles of wet-ability involves the measurement of the profile of a drop of liquid at rest on a solid surface. This method, called *sessile drop* [2,3], consists in measuring the “contact angle” between the tangent to the profile of a drop, deposited on the sample surface, and the surface itself.



Figure 1: sketch of the experimental setup built for the measurements and calibrate syringe.

The contact angles of drops of liquid (deposited on the surface by means of a calibrate syringe) were measured in a direct way by means of a webcam Philips CamSuite 2.0 aligned to the eyepiece of an optical microscope that records video images and pictures of the system formed by the solid sample and drop (Figure 1). Golden Ratio is a PC code based on a transparent mask to be placed over an image on the screen. It serves to analyze the image, while the axes instead can be used for measuring angles and lengths (Figure 2).

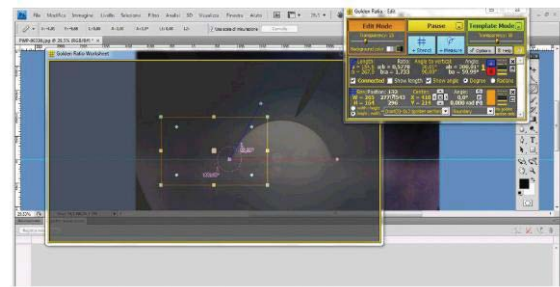


Figure 2: transparent mask software Golden Ratio to be placed above the picture on the screen.

The samples are cleaned on the surface with alcohol and are dried with a stream of dry air. It is good that the sample is always dry when you deposit the drops. As test liquid was used 1 µl of saline solution. The measurements were carried out at room temperature (T=22°, U.R.=35%, P=1atm) and for each material were made 6 measures, of which the average is calculated (Figure 3).

Measurement of wet-ability [3]: The contact angle was calculated by the size of the droplet itself. For very small droplets the effect of distortion of gravity is minimal and the droplet can be seen as the clove of a sphere. The contact angle ϑ (degree) was calculated from the height h (mm) and the base diameter d (mm):

$$\theta = 2\arctg\left(\frac{2h}{d}\right) \quad (1)$$

for $\vartheta < 90^\circ$, and

percentages of concentrations of Fe₂O₃, Methylene Blue (B.M.) and Carbon Nanotubes (CNT) are shown in Figure 6.

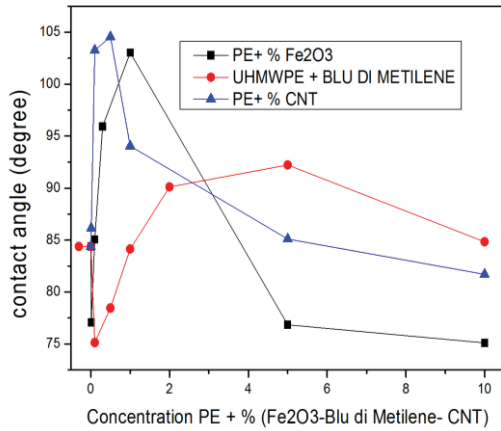


Figure 6: contact angle of PE at different percentages of concentrations: Fe₂O₃, B.M., CNT.

The variations of the contact angles of PMMA and of dental tooth of irrigants tested and the calculation of the relative surface tensions are shown in the figure 7.

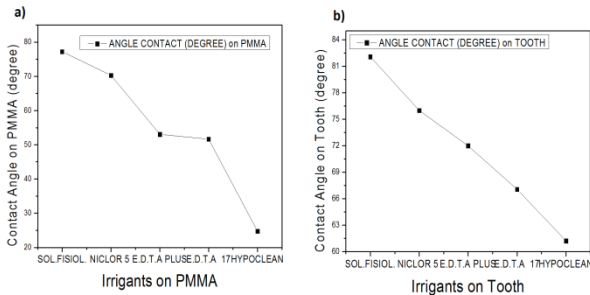


Figure 7: contact angle of dental irrigating a) PMMA, on b) tooth.

Discussion and Conclusion

The contact angle on the pure PMMA surface on which it was resting the drop for saline solution is approximately 77°. After irradiation by the Nd: YAG laser an incremental of about 7° or 10° is measured. The contact angle to 180mJ for 60 shots is about 84°, and for 100 shots laser and energy of 180 mJ is about 87° (see Figure 4 (a,b)). After irradiation through the Technolas of wavelength 193 nm, PMMA showed a change in wet-ability of the surface. The contact angle decreases by about 4° or 17°, explainable value considering the fact that

ultraviolet light induces photochemical and photo thermal effects [7,8] and that the polymer PMMA is not very permeable to UV rays. The contact angle to 160mJ for 60 shots is about 73°, and for 250 shots laser and energy of 160 mJ is about 60° (see Figure 4(c,d)). The irradiance from the D5-Doctor Smile of wavelength of 810nm allows to modify the surface of the PMMA and thus increase its wet-ability with a contact angle of about 12° to irradiation times of the order of ten minutes. The contact angle after irradiation 5W of 10 minutes is about 89° (see Figure 4-e).

As regards the metals the metal more hydrophobic (> 90 °) is copper with a contact angle of 109°. Poorly wettable is also the titanium alloy of the neck of a hip prosthesis which is inserted into the acetabulum ($\theta=103^\circ$), while the opposite part of the neck that must namely be introduced in the stem is hydrophilic (<90°) has a contact angle of 53° capable of forming chemical bonds directly with the bone tissue, but also with the soft tissues of living organisms. The humeral nail and the bone plate is made of stainless steel AISI 316L ($\theta=94^\circ$) (see Figure 5-a). Among ceramic materials analyzed, alumina is the most bioinert, characterized by a high chemical-physical environment biological showing a contact angle of 96°, while the silica is very wettable with a contact angle of 32° (see figure 5-b). Among the polymeric materials examined the biocompatible material that the highest value of the contact angle, hydrophobicity index, is the PLA ($\theta=110^\circ$), while the IOL AcrySof intraocular lens has a small contact angle ($\theta=79^\circ$, hydrophilic) particularly important in relation to the maintenance of the tear film, the maintenance of which is a necessary condition for compatibility between the eye and the lens. (see Figure 5-c).

Figure 6 shows the trend of polyethylene (PE) at different concentrations of Fe₂O₃, Methylene Blue (B.M.) and Carbon Nanotubes (CNT). The concentrations of Fe₂O₃ were added in PE with the percentage

of 0.01% - 0.1% - 0.3% - 1% - 5% - 10%. Concentrations of Methylene Blue (B.M.) were added in PE with the percentage of 0.1% - 0.5% - 1% - 2% - 5% - 10%. Concentrations of Carbon Nanotubes have been added in the PE with the percentage of 0.01% - 0.1% - 0.5% - 1% - 5% - 10%. These impurities give the surface of the PE different optical properties and therefore a significant variation of the contact angle. In fact, the contact angle of the untreated PE is of $\theta=84^\circ$. The wet-ability of the polyethylene can therefore be suitably varied by adding different concentrations of Fe_2O_3 , BM, and CNT with the possibility to make the hydrophobic PE ($\theta < 90^\circ$) or hydrophilic ($\theta > 90^\circ$) depending on the need (for example, to promote epitaxial growth or to its inhibition).

In the figure 7 (a-b) is shown the trend of the variation of the angle of contact of the endodontic irrigants used in dentistry of PMMA and of the tooth. The contact angles of irrigants on PMMA are respectively found: NICLOR 5 ($\theta=70^\circ$); E.D.T.A PLUS ($\theta=53^\circ$); E.D.T.A 17% ($\theta=51^\circ$); HYPOCLEAN ($\theta=25^\circ$). The contact angle of irrigants on the tooth are: NICLOR 5 ($\theta=75^\circ$); E.D.T.A PLUS ($\theta=72^\circ$); E.D.T.A 17% ($\theta=67^\circ$); HYPOCLEAN ($\theta=61^\circ$). The contact angle measurements may be influenced by a number of factors, including surface preparation, contamination, the environment, the temperature and the size of the droplet. The contact angles may increase or decrease as the temperature changes and do not change dramatically with it. The variations in surface wet-ability may be due to changes of roughness and / or modifications of the chemical properties of the surface. The action of the environment is generally determined by the absorption of vapour on the polymer surface, effect which reduces the surface tension. As reference liquid for the measurement of the angle of wet-ability in addition to the physiological solution and distilled water were considered four endodontic irrigants commonly used in dentistry. It has been found that the use of

endodontic irrigants to have the very low surface tension and that the wet-ability of the solution governs the capacity of its penetration in both the main and side channels, and in the dentinal tubule. Expect to deal with the biocompatible materials as well as with the laser also with the processes of ion implantation, thermal and chemical processes in order to modify the surface properties. To change the internal properties of the materials we will send beams of electrons and gamma rays.

References

- [1] J.Black, *Biological performance of materials: fundamentals of biocompatibility*, New York: Marcel Dekker, 1999.
- [2] D. Kwok, et al., *Contact angle measurements and contact angle interpretation. Contact angle measurements by axisymmetric drop shape analysis and a goniometer sessile drop technique*. Langmuir, 1997, Vol. 13, pp. 2880-2894.
- [3] W.A. Zisman, *Contact angle, wettability and adhesion*, in: R.F. Gould (Ed.), *Advances in Chemistry Series 43*, American Chemical Society, Washington DC, 1964, pp. 1–51.
- [4] C. Grigoropoulos. *Laser-induced surface modification*. Cambridge University Press, London, 2009.
- [5] V. Koutsos. *Introduction to polymers*. 2002.
- [6] Aktener BO, Bilkay U, *Smear layer removal with different concentrations of EDTA ethylenediamine mixtures*. J Endod 19(5):228- 31, 1993.
- [7] L.Torrisi, C.Scolaro, et al in: *Proceeding X Giornata di Studio Bioingegneria: Applicazioni di fasci laser al settore biomedico*, Catania, pp. 22-35.
- [8] M.Cutroneo, L.Torrisi, C. Scolaro in: *II Workshop PBSA: Laser Applications in Bio-Medical Field*, Lecce, pp.144-154.

Deposition of thick and thin nanocrystalline diamond films by microwave plasma enhanced chemical vapor deposition

G. Cicala¹, V. Magaletti²

¹CNR-IMIP, via Amendola 122/D, 70126 Bari, Italy grazia.cicala@ba.imip.cnr.it

²ALTA S.p.A., via Gherardesca 5, 56121 Ospedaletto (Pisa), Italy

Abstract

Thick (around 3 μm) and thin (48-310 nm) nanocrystalline diamond (NCD) films have been produced from Ar-rich $\text{CH}_4/\text{Ar}/\text{H}_2$ (1/89/10 %) and H_2 -rich CH_4/H_2 (1/99 %) microwave plasmas, respectively. The thick NCD films were obtained with and without an initial buffer layer (BL). The BL is easily obtained under typical microcrystalline diamond growth conditions (CH_4/H_2 mixtures). The effect of the deposition temperature (T_D , 630-900°C) was investigated on the morphology, the surface roughness and the bonding characteristics of the films grown with and without BL. The thin NCD films were grown on Si substrates treated by two different methods, i.e. ultrasonic agitation in a suspension of diamond powders of 40-60 μm or combinatorial approach in a suspension of mixed diamond powders of 250 nm and 40-60 μm . The present experimental results show that the buffer layer procedure allows a good preservation of the surface of treated Si substrate and the combinatorial approach promotes effectively the seeding of the Si surface.

Introduction

In the last years, nano- and ultranano-crystalline diamond (NCD and UNCD) films have attracted great interest as smooth materials. The advantage of these two types of nanostructured diamond over microcrystalline diamond (MCD) films consists in the smaller grain size and lower surface roughness.

The strategies to produce smooth thin NCD films consist in enhancing markedly the primary nucleation at the beginning of deposition process [1,2] or to promote the secondary nucleation during the growth process [3]. Usually diamond nucleation is difficult to occur on non-diamond substrates. For this reason the substrate surface must be treated in-situ (bias enhanced nucleation technique) or ex-situ (ultrasonic agitation, seeding and/or deposition of carbon/silicon carbide interlayer) in order to enhance the primary nucleation density. This paper

focuses on the nucleation and growth of nanocrystalline diamond. The NCD films used in this work have been produced at two different thickness scales: micrometer (around 3 μm) and submicrometer (48-310 nm). Micrometer-thick NCD films were obtained from a $\text{CH}_4/\text{Ar}/\text{H}_2$ (1/89/10 %, with modest renucleation process) gas mixture with and without a diamond interlayer of about 500 nm, called buffer layer (BL), between the NCD films and the treated Si substrate. Additionally, the effect of the substrate temperature was investigated on the morphology, the surface roughness and the bonding characteristics of films grown with and without a BL.

Nanometric-thick (48-310 nm) continuous films were produced under conventional conditions of microcrystalline diamond films (CH_4/H_2 , 1/99 %, with suppression/reduction of renucleation process) by precisely stopping the growth at the planned thickness by means of an in-situ, real time and non

invasive optical technique, i.e. laser reflectance interferometry (LRI) [1,2,4]. The NCD films were grown on Si substrates treated by two different methods, i.e. ultrasonic agitation in a suspension of diamond powders of 40-60 μm or combinatorial approach in a suspension of mixed diamond powders of 250 nm and 40-60 μm .

Materials and methods

The NCD films were deposited by the microwave plasma enhanced chemical vapor deposition technique in a home-made cylindrical stainless steel Astex-type reactor. Thick NCD films (Sets1 and 2 in Table 1) were produced using $\text{CH}_4/\text{Ar}/\text{H}_2$ (1/89/10%) gas mixtures, whereas very thin films were obtained using conventional CH_4/H_2 (1/99%) plasmas. During the deposition the working pressure and microwave power were 140 mbar and 950 Watt for $\text{CH}_4/\text{Ar}/\text{H}_2$ plasmas, and 50 mbar and 1000 Watt for CH_4/H_2 plasmas.

Table 1. Experimental parameters for the deposition of thick NCD films of Sets1 and 2. For all the samples the pressure (p), microwave power (P), total flow rate (Φ_{tot}) and percentages of $\text{CH}_4/\text{Ar}/\text{H}_2$ gas mixture were maintained constant at 140 mbar, 950 Watt, 100 sccm and 1/89/10%, respectively. For Set 2 films, the thickness (t_{BL}) of the buffer layer (BL) were fixed at 500 nm. The heater temperature (T_{PID}) and deposition temperature (T_{D}) were varied and listed with total film thickness (t_{film}) as evaluated by in situ PI measurements.

Sample	T_{PID} ($^{\circ}\text{C}$) at plasma		T_{D} ($^{\circ}\text{C}$)	t_{film} (nm) PI
	OFF	ON		
Set 1 without BL - 27min Ar/H_2 plasma exposure for parameters stabilization				
1A	25	462	652	2750
1B	585	585	748	2660
1C	700	700	823	2540
1D	780	780	875	2640
Set 2 with BL - 10min H_2 plasma exposure for parameters stabilization				
2A	25	473	653	2880
2B	585	585	775	3570
2C	700	700	833	3370
2D	780	780	884	3230

In the experiments the total flow rate (Φ_{tot} , 100 sccm) was held constant. For the thick films without and with a buffer layer the deposition temperature (T_{D} , 630-900 $^{\circ}\text{C}$) was varied. For the thin films (Sets3 and 4 in Table 2) the process time of deposition was varied from 7 to 66 min by keeping constant the deposition temperature around 815 $^{\circ}\text{C}$. In all the experiments the nucleation time, the deposition rate, the thickness and the

Table 2. Experimental parameters for the deposition of thin NCD films of Sets 3 and 4. The pressure (p), microwave power (P), total flow rate (Φ_{tot}), deposition temperature (T_{D}) and percentages of CH_4/H_2 gas mixture were maintained constant at 50 mbar, 1000 Watt, 100 sccm, 815 $^{\circ}\text{C}$ and 1/99%, respectively, whereas the Si substrate pretreatment was varied. The process time (t_{p}), nucleation time (t_{N}), deposition rate (r_{D}) and thickness (t_{film}) were measured by laser reflectance interferometry (LRI) and the surface roughness by atomic force microscopy (AFM).

Sample	t_{p} (min)	t_{N} (min)	r_{D} ($\mu\text{m}/\text{h}$)	t_{film} (nm)	Roughness $3\times 3\mu\text{m}^2$ (nm)
Untreated Si	----	----	----	----	0.17
Set3					
Si substrate treatment with 40-60 μm diamond powder					
3Treated Si					5.70
3A	7	----	----	----	9.79
3B	28	18	0.29	48	45.07
3C	31	14	0.29	81	25.71
3D	54	17	0.30	185	40.06
3E	63	15	0.36	290	39.43
Set4					
Si substrate treatment with 250 nm (50%) + 40-60 μm (50%) diamond powder					
4Treated Si					15.98
4A	7	7	----	----	16.14
4B	28	----	----	48	17.92
4C	24	6	0.28	84	21.11
4D	44	10	0.29	165	19.58
4E	66	4	0.30	310	19.50

deposition temperature were monitored in-situ and in real-time during the process by the pyrometric interferometry (PI) technique. Squared pieces of single crystal (100) p-type silicon wafers of 2.6 cm x 2.6 cm size were used as substrates and placed on a

molybdenum holder set on a graphite susceptor. Prior to the deposition, the substrate surface of the thick films was ultrasonically treated in an ethanol suspension containing diamond powders of 40-60 μm to obtain a high density of the initial diamond nucleation [5]. For Set4 samples the Si surface was ultrasonically treated in an ethanol suspension containing a mixture of diamond powders composed of 250 nm (50%) and 40-60 μm (50%) to cause a further nucleation enhancement [6,7].

The BL of all the films of Set2 was easily obtained under the typical conditions of microcrystalline diamond growth (gas mixture CH_4/H_2 1/99sccm; 50mbar; 1000W; heating at TPID 700°C), and was characterized by a very short nucleation time as monitored through pyrometric interferometry. Successively, the deposition was continued on the buffer layer in Ar-rich $\text{CH}_4/\text{Ar}/\text{H}_2$ gas mixture.

The very thin thickness of samples (Sets3 and 4) was well monitored in-situ and in real-time by LRI rather than by pyrometric interferometry not usable for monitoring film thickness less than 140 nm.

The chemical-structural features of all the films were determined at room temperature by means of a Raman confocal micro-spectrometry apparatus (Labram from Jobin-Yvon Horiba). The morphology of the coatings was evaluated by AFM (Park Systems Nanotechnology Solution Partner). The average values of root-mean-square (RMS) surface roughness were estimated on $10 \times 10 \mu\text{m}^2$, $5 \times 5 \mu\text{m}^2$ and $3 \times 3 \mu\text{m}^2$ surface areas by sampling three different regions for each film.

Results

All the Raman spectra of the Set 1 and 2 films, see Fig.1a-b, show typical features of nanocrystalline diamond. A typical NCD spectrum has a less intense diamond peak at 1332 cm^{-1} and different contributions of non-diamond phase, that are the D and G graphite bands (at 1360 cm^{-1} and 1550 cm^{-1} ,

respectively) and the transpolyacetylene (t-PA) bands at 1140 cm^{-1} and 1480 cm^{-1} [8,9]. In particular, the t-PA bands increase at the highest deposition temperature.

The AFM images clearly show the difference

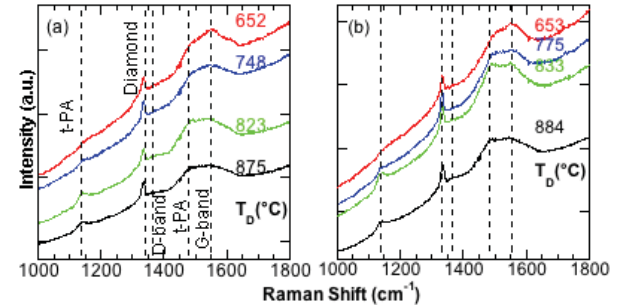


Fig.1a-b Raman spectra of thick NCD films without (a) and with (b) a buffer layer obtained at different deposition temperatures (T_D).

between the film without BL (Fig.2, Set1) and with BL (Fig.2, Set2).

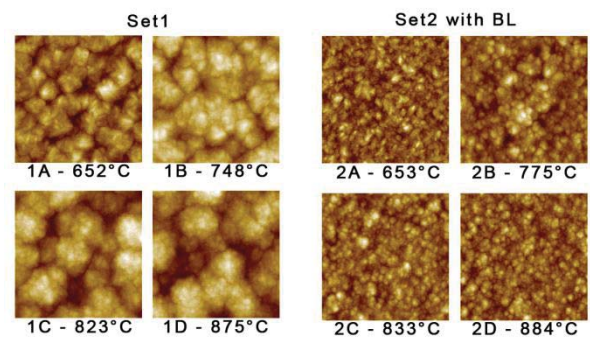


Fig.2 AFM images of thick NCD films on $10 \times 10 \mu\text{m}^2$ surface areas without (Set 1) and with (Set 2) a buffer layer (BL) obtained at different deposition temperatures (T_D).

The surface morphology of the samples without BL consists of cauliflower-shaped crystallites composed of small grains, as frequently observed in many NCD films.

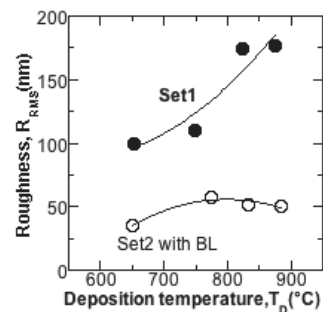


Fig.3 Root mean square (RMS) surface roughness (R_{RMS}) determined by AFM $10 \times 10 \mu\text{m}^2$ measurements of thick NCD films without (filled circle, Set 1) and with (empty circle, Set 2) a buffer layer (BL) as a function of deposition temperature (T_D).

On the contrary, the samples obtained in the same conditions, but deposited on a buffer layer, are also nanocrystalline and show uniform small grains of nanometric size. In Fig.3 the RMS surface roughness (R_{RMS}) data, estimated from the AFM images on $10 \times 10 \mu\text{m}^2$ areas, are shown for all the samples as a function of the T_D . The roughness values for films without BL are high (100-190nm) and increase by increasing the temperature, whereas for films with BL these are low (≤ 50 nm) and show a weak dependence on the temperature.

Figs.4a and b show the evolution of Raman spectra with increasing thickness of samples of Sets3 and 4. A sharp diamond peak at 1332 cm^{-1} is evident with a weak and broad G band

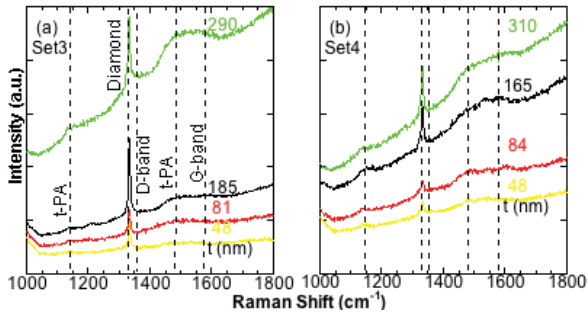


Fig.4a-b Raman spectra of thin NCD films grown at different thicknesses on Si substrates treated with a suspension containing diamond powders of $40\text{-}60 \mu\text{m}$ (a, Set3) and mixed diamond powders of 250 nm and $40\text{-}60 \mu\text{m}$ (b, Set4).

and new weak bands of t-PA of the non-diamond components. The features of the Raman spectra of Sets3 and 4 films are very similar, but the films of Set4 are more nano than those of Set3 due to the lowering and broadening of the diamond peak.

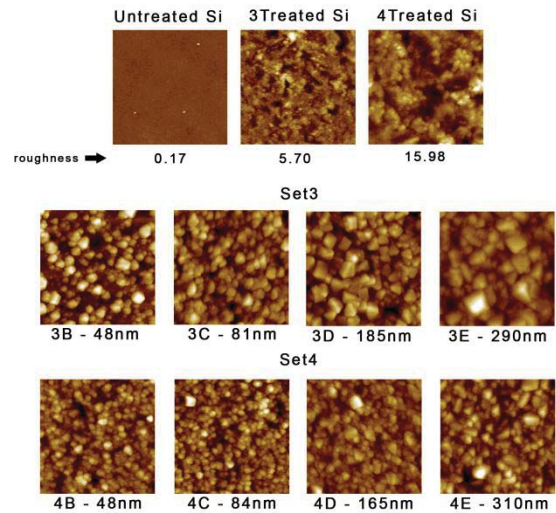


Fig.5 AFM images on $5 \times 5 \text{ mm}^2$ surface areas of untreated, treated Si substrates and AFM images on $3 \times 3 \text{ mm}^2$ surface areas of thin NCD films grown on Si treated with a suspension containing diamond powders of $40\text{-}60 \mu\text{m}$ (Set3) and mixed diamond powders of 250 nm and $40\text{-}60 \mu\text{m}$ (Set4) at different thicknesses.

Fig.5 displays the morphology of AFM images on surface areas of untreated, treated Si substrates and of films grown on Si wafers for the two treatments at different thicknesses (48-310nm). The AFM images of the nanometric films show that the diamond grain sizes of the Set3 are larger than those of the Set4.

Fig.6 reports the surface roughness of Sets3 and 4 NCD films as a function of the process time. The surface roughness of the diamond films is around 40 nm and 20 nm for samples of Sets3 and 4, respectively.

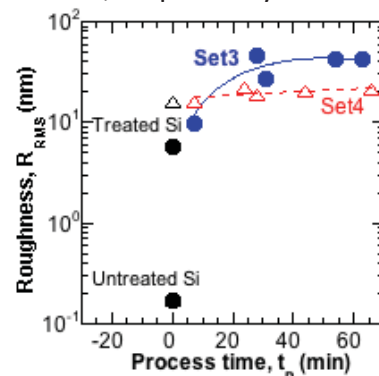


Fig.6 Root mean square (RMS) surface roughness (R_{RMS}) determined by AFM measurements of thin NCD films grown on Si treated with a suspension containing diamond powders of $40\text{-}60 \mu\text{m}$ (filled circle, Set3) and mixed diamond powders of 250 nm and $40\text{-}60 \mu\text{m}$ (empty triangle, Set4) vs process time.

Discussion

The above described results may be explained by assuming that the ultrasonic and combinatorial treatments of the Si substrate using diamond powders provide sites for nucleation with either embedment of diamond powder fragments or diamond seeds besides scratches and morphology changes of the substrate surface. The AFM topography of the Si surface treated by ultrasound in an ethanol suspension of 40-60 μm diamond powders and of mixed diamond powders composed of 250 nm and 40-60 μm shows that the dominant process is scratching and seeding, respectively.

The proposed initial deposition of a BL from H_2 -rich CH_4/H_2 mixture at a power of 1000 W and a pressure of 50 mbar is shown to facilitate the nucleation process of diamond reducing the nucleation time and forming easily the first layer of diamond. This because the 10-min H_2 -plasma exposure would leave the seed sites unmodified on the treated Si substrate. Although the deposition conditions are typical of MCD films, the low thickness (about 500 nm) of the BL ensures the formation of small grain sizes with surface roughness of 45 nm that is preserved during the subsequent deposition of NCD films from Ar-rich $\text{CH}_4/\text{Ar}/\text{H}_2$ mixture. The BL procedure, therefore, shortens the times for nucleation. The absence of BL and the long time of nucleation result in cauliflower-like films. On the contrary, the presence of BL brings to the formation of nanometric grain sizes thus improving markedly the smoothness of films obtained.

The different method used for the Si surface treatment in Set3 and 4 samples is well depicted by AFM images of treated Si in Fig.5, in which the scratching and seeding process becomes dominant in the mono-dispersed and poly-dispersed suspensions, respectively. Additionally, the comparison of AFM images of the nanometric films grown on Si surface in the two treatments shows that the film grain sizes of Set3 are larger than those of

Set4. The films of Set3 grown on Si treated in suspension of 40-60 μm diamond powders exhibit a surface roughness of 40 nm for the larger grain size, whereas the films of the Set4 show a roughness of about 20 nm for the smaller grain sizes.

Conclusions

The production of thick NCD films with the use of the BL procedure results in a fast nucleation stage, facilitates the growth process of nanocrystalline diamond and reduces the roughness of deposited material. The obtained films are smooth, continuous and uniform in comparison to those produced in the same conditions but without growing the buffer layer.

The production of thin NCD films with roughness around 20 nm from CH_4/H_2 (1/99 %) plasmas was easily performed when the Si substrate surface was treated with the combinatorial approach. This method exploits the hammering effect of large grains with respect to the small ones that are effectively seeded on the substrate surface promoting a primary nucleation density higher than that obtained on Si treated in suspension of mono-dispersed diamond powder.

References

- [1] Stoner BR, Williams BE, Wolter SD, Nishimura K, Glass JT, J Mater Res **7** 257-260 (1992)
- [2] Smolin AA, Ralchenko VG, Pimenov SM, Kononenko TV, Loubnin EN, Appl Phys Lett **62** 3449-3451 (1993)
- [3] Gruen DM, MRS Bulletin **26** 771-776 (2001)
- [4] Bruno G, Capezzuto P, Cicala G, Cramarossa F, Plasma Chem & Plasma Processing **6** 109-125 (1986)
- [5] Cicala G, Bruno P, Bénédic F, Silva F, Hassouni K, Senesi GS, Diam Relat Mater **14** 421-425 (2005)

- [6] Alkhvlediani R, Lior I, Michaelson Sh, Hoffman A, Diam Relat Mater **11** 545-549 (2002)
- [7] Buijnsters JG, Vazquez L, ter Meulen JJ, Diam Relat Mater **18** 1239-1246 (2009)
- [8] Ferrari AC, Robertson J, Phys RevB **63** 121405 1-4 (2001)
- [9] Pfeiffer R, Kuzmany H, Knoll P, Bokova S, Salk N, Gunther B, Diam Relat Mater **12** 268-271 (2003)

Fourier transform infrared spectroscopy (FTIR) investigation focused on Italian postage stamps in the course of time

Imperio E¹, Giancane G², Valli L³

¹ Department of Engineering for Innovation, University of Salento, via per Monteroni - 73100, Lecce, Italy

² Department of Cultural Heritage, University of Salento, via D. Birago, 64 - 73100, Lecce, Italy

³ Department of Biological and Environmental Science and Technology (Di.S.Te.B.A.), University of Salento, via per Monteroni - 73100, Lecce, Italy

Abstract

From the inscription of the General Post Office in Washington DC: “The stamp is the propagator of news, links between distant families, messenger between friends, solace in solitude, a vehicle for commerce and industry, an element of human progress, promoting brotherhood, peace, goodwill among men and nations”. It’s hard to imagine how much history can be held in a small piece of paper and how many purposes this little object was destined to have. This is why postage stamps have reached so much importance and interest, which they began to be considered as work of art actually. In order to see beyond the careful eye of the philatelist, FTIR (Fourier Transform Infrared Spectroscopy) in ATR (Attenuated Total Reflection) mode has been successfully employed in material characterization of many stamps. Samples since 1861, year of the unification of the Kingdom of Italy, until to date, across a vast philatelic collection, has been characterized in this study. The immediate response of this type of spectroscopic technique let to achieve significant data information, which led to design history changes in paper making technologies. The first mail stamps published in Italy portrayed King Vittorio Emanuele II and it showed to be made of sheet of cellulose paper. Going forward in years, many differences were detected in paper composition. The mail stamps were also observed by fluorescence microscopy, in order to determine differences in the application of fluorescence. The analyses were performed without any alteration of the samples and no removal of material was needed, which represents the “conditio sine qua non” for investigations on these kinds of Cultural Heritage.

Introduction

Philately can represent an unconventional way to follow the historical, economical, political and custom evolution of a country and society. It is a form of collecting that

suffers from the same problems of other kinds of collections, such as conservation, restoration, counterfeiting and understanding of materials and substances employed during the manufacturing procedure. Also stamps constitute a sort of

artwork which could be very rare and precious. In fact, it is reported that one of the surest way of investment is the collection in the field of cultural heritage, since the relative pieces constantly increase their economical and historical value.

The proposed analysis will possibly be employed in determining the period of manufacturing of the samples, which is of fundamental importance in the case of counterfeits.

Materials and methods

Fourier Transform Infrared Spectroscopy (FT-IR) Varian 600-IR series instrument in ATR (Attenuated Total Reflection) mode with an internal reflection element composed of zinc selenide (ZnSe) was used to perform the molecular analysis. The non-destructiveness of the set-up employed allowed to place every stamp directly onto the ATR window in order to achieve an optimal contact between the surface of the sample and the crystal. Thirty-two scans were collected for all the exemplars in the range between 4000 and 600 cm^{-1} . Italian exemplars starting from Unification of Italy in 1861 until today came from a wide philatelic collection. The wide period of time covered a lot of post issues which have been subjected to infrared analysis in order to characterize their constituents. In particular the fibers, fillers, glues and coating, eventually present on the surface, were investigated. Moreover, stamp fluorescence has been observed by means of an inverted system microscope, the Olympus IX50, with the objective of 10x.

Results

Blank regions of the stamp samples were analyzed. The corresponding infrared spectra revealed different information depending on the year of the stamp. Due to the small depth of penetration of the radiation in the ATR mode, the resulting signals in the spectra can be attributed to the surface components.

When the Kingdom of Italy was born in 1861 new postage stamps were needed to standardize mail payment in all the regions. The first issue of the Reign of Italy, which was composed by the same four values formerly used in the Reign of Sardinia, was released in 1862 [1]. It comprehended stamps of 10, 20, 40 and 80 cents that had Vittorio Emanuele II embossed effigy in the central oval and they were painted in yellow, blue and red alongside the rectangle.

The analysis on these first exemplars shows the typical signals of cellulose fibers at 1158, 1106, 1055 and 1030 cm^{-1} [2] attributed to the stretching vibrations of C-O groups in glucose chains (Figure 1, A). This proves that the support chosen for printing the stamps was a cellulose based paper. Going forward in time, it has been possible to individuate in the exemplars from 1896 the use of kaolin as filler into the paper pulp. The presence of just one small peak (Figure 1, B) in the spectrum, at about 3690 cm^{-1} , due to Si-OH stretching mode [3], can be related to the position of the kaolin filler into the fibers. Kaolinite, $\text{Al}_2\text{Si}_2\text{O}_5(\text{OH})_4$, is the principal mineral of kaolin clay used in paper manufacturing as filler [4]. Its powder interposes into cellulose fibers to fill the micro-holes in the paper making the sheet more compact and smooth, thus providing a finer support to be printed. The IR evanescent wave above the ATR crystal detects the first surface cellulose layer and only some kaolin particle emended in the sheet, can be detected.

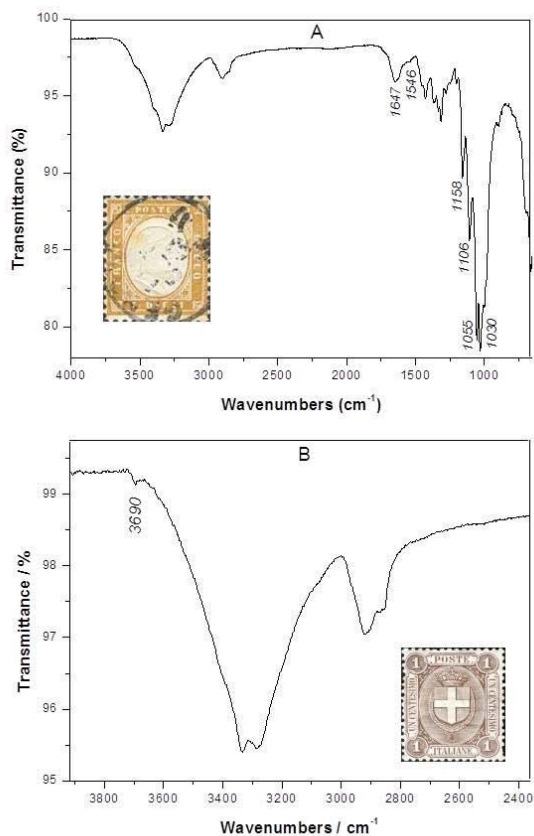


Figure 1. (A) FTIR-ATR spectra of 10 cent yellow stamp of the 1st issue of the Reign of Italy in 1862; (B) O-H stretching region in the FTIR-ATR spectrum of 1 cent brown stamp of the 1896.

The use of kaolin increased in the manufacturing of postage stamps. The analysis attest that the evolution of its employment, completely unknown until now, concerns stamps from 1915 in which kaolin acts as the coating layer above the front of mail stamp since that year. In figure 2, A is displayed the spectrum of the 15 cent value of Red Cross issue, where the kaolin bands become more intense with three distinctive signals in Si-OH stretching region at 3690, 3648 and 3616 cm^{-1} [2]. When kaolin is located as an external coating layer its peaks cover any other evidence of cellulose or glue and two intense signals related to calcium carbonate at 1412 and 870 cm^{-1} appear [5]. This is the case of most of the modern exemplars as visible in the spectrum of a stamp issued in 2004 (Figure 2, B). The improved definition of the pictures has been

possible because of the coating process in which the use of calcium carbonate in mixture with kaolin improves ink impermeability and smoothed characteristic to the stamp paper, as any other nowadays exemplar shows.

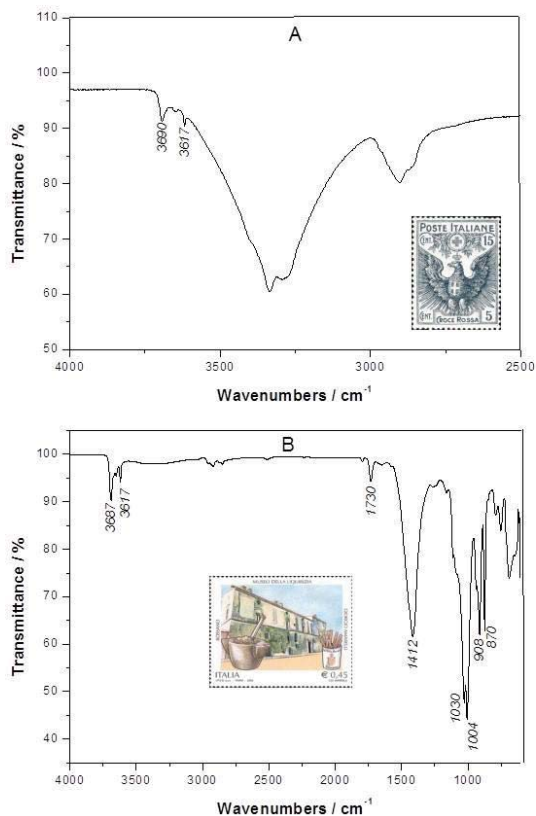


Figure 2. (A) O-H stretching region in the FTIR-ATR spectrum of 15 cent blue red cross stamp of the 1915 displays how Kaolinite was from then more visible due to its position above the cellulose fibers; (B) FTIR-ATR spectrum of 0.451 € stamp of 2004 in which are visible distinctive signals of kaolin coating.

Other changes in postage stamps production have affected the paper. They have been related to the introduction of the fluorescence. To allow the automatic marking of the mail and to stop the spreading of the fakes, fluorescence was applied to a large number of stamps. Hence, study on stamps fluorescence throughout time has been conducted by fluorescence microscope. It was known that in 1968 *Siracusana* issue was the first fluorescent issue. The fluorescent additives were introduced during the paper production, mixed in the pulp. Observing

Siracusana stamps, during excitation, only the paper support, not the printing ink, gave fluorescence response (Figure 3, A). In the 1980s in order to obtain a better resolution of the stamp subjects, fluorescent additives were no more included in the pulp, but they were introduced in the inks solutions [6]. Examination of modern stamps belonging to this class has been easily recognizable the distinction in the technique of production. In figure 3, A the particles are visibly spread on the paper surface, while in figure 3, B the luminescence is enclosed to the painted area, making visible only certain ink colors. In fact, in the pictures below, the first fluorescent stamps have luminescent centers within the fibres, while in today' stamp sample, rays of a drawn sun in the image can be seen. The usefulness of the proposed studies consists in easily determine if an exemplar is compatible or not with the correspondence standard postage stamp.

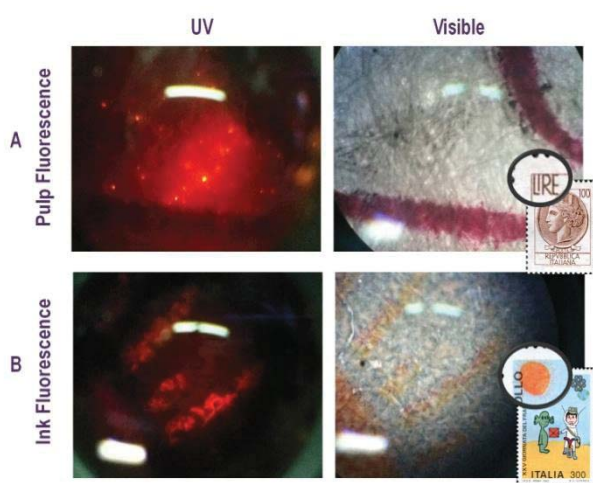


Figure 3. (A) Pulp fluorescence images of the 100 Lire *Siracusana* stamp exemplar of the 1968, under the UV and visible light; (B) Ink fluorescence images of the 300 Lire stamp exemplar of the 1983, under UV and visible light.

Conclusions

Chronologically analyzed stamps, throughout Italian history, let to know the materials employed in 150 years of postage stamps paper production. Paper was characterized by means of FTIR spectroscopy without

causing any alteration to the specimens. This work allows a good knowledge about each change made in the manufacture of stamps paper. This study constitutes an additional demonstration of the importance of performing new scientific approaches to the world of Cultural Heritage and of merging technological data with historical and classical information. In this particular case the analyses proved that FTIR spectroscopy in ATR mode is a powerful and not-destructive tool, ready to be employed against stamps forgery.

References

- [1] F. Zeri, *I francobolli Italiani*, Il Melangolo, Genova, 1993, pp.14-18 .
- [2] K. K. Pandey, *J. Appl. Polym. Sci* 1999, 71, 1969-1975.
- [3] . M. R. Derrick, D. Stulik, J. M. Landry in *Infrared Spectroscopy in Conservation Science*, Chapter 5, Getty Conservation Institute, Los Angeles, 1999, pp. 114-119.
- [4] B. J. Saikia, G. Parthasarathy, *J. Mod. Phys.* 2010, 1, 206-210.
- [5] H. Espinosa-Andrews, O. Sandoval-Castilla, H. Vázquez-Torres, E. Jaime Vernon-Carterb, C. Lobato-Calleros, *Carbohydr. Polym.* 2010, 79, 541-546.
- [6] G. Riggi Di Numana, *La fluorescenza nei francobolli d'Italia (1944-1994)*, Vaccari, 1995.

Sistemi di Computer-Assisted Detection e di Analisi di Dati Bio-medici

Donativi M^{1,2}, De Nunzio G^{1,2}, Cataldo R^{1,2}, De Mitri I^{3,2}, Pastore G⁴, Rucco M⁵, Carlà A², Peccarisi M^{3,2}, Massafra A^{3,2}, Demitri R³, Di Sabatino S⁶, Buccolieri R⁶, Quarta R⁶, Grimaldi M⁷, Manca AD⁷, Torsello M⁸, Zecca I⁸, Falini A⁹, Castellano A⁹, Bello L¹⁰, Soffietti R¹¹, Galluccio G¹², Batzella S¹²

¹Univ. del Salento, Dipart. di Matematica e Fisica "Ennio De Giorgi", Lab. di Fisica Biomedica e dell'Ambiente

²INFN (Istituto Nazionale di Fisica Nucleare), Lecce

³Univ. del Salento, Dipart. di Matematica e Fisica "Ennio De Giorgi"

⁴Istituto di Ricerche Cliniche Ecomedica, Centro di Radioterapia e IGRT, Empoli (Fi)

⁵Univ. di Camerino, Scuola di Computer Science

⁶Univ. del Salento, Dipart. di Scienze e Tecnologie Biologiche ed Ambientali, Lab. di Micrometeorologia

⁷Univ. del Salento, Dipart. di Studi Umanistici, Centro di Ricerca Interdisciplinare sul Linguaggio (CRIL)

⁸Presidio Ospedaliero "Vito Fazzi", UO di Radiologia, Lecce

⁹Ospedale San Raffaele e Univ. Vita-Salute S. Raffaele, Milano

¹⁰Univ. di Milano, Dipart. di Scienze Neurologiche, UO di Neuro-chirurgia

¹¹Univ. di Torino, Dipart. di Neuroscienze e Oncologia, UO di Neuro-oncologia

¹²Azienda Sanitaria "San Camillo-Forlanini", UO di Endoscopia Toracica, Roma

Abstract

Le applicazioni della Fisica e dell'Informatica alla Biomedicina includono i sistemi di individuazione di patologie (CAD, *Computer-Assisted Detection*) basati sul trattamento di dati provenienti da esami diagnostici (in particolare ma non limitandosi alle immagini diagnostiche quali TC, RM, etc.), gli strumenti di ausilio alla chirurgia (realtà virtuale, telechirurgia), l'analisi e l'interpretazione di segnali di interesse biomedicale (per esempio segnali da elettroencefalogramma, EEG, o da elettrocardiogramma, ECG). Questo lavoro presenta una rassegna di applicazioni, in cui gli autori sono impegnati, dandone alcuni dettagli implementativi e discutendone brevemente i risultati. Le applicazioni si differenziano per il tipo di dati analizzati (serie temporali provenienti da misure EEG, oppure dati bi- o tridimensionali contenuti in immagini diagnostiche), per il distretto corporeo di intervento, le finalità, la patologia.

Introduzione

L'articolo riporta alcuni risultati conseguiti dagli autori nel campo delle applicazioni della Fisica e dell'Informatica alla Biomedicina. Parte dei progetti è stata già pubblicata su rivista, o descritta in congressi internazionali. Ove non diversamente specificato, l'ambiente in cui i prototipi software sono

stati realizzati è MATLAB.¹ Per i dettagli, si rimanda agli articoli citati in Bibliografia.

¹ <http://www.mathworks.com/products/matlab>

Individuazione automatica di noduli polmonari pleurici

Il cancro al polmone è una delle cause principali di morte. L'individuazione precoce e la successiva resezione possono migliorare significativamente la prognosi. Lo sviluppo di tecniche di *Computer-Assisted Detection* (CAD) per l'individuazione automatica dei noduli, può migliorare la precisione della diagnosi. La Tomografia Computerizzata (TC) è considerata la migliore modalità di imaging per la rilevazione di noduli polmonari. In [1] si affronta l'individuazione di noduli neoplastici polmonari in immagini TC. La Ricerca è stata condotta con un finanziamento INFN (esperimenti MAGIC5, *Medical Applications on a Grid Infrastructure Connection*, e poi M5I, *MAGIC5 Lung*), in collaborazione con il Presidio Ospedaliero V. Fazzi di Lecce e con l'*Italung Study Research Group* (Regione Toscana). Il problema particolare affrontato è l'individuazione dei noduli a contatto con la pleura (juxta-pleurici, Fig. 1 in alto).

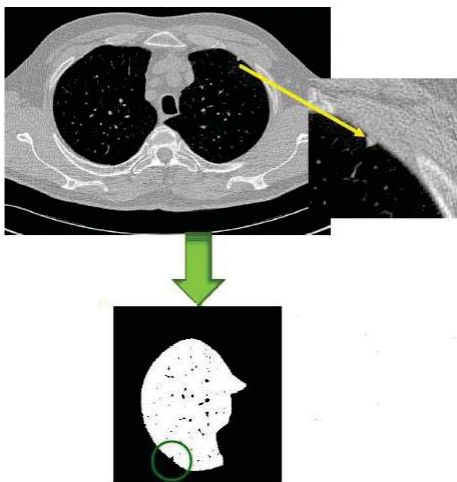


Fig. 1. Esempio di nodulo pleurico (in alto) e la maschera ottenuta con la segmentazione, in cui il nodulo compare come concavità.

Siccome tali noduli compaiono, nelle immagini TC, come protuberanze aventi origine nella pleura e dirette verso il parenchima polmonare, l'individuazione dei noduli è ottenuta "chiudendo" le concavità (*concavity patching*) che i noduli determinano sulla superficie pleurica quando si segmenta il volume polmonare,

confrontando poi (per sottrazione) l'immagine "chiusa" con quella originale.

Il lavoro confronta due differenti tecniche di chiusura di concavità in 2D (α -hull, e *closing* morfologico), valutandone l'efficienza nella localizzazione dei noduli. La chiusura morfologica usa come elemento strutturale (SE) un disco di raggio r variabile. L' α -hull [2] è una generalizzazione del *convex-hull*, in grado di rilevare concavità la cui forma dipende dal parametro di curvatura α .

Preliminare alla ricerca dei noduli è la segmentazione del polmone, ossia l'individuazione dei tessuti che costituiscono il parenchima polmonare [3]. Il risultato è una coppia di maschere binarie per i due polmoni. Noduli densi (e vasi) sono lasciati fuori dal volume segmentato; pertanto le regioni che li contengono mostrano, nelle maschere di segmentazione, cavità e concavità (Fig. 1 in basso). Le concavità originate da noduli juxta-pleurici (e da grandi vasi) sono trattate nella fase di *concavity patching*, che consente la ricostruzione di un bordo smussato del polmone, in cui le concavità vengono "chiusure". Applicando sezione per sezione l'operazione differenza tra la vecchia e la nuova frontiera, siamo in grado di rilevare concavità dove i due confini differiscono, e quindi individuare i (candidati) noduli. La Fig. 2 mostra il risultato dell'operazione ora descritta su una sezione del polmone, per un valore fissato di α (caso dell' α -hull). Ripetendo, per un insieme appropriato di valori α , la differenza tra confine del polmone e il medesimo smussato, è individuato un insieme di candidati noduli di varia dimensione.

La scelta di un insieme utile A di valori α ha richiesto una sperimentazione accurata, a causa di richieste tra loro in competizione: un insieme A molto ricco permette una più fine descrizione delle concavità, ma implica tempi di calcolo più lunghi e, anche, un maggior numero di falsi positivi (FP). I candidati noduli rilevati, sono classificati da una rete neurale *feed-forward* con uno strato nascosto di venti

neuroni, ottenendo la riduzione dei falsi positivi (concavità naturali, vasi...).

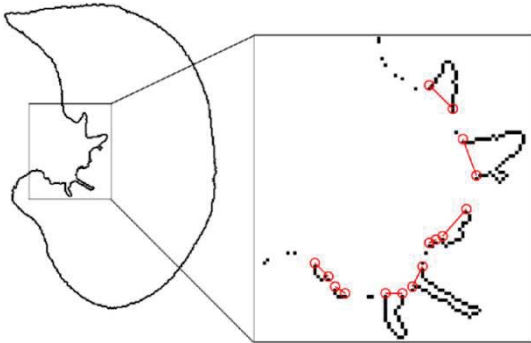


Fig. 2. Una sezione del polmone, e dettaglio dell'individuazione delle concavità dovute alla presenza di noduli o vasi.

Le *feature* adoperate per la classificazione sono state tredici, sia di tipo geometrico (area, raggio equivalente, circolarità) sia legate al contenuto in livelli di grigio (media, deviazione standard, skewness...).

I risultati ottenuti hanno dimostrato che l' α -*hull* è più sensibile, e appare vantaggioso anche perché computazionalmente meno pesante. La classificazione dei candidati noduli ha fornito valori accettabili di aree sotto la curva ROC, 0.80 e 0.84 per il closing morfologico e l' α -*hull* rispettivamente, con sensibilità/specificità (nel punto della curva ROC ove coincidono) di 72% e 75%.

Simulazioni CFD per la caratterizzazione della stenosi tracheale

Relativo al sistema respiratorio è lo studio, attualmente in corso tramite simulazione (CFD, *Computational Fluid Dynamics*), dell'influenza della stenosi tracheale (riduzione del lumen della trachea) sui processi respiratori. Essendo in preparazione un articolo che descrive i risultati ottenuti e il confronto con la clinica, daremo qui solo qualche cenno sulla procedura.

La Fig. 3 (sinistra) mostra la ricostruzione tridimensionale di una trachea stenotica, realizzata a partire da un'immagine TC.

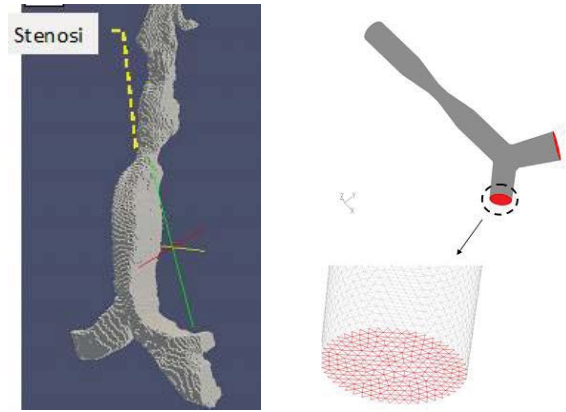


Fig. 3. Ricostruzione 3D di una trachea stenotica da immagine TC (sinistra) e modello geometrico patologico semplificato (destra).

La ricostruzione è stata adoperata per la realizzazione, in ambiente GAMBIT, di due modelli geometrici semplificati di trachea e bronchi principali, uno sano e uno con stenosi (Fig. 3, destra), che ne rispettasse i parametri geometrici: dimensioni e angoli. Per discretizzare il dominio computazionale del modello è stata scelta una mesh non strutturata contenente 250.000 tetraedri irregolari delle dimensioni di circa 10^{-1} cm, per la loro flessibilità ad adattarsi a geometrie irregolari. Il flusso d'aria nelle vie aeree è stato calcolato impiegando il modello k- ϵ , implementato in FLUENT. Il flusso d'aria in ingresso è stato simulato per differenti portate. Tra i risultati, mostriamo in Fig. 4 l'andamento della pressione, che mostra bene la caduta, soprattutto a livello della stenosi, nel caso patologico.

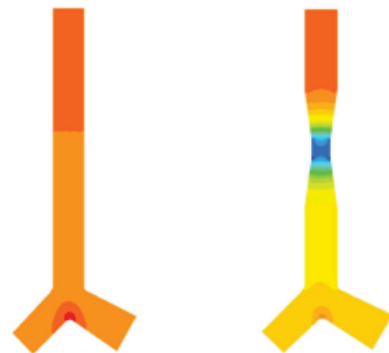


Fig. 4. Andamento qualitativo della pressione dell'aria P nel modello di trachea sano e in quello stenotico, in falsi colori (P diminuisce passando dai colori caldi a quelli freddi).

Standardizzazione delle scale di grigi in RM

In Risonanza Magnetica (RM) le intensità non hanno significato numerico specifico per ciascun tessuto, anche all'interno dello stesso protocollo di acquisizione, per la stessa regione del corpo, o per immagini dello stesso paziente ottenuti sullo stesso scanner in momenti differenti. Ciò influenza la post-elaborazione delle immagini acquisite come, per esempio, i metodi di segmentazione e registrazione che dipendono dalle intensità dei grigi. La mancanza di un'interpretazione standard spesso compromette l'accuratezza di tali applicazioni. Questa sezione descrive una tecnica di standardizzazione tissue-based (SBST: tiSSue-Based Standardization Technique), dedicata alle neuroimmagini. Il lavoro [4] è stato realizzato con finanziamento INFN, su immagini provenienti da Alzheimer's Disease Neuroimaging Initiative (ADNI), e da Open Access Series of Imaging Studies (OASIS).

Questa tecnica di standardizzazione, parzialmente descritta in [5] e ispirata da [6-8], ha dimostrato efficacia nel ridurre al minimo il rischio di "mischiare" tessuti cerebrali, ossia di assegnare, a causa dell'ambiguità nei valori dei grigi, un voxel di un tessuto o di liquor, ad una classe diversa da quella di appartenenza. Il metodo è basato sulla corrispondenza tra istogrammi, ma anche sulle informazioni di appartenenza di un voxel alle varie classi. Eseguo trasformazioni di intensità, lineari a tratti, tra le immagini, condividendo la semplicità della tecnica originariamente dovuta a Nyúl e Udupa (di seguito chiamata L4 [7]), ma con maggior robustezza. In L4 la standardizzazione dei livelli di grigio è ottenuta individuando un training-set di immagini, e selezionando poi per ogni loro istogramma, alcuni punti di riferimento (e.g. alcuni percentili), effettuandone la media per ottenere un elenco di valori di riferimento, e utilizzando questi ultimi come scala standard. L'istogramma di ogni immagine del training-

set, e delle successive immagini da standardizzare, è poi trasformato proiettando i suoi valori di riferimento su quelli standard, mentre i livelli di grigio intermedi sono linearmente interpolati. Così è ottenuta una mappatura di intensità lineare a tratti verso la scala standard.

In SBST la procedura è simile, ma è applicata singolarmente alla sostanza bianca (WM), grigia (GM), e liquor (CSF). Un numero consistente (>500) di immagini è stato utilizzato per lo sviluppo. È stato dapprima scelto un gruppo di *train*. Le immagini sono state suddivise in WM, GM, e CSF con il modulo di segmentazione di SPM², che include mappe spaziali a priori. Sono state poi calcolate tre trasformazioni di standardizzazione, una per ogni classe: WM, GM, CSF. La Fig. 5 mostra alcuni istogrammi di immagini pre- e post-standardizzazione.

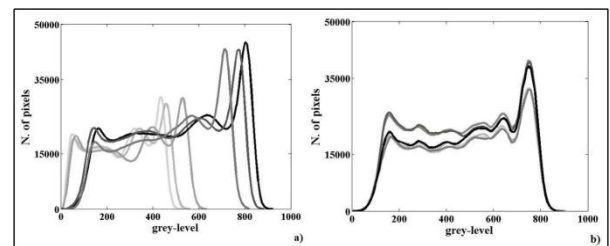


Fig. 5. Iistogrammi di alcuni volumi RM pre- (sinistra) e post-standardizzazione (destra). Gli istogrammi sono calcolati solo sulle classi di interesse, ossia GM, WM e CSF, con rimozione di altri tessuti e dello sfondo.

Il calcolo, previa coregistrazione non-lineare tra le immagini, dell'errore assoluto medio:

$$MAE = \frac{1}{N} \sum_{v=1}^N |I_{o,v} - I_{s,v}|$$

tra ciascuna immagine pre- e post-standardizzazione su un template di riferimento adoperato (da solo) per la definizione della scala standard, e il template stesso, mostra che SBST si rivela più efficace di L4 nel proiettare le scale di grigi su una scala standard, nel rispetto delle classi di appartenenza dei voxel delle immagini (N è il numero di voxel nella regione considerata,

² www.fil.ion.ucl.ac.uk/spm

CSF, WM, GM; $I_{o,v}$ e $I_{s,v}$ sono valori di intensità per il voxel v nel template e nelle immagini non standardizzata, e standardizzata con L4 o SBST).

Individuazione della regione ippocampale in RM

Questo paragrafo descrive un sistema [5] d'individuazione/estrazione di regioni ("box") ippocampali (Fig. 6) in neuroimmagini RM di pazienti con sospetto Alzheimer: l'operazione è preliminare alla valutazione dell'atrofia dell'ippocampo, indice della presenza e dell'avanzamento della demenza. Lo studio è stato realizzato con l'apporto di fondi INFN (esperimento MAGIC5), ed è stato effettuato su immagini ADNI. Nello studio sono compresi 190 pazienti.



Fig. 6. Sezione di una regione (box) ippocampale (HB)

La procedura completa prevede diverse fasi. In primo luogo è importante disporre di un metodo robusto per la standardizzazione della scala di intensità delle immagini: in tal modo tessuti simili assumono intensità di grigio simili, anche in immagini provenienti da fonti diverse. La standardizzazione è stata attuata tramite la procedura descritta nel paragrafo precedente. Si procede poi con l'estrazione automatica della regione cerebrale contenente l'ippocampo, con un algoritmo che parte da una scatola ippocampale fissa (detta HB0) individuata manualmente, e da un gran numero di immagini RM da cui estrarre le box successive. HB0 è confrontata (tramite coefficiente di correlazione normalizzato) con tutte le regioni corrispondenti del dataset di immagini, fino a individuare la più simile a sé. Questa è estratta e va ad aggiungersi (come HB1) alla HB0, nell'insieme di box estratte

detto HBS. La procedura reitera l'estrazione di box, tramite confronto tra le immagini rimanenti e tutte le $HB \in HBS$, con il criterio di individuare ed estrarre ogni volta la box più simile ad una delle HB precedentemente individuate. Il processo termina quando tutte le HB sono state estratte, fornendo un insieme HBS di potenziali "estrattori" di scatole ippocampali. La fase seguente riguarda la scelta di un sottoinsieme di HBS, di cardinalità inferiore (denominato HBT), che sia rappresentativo della variabilità degli ippocampi umani (sani o atrofici) in modo da semplificare e velocizzare, per suo tramite, l'estrazione da immagini arbitrarie. A questo scopo, le HB sono clusterizzate e si scelgono, come template, i centroidi dei cluster.

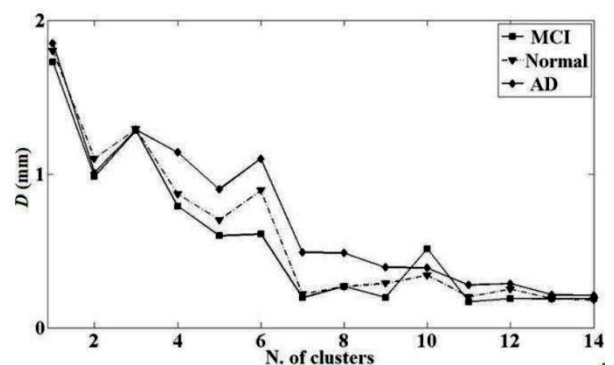


Fig. 7. Dipendenza del parametro D dalla cardinalità del set HBT di template.

Per stimare il numero "minimo" di modelli necessario in HBT, è proposta una metrica (distanza) basata sulla posizione geometrica delle scatole estratte tramite HBT (parametro D nella Fig. 7). Questo parametro globale diminuisce via via che la cardinalità di HBT aumenta (perché migliora l'accuratezza con cui le box sono estratte). Dall'andamento dei grafici, si deduce che è ragionevole impostare ad un valore ≥ 10 la cardinalità di HBT, in quanto un incremento non porta a sensibili miglioramenti del risultato. Questo numero "minimo" di modelli è in gran parte indipendente dal metodo di clusterizzazione e dal numero di immagini. L'insieme HBT può quindi essere usato per l'estrazione delle

regioni ippocampali in grandi database di immagini.

Sistema CAD per il glioma cerebrale in RM convenzionale e in tensore di diffusione

La realizzazione di sistemi CAD automatici per la segmentazione e il calcolo della volumetria dei gliomi cerebrali (i più diffusi tumori primitivi dell'encefalo) è di grande interesse per la valutazione dell'estensione tumorale nella diagnosi, la pianificazione terapeutica e il *follow-up*: l'uso di un CAD può ridurre la soggettività della diagnosi, aumentandone sensibilità e accuratezza. Questa sezione descrive un CAD [9, 10] per l'individuazione e il contornamento del glioma in RM convenzionale e in tensore di diffusione (DTI, *Diffusion-Tensor Imaging*). Il lavoro. Il lavoro è parzialmente finanziato dal Ministero della Salute.

Le immagini diagnostiche di pazienti affetti da glioma cerebrale sono state elaborate tramite analisi statistica tessiturale 3D (*feature* di Haralick) per caratterizzare matematicamente la struttura del tessuto tumorale e sviluppare un software di segmentazione supervisionata automatica.

Trentaquattro pazienti con gliomi di basso e alto grado sono stati sottoposti a studio RM a 3T con sequenze 3D-FLAIR assiali, 3D-T1w assiali e DTI (single-shot EPI, $b=1000$ s/mm², 32 direzioni). Dalle immagini DTI sono state ottenute le mappe tensoriali FA e MD; dalla decomposizione matematica del tensore di diffusione sono state calcolate le mappe p (isotropica) e q (anisotropica). In ogni mappa le regioni patologiche sono state segmentate manualmente e, a queste e al tessuto sano controlaterale, è stata applicata l'analisi tessiturale per identificare le *feature* discriminanti. La dimensionalità dello spazio delle *feature* è stata ridotta tramite *Linear Discriminant Analysis* (LDA), permettendo la classificazione e la segmentazione del tumore. Per ogni mappa sono state calcolate sensibilità, specificità e curve ROC, con ottimi

risultati ($0.92 \leq AUC \leq 0.97$). Le segmentazioni automatiche sono state confrontate con quelle manuali tramite il coefficiente di Jaccard JC, per determinare la qualità della segmentazione automatica (JC varia da 0 a 1, ed è pari a 1 per una sovrapposizione perfetta). I risultati sono interessanti, con valori medi di JC intorno a 0.7. In Fig. 8 sono mostrate alcune segmentazioni automatiche confrontate con le corrispondenti manuali.

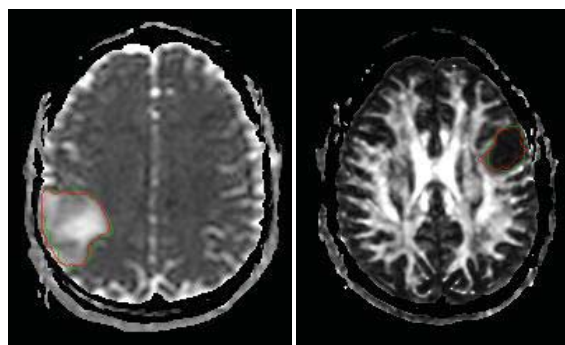


Fig. 8. Due segmentazioni (manuale in verde, e CAD in rosso) in immagini di isotropia (sinistra) e anisotropia.

Un'interfaccia cervello-macchina per la sintesi vocale

Chiude la rassegna un esperimento finalizzato all'individuazione di una metodologia idonea per un'interfaccia cervello-macchina (BCI, *Brain-Computer Interface*) pilotata dal segnale EEG. L'obiettivo finale sarà un sintetizzatore vocale pilotato dal pensiero. Esso può avere applicazioni nelle patologie, come la *sclerosi laterale amiotrofica* (SLA), in cui il paziente incorre in una riduzione o nella perdita della facoltà di comunicare attraverso l'apparato fonatorio. Lo scopo al momento perseguito è apparentemente poco ambizioso: distinguere, tramite *signal processing* e *pattern recognition*, tra i due eventi: "il soggetto ha pensato di articolare la vocale /a/", e "il soggetto ha pensato di articolare la vocale /i/". Dopo aver verificato la fattibilità per due vocali, la prospettiva è includere le altre, poi le consonanti, le sillabe, etc. Essendo in preparazione l'articolo che descrive i risultati ottenuti, daremo qui solo qualche cenno sulla procedura seguita.

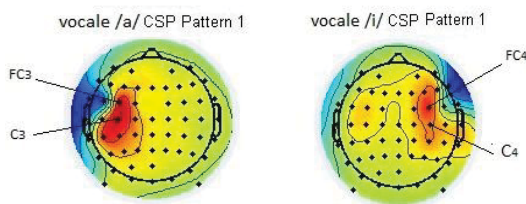


Fig. 9. Common Spatial Patterns per l'individuazione delle vocali pensate /a/ e /i/.

Il segnale EEG di 12 soggetti, 6 uomini e 6 donne, di età media pari a (25 ± 3) anni, è stato catturato da una Cuffia actiCAP a 64 canali della Brain Product, mentre i soggetti eseguivano i compiti previsti (pensare di produrre /a/ o /i/) seguendo un preciso protocollo. La tecnica ICA (*Independent Component Analysis*) è stata applicata allo scopo di individuare artefatti muscolari e, in particolare, quelli dovuti ai movimenti oculari, ed altre eventuali fonti di disturbo (e.g. rumore a 50Hz). Segue il calcolo di *feature* discriminanti, ottenute con il metodo dei *Common Spatial Patterns* (CSP) (Fig. 9), e con un'analisi tempo-frequenza. Avviene infine la fase di classificazione delle vocali pensate, tramite rete neurale. I risultati sono variabili ma interessanti, con valori elevati di area sotto la curva ROC, ed errori di classificazione spesso ben inferiori al 10%.

Conclusioni

Nell'articolo sono descritte alcune applicazioni di Fisica e Informatica alla Medicina e all'analisi di dati biomedici. Molte tecniche sono comuni ai diversi esperimenti, come quelle di pattern recognition (reti neurali), riduzione del rumore, individuazione del contenuto in frequenza di un segnale unidimensionale (e.g. una serie temporale quale l'EEG) o bi- e tri-dimensionale (un'immagine). Tali applicazioni testimoniano l'importanza, per il progredire della tecnologia applicata alla Medicina, di una stretta sinergia interdisciplinare tra specialisti delle diverse discipline.

Bibliografia

- [1] G. De Nunzio, et al., Approaches to juxtapleural nodule detection in CT images within the MAGIC-5 Collaboration, Nuclear Inst. and Methods in Physics Research (2011)
- [2] W.F. Sensakovic, et al., A general method for the identification and repair of concavities in segmented medical images, in: Proc. of the Medical Image Conference 2008, Dresden.
- [3] G. De Nunzio, et al., Automatic lung segmentation in CT images with accurate handling of the hilar region. J Digit Imaging 24, Issue 1 (2011)
- [4] G. De Nunzio, et al., Robust intensity standardization in brain Magnetic Resonance images, sottomesso a J Magn Reson Im
- [5] R. Cataldo, et al., Generating a Minimal Set of Templates for the Hippocampal Region in MR Neuroimages. J Neuroimaging. 2012 doi: 10.1111/j.1552-6569.2012.00713.x [Epub ahead of print]
- [6] L. G. Nyúl e J. K. Udupa, On Standardizing the MR Image Intensity Scale. Magn Reson Med 1999; 42:1072–1081.
- [7] L. G. Nyúl, et al., New variants of a method of MRI scale Standardization. IEEE Trans Med Imag 2000;19 (2):143–150.
- [8] Y. Ge, et al., Numerical tissue characterization in MS via standardization of the MR image intensity scale. J Magn Reson Imag 2000; 12(5):715–721.
- [9] G. De Nunzio, et al., A CAD system for cerebral glioma based on texture features in DT-MR images, Nucl Instrum Meth A, doi: 10.1016/j.nima.2010.12.086, (2011)
- [10] G. De Nunzio, et al., GLIOtest - A CAD system for cerebral gliomas based on texture features, in preparazione

Multi MeV protons, deuterons and carbon ions produced by the PALS laser system

Krása J¹, Margarone D¹, Velyhan A¹, Pfeifer M¹, Ullschmied J², Klír D³, Řezáč K³

¹ Institute of Physics, ASCR, 182 21 Prague, Czech Republic, krasa@fzu.cz

² Institute of Plasma Physics, ASCR, 180 21 Prague, Czech Republic

³ Czech Technical University in Prague, 166 27 Prague, Czech Republic

Abstract

Multi MeV ions and fusion neutrons were generated by focused radiation of the 3–TW Prague Asterix Laser System (PALS). The use of 8– μm Al foil as XUV filter positioned in front of an ion collector allowed measuring currents of 4-MeV protons emitted behind a thin target in the forward direction. The proton energy of 4 MeV generated by a PALS laser irradiance $I\lambda^2 \sim 5 \times 10^{16} \text{ W cm}^{-2} \mu\text{m}^2$ on target is nominally reachable for picosecond lasers when they deliver the intensity $I\lambda^2 \sim 3 \times 10^{18} \text{ W cm}^{-2} \mu\text{m}^2$. The enhanced maximum proton energy is favoured by a non-linear interaction of the laser beam with the pre-generated plasma. Non-linear processes also cause enhancement in the yield of fusion neutrons per focused laser energy from the CD_2 plasma. The obtained results show that an equivalent neutron yield was reached by ps- and sub-ps laser beams for $I\lambda^2 \sim 10^{19} \text{ W cm}^{-2} \mu\text{m}^2$. The hampering influence of the electromagnetic pulse generated within the interaction chamber on diagnostics signals was eliminated.

Introduction

Laser-production of plasmas is a promising technique not only in the field of ion and x-ray sources with a well characterized emission but also in the field of laser induced nuclear reactions and secondary particles generation. As in every new advanced technology there are a number of different constraints that must be overcome in order to progress. One of them is the electromagnetic pulse (EMP) which can be generated within the interaction chamber where the interaction of the high power laser with the target occurs [1]. Signals from plasma diagnostics can be strongly degraded and some item which is part of the electrical

equipment can be damaged by the EMP. Another difficult issue is the detection of multi MeV ions with the use of time-of-flight (TOF) detectors. The velocity of these ions being higher than $1 \times 10^7 \text{ m/s}$ results in interference of an ion collector (IC) signal generated by them with a signal induced by XUV radiation which is generally produced within the target chamber for a time period of about 50 to 100 ns. A possible solution lies in extending the flight distance, L , between the target and the detector. Since the ion current decreases as L^{-3} , there is a limit for the distance given by the sensitivity of the signal-detection system. In this contribution we present methods of protection of diagnostics signals against their

degradation by the EMP and a separation of IC signals induced by fast ions from an XUV signal to obtain a clear cut evidence of production of multi MeV protons and other ions.

Experimental arrangement

The 3-TW PALS laser system was operated at $\lambda_0 = 1.35 \mu\text{m}$ [2]. 300-ps pulses irradiated Si, $(\text{CD}_2)_n$ and graphite targets at 0° and 30° with respect to the target normal. The emission of ions was measured with the use of TOF ion collectors. Fusion neutrons were detected employing TOF detectors composed of a fast plastic scintillator and of a photomultiplier tube and their flux was measured with bubble dosimeters.

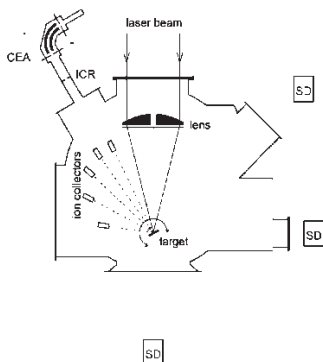


Fig. 1 Scheme of the experiment: CEA – cylindrical ion energy analyser or Thomson parabola spectrometer, ICR – ion ring collector, SD – scintillation detector. The bubble detectors were positioned inside and around the target chamber in various distances.

Results and discussion

Multi-MeV protons

Figure 2 shows a typical example of a strongly degraded ion collector signal by the EMP interference. The signal smoothing was not effective in separating the signals induced by XUV/soft X-ray radiation and multi-MeV carbon ions from the EMP one. Although the characteristics of this EMP are not accurately understood, its effect on diagnostics signals can be eliminated by inserting a delay unit between the IC output and the input of an oscilloscope. The 40-m length of the coaxial

cable allowed to separate the EMP pulse from the XUV and ion signals, as Fig. 3 shows. Since the intense XUV signal overlaps the fast proton signal in the TOF spectrum, as Fig. 3 shows, the IC was shielded with $8\text{-}\mu\text{m}$ Al foil in order to cut off this plasma photopeak signal [3].

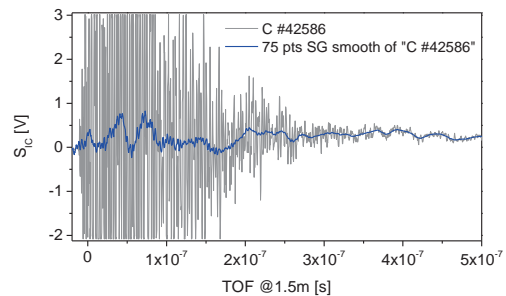


Fig. 2 Strong degradation of the ion collector signal by the electromagnetic pulse (EMP) interference.

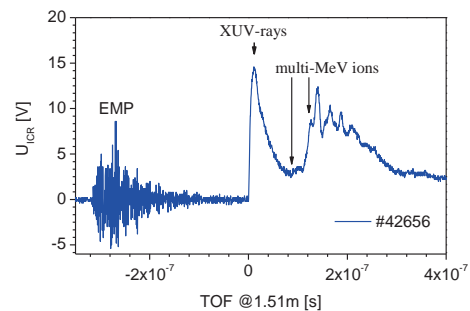


Fig. 3 Separation of the EMP from the ion collector signal using a delay unit. The $(\text{CD}_2)_n$ target was exposed to the laser intensity of $\sim 2 \times 10^{16} \text{ W/cm}^2$.

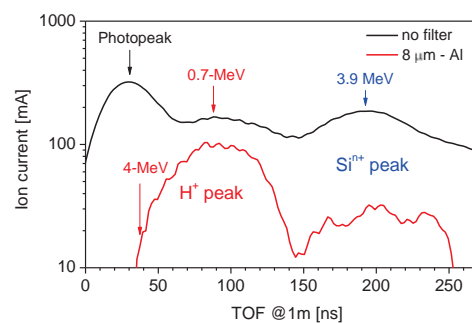


Fig. 4 TOF spectra of accelerated protons and Si ions emitted from the rear side of artificially hydrogenated $17\text{-}\mu\text{m}$ Si single crystalline target irradiated by the laser intensity of $\sim 2 \times 10^{16} \text{ W/cm}^2$ [5].

This technique was successfully applied in an experiment devoted to the forward acceleration of protons which were emitted from a rear side of a $17\text{-}\mu\text{m}$ thin hydrogenated Si membrane [4].

This method allowed the exact determination of v_{MAX} by elimination of the XUV photopeak from the IC signal. It is evident that the fastest protons expand with of $2.84 \times 10^7 \text{ m/s}$ ($E_{MAX} \approx 4.2 \text{ MeV}$), which exceeds the expected value of $1.3 \times 10^7 \text{ m/s}$ ($E_{MAX} \approx 1 \text{ MeV}$) for the value $I\lambda^2 = 3.6 \times 10^{16} \text{ W cm}^{-2} \mu\text{m}^2$, as Fig. 5 shows [5]. Thus, for the corresponding effective target irradiance it holds $I_{eff} \sim 55 \times I_0$, where the target irradiance I_0 is specified by the laser power divided by the focal spot area. The disagreement may lie in the self-focusing effect of the laser beam in the pre-generated plasma, as it was suggested in the case of generation of highly charged Ta^{q+} and Au^{q+} ions carrying the maximum charge state of ~ 50 [6]. In this case it was estimated that the self-focusing increased the value of the target irradiance up to $\sim 1 \times 10^{19} \text{ W/cm}^2$.

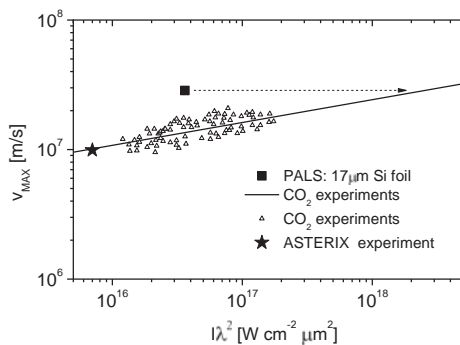


Fig. 5 Maximum proton velocity as a function of a similarity parameter $I\lambda^2$. Square stands for experiment performed with the PALS laser: emission from the rear surface of a 17- μm Si target [5].

γ -rays and neutrons

The laser-plasma interaction gives rise to various secondary processes. One of them is the generation of MeV γ -rays, which are emitted similarly to the MeV bremsstrahlung from a solid target being struck by fast electrons. Their temperature was measured to be $T_e \approx 0.9 \text{ MeV}$ when 200 mJ, 130 fs Ti:sapphire laser pulses irradiated various massive targets [9].

Figure 6 shows a scintillation detector's signal induced by γ -photons and neutrons emitted by CD_2 plasma produced by $I \sim 2 \times 10^{16} \text{ W/cm}^2$. The detector was placed 221 cm far from the

target. It is evident that the EMP destroys the γ -signal when no shielding of the detector is applied. The best protection against the EMP is the use of Faraday cages for all detectors and oscilloscopes including uninterruptible power supplies that are connected with double-shielded coaxial cables. The signal without the EMP interference is shown in Fig. 7. The shielded scintillation detector was placed 320 cm away from a silicon foil target and was surrounded by an enclosure of lead bricks of 20 cm thickness towards the target and 5 cm on all other sides. In contrary to the femtosecond-experiments where over 2000 shots had to be accumulated to obtain a photon spectrum up to $\sim 2.2 \text{ MeV}$ due to the low number of γ photons [9], the intensity of γ -rays in this PALS experiment was so high that only a single shot was needed to obtain high response amplitude, as Fig. 7 shows. The estimated energy of the detected γ photons is higher than $\sim 1.5 \text{ MeV}$.

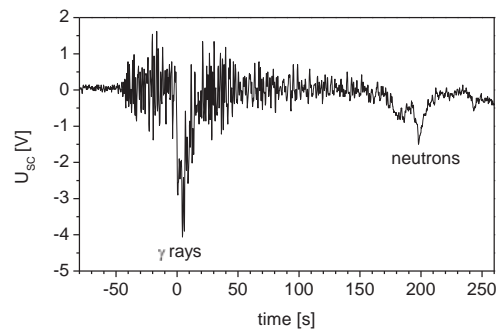


Fig. 6 Scintillation detector signal induced by fusion neutrons and γ radiation emitted from laser-produced CD_2 plasma.

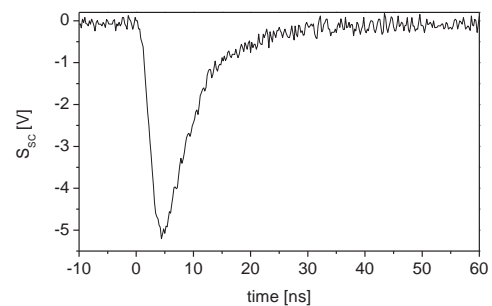


Fig. 7 Scintillation detector response to γ radiation generated with a single laser-pulse (627 J, 300 ps) focused onto a 10- μm Si foil. The radiation penetrated 20-cm lead shielding.

The total flux of neutrons was measured with the use of bubble detectors that are sensitive only to neutrons. Fig. 8 shows a photo of one of irradiated detectors.

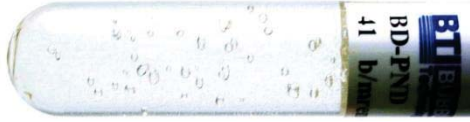


Fig. 8 Bubble detector exposed to 2.45-MeV neutrons emitted by CD_2 plasma which was produced with a $1.7 \times 10^{16} \text{ W cm}^{-2}$ intensity.

The maximum total yield of neutrons observed in this PALS experiment reached a value of 2×10^8 neutrons per laser shot. The yields per laser energy, Y/E_L , obtained in other experiments and giving comparable value Y/E_L with the PALS one are presented in Table 1. It is evident that the PALS result belongs to a group of laser-plasma experiments with a higher efficiency of DD-neutron production. Two experiments [8, 9] giving similar values of $1\text{--}10 \times 10^5$ neutrons/J also imply that the target irradiance of $2 \times 10^{16} \text{ W/cm}^2$ deposited by the PALS laser induces non-linear effects enhancing the efficiency of neutron production.

Target thickness	Y/E_L [n/J]	E_L [J]	τ_L [ps]	I_0 [W/cm^2]	Reference
60 μm	1×10^5	400	1	4×10^{20}	[8]
300 μm	4×10^5	500	250	2×10^{16}	PALS
400 μm	1×10^6	6	0.3	3×10^{19}	[9]

Table 1 Comparison of neutron yields per laser energy measured in various experiments [5].

Conclusions

The irradiation of different targets by the same intensity of $\sim 2 \times 10^{16} \text{ W/cm}^2$ delivered by the PALS laser resulted in generation of about 4-MeV protons, multi-MeV ions, fusion neutrons with a maximum yield of $(1.7 \pm 0.3) \times 10^8$ neutrons/shot as well as of a very strong electromagnetic pulse. The PALS experiment has also shown that the "long-pulse" laser interaction does not depend only on the value of similarity parameter $I\lambda^2$, angle

of incidence, pulse duration and polarization, pre-pulse and target properties, uncertainties in the measurements, intensity assignments and random shot-to-shot fluctuations in the laser beam, but it is also significantly influenced by non-linear laser-plasma interaction. Just both the observed maximum proton energy and the neutron yield per energy already denote that these enhanced values could correspond to the self-focusing which causes the shrinking down of the laser beam spot diameter. Then the irradiance can reach a level of up to 10^{19} W/cm^2 [6].

Acknowledgement

This work benefited from support of the Czech Science Foundation (P205/12/0454), and of the Czech Republic's Ministry of Education, Youth and Sports to the PALS RI (LM2010014), OPVK (CZ.1.07/2.3.00/20.0279, CZ.1.07/2.3.00/20.0087) projects.

References

- [1] M. J. Mead et al., Rev. Sci. Instrum. **75** (2004) 4225.
- [2] K. Jungwirth et al., Phys. Plasmas **8** (2001) 2495
- [3] D. Margarone et al., Rev. Sci. Instrum. **81** (2010) 02A506.
- [4] A. Picciotto et al., Appl. Phys. Express **4** (2011) 126401.
- [5] J. Krása et al. in EAPPC2012/BEAMS 2012 Conf. Proc., Karlsruhe, Germany, p. 204.
- [6] L. Lásková et al., Laser Part. Beams **24** (2006) 175.
- [7] C. Gahn et al., Appl. Phys. Lett. **73** (1998) 3662.
- [8] A. Norreys et al., Plasma Phys. Control. Fusion, **47** (2005) L49.
- [9] L. Disdier et al., Phys. Rev. Lett., **82** (1999) 1454.

Dispositivi acustici impiantabili

Silvano Vitale
Otorinolaringoiatra

ASL Lecce – Ospedale V. Fazzi – U.O.C. ORL
vitasi@libero.it

Abstract

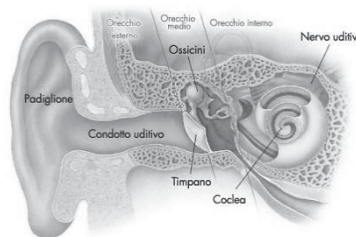
I Dispositivi Acustici Impiantabili (DAI) sono degli ausili per l'udito. Presupposto indispensabile è, pertanto, che il paziente sia affetto da una diminuzione dell'udito. La perdita uditiva (ipoacusia) può essere di diverso tipo (neurosensoriale, trasmissiva, mista) e diversa entità (lieve, media, grave, profonda). Fra i DAI più noti possono essere menzionate due tipologie: 1. Impianti cocleari e 2. BAHA. Gli impianti cocleari trovano indicazione nel caso di ipoacusia neurosensoriale bilaterale di grave-profonda entità. Sia in età pediatrica che in età adulta. Il device viene posizionato (impiantato) all'interno della coclea (recettore dell'udito non più funzionante) e di fatto la sostituisce. Gli stimoli sonori che qui giungono stimolano elettricamente il nervo acustico che parte dalla coclea e che, a sua volta, invia questi impulsi al cervello per la loro interpretazione. Il sistema BAHA è un dispositivo finalizzato al recupero di perdita uditiva di tipo trasmissivo o misto. Ha quindi indicazioni totalmente diverse rispetto ad un impianto cocleare. Questo tipo di dispositivo prevede l'impianto di un pezzo di titanio (cosiddetta vite-pilastro) che viene inserito nella teca cranica dietro l'orecchio. Dopo un adeguato periodo necessario per la osteo-integrazione, viene connesso un processore esterno per la elaborazione dei suoni che vengono trasmessi attraverso il pilastro-vite alle vie acustiche con ripresa della funziona uditiva.

Per Dispositivi Acustici Impiantabili (DAI) si intendono sofisticate apparecchiature, per lo più elettroniche, che sono di ausilio per il ripristino della funzione uditiva danneggiata (ipoacusia). Si definiscono impiantabili perché almeno una loro parte è inserita (impiantata) all'interno del corpo umano e comunque a contatto con le vie acustiche. Sono pertanto dei provvedimenti terapeutici utilizzabili in caso di diminuzione della funzione uditiva (ipoacusia) e rispondono pienamente al concetto di appropriatezza delle cure. Infatti la U.S. Food and Drug Administration (FDA) ha ampiamente approvato il loro utilizzo. In questa circostanza l'autore ha focalizzato l'attenzione su due categorie di questi dispositivi:

1. Impianto Cocleare (IC)

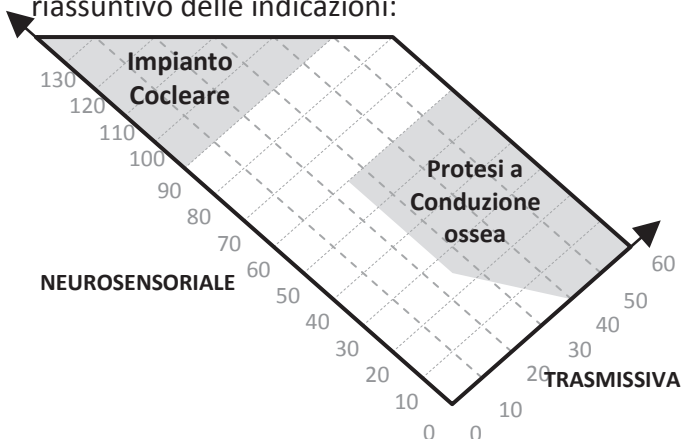
2. Protesi Acustica Ancorata all'Osso - Implantable Bone Conduction Hearing Aids (BAHA)

Queste due categorie di dispositivi differiscono per moltissimi aspetti che riguardano sia il vero e proprio aspetto tecnologico che il paziente a cui vengono impiantati. Partendo da quest'ultimo



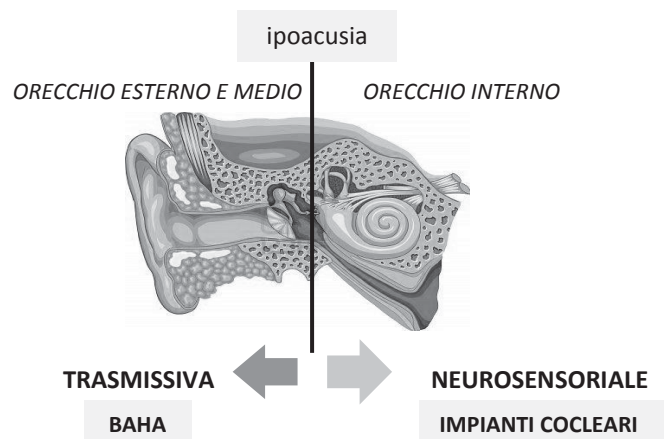
aspetto è utile ricordare che la diminuzione dell'udito può realizzarsi per varie malattie che danneggiano le due vie

attraverso cui viene veicolata l'informazione uditiva: 1. la via neurosensoriale e 2. la via trasmissiva. Detto in modo molto sintetico, la via neurosensoriale è rappresentata dalla coclea all'interno della quale è alloggiato l'organo del Corti che è il vero e proprio organo recettoriale della informazione uditiva. Il suo mal funzionamento determina un danno, irreversibile, alla via neurosensoriale. Di conseguenza avremo pazienti che risulteranno affetti da ipoacusia neurosensoriale di entità variabile in proporzione al danno subito dall'organo del Corti. La via trasmissiva è invece rappresentata dalle strutture anatomiche che costituiscono il cosiddetto orecchio esterno e soprattutto quello medio (membrana timpanica, martello, incudine e staffa), oltre che dalle ossa che formano nel loro insieme la scatola cranica. Il suo danneggiamento determinerà l'instaurarsi di una ipoacusia trasmissiva di entità variabile in proporzione al danno subito. E' solo il caso di ricordare che le due tipologie di ipoacusia (trasmissiva e neurosensoriale) possono coesistere realizzandosi in tal modo la ipoacusia mista. Nel caso di ipoacusia neurosensoriale sarà possibile fare ricorso ad un impianto cocleare; mentre nel caso di una ipoacusia di tipo trasmissivo (o misto) sarà possibile fare ricorso ad una protesi acustica a conduzione ossea come la BAHA. E' bene sottolineare che non tutti i pazienti che soffrono di ipoacusia possono fare ricorso a questi dispositivi ma, solo coloro i quali hanno un determinato grado di danneggiamento. Nella figura sottostante è riportato uno schema riassuntivo delle indicazioni:



Impianto cocleare

L'IC è un dispositivo elettronico messo a punto per la ripresa della funzione uditiva in soggetti affetti da ipoacusia di grave-profonda entità realizzando una stimolazione elettrica del nervo acustico. L'IC è l'unico dispositivo medico attualmente in grado di sostituire completamente un organo di senso ed è per questo che viene utilizzato solo quando la funzione uditiva è molto, molto compromessa in entrambi gli orecchi.



Esso consta di due parti:

1. Esterna: a sua volta costituita dal processore, batterie e coil-magnete
2. Interna: a sua volta costituita dal ricevitore-stimolatore e dal gruppo elettrodo



Nella sua composizione l'IC rimane sostanzialmente eguale sia che si tratti di popolazione pediatrica che adulta. La parte



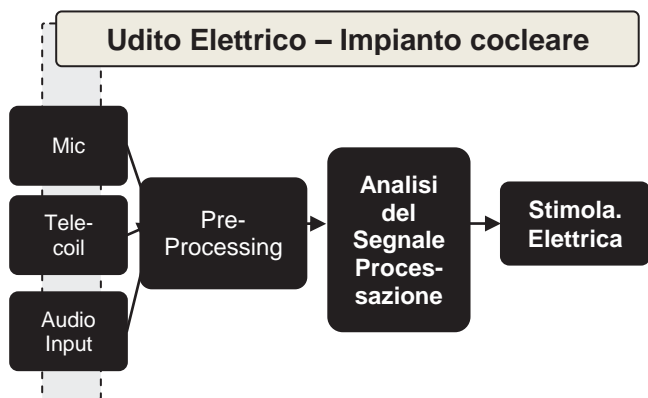
interna è posizionata, una volta per tutte, all'interno dell'organismo e precisamente nella coclea, che è la parte danneggiata, di fatto sostituendola e così by-

passando il tratto non più funzionante della via uditiva, realizzandosi i presupposti per una stimolazione elettrica nel nervo uditivo. La parte esterna e quella interna hanno funzioni nettamente diverse. La parte esterna servirà alla raccolta ed elaborazione degli stimoli sonori mentre la parte interna provvederà, mediante varie strategie di codifica (ACE, SPEAK), a stimolare elettricamente il nervo acustico che, a sua volta, trasporterà l'informazione uditiva verso il cervello dove lo stimolo sonoro potrà essere interpretato.



Parte interna

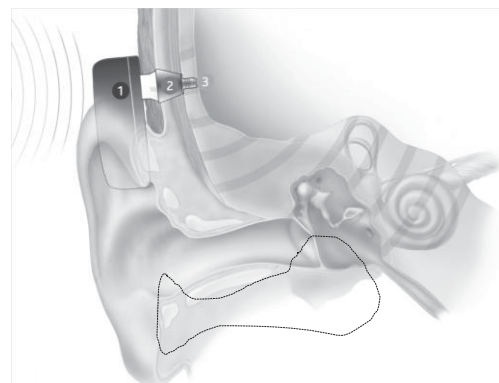
Fra i componenti della parte esterna gioca un ruolo fondamentale il processore (sound processor) che fornisce energia all'impianto, raccoglie, digitalizza e codifica le informazioni che vanno a costituire lo stimolo elettrico. Il processore è dotato di algoritmi di "pre-processing" che puliscono il segnale di ingresso e presentano alla codifica un segnale ottimizzato relativo al parlato. Successivamente il segnale transita attraverso un filtro passabanda che lo scompone in canali (22).



Il segnale così codificato viene utilizzato facendo ricorso a varie "strategie" (ACE, SPEAK) che selezionano i canali e lo convertono in parametri per lo stimolo elettrico tenendo presente vari diversi settaggi (T&C, pulse width, rate,...).

Una volta che la parte esterna ha esaurito la sua funzione, entra in gioco la parte interna che è stata impiantata all'interno della coclea che, ricevendo le informazioni dalla parte esterna, provvederà a realizzare la vera stimolazione elettrica del nervo acustico. La parte interna, costituita da un numero variabile di elettrodi, è pertanto, l'interfaccia di stimolazione elettrica.

Protesi impiantate a conduzione ossea (BAHA)



Alcuni soggetti possono soffrire di una ipoacusia trasmissiva (o mista) in cui vi è il

danneggiamento delle strutture anatomiche che servono per la trasmissione meccanica del suono (cosiddetta via ossea) fra cui il sistema timpano-ossiculare (membrana timpanica, martello, incudine e staffa) e le ossa della scatola cranica. In alcuni di questi casi è possibile fare il ricorso ad un dispositivo acustico che migliora la conduzione del suono per via ossea come la cosiddetta BAHA che è l'acronimo di protesi acustica ancorata all'osso [Bone-Anchored Hearing Aid]. Questo dispositivo dovendo stimolare la via ossea ha una parte impiantata lungo la via trasmissiva. Questa parte è inserita nell'osso, dietro l'orecchio, ed è rappresentata da una vite in titanio. Questa vite interagisce con l'osso circostante realizzando un processo fondamentale chiamato "osteointegrazione". Questa vite è inoltre un tutt'uno con un altro frammento metallico che fuoriesce, per pochissimi millimetri, dalla cute del soggetto impiantato e a cui verrà accoppiato un processore esterno. BAHA è quindi un sistema vibrante che raccoglie i suoni e con la sua vibrazione mette in vibrazione le ossa del cranio così che i suoni possano raggiungere la coclea.



Bibliografia

FDA: <http://www.fda.gov/>

1. Brown KD, Balkany TJ. Benefits of bilateral cochlear implantation: a review. *Current Opinion in Otolaryngology and Head and Neck Surgery*. 2007;15(5):315–318
2. Dettman SJ, Pinder D, Briggs RJ, Dowell RC, Leigh JR. Communication development in children who receive the cochlear implant younger than 12 months: risks versus benefits. *Ear Hear*. 2007 Apr;28(2 Suppl):11S-18S.
3. Hang AX, Kim GG, Zdanski CJ. Cochlear implantation in unique pediatric populations. *Curr Opin Otolaryngol Head Neck Surg*. 2012 Nov 2.
4. Lenarz T, Pau HW, Paasche G. Cochlear Implants. *Curr Pharm Biotechnol*. 2012 Oct 19.
5. Moeller MP. Early intervention and language development in children who are deaf and hard of hearing. *Pediatrics*. 2000;106(3):E43–E52.
6. Parks TN, Rubel EW, Popper AN, Fay RR. *Plasticity of the Auditory System*. New York, NY, USA: Springer; 2004.
7. Shepherd RK, Hatsushika S, Clark GM. Electrical stimulation of the auditory nerve: the effect of electrode position on neural excitation. *Hear Res*. 1993 Mar;66(1):108-20.
8. Snik AFM, Bosman AJ, Mylanus EAM, Cremers CWRJ. Candidacy for the bone-anchored hearing aid. *Audiol Neurotol*. 2004;9:190--6.
9. Waltzman SB, Roland JT., Jr. Cochlear Implant Candidates in Cochlear Implants. New York, NY, USA: Thierme Medical Publishers; 2006.

La fragilità ossea svelata dagli ultrasuoni può consentire la “produzione di salute” su larga scala: studio pilota in pazienti talassemici.

P. Piscitelli^{1,3}, A. Argentiero^{1,2}, C. Neglia¹, A. Peluso⁴, S. Di Rosa⁴, A. Ferrarese⁴, V. Caiaffa⁴, N. Agnello¹, G. Chitano¹, G. Gaudino¹, I. Bortone¹, M. Benvenuto¹, A. Distante¹

¹ ISBEM, Istituto Scientifico Biomedico Euro Mediterraneo, Brindisi, Italy

² Università di Pisa, Pisa, Italy - ³ Università di Firenze, Italy -

⁴ Azienda Sanitaria Locale di Taranto, Taranto, Italy

Abstract

Negli ultimi anni nuove tecnologie sono state rese disponibili per determinare la massa ossea basandosi sull'uso degli ultrasuoni, la cui trasmissione in una struttura porosa - come l'osso - dipende sia dalle caratteristiche fisiche del tessuto sia dalla sua microarchitettura. Nell'ambito del *PROF* (Prevenzione Osteoporosi Fratture) - progetto curato dall'ISBEM fin dal 2009 con alcune ASL del Sistema Sanitario Regionale pugliese - è stato attivato nell'ASL di Taranto un protocollo di studio su una specifica popolazione a rischio, quella dei soggetti affetti da β -talassemia, malattia genetica che causa una ridotta o una mancata sintesi della catena β -globinica dell'emoglobina, determinando un'anemia significativa. Tra le comorbidità maggiormente associate alla talassemia, di certo vi è l'osteoporosi che colpisce i pazienti fin da giovane età, con una prevalenza stimata intorno al 50-70% (vs il 15-17% della popolazione generale). Tutti i soggetti talassemici (n=88) hanno eseguito sia la densitometria ad ultrasuoni (QUS) sia quella basata su raggi X (DEXA) fra il 2008 e il 2010. Nonostante la prevalenza generale di osteoporosi misurata con le due tecniche risulti differente, dall'analisi dei dati emerge come la QUS sia in grado - al pari della DEXA, *gold standard* nella valutazione densitometrica ossea - di discriminare uno stato di demineralizzazione ossea in quei soggetti che avevano già subito una frattura ossea da fragilità. Il nostro studio dimostra come la QUS - metodica poco costosa e priva di radiazioni ionizzanti - fornisca una buona e affidabile stima del rischio fratturativo al pari della DEXA.

Introduzione

Le moderne tecnologie hanno notevolmente migliorato l'approccio alla diagnosi di osteoporosi, consentendo una migliore quantificazione sia della massa sia della densità ossea rispetto a quanto non fosse possibile con la diagnostica radiologica tradizionale. Tra le diverse metodologie oggi disponibili, la densitometria ossea basata sull'utilizzo dei raggi X, Dual Energy X-ray Absorptiometry (DEXA), è ritenuta il *gold standard*. Negli ultimi anni nuove tecnologie sono state realizzate e rese disponibili per determinare la massa ossea basandosi sull'uso degli ultrasuoni, la cui trasmissione in una struttura porosa, come quella ossea, non dipende solo dalle caratteristiche fisiche del tessuto ma anche dalla sua architettura.

Essendo delle vibrazioni meccaniche, gli ultrasuoni sono in grado di propagarsi attraverso materiali e tessuti biologici come quello osseo caratterizzato in condizioni normali da un'elevata densità. I vantaggi che l'ultrasonografia ossea quantitativa (QUS) offre, rispetto alla densitometria tradizionale, risiedono nella sua capacità di fornire informazioni non solo quantitative ma anche qualitative oltre che nell'assenza di radiazioni ionizzanti e quindi nocive, già ampiamente utilizzate in medicina.

Numerosi studi hanno validato scientificamente l'ultrasonografia ossea nell'individuazione dei cambiamenti a carico del tessuto osseo durante la menopausa e l'invecchiamento^{1,2}. Studi prospettici hanno dimostrato come i parametri QUS siano

significativamente correlati al grado di fragilità ossea e, conseguentemente, con il rischio di frattura³. I siti scheletrici d'indagine mediante QUS sono le falangi della mano e il calcagno. Pur trattandosi di siti "periferici", è stato visto che la loro efficacia nella predizione delle fratture osteoporotiche è simile a quella osservata nei siti "centrali" (femore e vertebre). Nell'ultrasonografia falangea la misurazione è effettuata a livello della metafisi distale delle falangi prossimali delle dita II-V (indice, medio, anulare e mignolo) in prossimità dei condili. L'esame può essere eseguito indistintamente su una delle due mani⁴.

Lo strumento è caratterizzato dalla presenza di due sonde piezoelettriche (*emittente* e *ricevente*) montate coassiali su un calibro di precisione posizionate da una parte e dall'altra rispetto alla falange in modo da poggiare sulle superfici latero-mediali della stessa. E' necessario assicurarsi che il contatto delle sonde piezoelettriche con la pelle sia mediato da gel standard per ecografia. Per quanto riguarda la QUS, il range di frequenze utilizzato è compreso tra 200 kHz e 1.5 MHz, notevolmente inferiore rispetto ai valori di frequenza comunemente usati in ecografia. Il tessuto osseo ha un elevato coefficiente di attenuazione dell'ultrasuono, che aumenta esponenzialmente con il crescere della frequenza dell'onda, per cui per lo studio dell'osso è necessario utilizzare frequenze più basse rispetto all'ecografia tradizionale.

Fisica degli Ultrasuoni

La QUS - a differenza dell'ecografia tradizionale basata sulla riflessione delle onde ultrasonore - prevede la generazione di impulsi di ultrasuoni, ad una frequenza di 1,25 MHz con un tempo di ripetizione di circa 100 microsecondi trasmessi (trasversalmente o longitudinalmente) attraverso il tessuto osseo indagato. La sonda emittente genera un segnale ultrasonoro rilevato dalla sonda ricevente una volta che ha attraversato il segmento osseo. Dall'elaborazione del

segnale registrato, lo strumento fornisce una serie di parametri ultrasonografici: AD-SoS, UBPI, T-score e Z-score, nonché l'osteosonogramma. L'AD-SoS (*Amplitude-Dependent Speed of Sound*) è la misura ampiezza-dipendente della velocità di trasmissione dell'onda sonora attraverso l'osso (varia tra 1650 e 2250 m/s). Questo parametro è calcolato quando il segnale raggiunge l'ampiezza di 2 mV. In associazione alla velocità del suono è fornita una traccia grafica rappresentativa delle modificazioni che l'onda ha subito nell'attraversamento dell'osso (l'osteosonogramma) e dal quale è possibile trarre informazioni più dettagliate sulla microarchitettura dell'osso. Dall'analisi della struttura ossea viene elaborato un indice, l'UBPI (*Ultrasound Bone Profile Index*) che fornisce una stima della probabilità che il soggetto incorra in una frattura osteoporotica. Infine T-score e Z-score, espressi in deviazioni standard (DS), nella tecnologia QUS corrispondono a:

$$T - score = \frac{V - V_r}{DS_r}$$

- V è la velocità di trasmissione dell'ultrasuono misurato;
- V_r è il picco medio della velocità di trasmissione dell'ultrasuono in soggetti giovani;
- DS_r è la DS della velocità di trasmissione dell'ultrasuono in soggetti giovani.

$$Z - score = \frac{V - V_e}{DS_e}$$

- V è la velocità di trasmissione dell'ultrasuono misurato;
- V_e è il picco medio della velocità di trasmissione dell'ultrasuono in una popolazione di pari età;
- DS_e è la DS della velocità di trasmissione dell'ultrasuono in una popolazione di pari età.

Il T-score è quindi l'unità di misura derivante dalla differenza - espressa in DS - tra il valore osservato di velocità dell'ultrasuono e il valore medio di velocità dell'ultrasuono in giovani adulti, mentre lo Z-score è invece la

differenza tra il valore osservato di velocità dell'ultrasuono e il valore medio di velocità dell'ultrasuono in soggetti di pari età. Il *T*-score è il parametro su cui è basata la classificazione dei soggetti nelle tre categorie di seguito elencate⁵:

- *Normalità*, per *T*-score superiori a -1 SD;
- *Osteopenia*, per *T*-score compresi tra -1 SD e -3.2 SD;
- *Osteoporosi*, per *T*-score inferiori a -3.2 SD.

Il progetto PROF

Al fine di promuovere diagnosi tempestive dello stato di osteoporosi con l'obiettivo di migliorare l'*outcome* per il paziente e al contempo razionalizzare la spesa a carico dell'organizzazione sanitaria, l'ISBEM ha avviato - dal 2009 in collaborazione con la ASL di Brindisi e dal 2010 con la ASL di Taranto - una campagna di prevenzione primaria abbinata a un programma di ricerca denominato *PROF* (PREvenzione Osteoporosi e Fratture). Il *PROF* è un programma di *disease management* in cui i ricercatori affiancano i clinici e gli specialisti ASL per fornire *know-how*, aggiornamento scientifico e tecnologie densitometriche in molti ospedali o distretti altrimenti sprovvisti. Al fine di una raccolta dei dati anagrafici e anamnestici dei soggetti esaminati è stato creato un registro informatizzato, il R.O.I.S. (Registro Osteoporosi Ionico Salentino), necessario al monitoraggio dell'osteoporosi nel territorio ionico-salentino caratterizzato da un indice di vecchiaia tra i più alti in Italia. Circa 9000 soggetti sono già confluiti nel ROIS permettendo la pubblicazione di numerosi lavori scientifici.

Secondo quanto stabilito dalle Linee Guida Internazionali l'esame densitometrico è stato eseguito in soggetti ricadenti in una delle seguenti classi di rischio:

- donne con più di 65 anni;
- donne in menopausa precoce (<45 anni) o da almeno 10 anni;
- donne con amenorrea prolungata per più di 1 anno; donne in menopausa molto magre o con intolleranza a latte/latticini;

- donne in menopausa con storia familiare di fratture femorali, vertebrali o di polso in età inferiore a 75 anni;
- uomini con più di 70 anni;
- donne e uomini in terapia con cortisonici;
- donne e uomini che, in seguito a traumi minori, hanno avuto fratture di polso, costole, vertebre o femore;
- donne e uomini affetti da malattie che predispongono all'osteoporosi - disturbi della tiroide, del fegato, morbo di Crohn, retto colite ulcerosa, celiachia, mieloma, artrite reumatoide, insufficienza renale cronica, anoressia, talassemia, etc.

Grazie alla collaborazione con il Centro di Microcitemia e di Medicina Nucleare dell'ASL di Taranto è stato generato un protocollo di ricerca finalizzato alla valutazione della densità ossea in una specifica popolazione a rischio, quella dei soggetti affetti da β -talassemia. Si tratta di una malattia genetica che causa ridotta o mancata sintesi della catena β -globinica dell'emoglobina⁶, determinando ridotta emivita dei globuli rossi e quindi un'anemia rilevante. L'osteoporosi è una delle comorbilità maggiormente associate alla talassemia colpendo i pazienti fin da giovane età con una prevalenza stimata intorno al 50-70% (nella popolazione generale è fra 15% e 17%)^{7,8}.

Materiali and metodi

Allo scopo di valutare lo stato di mineralizzazione ossea, i soggetti talassemici che hanno aderito allo studio (n=88) sono stati invitati ad eseguire la QUS falangea mediante strumentazione DBM Sonic 1200 Bone Profiler (IGEA®, Carpi, Modena). Le misurazioni DEXA a livello della colonna vertebrale sono state ottenute mediante strumentazione Hologic QDR 4000 (Bedford, MA, USA). Le rilevazioni sono state eseguite tra il 2008 e il 2010. Il consenso informato è stato ottenuto da tutti i partecipanti allo studio. Degli ottantotto soggetti arruolati (42 uomini, età media 34.1; 46 donne, età media 34.6), il 66% risultava essere affetto da

talassemia *major* e il 34% da talassemia *intermedia*. I due gruppi sono sottoposti a regimi terapeutici diversi: i *major* sono sottoposti a trasfusioni di sangue più frequenti e a trattamenti con farmaci ferrochelanti più rigidi rispetto agli *intermedi*.

Risultati

L'analisi dei dati anamnestici raccolti ha permesso di ottenere un quadro completo delle comorbidità di cui questi soggetti erano affetti. Nove pazienti su 88 (10% del campione) presentavano diagnosi di diabete mellito, mentre 10 erano affetti da ipoparatiroidismo (11%), 43 da epatite B (49%) e 52 da ipogonadismo. I soggetti che hanno dichiarato di aver già subito una frattura da fragilità erano 23 (26%).

Per tutti i soggetti esaminati sono stati rilevati i valori di *T*-score e *Z*-score sia con DEXA sia con QUS. Comparando questi valori in soggetti affetti β -talassemia *major* e *intermedia* non è emersa alcuna differenza statisticamente significativa tra le due tecniche. Mentre si è osservata la presenza di valori di *T*-score più bassi nei soggetti affetti da ipogonadismo rispetto ai non affetti. La stessa differenza è stata misurata in soggetti affetti da ipotiroidismo, diabete ed epatite B. Di particolare interesse è la capacità della QUS di rilevare la presenza di demineralizzazione in quasi la totalità dei pazienti che avevano dichiarato di aver già subito una frattura da fragilità, similmente alla DEXA.

Dal calcolo della prevalenza generale dello stato di demineralizzazione ossea emergono differenze sostanziali tra le due tecniche. In generale, osteoporosi è stata misurata nel 52% del campione misurato attraverso DEXA mentre solo il 10% dello stesso campione presentava osteoporosi se misurato con tecnica QUS. Viceversa, percentuali di normalità è stata rilevata nel 16% e nel 30% del campione usando DEXA e QUS rispettivamente.

Discussione

Questo è il primo studio in cui è stata comparata la capacità delle metodiche DEXA e QUS di rilevare la presenza di demineralizzazione ossea in soggetti talassemici affetti da comorbidità e con pregresse fratture ossee da fragilità. In un precedente studio finalizzato a comparare la DEXA e la Tomografia Quantitativa Computerizzata (QCT) è stata osservata una forte differenza nella prevalenza dello stato di osteoporosi e osteopenia misurato, similmente a quanto rilevato nel nostro studio⁹. Il risultato del nostro lavoro pone la tecnica ultrasonografica in una posizione intermedia tra DEXA e QCT le quali forniscono una misura della BMD (*Bone Mineral Density*) che si ritiene sia il miglior indice predittore del rischio fratturativo. Diversi studi ipotizzano che la BMD rappresenti solo uno dei tanti fattori coinvolti nella determinazione della resistenza ossea e che la qualità ossea (microarchitettura, geometria ed elasticità) sia indipendente dalla densità minerale. Se si considera la DEXA come *gold standard* delle tecniche densitometriche, la maggior parte dei soggetti dovrebbe essere classificata come osteoporotica: questo dato non spiega però il basso numero di fratture da fragilità verificatesi in questi soggetti.

Conclusioni

Il nostro studio dimostra come la QUS - metodica poco costosa e basata su energia meccanica, quindi priva di radiazioni ionizzanti - fornisca una buona ed affidabile stima del rischio fratturativo che la mette al pari della DEXA, ritenuta ad ora il *gold standard* nella valutazione densitometrica ossea, comunemente eseguita in ospedale e/o in ambulatorio ma poco adatta per campagne di prevenzione su larga scala.

Bibliografia

[1] Piscitelli P et al. Incidence and socioeconomic burden of hip fractures in

- Italy: extension study 2003-2005. *Reumatismo* 2010, 62(2):113-118.
- [2] Piscitelli P et al. Hip fractures in Italy: 2000-2005 extension study. *Osteoporosis Int.* 2010, 21(8):1323-1330.
- [3] Mussolino ME et al. Phalangeal bone density and hip fracture risk. *Archives of Internal Medicine* 1997; 157: 433-8.
- [4] Ventura V et al. Ultrasound velocity changes at the proximal phalanges of the hand in pre-, peri-, and postmenopausal women. *Osteoporosis International* 1996; 6: 368-375.
- [5] Wuster C et al. The phalangeal osteosonogrammetry study group. Phalangeal osteosonogrammetry study: age-related changes, diagnostic sensitivity, and discrimination power. *Journal of bone and mineral research* 2000; 8:1603-1614.
- [6] Origa R and Galanello R. Pathophysiology of Beta Thalassemia. *Pediatric Endocrinology Reviews* 2011; 8 Suppl 2:263-70
- [7] Voskaridou E and Terpos E. New insights into the pathophysiology and management of osteoporosis in patients with thalassemia major. *British Journal of Haematology* 2004; 127:127-139.
- [8] Jensen CE et al. High prevalence of low bone mass in thalassemia major. *British Journal of Haematology* 1998; 103:911-915.
- [9] Mylonas et al. Comparison of DXA, QCT and trabecular structure in beta-thalassaemia. *Eur J Haematol* 2005; 74:430-437.

Intensity Modulated Radiation Therapy with volumetric modulation (VMAT)

D. Russo*, E. Cavalera*, A. Papaleo*, A. Leone*, F.P. Ricci*, G. Di Paola*, C. Capomolla**, M. Natali**, G. Pastore**, M. Santantonio*

** Department of Radiation Oncology,*

*** Department of Medical Physics, V. Fazzi Hospital, Lecce, Italy.
donatellarusso@libero.it'*

Abstract

IMRT (Intensity Modulated Radiation Therapy) is the latest radiotherapy technique for high dose treatment of complex shaped tumors or neoplasm close to sensitive organs at risk. VMAT (Volumetric Modulated Arc Therapy) is next generation arc therapy technique which performs uninterrupted arc(s) around the patient, dramatically speeding treatment delivery and reducing treatment times to those required for "conventional" radiation therapy. Beam modulation is obtained by continuous changes in collimator morphology on the basis of target shape and in dose rate during gantry rotation around the patient. Since November 2010, in our institution, 257 patients were treated with VMAT. Plan evaluation was performed using Homogeneity and Conformity Index and a phantom (Delta 4) to control correspondence between calculated and delivered dose. In our experience VMAT provides to dose distributions comparable with most of other IMRT systems, but with a dramatic shortening of delivery time with considerable advantages in terms of treatment reproducibility (reduction of intrafraction movement of the patient), radioprotection and organization of LINAC spaces.

Introduction

IMRT represents the most recent evolution of radiation technologies. It allows improvement of therapeutic index both arising tumor control probability, due to dose increment to target, and reducing side effects.

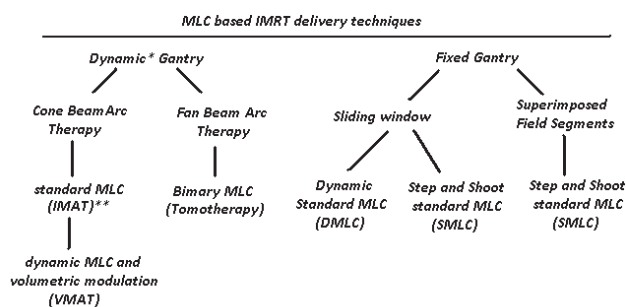
Dose modulation and escalation can be achieved by an increment of beam number, a gantry rotation (arc therapy), multileaf collimator (MLC) shape dynamic modification or dose rate modulation (fig 1).

The main limit of IMRT treatments is represented by long fraction delivery time

and high number of monitor units per fraction. Furthermore, using a multiple field-IMRT or Serial Tomotherapy, radiation linkage and scattering is not trascurable, probably affecting effective delivered dose.

The aim of this paper is to describe a dynamic IMRT technology, VMAT® (Volumetric Modulated Arc Therapy), in use in Radiation Oncology Unit of "Vito Fazzi" Hospital (Lecce) since November 2010. In particular, we will describe VMAT application in the care of Head and Neck, Pelvic primitive neoplasm

and brain metastasis and its utility in



* The word "dynamic" is used in this chart is used in this chart to define movement of the component with the treatment beam turned on

**{.....}= common used abbreviation or name

Fig.1: Multileaf collimator (MLC)-based intensity modulated radiation therapy (IMRT) delivery techniques.

DMLC: dynamic multileaf collimation

IMAT: intensity modulated arc therapy

SMLC: segmental multileaf collimation

Materials and methods

VMAT delivers radiation by rotating the gantry of linac around the patient through one or more arcs with radiation continuously on. As it do so, a number of parameters can be varied. These include:

- MLC aperture shape
- the fluence output rate (dose rate)
- the gantry rotation speed
- the MLC orientation [1]

Treatment is performed by rotating the gantry over a single or dual arc(s), with MLC set and shaped to cover target. This entails rapid execution of a sequence of control points each defining multileaf collimator (MLC) shape, MLC segment dose, and a gantry-angle window across which each shape sweeps dynamically (Fig 2).

The genesis of the method was with intensity modulated arc therapy (IMAT) from Cedric Yu back in 1995, but VMAT adds the variability of parameters above mentioned, thus reducing the need to use as many arcs as there are maximum number of field components (fig 1).

VMAT can deliver highly conformal dose distributions similar to those created by other forms of intensity-modulated radiation therapy (IMRT), including the multiple-static

overcoming IMRT limits.

field MLC technique, the dynamic MLC (DMLC) technique, static and helical tomotherapy, the CyberKnife, scannedbeam therapy and so on (hereafter referred to as "conventional" IMRT).

Provided that the gantry speed can be varied continuously, it does not require a continuous variation of fluence-output rate to obtain a continuous variability of fluence output rate per degree.

The minimum fluence-output rate and the maximum gantry speed determine the constraining minimum fluence output rate per degree. Where there is a maximum fluence-output rate and minimum gantry speed, there will be a constraining maximum fluence output rate per degree.

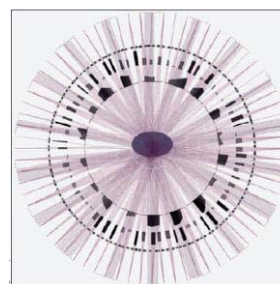


Fig 2:VMAT: the divergent ray paths, leaf positions and segment weighting at each gantry angle. The reconstructed parallel rays and associated intensity-modulated beam are shown for every 4th angle. From a set of unmodulated VMAT fields, the parallel rays are spatially modulated.

Since November 2010, in our institution, 257 patients were treated with VMAT. Schematic representation of patients who underwent to this therapy and their disease is shown in table 1.

In every patient, a 3 mm thickness-CT scan of tumor site was acquired in treatment position. On every slice were defined one or more PTV(s) (planned target volume) and the organs at risk of side effects development (OARs). Treatment planning was calculated on Oncentra Masterplan®, using a specific inverse planning system. Treatment plans were evaluated using isodose distribution, DVH (dose-volume histogram) and a quality index (CI) :

$$\text{Conformity Index (CI)}: \frac{TV_{RI} \times TV_{RI}}{TV \times V_{RI}};$$

TV_{RI} : Target volume covered by the reference isodose; TV : Target volume; V_{RI} : Volume of the reference isodose)

Disease site	Number of patients
Head and Neck	91
Lung	31
Brain	30
Prostate gland	29
Gynecologic neoplasm	29
Anus	11
Superior Abdomen	11
Rectum	5
Oesophagus	5
Boost in craniospinal irradiation	5
Other	10
Total	257

Table 1: patients treated with VMAT in our institution

In every treatment plan, target volumes called PTV were delineated and a potential curative dose is prescribed. To avoid or to reduce incidence of side effects, constraints to OARs were individualized. These constraints corresponds to doses that produce toxicity in 5% of cases in 5 years (table 2) (2-10).

Target coverage and OARs doses are evaluated on DVH.

Organ at risk	Constraints
Spine	$D_{max} = 45 \text{ Gy}$
Brainstem	$D_{max} = 54 \text{ Gy}$
Parotid Glands	$D_{mean} = 26 \text{ Gy}$
Eye	$D_{mean} = 35 \text{ Gy}$
Lens	$D_{max} = 5 \text{ Gy}$
Optic nerve	$D_{max} = 60 \text{ Gy}$
Optic chiasma	$D_{max} = 54 \text{ Gy}$ $V_{50} = 1\%$
Small bowel	$V_{15} < 120 \text{ cc}$ $V_{45} < 195 \text{ cc}$ $V_{50} < 50\%$
Rectum	$V_{50} < 35\%$ $V_{70} < 25\%$ $V_{75} < 20\%$ $V_{75} < 15\%$
Bladder	$V_{50} < 50\%$ $V_{70} < 35\%$ $V_{75} < 25\%$
Femoral heads	$V_{40} < 40\%$ $D_{max} = 50 \text{ Gy}$

Table 2: OARs in Head and Neck and Pelvic neoplasm treatment and constraints commonly used in IMRT plans

Head and Neck

In Head and Neck cancer treatment, three PTVs with three different dose levels were defined as below:

- PTV1: primary and positive nodes. Prescription dose 69.9 Gy in 2.33 Gy-daily fractions

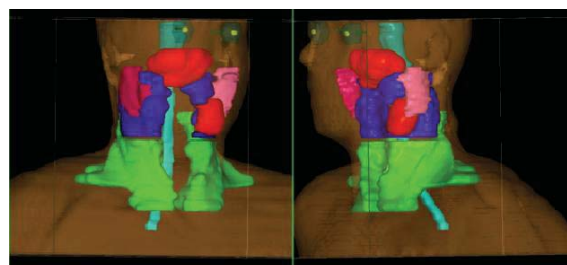
- PTV2: nodes at high risk of subclinical involvement. Prescription dose 60 Gy in 2 Gy-daily fractions
- PTV3: nodes at low risk of subclinical involvement. Prescription dose 54 Gy in 1.8 Gy-daily fractions

Total fractions number is 30.

Organs at risk to develop toxicity were:

- spine
- brainstem
- parotid glands
- optic and ocular structures (eyes, lenses, optic nerves, optic chiasma)

Contouring of PTVs and OARs is shown in fig. 3.



PTV1
PTV2
PTV3

contralateral parotid gland
lenses
brainstem
omolateral parotid gland
spine

Fig 3: Example of contouring in Head and Neck cancer: 3D-reconstruction of Target Volumes and Organs at Risk

Pelvic Malignancies

Prostate cancer

In Prostate Cancer, treatment volumes were often represented by prostate and seminal vesicles (fig 4A).

Prescription dose were 78.4 Gy in 35 fractions for prostate (fraction dose: 2.24 Gy) and 66.5 Gy for seminal vesicles (fraction dose: 1.9 Gy).

In case of high risk of subclinical involvement, prophylactic irradiation of pelvic nodes was indicated. In this case, target volumes and prescription doses were PTV1 (prostate, seminal vesicles and macroscopically involved nodes) treated with 70 Gy and PTV2 (negative pelvic nodes) treated with 50-56 Gy in 28 fractions

(fraction doses 2.5 and 1.8-2 Gy respectively) (fig 4B).

Gynecologic cancers

PTVs (fig. 5) and prescription doses were:

- Tumor side and involved Nodes: 66 Gy 30-33 fraction of 2.33-2 Gy
- Rest of uterus (when it is surely not involved; PTV2): 60 Gy in 30-33 fractions of 2-1.8 Gy
- Negative nodes (PTV3): 54-56 Gy in 30-33 fractions of 1.8-1.7 Gy

OARs were small bowel, rectum, bladder.

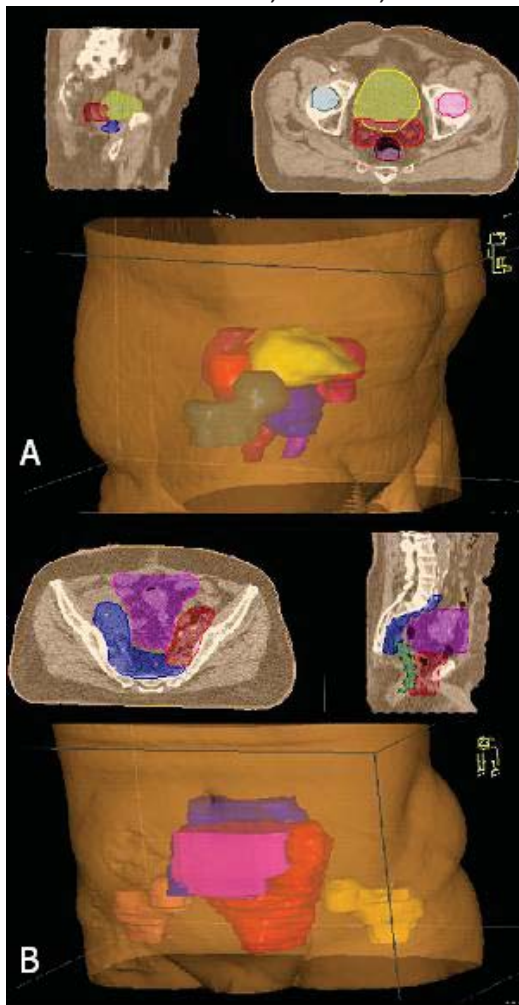


Fig. 4: example of contouring in prostate cancer and 3D reconstruction of PTVs and OARs
 A: without lymphnodes
 B: with lymphnodes

Brain metastasis

IMRT with VMAT was indicated in patients with 1-3 brain metastases (maximum diameter of largest metastasis ≤ 3 cm). A GTV (Gross Tumor Volume) including the lesions macroscopically visible was delineated on CT

scan. PTV1 derived from GTV with 3mm margin. PTV2 included the whole brain. Prescription doses were: 40Gy in 4Gy-daily fraction for PTV1 ≥ 2cm and 50Gy in 5Gy-daily fractions for PTV1 <2cm.

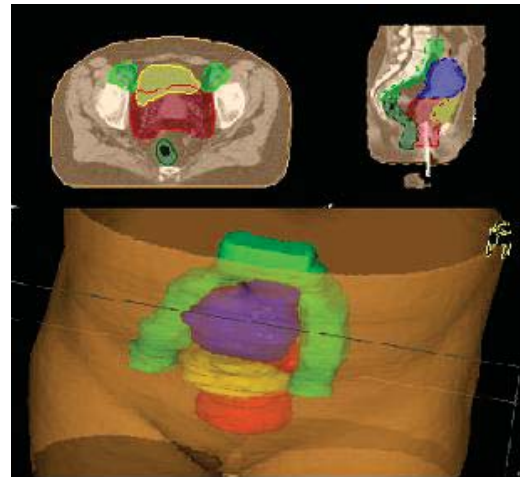


Fig. 5: Example of contouring in Gynecologic Cancer and 3D reconstruction of PTVs and OARs

Total dose for whole brain was 30Gy in 3Gy-daily fractions.

OARs were:

- Ocular and optic structures
- Auricular and acoustic structures
- Brainstem

Results

In every treatment plan, high dose conformation around target was required before final approval. In particular, all plans had Conformity Index included between 0 and 1, that means in line with IMRT protocols or with only a minor violation.

In **Head and Neck cancer**, spine sparing was performed in all plans and parotid sparing was achievable in 90% of cases.

In all plan 95% of prescribed dose covered 95% of target volume (fig. 6A). To obtain acceptable dosimetric result and OARs sparing, it was necessary to program treatment using two 340-degree arcs. Fraction duration was 12-20 minutes.

In **Pelvic Malignancies** bladder and rectum sparing was achievable in all treatment plans

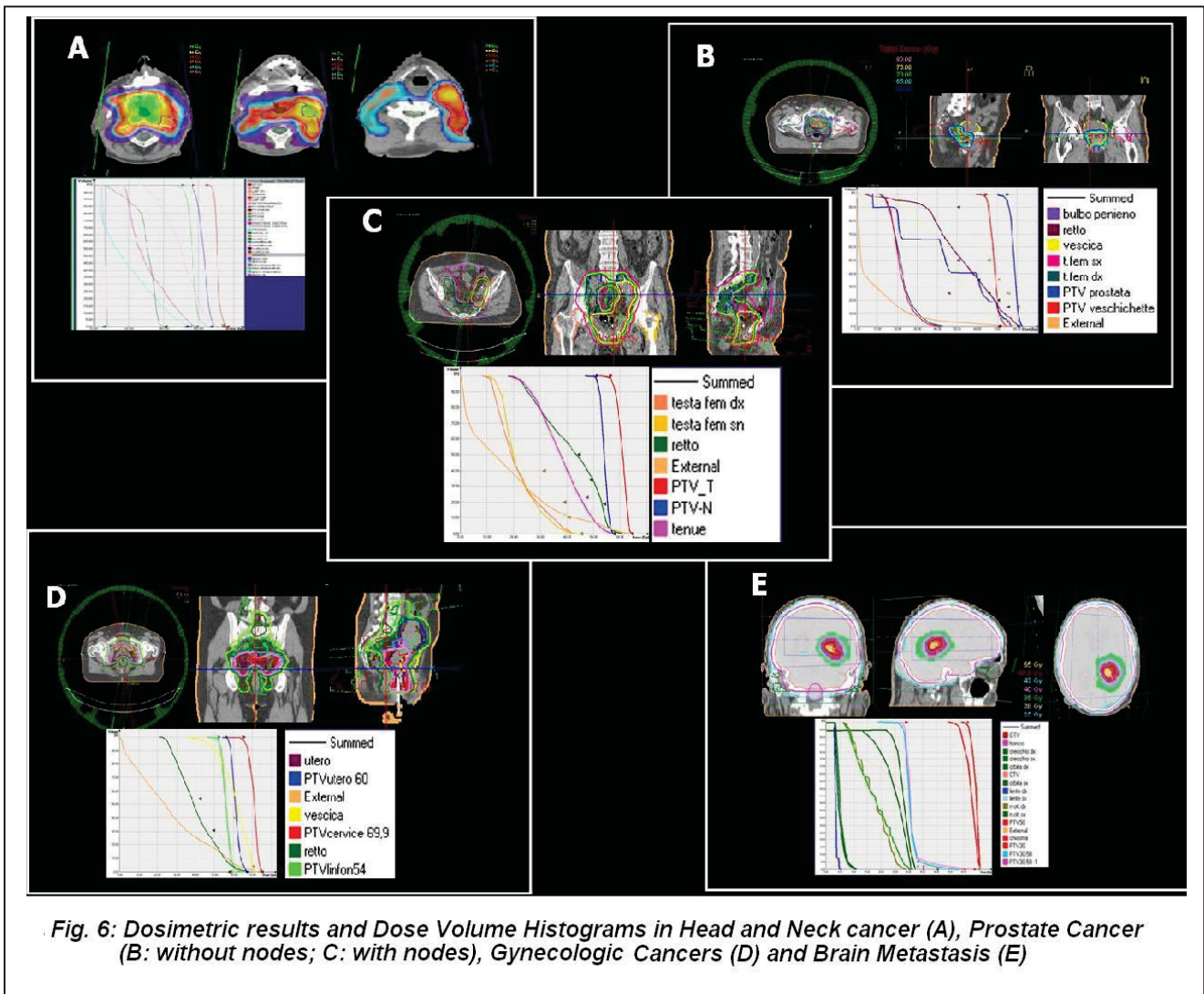


Fig. 6: Dosimetric results and Dose Volume Histograms in Head and Neck cancer (A), Prostate Cancer (B: without nodes; C: with nodes), Gynecologic Cancers (D) and Brain Metastasis (E)

(fig. 6 B, C, D). In prostate cancer, when nodal irradiation was not required, acceptable dosimetric result could be achieved using only an arc. In this case, treatment duration was 5-7 minutes. To obtain an adequate coverage of nodal pelvic chains, in prostate and gynecologic neoplasm, two 340° arcs are required, with a fraction time of 12-15 minutes.

Also in **Brain Metastasis** treatment, high dose and conformation around target and OARs sparing can be easily achieved using a double arc VMAT plan. Treatment duration was 12-15 minutes.

Discussion and Conclusions

VMAT is characterized by a series of technical advantages listed below:

- Fast Seamless Field Delivery

- Continuously Variable Dose-Rate
- Variable Gantry Speed
- Optimized Patient Positioning (couch movement in the three dimensions)
- Optimized Collimator Angle
- Seamless Field Delivery Interdigitation

These advantages provide to an easy delivery of intensity modulated radiation treatment and, in particular, simultaneous delivery of different dose levels to different target volumes (SIB: simultaneous integrated boost).

SiB obtained with a single treatment plan, allows reduction in overall treatment time with consequent reduction in tumor repopulation probability. Moreover, using a daily fraction higher than 2 Gy (daily-2 Gy = Conventional Fractionation= CF), biological

equivalent dose (BED) on target volume is higher than the nominal dose, with an improvement in tumor control probability. The calculation of BED is effectuated using the formula below:

$$\text{BED} = D \frac{\alpha/\beta + d}{\alpha/\beta + 2}$$

Where: D= nominal prescribed dose; α/β = ratio specific for different tissue, describing tissue sensibility to radiation; d= fraction dose; 2= dose fraction in CF.

Result of VMAT optimization may, however, depend on number of arcs, maximal delivery time and gantry angle spacing between subsequent control points. Some studies demonstrate that a single arc can achieve dosimetry comparable with IMRT for prostate cancer, but not for more complicated PTV, so in most cases a double arc treatment is necessary to achieve acceptable dosimetric results, affecting the duration of fraction delivery.

Although in a study single arc-VMAT seems to produce in Head and Neck cancer similar dosimetric results with less Monitor Unit than Step and Shoot IMRT (11), most series suggest that dual arc provide to an higher plan quality. Using dual arc increase calculation time. However, both single and dual arc reduce delivery time compared with other IMRT. Optimization using larger spacing between control points can reduce calculation time. In fact, dosimetric results are comparable using an interval of 6° or 4° or 2° (12)

In treatment of brain metastasis with SIB and high dose fraction, with a theoretical arising of tumor control probability, there is an increased probability of developing side effects like cognitive functions. A study demonstrate that this effect is more evident in questionnaire of patients treated with SIB-higher fraction doses, without a worsening in Quality of Life (13). VMAT is a quite rapid IMRT technique. It is more accurate and efficient in delivery than the other IMRT, because of a drastic (8.5%)

reduction in Monitor Unit (11). This data suggest that VMAT could be the ideal technique to treat also volume fast modifying (e.g. bladder).

In our experience, VMAT is an efficient IMRT technology, able to join excellent dosimetric results with rapid delivery. Unfortunately, the calculation time is too long and this creates difficulties in Radiotherapy and Physics Units organization since it is necessary that part of the staff has to be exclusively dedicated to the optimization of these treatment plans.

References

1. Steve Webb: "VMAT its role in Radiotherapy". *Medicalphysicsweb-Review; Winter 2009*
2. Emami B et al: "Tolerance of normal tissue to therapeutic irradiation". *Int J Radiat Oncol Biol Phys* 1991;21(1): 109-122
3. Mayo C et al: "Radiation Dose-Volume Effects of Optic Nerves and Chiasm" *Int J Radiat Oncol Biol Phys* 1991;21(1):S28-S35
4. Mayo C et al: "Radiation associated BarinSTEM Injury" *Int J Radiat Oncol Biol Phys* 1991;21(1):S36-S41
5. John P. Kirkpatrick et al: "Radiation Dose-Volume Effects in the Spinal Cord" *Int J Radiat Oncol Biol Phys* 1991;21(1):S42-S49
6. Niranjana Bhandare et al: "Radiation Therapy and Hearing Loss". *Int J Radiat Oncol Biol Phys* 1991;21(1): S50-S57
7. Joseph O. Deasy et al: "Radiation Dose-Volume Effects on Salivary Gland Function". *Int J Radiat Oncol Biol Phys* 1991;21(1): S58-S63
8. Brian D. Kavanagh et al: "Radiation Dose-Volume Effects in the Stomach and Small Bowel". *Int J Radiat Oncol Biol Phys* 1991;21(1): S101-S107
9. Akila N. Viswanathan et al: "Radiation Dose-Volume Effects of the Urinary

- Bladder*". Int J Radiat Oncol Biol Phys 1991;21(1): S116-S122
10. Jeff M. Michalski et al : "*Radiation Dose–Volume Effects in Radiation-Induced Rectal Injury*". Int J Radiat Oncol Biol Phys 1991;21(1): S123-S129
 11. Anders Bertelsen, "*Single Arc Volumetric Modulated Arc Therapy of Head and Neck Cancer*". Radiat Onc, 2010; 95(2): 142-148
 12. Judith Alvarez Moret et al: "*Evaluation of volumetric modulated arc therapy (VMAT) with Oncentra MasterPlan® for the treatment of head and neck cancer*" Radiat Oncol 2010; 5:110-120
 13. Damien C Weber et al "*Simultaneous in-field boost for patients with 1 to 4 brain metastasis/es treated with volumetric modulated arc therapy: a prospective study on quality-of-life*" Radiat Oncol 2011; 6: 79-87

Dosimetric verification of vmat dose distribution with DELTA4® Phantom

M. Natali¹, C. Capomolla¹, D. Russo², G. Pastore¹, E. Cavalera², A. Leone², A. Zagari¹, M. Santantonio²

¹U.O.C. Fisica Sanitaria P.O. "Vito Fazzi", Lecce (Italy)

²U.O.C. Radioterapia - P.O. "Vito Fazzi", Lecce (Italy)

Abstract

Radiation Oncology, has changed a great deal, undergoing an innovation and technical development; there has been an evolution from conformal radiotherapy techniques (3D-CRT), through advanced modalities like intensity-modulated radiation therapy (IMRT) and next volumetric modulated arc therapy (VMAT). VMAT technique requires a dedicated QA (Quality Assurance) procedure for dosimetric verification of a planned dose distribution to check for the agreement between a dose distribution calculated by the Treatment Planning System (TPS) and the corresponding measured dose distribution. Since November 2010, in Radiation Therapy Department of "V. Fazzi" hospital in Lecce (Italy), 257 patients were treated with VMAT and the corresponding dose distribution were verified with the Delta4[®] diode array phantom. Parameters used in the comparison between calculated e measured dose are the dose agreement (DA), the distance to agreement (DTA) and the γ -index. The phantom measurements closely match the planned dose distributions in high and low dose-gradient region.

Introduction

Volumetric Modulated Arc Therapy (VMAT) is a new intensity-modulated radiation therapy (IMRT) technique that improves critical structures and healthy tissue sparing, in dramatically shorter treatment times all without comprising target coverage and patient safety.

The sharp dose gradients found in VMAT, make critical the deviations between calculated and real dose distribution even if they are very small, especially in regions close to organs at risk; in addition, each VMAT plan is strictly tailored on the patient because the various leaf position and leaf speed may be quite different, even case of target and organs at risk very similar, because it is dependent on multiple factors,

each of them influencing dose effectively delivered to the patient.

Complex radiotherapeutic treatment plans such as those obtained with VMAT require dosimetric verification before clinical delivery.

Materials and methods

In Radiation Therapy Department of "V. Fazzi" hospital in Lecce (Italy), 257 patients were treated with VMAT.

In our institution, planned dose distribution is checked using the Delta4[®] diode array phantom.

During verification process the planned treatment is transferred from the patient (Fig 1a) to the phantom (Fig 1b), the treatment plan is recalculated on a CT scan of the phantom and then the dose

distribution is measured using Delta4[®] device.



Fig. 1a VMAT planned dose

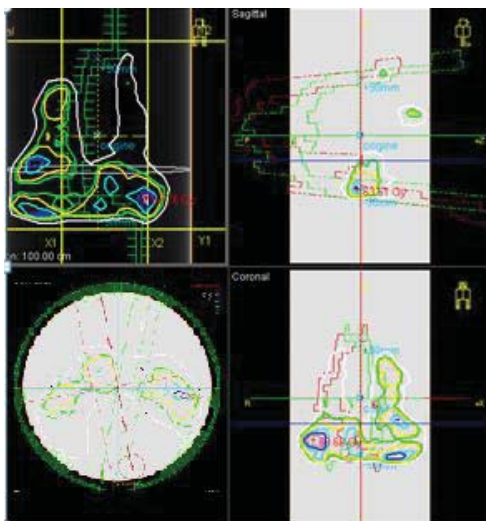


Fig. 1b recalculated VMAT dose on the Delta4[®]

The Delta4[®] diode array phantom (Scandidos, Uppsala, Sweden) consists of 1069 p-type Silicon diodes in a crossed array inside a cylindrical polymethylmethacrylate (PMMA) phantom with associated a computer software that allows the user to compare the measured dose distribution for a complete treatment plan with the dose distribution predicted by the treatment planning system (Oncentra Masterplan[®]). The diodes are cylindrical, have an area of 0.0078 cm² and are spaced at 0.5 cm intervals over the central 6 x 6 cm of the planes and at 1 cm intervals over the remainder of the central 20 x 20 cm of the planes. The crossed planes are achieved by means of a main detector board

which passes through the entire diameter of the phantom and two wing detector boards which are separated to allow the main detector board to pass between them. The phantom itself has a diameter of 22 cm and length of 40 cm (Figure 2).

The device records measured dose in relation to the individual accelerator pulses by using a trigger signal from the accelerator, facilitating time-dependent four-dimensional applications. Gantry angle is independently sensed by means of an inclinometer attached to the gantry or accelerator head. This allows the device to identify which control point of a dynamic arc delivery is being delivered, so that the measured dose can be associated with this control point, and the appropriate correction for gantry angle applied.

When the measure with the Delta4[®] has been performed, the agreement between calculated and measured dose distributions must be analyzed.

A qualitative check of the agreement is usually performed by dose profiles along selected lines or isodose comparisons.

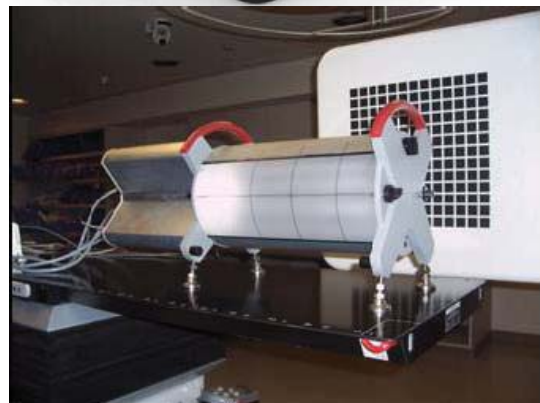
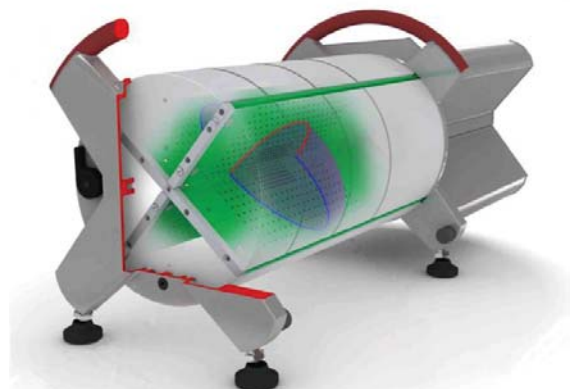


Fig.2 Delta4[®] phantom

If quantitative comparisons are required, the choice of the correct parameters to be employed is critical.

In standard techniques, the most important parameters are: “dose agreement” or DA and “distance to agreement” or DTA.

DA is the percentage or absolute difference between measured and calculated dose, unfortunately it is not suitable for high dose gradient region, where even small spatial errors may lead to large but not significant errors. So in high dose gradient regions it is used the DTA, defined as the minimum distance, in the plane, between a measured point and the nearest point in the calculated dose distribution that has the same dose. It is defined 3mm as distance limit.

It is important to underline that DTA depend on the choice of the correct common coordinate system between measured and calculated dose, otherwise results are not significant.

The DTA and the DA% are quantitative tools but they still have important limitations when applied to IMRT dose distributions.

To overcome all these problems, a new parameter (γ -index) that it includes in a single data set DA% and DTA has been introduced.

The γ -index is defined as follows: given a point in the reference distribution, r_r , and the relative dose D_r , an “acceptance ellipsoid” for point r_r is defined by :

$$\gamma(\vec{r}_m) = \min \left[\sqrt{\left(\frac{\delta d(\vec{r}_m, \vec{r}_c)}{\Delta d_M} \right)^2 + \left(\frac{\delta r(\vec{r}_m, \vec{r}_c)}{\Delta r_M} \right)^2} \right] \forall \vec{r}_c$$

Δd_M e Δr_M the acceptance criteria for distance e dose

δr is the distance between the measured point r_m and a point r_c chosen in calculated dose distribution

δd is the corresponding dose difference.

As a general rule, acceptance criteria of 3 % dose difference and 3 mm distance to agreement are adopted and more than 90%-÷95% of points passing the chose criterion.

Results

All 257 VMAT treatment plans were recalculated on a CT scan of Delta4[®] phantom and the corresponding dose distributions were verified with the Delta4[®] diode array phantom.

All plans were analyzed using the three parameter %DA (limit 3%), DTA (limit 3%), (limit 3 mm), and γ -index with the 3% dose tolerance and 3 mm distance to agreement in relation to the treatment planning system.

The gamma criterion was considered fulfilled if $\gamma < 1$ in at least 90÷95% of the points.

Results confirmed a good agreement between the two distribution with high and conformed dose to the target and low dose to the organ at risk.

Fig.3 shows Delta4 output for head and neck cases, the planned dose distribution in grayscale and the measured dose in color over the wing detector boards (at left) and the main detector board (at right) and the histograms of %DA, DTA, and γ -index are in reported.

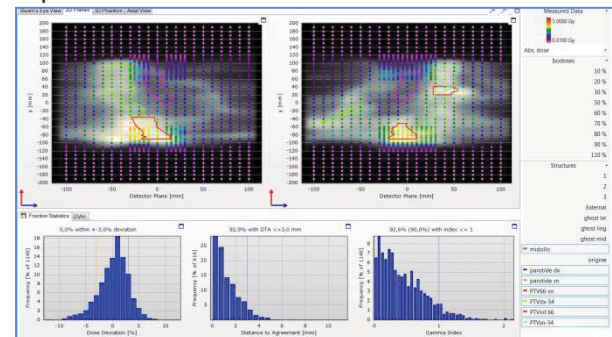


Fig. 3 Delta4[®] software analysis

Furthermore because the software shows the matrix of γ statistics points (blue pass ($\gamma < 1$) and red fall ($\gamma > 1$)), it was also possible to investigate a plan respect the position of the “red points” and the organ at risk.

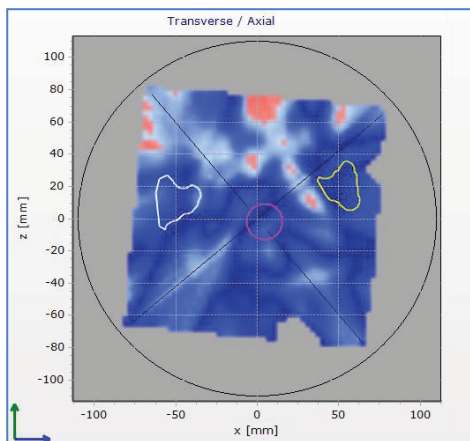


Fig. 4a Example of γ matrix in axial plan

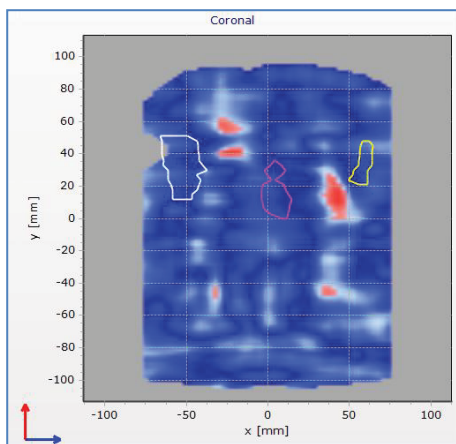


Fig. 4b Example of γ matrix in coronal plan

Discussions and Conclusions

Verification of a planned dose distribution is a complex and time consuming procedure because all described parameters DTA, %DA and γ -index are very important and using only one of them is not enough to accept a treatment plan.

The plan must be investigated using every instrument and always taking in consideration the clinical meaning of eventual disagreement: for example a plan with $\gamma < 1$ in 90% of the analyzed points is not a good plan, but it is necessary to verify the distribution of the points with $\gamma > 1$; if they are distant from target and organ at risk the plan can become acceptable.

Although Delta4 appears a straightforward device for measuring dose and allows measurement in real time, it is a complex device

and careful quality assurance before its use is therefore recommended.

References

- [1] Report AIFM "Intensity Modulated Radiation Therapy (IMRT): Dosimetric and Computational Aspect" N.3 (2006)
- [2] James L Bedford, Young K Lee et al. "Evaluation of the Delta4 phantom for IMRT and VMAT verification" Phys. Med. Biol. 54 pp. 167-176; 2009
- [3] B.E. Nelms, Jeff A. Simon "A survey on planar IMRT QA analysis", Journal of Applied Clinical Medical Physics, vol. 8, n.3 2007
- [4] Judith Alvarez-Moret, Fabian Pohl et al "Evaluation of volumetric modulated arc therapy (VMAT) with Oncentra MasterPlan® for the treatment of head and neck cancer" Radiation Oncology 2010, 5:110
- [5] T. Depuydt, A. Van Esch, and D.P. Huyskens. "A quantitative evaluation of IMRT dose distributions: refinement and clinical assessment of the gamma evaluation" Radiotherapy and Oncology, 62:309_319, 200

Dinamic-arc-IMRT with Serial Tomotherapy

A. Papaleo*, E. Cavalera*, D. Russo*, A. Leone*, G. Di Paola*, F.P. Ricci*, C. Capomolla**, M. Natali**, M. Santantonio*

*Department of Radiation Oncology,

**Department of Medical Physics, V. Fazzi Hospital, Lecce, Italy.

Abstract

Intensity-modulated radiotherapy (IMRT) has been introduced into a wide spectrum of clinics worldwide. In tomotherapy, literally “slice therapy”, highly conformal treatments are possible because of an increase in the number of treatment slices into which the target is segmented would lead directly to an improvement in three-dimensional dose conformality. With Peacock System (NOMOS Corporation), the IMRT is doing so using conventional clinical linear accelerators (Linacs) fitted with an integrated multileaf collimator (MLC). This system comprised of the MIMiC, a tertiary “bolt-on” MLC, and a dedicated inverse treatment planning system (Corvus). The introduction of dynamic-arc-IMRT with Serial Tomotherapy started in the mid 1990. The first patient was treated in 1994. Between November 2007 and September 2012, at the Operative Unit of Radiotherapy of V. Fazzi Hospital of Lecce, 180 patients were treated with Serial Tomotherapy. Of those, 52 patients received Cerebral Ipfractionated Stereotactic IMRT with Talon; 66 prostate cancer patients were designed to deliver SIB-IMRT (78,4Gy to the prostate while simultaneously delivering 66,5Gy to seminal vesicles in 35 fractions); 20 patients received SIB-IMRT for Nasopharyngeal cancer (69.9Gy in 2.33Gy fractions to PTV1, 60Gy in 2Gy fractions to PTV2 and 54Gy in 1.8Gy fractions to PTV3), 28 patients received brain IMRT and 14 patients were irradiated on the spine and bone marrow for palliation or other. This slice-wise method of treatment is known to produce extremely conformal dose distributions due to its ability to specifically match the dose distribution on each slice to the shape of the target volume on that same slice. The major criticism of contemporary IMRT is that we cannot be certain of the geometry (relative position and shape) of the tumour or organs at risk (OARs) at each treatment episode. Careful and exacting protocols are employed to attempt to localize these in the treatment plan and during the patient’s set-up.

Introduction

Intensity-modulated radiotherapy (IMRT) is based on the use of optimized non-uniform radiation beam intensities incident on the patient.

IMRT treatment plans are often generated using inverse planning or automated optimization 3D-RTP systems, which use computer optimization techniques to help determine the

distribution of intensities across the target volume. (Fig. 1).

IMRT does provide the ability to spare normal tissues that are surrounded by targets with concave surfaces, and this advantage is currently being exploited to escalate tumor dose.

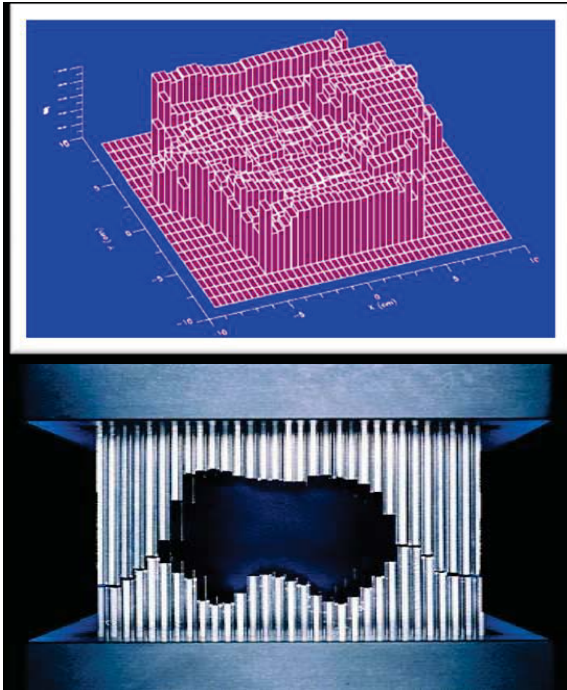


Fig.1. High Conformity to target Volume

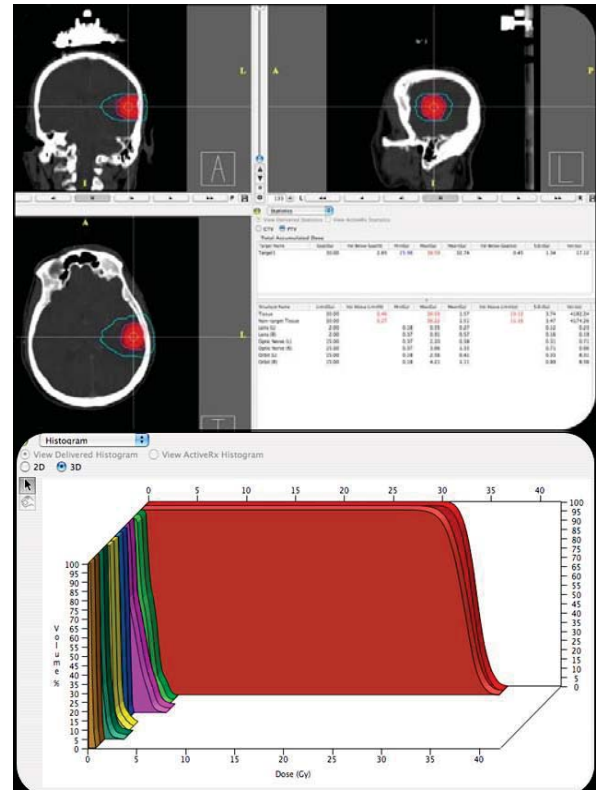


Figure 2. High dose gradients that can be formed at structure interfaces due to Cerebral Stereotactic RT with Talon

Materials and methods

Between November 2007 and September 2012, at the Operative Unit of Radiotherapy of V. Fazzi Hospital of Lecce, 180 patients were treated with Serial Tomotherapy. Of those, 52 patients received Cerebral Stereotactic RT with Talon (Fig. 2); 66 prostate cancer patients were designed to deliver SIB-IMRT: 78,5Gy to the prostate while simultaneously delivering 66,5Gy to seminal vesicles in 35 fractions (Fig. 3); 20 Patients received SIB-IMRT for Nasopharyngeal cancer: 69.9 Gy in 2.33 Gy fractions to PTV1, 60 Gy in 2 Gy fractions to PTV2 and 54 Gy in 1.8 Gy fractions to PTV3 (Fig. 4); 28 patients received brain IMRT (Fig. 5) and 14 patients were irradiated on the spine for palliation or other (Fig. 6).

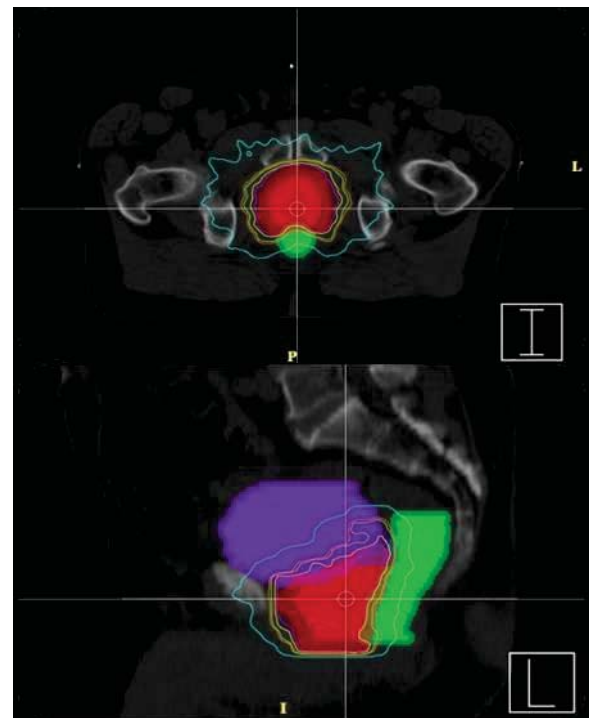


Figure 3. High dose conformity in IMRT plan of a prostate cancer patient

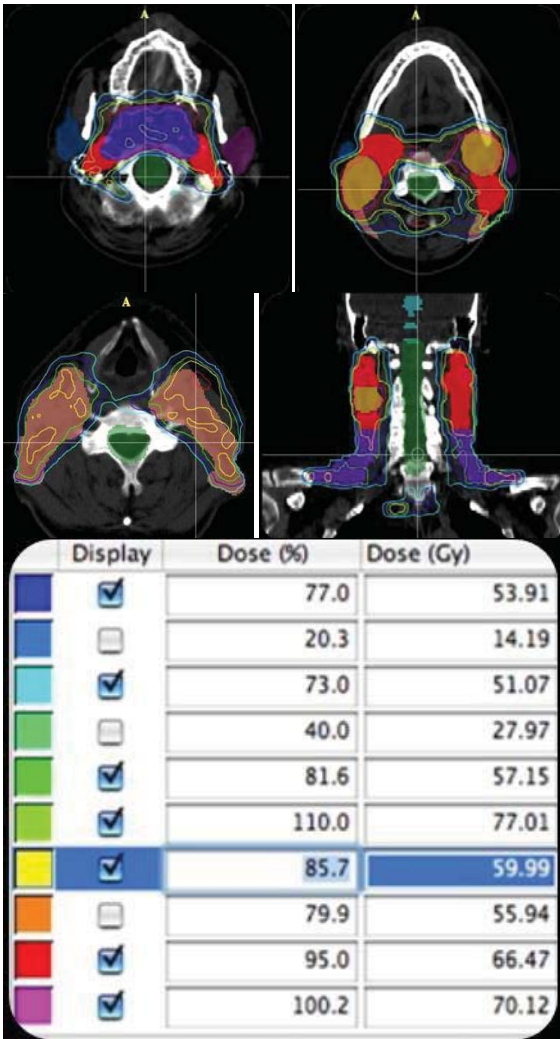


Figure 4. High dose gradients that can be formed at structure interfaces due to Cerebral Stereotactic RT with Talon

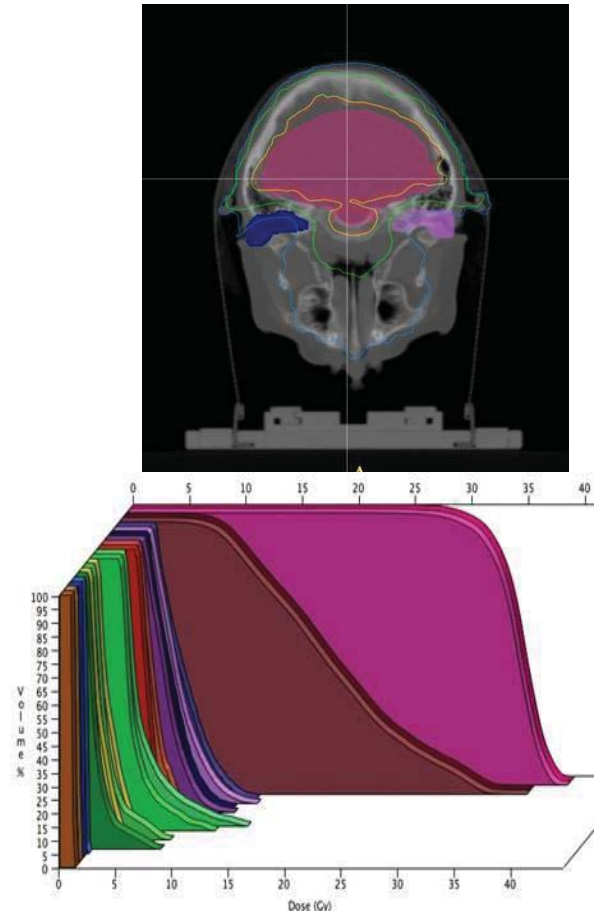


Figure 5. Brain IMRT with Serial Tomotherapy

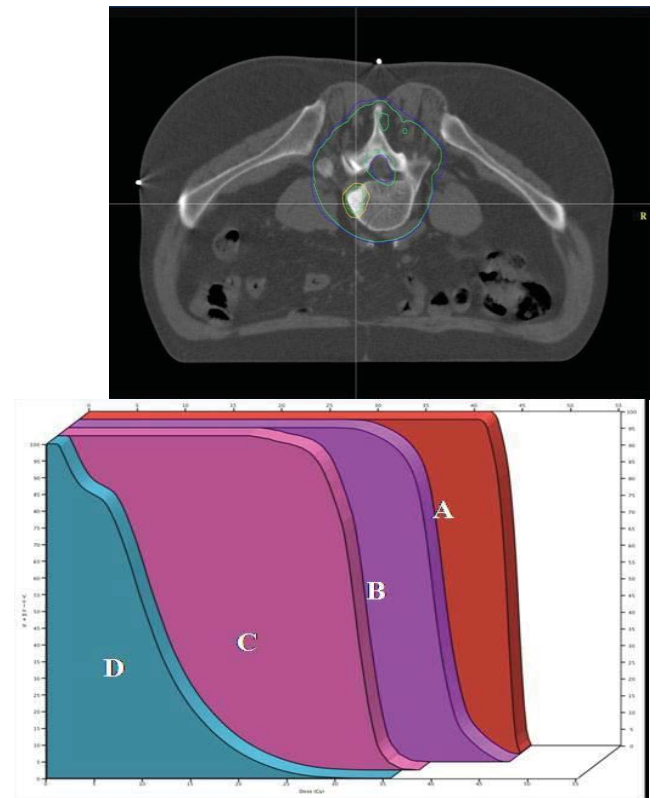


Figure 6. IMRT plan for spine metastases treatment with Serial Tomotherapy

Calculations are based on a Siemens Primus linac with a dose rate of 200 MU/min.

Treatment plans are created with Corvus 6.0 and 7.0. Steepness of dose gradients, homogeneity and conformity were assessed by the following parameters: Volume encompassed by certain isodoses outside the target as well as homogeneity and conformity as indicated by Homogeneity- and Conformity-Index.

Results

Six clinical examples are chosen to illustrate the quality of IMRT treatment plan with serial tomotherapy.

These are 1- and 2-cm modes with single-couch position for prostate, head and neck, brain and spine treatment.

The plan in Fig.2, highlights the intracranial ipofractionated stereotactic radiotherapy of brain metastases, with Serial Tomotherapy and Talon Immobilization. It can be seen that the 0,8-cm mode with beak collimator has the 100% of target volume coverage.

DVHs of the target volumes and selected critical structures highlight the increased dose heterogeneity often encountered as a consequence of conformal avoidance.

The isodose distributions for the rinopharyngeal cancer case are shown in Fig. 4. Is a typical head-and-neck IMRT treatment plan showing conformal avoidance of the spinal cord and parotid glands while simultaneously delivering multiple dose prescriptions (69,9 Gy, 60 Gy and 54 Gy in 30 fractions) to the two target volumes.

The average values for the percent volume that received at least 95% of the prescription dose (V95), the target volume covered by 100% of the prescription dose (D100%) and the conformity index of the PTV were 99,3%, 97,8% and 0,9 for IMRT, 100%, 99,8%, and 1 for the Stereotactic-RT, respectively.

Discussion

Computerized RT planning was first reported 40 years ago (1). Early dedicated RTP systems depended on twodimensional (2D) contour information and calculated doses based on relatively simple 2D dose models (2, 3). The first 3D approach to treatment planning dose calculation and display is credited to Sterling et al. (4, 5), who demonstrated a computergenerated film loop that gave the illusion of a 3D view of the anatomy and the calculated isodose distribution (2D color washes) throughout a treatment volume. Van de Geijn (6), Cunningham (7), Beaudoin (8), and Sontag and Cunningham (9) also performed early work in 3D dose-calculation models. Reinstein et al. (10) and McShan et al. (11) took the first real step toward clinically usable 3D-RTP in 1978 with the development of the beam's-eye view display. The beam's-eye view display provides the planner with a view from the perspective of the source of the radiation beam, looking down the rays of the divergent beam, and results in a view of the anatomy similar to a simulator radiograph. At the same time, the introduction of CT scanning and its use for RT significantly improved the way patient anatomy could be specified in treatment planning (12). In 1983, Goitein and Abrams (13) and Goitein et al. (14) demonstrated how CT data made possible high-quality color beam's-eye view displays and simulated radiographs computed from CT data (referred to as digitally reconstructed radiographs).

Finally, between 1986 and 1989, several robust university-developed 3D-RTP systems began to be implemented in clinical use (15,16). The additional development of 3D-RTP systems throughout the past 20 years. One of the keys to the acceptance of 3D-RTP throughout the community was a series of research contracts funded by the National Cancer Institute in the 1980s and

early 1990s to evaluate the potential of 3D-RTP and to make recommendations to the National Cancer Institute for future research in this area (17).

Important developments and refinements in 3D planning technology came from these contracts, particularly plan evaluation software tools, such as dose-volume histograms (DVHs) (18, 19), and biologic effect models, such as tumor control probability (TCP) and normal tissue complication probability (NTCP) (20, 21) models, as well as efforts to stimulate and document the current state of knowledge about these effects (22). Many of these features are crucial parts of plan optimization, which is critical to IMRT.

Early IMRT delivery concepts were pioneered several decades ago. Particularly important were the early efforts of Dr. Shinji Takahashi and colleagues, from Nagoya, Japan (23). Their work illustrated some of the important concepts in both conventional 3D-CRT and IMRT delivery. Dynamic treatments were planned and delivered by Takahashi's group using what may have been the first multileaf collimator (MLC) system. The MLC system used a mechanical control system to conform the beam aperture to the projected target shape as the machine was rotated around the patient. Another pioneering effort in CRT was conducted by the group at the Massachusetts Institute of Technology Lahey Clinic (24–26), who independently developed an asynchronous portal-defining device similar to that of Takahashi (23).

The Royal Northern Hospital in England also pioneered an early CRT effort (27). The group developed a series of cobalt-60 teletherapy machines in which the patient was automatically positioned during rotational therapy by moving the treatment couch and gantry during the radiation delivery using electromechanical systems. This was called the "Tracking Cobalt Project," because the planning and delivery system attempted to track around the path

of disease spread and subsequently conform the dose distribution.

By the mid-1990s (and before much additional discussion had occurred in the literature about IMRT delivery methods), several other kinds of delivery techniques relevant to modern IMRT had evolved. The use of a computer-controlled scanned beam, available in the Scanditronix Racetrack Microtron System, was the first modern IMRT delivery technique described in the literature (28). Resolution of this technique is limited, as demonstrated by Karlsson et al. (29) and Lief et al. (30, 31).

The second IMRT delivery technique described in the literature defined an approach called tomotherapy by which IMRT is delivered using a narrow slit beam (32).

In tomotherapy, literally "slice therapy", highly conformal treatments are possible because of an increase in the number of treatment slices into which the target is segmented would lead directly to an improvement in three-dimensional (3D) dose conformality (fig. 7).

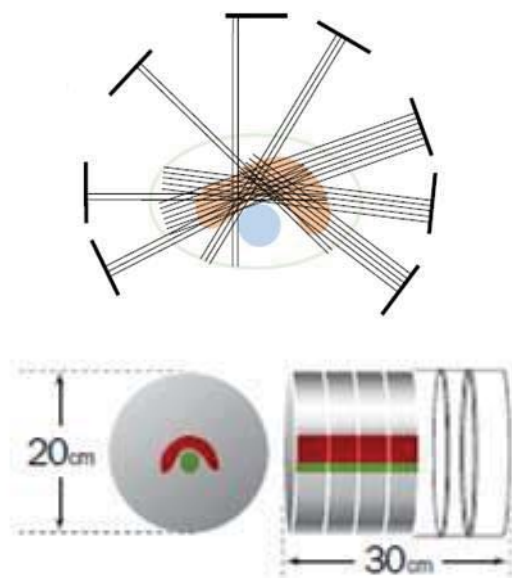


Figure 7. IMRT with Serial Tomotherapy

This technique is very analogous to the tomography techniques used for CT and other such imaging systems. A temporally modulated binary mini-MLC of the type proposed by Mackie et al. (32) for

tomotherapy IMRT was developed commercially (Peacock MIMiC, Nomos Corp.) (33-35). The Peacock system's MIMiC is mounted to a conventional low-energy megavoltage medical linear accelerator, and treatment is delivered to a narrow slice of the patient using arc rotation. The beam is collimated to a narrow slit (approximately 2cm-20cm), and beamlets of varying intensity are created by driving the MIMiC's leaves in and out of the radiation beam's path as the gantry rotates around the patient. A complete treatment is accomplished by serial delivery to adjoining axial slices. The clinical use of the Peacock system was first implemented at the Baylor College of Medicine in Houston, Texas (36).

Since then, it has been implemented in a large number of clinics worldwide, and several other institutions have reported their experience with the Peacock IMRT system (37-38). The treatment delivered by this system is described as serial tomotherapy, since it is delivered by a number of discrete arcs or indexed arcs of finite width, between which the treatment couch is moved longitudinally.

The popular introduction of IMRT started in the mid 1990s when the NOMOS Corporation (Swickley, Pennsylvania, USA) introduced the PEACOCK system [33, 39], this comprised of the MIMiC, a tertiary "bolt-on" multileaf collimator (MLC), and a dedicated inverse treatment planning system. The first patient was treated in 1994 and until around the turn of the century most patients who received IMRT in the world were treated on this system (39).

CONCLUSIONS

The MIMiC delivery system, when used appropriately, is an extremely versatile system for treating a large variety of disease conditions. Typically, irregular-shaped and small-to-medium size tumors with adjacent critical structures are the most suitable candidates. One has to be vigilant on noting

the limitation of the 20-cm width of the collimator.

This slice-wise method of treatment is known to produce extremely conformal dose distributions due to its ability to specifically match the dose distribution on each slice to the shape of the target volume on that same slice.

The major criticism of contemporary IMRT is that we cannot be certain of the geometry (relative position and shape) of the tumour or organs at risk (OARs) at each treatment episode.

Careful and exacting protocols are employed to attempt to localize these in the treatment plan and during the patient's set-up.

References

- 1) Tsien KC. The application of automatic computing machines to radiation treatment planning. *Br J Radiol* 1955;28:432-439.
- 2) Holmes WF. External beam treatment-planning with the programmed console. *Radiology* 1970;94:391-400.
- 3) Bentley RE, Milan J. An interactive digital computer system for radiotherapy treatment planning. *Br J Radiol* 1971;44: 826-833.
- 4) Sterling TD, Perry H, Katz L. Automation of radiation treatment planning V. Calculation and visualisation of the total treatment volume. *Br J Radiol* 1965;38:906-913.
- 5) Sterling TD, Knowlton KC, Weinkam JJ, *et al.* Dynamic display of radiotherapy plans using computer-produced films. *Radiology* 1973;107:689-691.
- 6) Van de Geijn J. A computer program for three-dimensional planning in external-beam radiation therapy, EXTDOSE. *Comput Prog Biomed* 1970;1:45-57.
- 7) Cunningham JR. Scatter-air ratios. *Phys Med Biol* 1972;17: 42-51.
- 8) Beaudoin L. Analytical approach to the solution of dosimetry in heterogeneous media [Ph.D. Thesis]. Toronto, Ontario: University of Toronto; 1968.
- 9) Sontag MR, Cunningham JR. The equivalent tissue-air ratio needed for making absorbed dose calculations in a heterogeneous medium. *Radiology* 1978;129:787-794.
- 10) Reinstein LE, McShan D, Webber BM, *et al.* A computer-assisted three-dimensional treatment planning system. *Radiology* 1978;127:259-264.

- 11) McShan DL, Silverman A, Lanza D, *et al.* A computerized three-dimensional treatment planning system utilizing interactive color graphics. *Br J Radiol* 1979;52:478–481.
- 12) Ling CC, Rogers CC, Morton RJ, eds. Computed tomography in radiation therapy. New York: Raven Press; 1983.
- 13) Goitein M, Abrams M. Multi-dimensional treatment planning: I. Delineation of anatomy. *Int J Radiat Oncol Biol Phys* 1983;9:777–787.
- 14) Goitein M, Abrams M, Rowell D, *et al.* Multi-dimensional treatment planning: II. Beam's eye view, back projection, and projection through CT sections. *Int J Radiat Oncol Biol Phys* 1983;9:789–797.
- 15) Fraass BA, McShan DL. 3-D treatment planning. I. Overview of a clinical planning system. Proceedings of the 9th International Conference on the Use of Computers in Radiation Therapy, Scheveningen, The Netherlands, 1987.
- 16) Purdy JA, Wong JW, Harms WB, *et al.* Three dimensional radiation treatment planning system. Proceedings of the 9th International Conference on the Use of Computers in Radiation Therapy, Scheveningen, The Netherlands, 1987.
- 17) Smith AF, Purdy JA. Editors' note. *Int J Radiat Oncol Biol Phys* 1991;21:1.
- 18) Austin-Seymour MM, George MD, Chen GTY, *et al.* Dose volume histogram analysis of liver radiation tolerance. *Int J Radiat Oncol Biol Phys* 1986;12:31–35.
- 19) Drzymala RE, Holman MD, Yan D, *et al.* Integrated software tools for the evaluation of radiotherapy treatment plans. *Int J Radiat Oncol Biol Phys* 1994;30:909–919.
- 20) Lyman JT. Complication probability as assessed from dose volume histograms. *Radiat Res* 1985;104:S13–S19.
- 21) Lyman JT, Wolbarst AB. Optimization of radiation therapy. III. A method of assessing complication probabilities from dose-volume histograms. *Int J Radiat Oncol Biol Phys* 1987; 13:103–109.
- 22) Smith AR, Purdy JA, eds. Three-dimensional photon treatment planning. Report of the Collaborative Working Group on the Evaluation of Treatment Planning for External Photon 908 I. J. Radiation Oncology • Biology • Physics Volume 51, Number 4, 2001 Beam Radiotherapy. *Int J Radiat Oncol Biol Phys* 1991;21: 3–268 (entire volume).
- 23) Takahashi S. Conformation radiotherapy: Rotation techniques as applied to radiography and radiotherapy of cancer. *Acta Radiol Suppl* 1965;242:1–42.
- 24) Proimos BS. Synchronous field shaping in rotational megavoltage therapy. *Radiology* 1960;74:753–757.
- 25) Wright KA, Proimos BS, Trump JG, *et al.* Field shaping and selective protection in megavoltage therapy. *Radiology* 1959; 72:101.
- 26) Trump JG, Wright KA, Smedal MI, *et al.* Synchronous field shaping and protection in 2-million-volt rotational therapy. *Radiology* 1961;76:275.
- 27) Jennings WA, Green A. The tracking cobalt-60 method, or programmed 3D irradiation. In: Abstracts of the Second Congress of the European Association of Radiology, 1971. Amsterdam: Excerpta Medica; 1971. p. 154.
- 28) Brahme A. Design principles and clinical possibilities with a new generation of radiation therapy equipment: A review. *Acta Oncol* 1987;26:403–412.
- 29) Karlsson MG, Karlsson M, Zackrisson B. Intensity modulation with electrons: Calculations, measurements and clinical applications. *Phys Med Biol* 1998;43:1159–1169.
- 30) Lief EP, Larsson A, Humm JL. Electron dose profile shaping by modulation of a scanning elementary beam. *Med Phys* 1996;23:33–34.
- 31) Lief EP, Lo YC, Humm JL. Electron wedges for radiation therapy. *Int J Radiat Oncol Biol Phys* 1998;40:233–243.
- 32) Mackie TR, Holmes T, Swerdloff S, *et al.* Tomotherapy: A new concept for the delivery of dynamic conformal radiotherapy. *Med Phys* 1993;20:1709–1719.
- 33) Carol M. Peacock: a system for planning and rotational delivery of intensity-modulated fields. *Int J Imag Syst Technol* 1995;6:56–61.
- 34) Carol MP. Integrated 3-D conformal multivane intensity modulation delivery system for radiotherapy. Proceedings of the 11th International Conference on the Use of Computers in Radiation Therapy, Madison, WI, 1994.
- 35) Carol MP. Integrated 3D conformal planning/multivane intensity modulating delivery system for radiotherapy. In: Purdy JA, Emami B, editors. 3D radiation treatment planning and conformal therapy. Madison, WI: Medical Physics Publishing; 1995. p. 435–445.
- 36) Grant W III. Experience with intensity modulated beam delivery. In: Palta J, Mackie TR, editors. Teletherapy: Present and future. College Park, MD: Advanced Medical Publishing; 1996. p. 793–804.
- 37) Sultanem J, Shu HK, Xia P, *et al.* Three-dimensional intensity-modulated radiotherapy in the treatment of nasopharyngeal carcinoma: The University of California–San Francisco experience. *Int J Radiat Oncol Biol Phys* 2000;48:711–722.
- 38) Williams PCW. IMRT: delivery techniques and quality assurance. *Br J Radiol* 2003;76:766–76.
- 39) Woo SY, Butler B, Grant III W. Clinical experience: benign tumours of the CNS and head and neck tumours. In: Sternick ES, editor. Intensity modulated radiation therapy. Madison WI: Advanced Medical Publishing; 1997:195–8.

Analysis of uncertainties in dose distribution due to geometrical deviation of target from isocenter in serial tomotherapy

C. Capomolla ¹, S. Quarta ¹, G. Ciccarese ², M. Natali ¹, M. Cazzato ³, A. Papaleo ⁴, D. Russo ⁴,
A. Zagari ¹

¹U.O.C. Fisica Sanitaria P.O. "Vito Fazzi", Lecce (Italy) capomolla.caterina@gmail.com

²Servizio di Radioterapia – Istituto Clinico "Beato Matteo" Vigevano (PV) (Italy)

³Scuola di Specializzazione in Fisica Medica – Università "Sapienza" Roma (Italy)

⁴U.O. Radioterapia - P.O. "Vito Fazzi", Lecce (Italy)

Abstract

The tomotherapy system in radiation therapy department of "V. Fazzi" hospital in Lecce (Italy) is a serial device. It means that the coverage of the target is obtained by moving the couch in and out the gantry position. It has been shown that the choice of target positioning respect to the isocenter reflects on dose distribution in terms of heterogeneities. The entity of the heterogeneities can reach 10% in abutment regions nearby the isocenter. Moreover, by using gantry rotations less than 300 degrees, hot and cold spots can be seen above and over the isocenter. Aim of the present work is to characterize the performance of the serial tomotherapy device in order to avoid, as more as possible, heterogeneities in the abutment regions.

Introduction

Serial tomotherapy is a dynamic arc IMRT highly conformal it allows a slice by slice target irradiation thanks to the poor dimension of the collimator.

Treatment is performed by rotating the gantry over a certain arc for a fixed couch position and the leaf positions changing during rotation. To deliver the dose distribution to a volume of greater collimator size, sequential treatment arcs are required, with the patient moved (indexed) longitudinally between arcs [1] [2].

The analysis of dose distribution in abutment regions due to adjacent arcs is the aim of this work.

Materials and methods

The tomotherapy system in use in our hospital is made with a dynamic multi-vanes collimator (MIMiC - Best Nomos[®]) and a device for couch translation (Autocrane - Best Nomos[®]) attached on a 6 MV linac (mod. Primus Siemens).

MIMiC collimator (Fig. 1a) is constituted by two opposite parts each constituted by 20 tungsten vanes 8 cm thick and 1 cm large.

The binary aperture (closed or opened) of each vane allows the photon beam modulation during the gantry rotation according three modalities: *1cm mode*: with each pencil-beam ~ 1cm x 1cm so that each



Fig.1 MIMiC view from patient toward target of the gantry

slice treats ~2 cm of tissue, *2cm mode*: requiring fewer slices and less time since each pencil-beam is ~ 1 cm x 2 cm so that each slice treats ~4 cm of tissue **and Beak mode**. In the last mode a pencil-beam 1 cm x 0,4 cm slices treats ~ 0,8 cm of tissue. The beak mode is used only for stereotactic treatment.

In order to treat target longer than 1.7 cm longitudinally the couch is moved in and out in gantry direction by a device called Autocrane (Fig. 2). It is a simple double motorized translation rail whose precision is 0.1 mm.



Fig.2 AutoCrane mounted on linac couch

The couch index is very important in terms of heterogeneities in the abutment regions in fact overlapping should be considered with a lot of attention [3].

If ideal delivery conditions are assumed, the heterogeneity within the abutment region should be minimal if each delivery is conducted using 360° arcs. However, the total arc angle range is often limited by physical constraints, such as the patient

support hardware. When a reduced angle range is used, dose heterogeneity may be generated in the abutment region up and down the rotation axis due to beam divergence uncompensated by a symmetrical irradiation (Fig. 3).

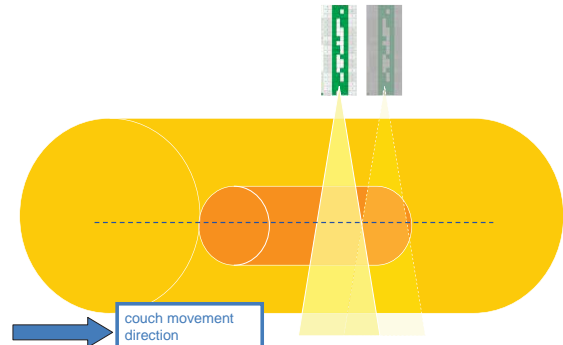


Fig. 3

Two irradiation positions dotted lines are for the former situation, continuous for the latter. Under-beaming and over-beaming situations are compensated if gantry rotation is complete (a). They remain in case of uncomplete gantry rotation.

It has been shown [4] that the magnitude of the heterogeneities will depend on:

the total arc angle range, the projected leaf size (1cm mode, 2 cm mode, use of beak), the distance from gantry rotation axis.

In our work, in order to evaluate the performance of the entire tomotherapy system, several dose distributions were analyzed:

- at different **distances** from the rotation axis, and arc delivery limited to 290°
- at different **arc angle range** (180° and 290°)
- at different **modality** (1cm and 2cm)

Dose distribution heterogeneities was investigated by examining treatment plans generated using 8.0 cm diameter cylindrical target volumes within a homogeneous rectilinear phantom.

EDR2 type radiographic films were used to estimate dose distribution at various depths inside the water equivalent multi-layer phantom. The films were analyzed by

Omnipro I'mrt[®] software. The experimental set-up is shown in Fig.4

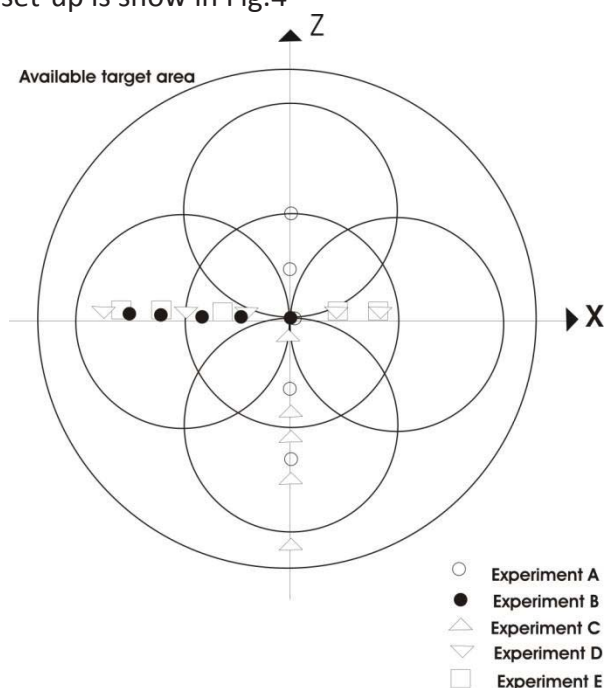


Fig.4 -Relative geometry of the 8 cm diameter target volumes used to measure the intrinsic abutment region dosimetry. The measured dose profile locations are shown positions (on the figure surface)

Results

Figure 5 shows an example of inhomogeneities (film obtained according to experiment A set-up in $z=+7$ cm): five regions of underlap, corresponding to the abutments of the six delivered arcs.

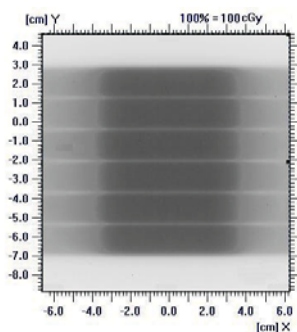


Fig.5 - film obtained according to experiment A set-up in $z=+7$ cm

The profiles in Fig.6 (a), (b) and (c) describe respectively the situation in $z = 3$ cm, $z = 0$ cm and -3 cm.

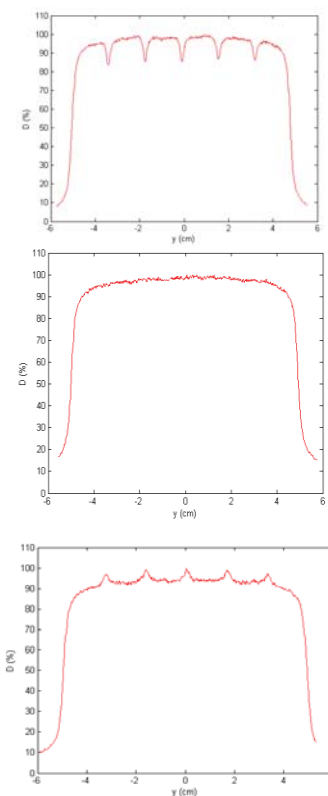


Fig.6- Dose profiles acquired perpendicularly respect to the abutment regions

The results of the different experiments are summarized in the following figures (Fig.7, Fig.8, Fig.9, fig.10).

In Fig. 7 and Fig.8 heterogeneity vs the distance of the target from isocenter are plotted. Heterogeneities are almost zero near gantry axis rotation and are quite different in the peripheries.

Moreover, a clear dependence of the heterogeneity on the z position can be observed in Fig.7 with 6% hot spots and -16% cold spots at $z = -7$ and $z = 7$ respectively. Little heterogeneity is observed as function of a x off-axis, with -4% cold spots and 2% hot spots in Fig.8.

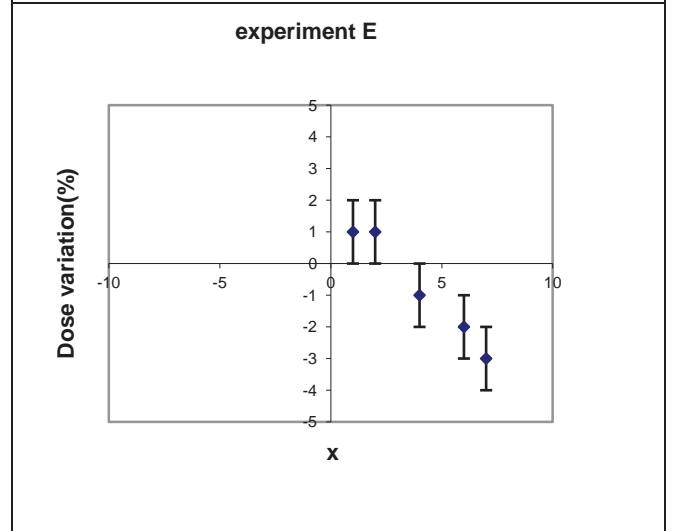
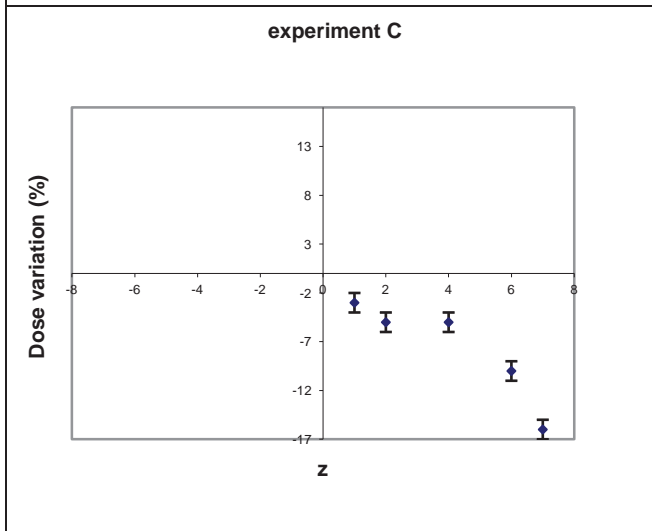
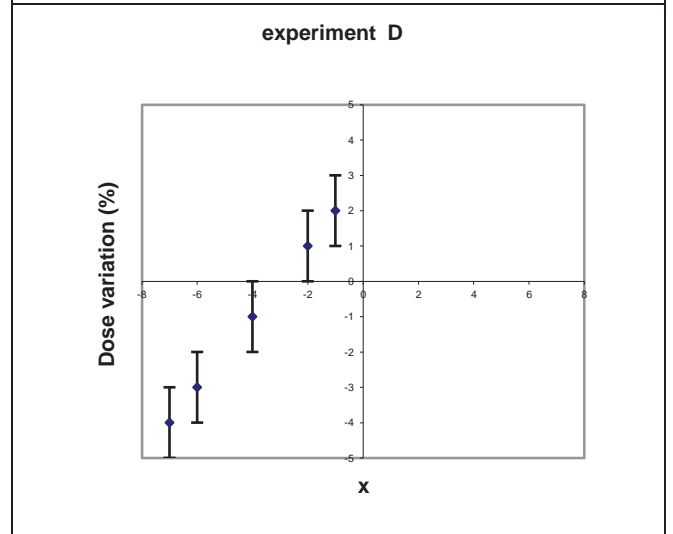
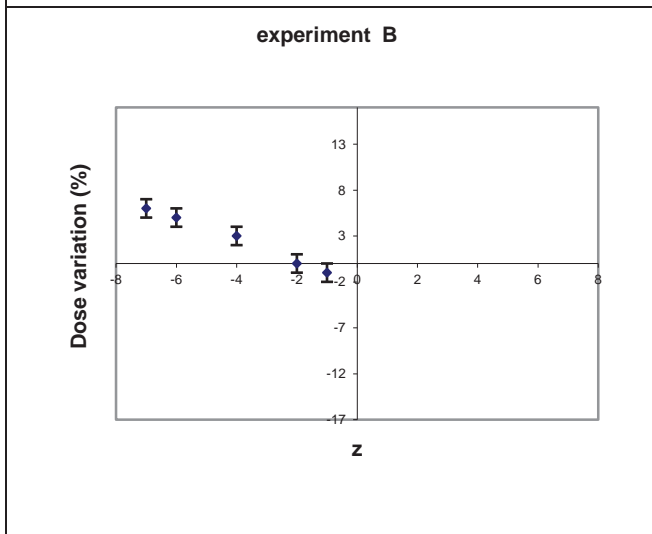
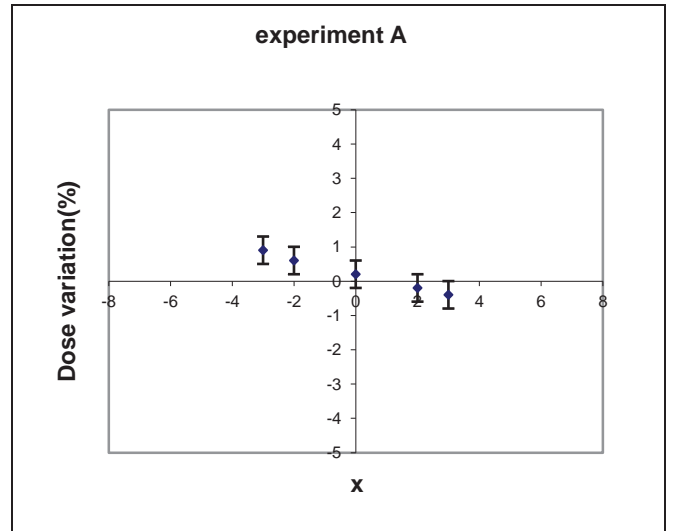
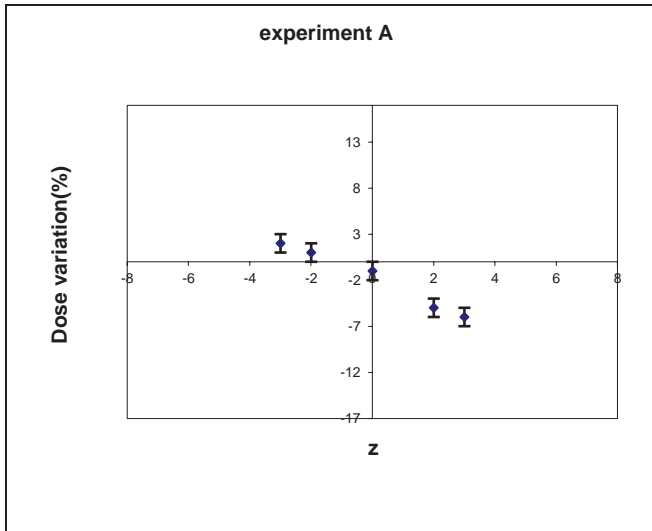


Fig.7: Dose variation trend as a function of off-axis position along the vertical direction: (a) target center and axis of rotation coincide; (b) target centered 4 cm upper the rotation axis; (c) target centered 4 cm lower the rotation axis.

Fig.8: Dose variation trend as a function of off-axis position along the horizontal direction: (a) target center and axis of rotation coincide; (b) target centered 4 cm right the rotation axis; (c) target centered 4 cm left the rotation axis.

In Fig.9 an increment in dose variation can be seen as the size of the radiation field grows. The highest dose variation according to "1 cm mode" irradiation was -6% . In "2 cm mode" the maximum dose variation was 12%.

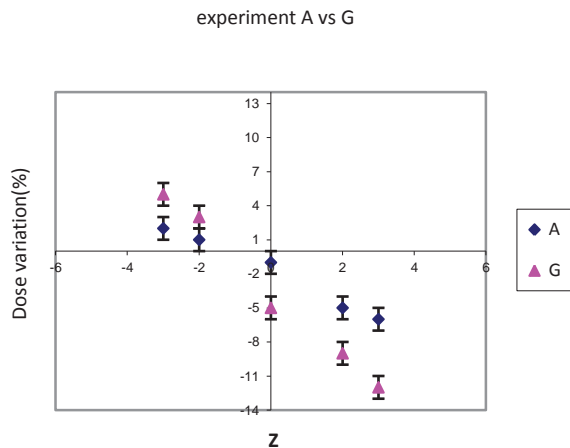


Fig.9: Dose distribution heterogeneities investigated at 1 cm mode (experiment A) and at 2 cm mode (experiment G).

Experimental data for an arc length equal to 290 degrees (A) and 180 degrees (F) are shown in Fig. 10

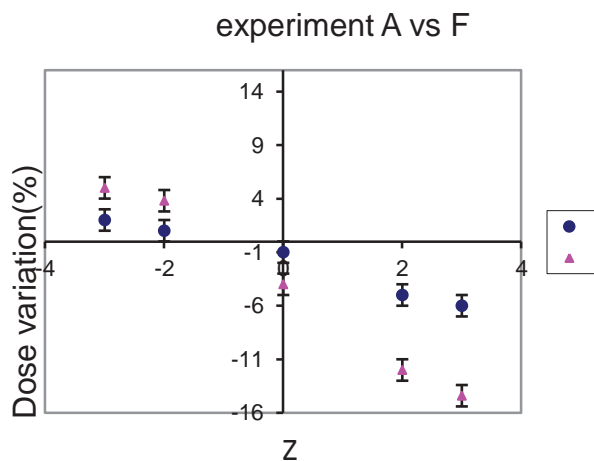


Fig.10: Dose distribution heterogeneities investigated at different arc angle range : 290° (experiment A) and 180° (experiment F).

Using 290° gantry angle and 1 cm mode yielded 2% hot and 6% cold spots 3 cm below and above isocenter, respectively. When a 180° gantry angle was used, the values changed to 5% hot and 14.4% cold spots for the same locations.

Discussion and Conclusions

The use of arc-based IMRT delivery requires an understanding of the consequences of isocentre placement. The measurement have confirmed that under-dose and over-dose areas depend strongly on target position respect to isocenter, on collimator aperture (1 cm mode or 2 cm mode) and on arc length. As a consequence it would be preferable to align target and isocenter and to use the maximum allowed arc length.

As regards the choice of collimation it depends on the clinical requirements, a more extensive area in the abutment region in "2 cm mode" is compensated by a double number of smaller inhomogeneities in "1 cm mode". The current work permitted us to verify assumptions made by other authors [5] [6] and to evaluate the real performance of the tomotherapy system. The obtained results have lead us to spend more time in treatment planning in order to minimize and, when possible, to avoid inhomogeneities.

References

- [1] Verellen D, Linthout N, Berge DVD, et al. Initial experience with intensity-modulated conformal radiation therapy for treatment of the head and neck region. *Int J Radiat Oncol Biol Phys* 1997;39:99–114.
- [2] Tsai J-S, Wazer DE, Ling MN, et al. Dosimetric verification of the dynamic intensity-modulated radiation therapy of 92 patients. *Int J Radiat Oncol Biol Phys* 1998; 40:1213–1230.
- [3] Low DA, Chao KSC, Mutic S, et al. Quality assurance of serial tomotherapy for head and neck patient treatments. *Int J Radiat Oncol Biol Phys* 1998;42:681–692.
- [4] Low DA, Mutic S. Abutment region dosimetry for serial tomotherapy *Phys Med Biol* 1997;42:1465–1470
- [5] D. A. Low, S. Mutic, M.S. James, F. Dempsey, J. Markman, S. M. Y Goddu, J. A. Purdy *Abutment region dosimetry for sequential arc imrt delivery Int. J. Radiation Oncology Biol. Phys.*, Vol. 45, No. 1, pp. 193–203, 1999
- [6] Carol M, Grant WH, Blier AR, et al. *The field-matching problem as it applies to the Peacock three dimensional conformal system for intensity modulation. Int J Radiat Oncol Biol Phys* 1996;34:183–187.

Analysis of time statistics of extreme variations of heart beat fluctuations

Pennetta C¹, Palatella L²

¹ *Dipartimento di Matematica e Fisica "Ennio De Giorgi", Università del Salento and INFN, Lecce, Italy
cecilia.pennetta@unisalento.it*

² *Istituto di Scienze dell'Atmosfera e del Clima, ISAC- CNR and INFN, Lecce, Italy*

Abstract

We analyzed heart beat fluctuations in terms of return times of extreme values of the RR increments. We considered 24 hours Holter ECG signals of 90 healthy individuals and 90 unhealthy ones suffering of congestive heart failure (chf). The increment time series ΔRR corresponding to sleep and daily activity were studied separately. In both cases, our results pointed out strong differences in the median return times of the positive high thresholds between healthy and unhealthy people.

Introduction

In recent years it has become clear that many physiological signals contain much more information than that caught by conventional statistical tools [1,2]. In particular, the detection in heart beats time series of several features typical of complex systems, like long-term correlations [3-6], multifractality [4], non-Gaussianity [7,8], etc., stimulated the use of advanced statistical methods, as detrended fluctuation analysis [3], multifractal detrended fluctuation analysis [6], wavelet transform [9], diffusion entropy [10,11] and the development of models of the intrinsic dynamics of the heart regulatory systems [1,12,13]. Recently, some authors [14-17] highlighted the effectiveness of extreme value analysis in the study of several complex systems of different nature. Therefore we performed this kind of analysis on time series of heart beat increments [18].

In the following, we shortly present the procedure that we adopted in this study and some of its results. Further details and results can be found in Ref. [18].

Materials and methods

The time series analyzed consisted of three groups of 24 hours Holter ECG signals [18]:

- **rlvs group:** The rlvs group consisted of 90 patients hospitalized in the 1st Department of Cardiology of Medical University in Gdansk, Poland (9 women, 81 men, the average age was 57 ± 10) all suffering of reduced left ventricular systolic function, as recognized by echocardiogram in terms of low left ventricular ejection fraction ($LVEF \leq 40$, mean $LVEF = 30.2 \pm 6.7$) [9]. The additional criteria which excluded subjects from the rlvs group were: the myocardial infarction or coronary revascularization in the last

six months, persistent atrial fibrillation, sinus-node disease, diabetes mellitus, kidney failure with creatine level greater than 2 in the last six months.

- **nsr_gda group:** One of the two control groups was made of 39 healthy individuals (4 women, 35 men, the average age is 54 ± 7) without past history of cardiovascular disease, with both echocardiogram and electrocardiogram in normal range [9].
- **nsr2db group:** Another control group was provided by the Physionet database [19-23] and it included beat annotation files for 54 long-term ECG recordings of subjects with normal sinus rhythm (30 men, aged 28.5 to 76, and 24 women, aged 58 to 73).

The rlv and nsr_gda groups were digitized by using Delmar Avionics recorder (Digitorder) and then analyzed and annotated by means of a Delmar Accuplus 363 system (fully interactive method) by an experienced physician to extract the interbeat RR records [9]. Only the intervals between normal beats (NN) were considered while intervals associated with non-normal beats were eliminated. The minimum number of qualified sinus beats required for the signal to enter into the study was 85% [9]. A moving window average filter was applied to eliminate outliers due to the missed beat detection. No interpolation was done for the eliminated intervals. Further details concerning the treatment of the RR data can be found in Refs. [9,18]. The third group of signals were digitized at 128 samples per second and the beat annotations were obtained by automated analysis with manual review and correction. The same filtering procedure was applied also to this group of signals. For other details see Refs. [19-23]. Two continuous subsets were extracted manually from each RR signal: one corresponding to daily activity and the other to sleep [9,18]. We grouped together the 39

nsr_gda time series and 51 time series chosen among the nsr2db group, obtaining 90 control group signals, from now denoted as "healthy" while the rlv signals are denoted as "unhealthy".

We denoted as r_i the i -th interval RR (expressed in milliseconds) with $i \in [1, N]$ ($N \approx 2 \times 10^4$ for the sub-series considered here). As usual in the literature, the increment Δr_i was defined as: $\Delta r_i \equiv r_{i+1} - r_i$ with $i \in [1, N-1]$. Then we considered:

$$x_i = \frac{\Delta r_i - m}{\sigma} \quad (1)$$

where m and σ are respectively the average and the standard deviation of the Δr_i series. Therefore, the normalized series x_i had zero mean and unit standard deviation. We looked for extreme events in the Δr_i series defined in terms of a threshold q expressed in units of σ .

The time t_j associated with the occurring of j -th extreme event was defined by the following condition:

$$t_j^q \text{ is event if } \begin{cases} x_j > q \text{ for } q > 0 \\ x_j < q \text{ for } q < 0 \end{cases} \quad (2)$$

The return time τ_j^q of the threshold q was defined as the time interval between two consecutive overcoming of the threshold [15-18], i.e. as:

$$\tau_j^q \propto t_{j+1}^q - t_j^q \quad (3)$$

For each series we computed the mean return time $\langle \tau \rangle_k^q$ as mean of the τ_j^q over the n_k^q events occurring for the k -th individual, and the median return time M_k^q , defined as the median of the distribution of τ_j^q [18]. The results of our analysis are reported in the next section.

Results and Discussion

Figure 1 displays the median return times to the threshold $q=2.5$ of the x_i for all the 90 healthy individuals, M_k^q with $k=1, \dots, 90$. The median return times in this figure were obtained from the time series corresponding to daily activity. Figure 2 shows the same quantities, M_k^q with $k=1, \dots, 90$, calculated for the unhealthy patients (again daily activity). The differences between the median return times of the two sets of data are evident, at a qualitative level, even by eyes. The value 2.5 of the threshold q for these figures was selected because it provided a good compromise between enough statistics and significant difference between healthy and unhealthy individuals expected for high thresholds.

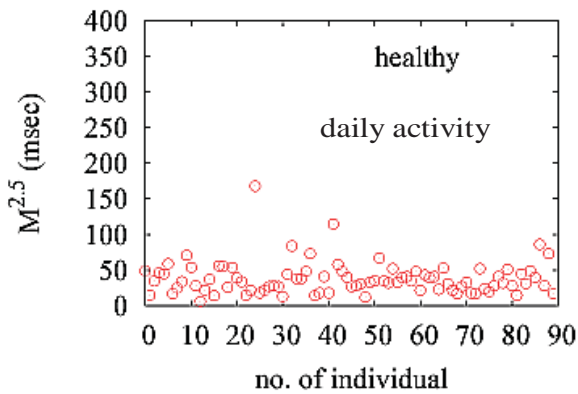


Figure 1. Median return times of the threshold $q=2.5$ (in σ units) during daily activity for 90 healthy people (nsr_gda and nsr2db groups).

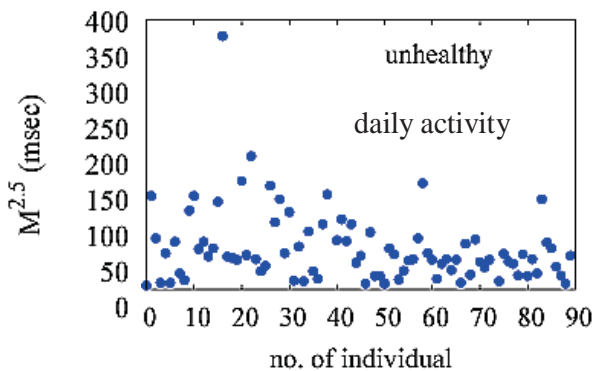


Figure 2. Median return times of the threshold $q=2.5$ (in σ units) during daily activity for 90 unhealthy people (rlvs group).

A similar behavior was found by comparing the median return times to the threshold $q=2.5$ of the x_i coming from the sleeping state time series, calculated for all the 90 healthy individuals, Fig.3, and the 90 unhealthy ones, Fig. 4.

Moreover, for each individual k series, separately for daily activity and sleep and for healthy and unhealthy people, we performed a systematic extreme value analysis, calculating the mean $\langle \tau \rangle_k^q$ and the median return times M_k^q for several threshold values, $q>0$ and $q<0$.

By making use of the Mann-Whitney non-parametric test, we performed, for each threshold q , the comparison between the two sets of data, M_k^q with $k=1, \dots, 90$, for healthy and unhealthy individuals. The same procedure was also applied to compare the sets of data, $\langle \tau \rangle_k^q$ with $k=1, \dots, 90$, for healthy and unhealthy individuals as a function of q . Before commenting the results of this analysis, it must be noted that for our sample sizes the results of the Mann-Whitney test can be interpreted in terms of the so called Z statistics. This implies that values $Z > Z_c = 1.96$ allow to discard the null hypothesis that two sets of data (two distributions) are the same at the significance level of 5%.

We found that for positive and quite large values of q , typically $q > 2.5$, the statistics of healthy and unhealthy individuals is significantly different, as proved by values of the Z -score greater than Z_c . Instead, no statistically significant difference between healthy and unhealthy time series was found for the return times of the x_i to negative thresholds. All the details of these calculations can be found in Ref. [18], including the Z -score values and the values of $\langle M^q \rangle$ and σ_q , respectively average and standard deviation over the 90 patients of M_k^q for each of the two groups (healthy/unhealthy) and for several positive and negative q values.

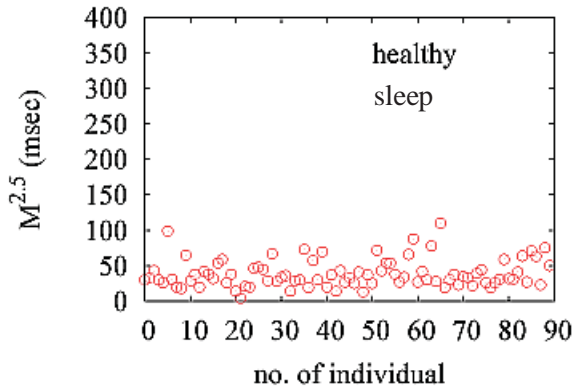


Figure 3. Median return times of the threshold $q=2.5$ (in σ units) during sleep for 90 healthy people (nsr_gda and nsr2db groups).

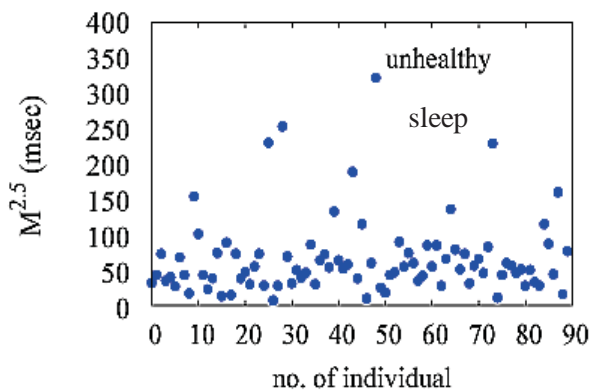


Figure 4. Median return times of the threshold $q=2.5$ (in σ units) during sleep for 90 unhealthy people (rlvs group).

This result can be explained by saying that healthy individuals have more often than the unhealthy the tendency to suddenly slow their heartbeat rate (thus more frequently obtaining larger positive increments of the RR intervals). This behavior is not so trivial because an intuitive reasoning should lead to a tendency of unhealthy people to avoid sudden increase of heartbeat rate but, as stated before, we didn't observe significant differences for $q < 0$.

Finally, we checked the stability of our results with respect to the sampling rate. To this purpose, we added a white Gaussian noise to the RR intervals and we took the Gaussian width equal to half of the sampling time [18]. We found that our results are quite robust, at least for sampling rate greater than or equal

to 128 that is the lowest used for the data of this paper.

Conclusions

We performed an extreme value analysis of the RR intervals times series extracted from 24-h Holter ECG signals of 90 healthy people (nsr_gda and nsr2db groups [9]) and 90 unhealthy people suffering of congestive heart failure (rlvs group [9]). We studied separately sub-series corresponding to daily activity and sleep. We focused on the return times of threshold values of the normalized RR increments, x_i [18]. Despite the simplicity of the technique used, our analysis pointed out some interesting features [18]. In particular, we found significant differences in the median return times M_k^q of a high positive thresholds between healthy and unhealthy individuals. We underline that, to our knowledge, our study is the first in the literature of the heart beat fluctuations in terms of extreme value analysis. In any case these features need further investigations to be fully understood also from a physiological point of view and eventually correlated with the disease evolution and mortality risks.

Acknowledgements

The authors are deeply indebted to Prof. D. Makowiec (University of Gdańsk) which kindly provided the time series analyzed in this work. The authors also thank Dr. L. Urso (Clinica "Petrucciani", Lecce) for helpful and stimulating discussions.

References

- [1] Y. Shiogai, A. Stefanovska, P. V. E. McClintock, Phys., Rep., 488 (2010) 51.
- [2] Task Force of the European Society of Cardiology and North American Society of Pacing and Electrophysiology, Heart rate variability. Standards of measurement, physiological interpretation and clinical use, Eur. Heart J., 17 (1996) 354.

- [3] C. K. Peng, J. Mietus, J. M. Hausdorff, S. Havlin, H. E. Stanley, A. L. Goldberger, *Phys. Rev. Lett.*, 70 (1993) 1343; C. K. Peng, S. Havlin, H. E. Stanley, A. L. Goldberger, *Chaos*, 5 (1995) 82.
- [4] P. Ch. Ivanov, L. A. N. Amaral, A. L. Goldberger, S. Havlin, M. G. Rosenblum, Z. R. Struzik, H. E. Stanley, *Nature*, 399 (1999) 461.
- [5] A. Bunde, S. Havlin, J. W. Kantelhardt, T. Penzel, J. H. Peter, K. Voigt, *Phys. Rev. Lett.*, 85 (2000) 3736.
- [6] Y. Ashkenazy, P. Ch. Ivanov, S. Havlin, C. K. Peng, *Phys. Rev. Lett.*, 86 (2001) 1900.
- [7] K. Kiyono, Z. R. Struzik, N. Aoyagi, S. Sakata, *Phys. Rev. Lett.*, 93 (2004) 178103; K. Kiyono, Z. R. Struzik, N. Aoyagi, F. Togo, Y. Yamamoto, *Phys. Rev. Lett.*, 95 (2005), 058101.
- [8] K. Kiyono, J. Hayano, E. Watanabe, Z. R. Struzik, Y. Yamamoto, *Heart Rhythm*, 5 (2008) 261.
- [9] D. Makowiec, R. Galaska, A. Dudkowska, A. Rynkiewicz, M. Zwierz, *Physica A*, 369 (2006) 632; A. Dudkowska, D. Makowiec, *Physica A*, 336 (2004) 174.
- [10] P. Allegrini, P. Grigolini, P. Hamilton, L. Palatella, G. Raffaelli, *Phys. Rev. E*, 65 (2002) 041926.
- [11] P. Allegrini, R. Balocchi, S. Chillemi, P. Grigolini, P. Hamilton, R. Maestri, L. Palatella, G. Raffaelli, *Phys. Rev. E*, 67 (2003) 062901.
- [12] D. G. Luchinsky, M. M. Millonas, V. N. Smelyanskiy, A. Pershakova, A. Stefanovska, P. V. E. McClintock, *Phys. Rev. E*, 72 (2005) 021905.
- [13] N. B. Janson, A. G. Balanov, V. S. Anishchenko, P. V. E. McClintock, *Phys. Rev. E*, 65 (2002) 036212.
- [14] S. Kotz, S. Nadarajah, *Extreme Value Distributions, Theory and Applications*, Imperial College Press, London (2002).
- [15] A. Bunde, J. F. Eichner, S. Havlin, J. W. Kantelhardt, *Physica A*, 330, (2003) 1; A. Bunde, J. F. Eichner, J. W. Kantelhardt, S. Havlin, *Phys. Rev. Lett.*, 94 (2005) 048701.
- [16] E. G. Altmann, H. Kantz, *Phys. Rev. E*, 71 (2005) 056106.
- [17] C. Pennetta, *Eur. Phys. J. B*, 50 (2006) 95.
- [18] C. Pennetta, L. Palatella, *Fluctuation and Noise Letters*, 11 (2012) 1240015.
- [19] PhysioNet, <http://www.physionet.org> PhysioNet Data Banks
- [20] R. L. Goldsmith, J. T. Bigger, R. C. Steinman, *J. Am. Coll. Cardiol.*, 20 (1992) 552.
- [21] J. T. Bigger, L. F. Fleiss, R. C. Steinman, L. M. Rolnitzky, W. J. Schneider, P. K. Stein, *Circulation*, 91 (1995) 1936.
- [22] P. K. Stein, A. A. Ehsani, P. P. Domitrovich, R. E. Kleiger, J. N. Rottman, *Am. Heart J.*, 138 (1999) 567.
- [23] J. E. Mietus, C. H. Peng, I. Henry, R. L. Goldsmith, A.L. Goldberger, *Heart*, 88 (2002) 378.

Stress da radiazione RF a 900 MHz ed attivazione di elementi trasponibili in tessuti germinali di *Drosophila melanogaster*

V. Specchia¹, A. Friscini¹, D. Dell'Isola¹, D. Delle Side², L. Velardi², V. Nassisi², S. Pimpinelli³ and M.P. Bozzetti¹

¹Dipartimento di Scienze e Tecnologie Biologiche ed Ambientali, Laboratorio di Genetica - Università del Salento, Via Provinciale Lecce-Monteroni, C.P. 193, 73100 Lecce, Italy

²Dipartimento di Matematica e Fisica, Laboratorio di Elettronica Applicata e Strumentazione, LEAS Università del Salento, Via provinciale Lecce-Arnesano, C.P. 193, 73100 Lecce, Italy

³Dipartimento di Biologia e Biotecnologie "Charles Darwin"-Sapienza Università di Roma, Piazzale Aldo Moro, 00185 Roma, Italy
e-mail: maria.bozzetti@unisalento.it

Abstract

Nel mondo naturale gli individui, le popolazioni e le specie si devono confrontare con variazioni delle condizioni ambientali. Gli organismi e le loro cellule mettono in atto un adattamento fisiologico attraverso risposte che sono immediate e reversibili. Condizioni di stress però, possono causare modificazioni a livello genomico che possono alterare processi biologici fondamentali conducendo a trasformazioni cellulari. È noto da tempo che fattori ambientali provocano condizioni di stress che possono indurre in vari organismi l'attivazione di elementi genetici mobili o elementi trasponibili (TEs) il cui movimento è tra le cause di instabilità genomica. In questo lavoro, individui di *Drosophila melanogaster* sono stati sottoposti a stress da radiazione RF a 900 MHz ed esaminati per l'attivazione di TEs nei tessuti germinali di entrambi i sessi. Tale stress ha causato un significativo incremento dell'attivazione di tali elementi, confermando che diversi stress ambientali possono avere come conseguenza l'instabilità dei genomi e la comparsa di mutazioni *de novo* dovute all'inserzione di elementi trasponibili in geni codificanti.

Introduzione

Le condizioni di "instabilità" genomica derivano dalla presenza di mutazioni e riarrangiamenti cromosomici; l'instabilità genomica è generalmente associata con patologie umane, ma è anche cruciale per l'evoluzione.

Le cause dell'instabilità genomica sono molteplici e comprendono errori durante la replicazione del DNA, difetti di controllo del ciclo cellulare, mutazioni di geni preposti a prevenire l'integrità genomica quali i geni soppressori di tumore e gli oncogeni [1]. Tra le cause di danni al DNA e di

instabilità genomica vi sono sequenze di DNA ripetute e potenzialmente invasive, note come elementi trasponibili (TEs) [2-4]. I TEs che comprendono due principali classi (i retrotrasposoni e i trasposoni a DNA) sono componenti ubiquitari dei genomi eucariotici. La loro presenza può influenzare l'espressione di geni localizzati nelle regioni adiacenti [5] oltre che provocare rotture cromosomiche [6]. Gli organismi hanno evoluto meccanismi preposti al silenziamento dei TEs. Studi condotti nell'ultimo decennio, in particolare in *Drosophila*, hanno iniziato a chiarire i meccanismi molecolari alla

base del silenziamento dei trasposoni e di altre sequenze ripetute. Elementi chiave di questa regolazione sono piccole molecole di RNA e proteine di una famiglia conservata detta Argonauta [7]. Nelle gonadi opera uno specifico pathway di regolazione dei TE noto come piRNA pathway. In esso intervengono le proteine della sottofamiglia Piwi della famiglia Argonauta e i piwi-interacting RNA o piRNA, entrambi questi componenti sono presenti esclusivamente o prevalentemente nelle gonadi di entrambi i sessi. Un ruolo chiave è svolto da Aubergine, una di queste "Piwi-proteins" [8, 9]; altri componenti importanti sono la proteina heat shock HSP90 [10] e il cochaperone di HSP90, Shutdown [11].

E' stato osservato da tempo che gli stress ambientali inducono l'attività degli elementi trasponibili in vari organismi e questo rappresenta un legame fondamentale tra i fattori ambientali e le variazioni dei genomi [4, 12]. È già noto l'effetto dello stress di temperatura (heat shock) che determina movimento di elementi trasponibili [13]. Abbiamo voluto verificare se un diverso tipo di stress, come le onde elettromagnetiche (EM) nel range della radiofrequenza (RF), potesse determinare effetti simili sugli elementi trasponibili e, in generale, sulle sequenze ripetute.

Recentemente l'uso delle RF ha dimostrato una risposta sugli organismi viventi modificando la velocità di mutazione [14, 15] e causando una mancata regolazione delle sequenze ripetute *Stellate* in *Drosophila* [16]. Le sequenze ripetute *Stellate* sono peculiari del genoma di *Drosophila* e il loro mancato silenziamento determina, nei tessuti germinali maschili, la produzione di una proteina specifica, la proteina *Stellate*, che forma aggregati cristallini negli spermatozoi [17]. Le sequenze *Stellate* sono regolate, al pari degli elementi trasponibili, dal piRNA pathway [8]. La ricerca di cristalli di *Stellate* negli spermatozoi è quindi uno strumento utile per identificare condizioni (genetiche o ambientali) che alterano il pathway di silenziamento degli elementi trasponibili e che possono quindi determinare instabilità genomica.

Apparato sperimentale

E' stata utilizzata la radiazione elettromagnetica nel range delle radiofrequenze, essendo allo stato

attuale quella più diffusa per l'uso della telefonia mobile. Allo scopo è stata costruita una linea di trasmissione per permettere di controllare il campo interagente con i nostri campioni. Il generatore RF è un RHODE & SCHWARZ SM300. La sua frequenza massima è di 3 GHz e la potenza di uscita 20 mW. L'impedenza caratteristica, e quindi la resistenza d'uscita, è di 50 Ω. Al fine di limitare gli effetti di disadattamento e controllare il campo, la linea è stata realizzata con due conduttori piani di lunghezza $l=15\text{ cm}$ e larghezza $a=10\text{ cm}$, separati da 4 supporti in PVC di spessore $h=2\text{ cm}$, Fig. 1.

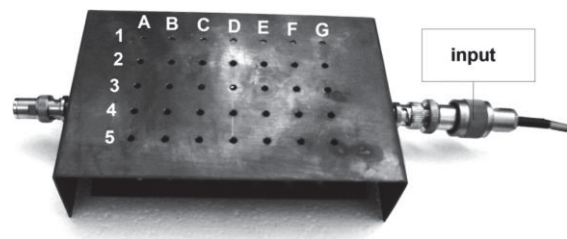


Fig. 1. Foto della linea di trasmissione.

Teoricamente la lunghezza della linea non influenza l'impedenza caratteristica essendo espressa dalla seguente formula:

$$R_0 = \sqrt{\frac{L}{C}} = \sqrt{\frac{\mu_0}{\epsilon_0} \frac{h}{l}} \quad (1)$$

dove si è escluso l'irraggiamento esterno e indicato con ϵ_0 e μ_0 rispettivamente la permittività elettrica e la permeabilità magnetica. Chiudendo la linea su un carico di 50 Ω il campo al suo interno è risultato misto, cioè composto da un'onda progressiva ed un'onda stazionaria, come si può vedere dalla Fig. 1[13], a causa dell'irraggiamento esterno.

Per meglio comprendere il funzionamento riportiamo in Fig. 2 uno schema del set up sperimentale.

In Fig. 3 è riportata la mappatura del campo misurando in ogni foro della linea di trasmissione con una sonda elettrica.

La mappatura riporta un campo intenso di 170 V/m sul lato *out* della linea ed un campo di 100 V/m sul lato *input*.

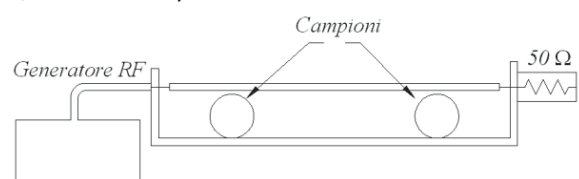


Fig. 2. Schema del set up sperimentale.

Distribuzione del campo elettrico nella cella TEM

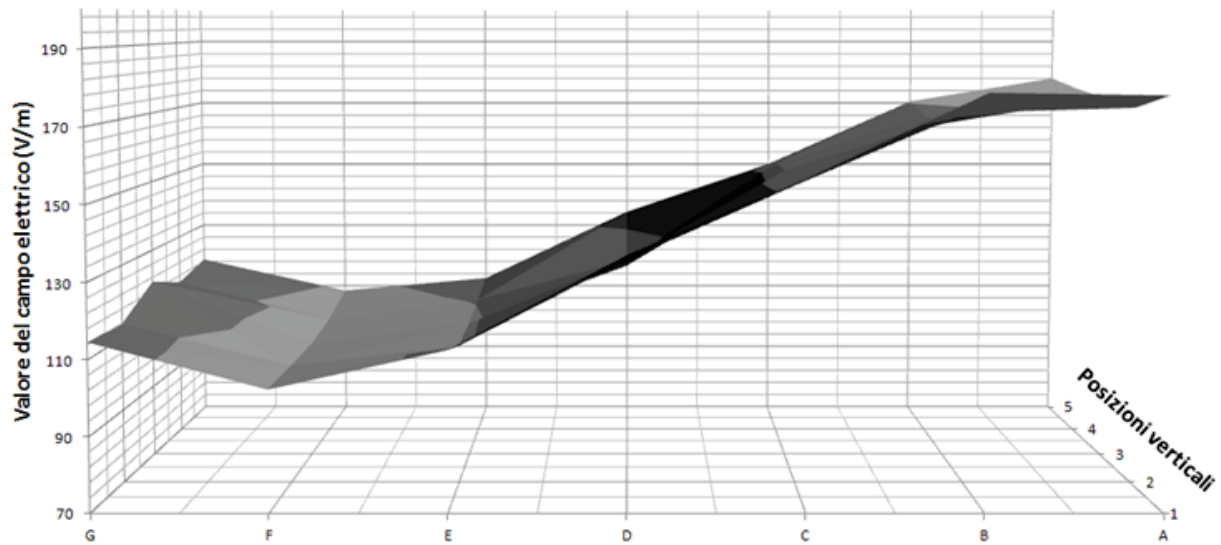


Fig. 3. Mappa indicante la distribuzione del campo elettrico all'interno della linea a 900 MHz.

Materiali e Metodi

Materiali: Individui provenienti da un ceppo selvatico *OregonR*, 50 femmine e 100 maschi, tutti giovani di due-tre giorni) sono stati introdotti in barattoli contenenti il mezzo di coltura in cui normalmente si sviluppano, costituito da: farina di mais, agar, zucchero e lievito.

Metodi, Condizioni di stress: Due barattoli contenenti le mosche sono stati sottoposti all'azione costante della RF a 900 MHz ad una intensità di 170 e 100 V/m per 5 giorni consecutivi nella linea di trasmissione alla temperatura di 20 °C e umidità costante. Altri due barattoli sono stati tenuti alle stesse condizioni di temperatura ed umidità senza l'azione della RF, per essere usati come controllo.

Estrazione di RNA totale da gonadi di *Drosophila* e sintesi della prima strand di cDNA: I testicoli e gli ovari sono stati dissezionati in soluzione Ringer (NaCl 47 mM, KCl 183 mM, Tris-HCl 10 mM pH 6,8). Per l'estrazione sono stati utilizzati 30 mg di tessuto (che corrispondono a circa 70 coppie di testicoli e circa 40 coppie di ovari) di individui sia stressati che di controllo.

Per l'estrazione dell'RNA totale è stato utilizzato il Kit RNAqueous-4PCR della ditta Ambion. Dopo trattamento dell'RNA con DNaseI, la sintesi della prima strand di cDNA è stata effettuata utilizzando il Kit SuperScript first-strand synthesis system (Invitrogen).

Real Time PCR: La Real Time PCR è una *Polinucleotide Chain Reaction* (PCR) in cui l'amplificazione e il rilevamento dell'amplificato avvengono nello stesso momento, stabilisce quindi la quantità relativa di uno specifico RNA trascritto, è anche chiamata "RT-PCR quantitativa o qRT-PCR". Lo strumento utilizzato per effettuare gli esperimenti di Real Time PCR è stato lo Smart Cycler della Cepheid. La Master Mix utilizzata è Fluo Cycle, SYBR Green (2X) della Celbio costituita da Tris-HCl (pH 8.3) 20 mM, mix dNTPs 20 mM, 0.02% Tween-20, KCl 100 mM, MgCl 8 mM, SYBR Green.

La reazione è stata allestita nel modo seguente in un volume totale di 25 µl: Master Mix 1X, Primer Forward 10 pmoli, Primer Reverse 100 pmoli, cDNA 1 µl. Il protocollo eseguito ha previsto 10' a 95°C e 45 cicli di cui ciascuno prevede: 30'' a 95°C, 30'' alla temperatura di annealing ottimale per la coppia di primers utilizzata, 30'' a 72°C. Per

L'analisi dei dati è stato utilizzato il metodo del $2\Delta\Delta Ct$ [18]. Per ciascun trasposone analizzato è stata utilizzata una coppia di oligonucleotidi scelta con caratteristiche specifiche per l'esecuzione di protocolli di Real Time PCR.

Risultati

Trascorsi 5 giorni dall'applicazione della frequenza costante a 900 MHz, i moscerini sono stati sottoposti a dissezione per ottenere i testicoli e gli ovari da cui è stato estratto l'RNA totale. Successivamente è stato sintetizzato il cDNA e i campioni sono stati utilizzati per reazioni di qRT-PCR. Sono stati utilizzati per tali reazioni primers specifici per alcuni elementi trasponibili e primers specifici per un gene ad espressione costitutiva, *rp49*, che rappresenta il controllo interno di quantità di RNA. In particolare sono stati esaminati tre retrotrasposoni normalmente silenziati nelle cellule germinali: *R1*, *roo* e *springer*. Sono state effettuate tre reazioni di amplificazione per ciascun cDNA preparato e sono stati calcolati i valori medi di C_T (primo ciclo di amplificazione a cui si rileva una fluorescenza non dovuta al fondo) e le deviazioni standard. Successivamente è stato calcolato il numero di volte di incremento (fold change) del trascritto di ciascun elemento trasponibile esaminato secondo i metodi riportati in [9,18]. I valori ottenuti per i trasposoni che hanno mostrato attivazione sono riportati nelle Tab. 1 e 2 e sono stati utilizzati per la costruzione dei grafici riportati rispettivamente in Fig. 4 e 5.

Trasposone	Fold change in ovari stressati vs. controllo	Coefficiente di variazione
<i>R1</i>	2,0	0,01
<i>roo</i>	2,2	0,03
<i>springer</i>	2,1	0,10

Tabella 1: Valori di numero di volte di incremento del trascritto di elementi trasponibili in ovari di individui sottoposti a stress rispetto ad individui di controllo.

Trasposone	Fold change in testicoli stressati vs controllo	Coefficiente di variazione
<i>l</i>	3,30	0,03
<i>roo</i>	2,53	0,05
<i>springer</i>	2,63	0,01

Tabella 2: Valori di numero di volte di incremento del trascritto di elementi trasponibili in ovari di individui sottoposti a stress rispetto ad individui di controllo.

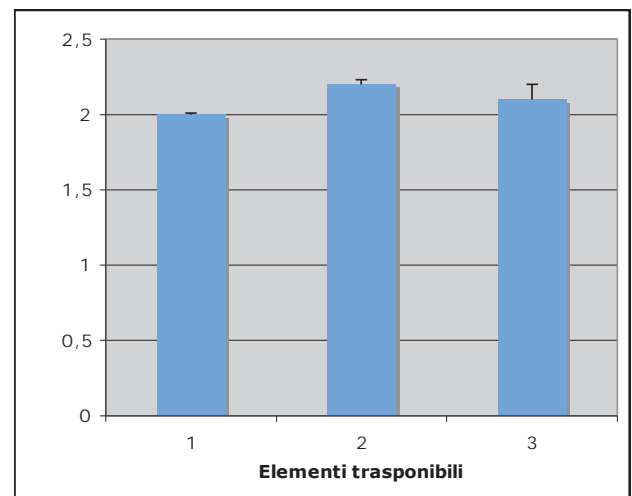


Fig. 4: Grafico relativo al numero di volte di incremento del trascritto di elementi trasponibili in ovari di individui sottoposti a stress rispetto ad individui di controllo. 1= *R1*; 2= *roo*; 3=*springer*.

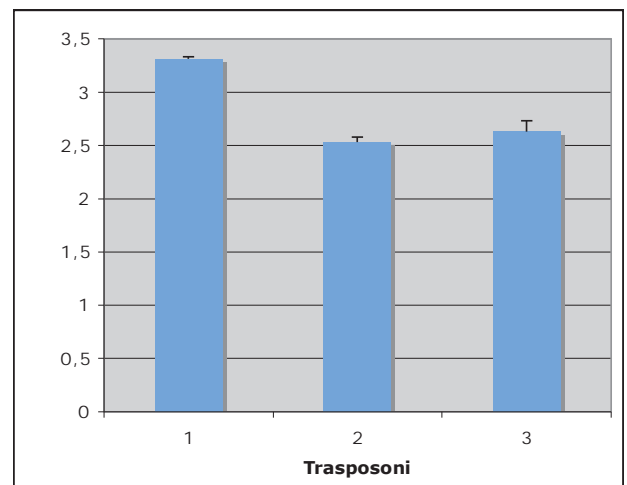


Figura 5: Grafico relativo al numero di volte di incremento del trascritto di elementi trasponibili in testicoli di individui sottoposti a stress rispetto ad individui di controllo. 1= *l*; 2= *roo*; 3=*springer*.

Conclusioni

Lo studio ha dimostrato che le RF a 900MHz, a cui i moscerini sono stati sottoposti, sono in grado di alterare la regolazione del silenziamento delle sequenze ripetute corrispondenti ad elementi trasponibili. Infatti, è stato riscontrato un incremento significativo della quantità di trascritto di vari retrotrasposoni nelle gonadi maschili e femminili di individui sottoposti a RF a 900 MHz rispetto al controllo. L'aumento del trascritto di vari elementi trasponibili è sintomo di un loro possibile movimento e quindi misura la capacità di alterare la funzionalità genica che potrebbe causare mutazioni. Questa indagine potrà essere estesa valutando la frequenza di alterazioni morfologiche nella progenie di individui sottoposti all'azione delle RF 900 MHz che potrebbe derivare dall'insorgenza di mutazioni *de novo* causate dal movimento degli elementi trasponibili.

Acknowledgments

Il lavoro qui presentato è stato parzialmente supportato attraverso il PON 254/Ric. (Cod. PONA3_00334).

References

- [1] A. Aguilera and B. Gómez-González Nat Rev Genet. **9** (3): 204-217 (2008).
- [2] B. McClintock Science **226**: 792–801 (1984).
- [3] S. Pimpinelli, M. Berloco, L. Fanti, P. Dimitri, S. Bonaccorsi, E. Marchetti, R. Caizzi, C. Caggese and M. Gatti PNAS **92**: 3804-3808 (1995)
- [4] E.S. Lander Nature **470**, 167-197 (2011).
- [5] J. Häslér , T. Samuelsson and K. Strub Cell Mol Life Sci. **64**(14): 1793-1800 (2007)
- [6] S.L. Gasior, T.P. Wakeman, B. Xu and P.L. Deininger J Mol Biol. **357**(5):1383-1393 (2006)
- [7] Ghildiyal, M. and Zamore, P.D. Nature Reviews Genetics **10**: 94-108 (2009)
- [8] V.V. Vagin, A. Sigova, C. Li , H. Seitz, V. Gvozdev and P.D. Zamore Science. **313**(5785): 320-324 (2006).
- [9] V. Specchia, C. Benna, G.M. Mazzotta A. Piccin, M.A. Zordan , R. Costa and M. P. Bozzetti Genetics. **178**(3):1271-1282 (2008).
- [10] V. Specchia, L Piacentini, P. Tritto, L. Fanti, R. Dalessandro, G. Palumbo, Pimpinelli S. and M.P. Bozzetti Nature **463**: 662-665 (2010)
- [11] D. Olivieri , K.A. Senti, S. Subramanian , R. Sachidanandam J. Brennecke Mol Cell. **28**;**47**(6):954-69 (2012)
- [12] P. Capy, G. Gasperi, C. Biemont, and C. Bazin Heredity **85**, 101–106 (2000)
- [13] C. Vieira, P. Aubry, D. Lepetit and C. Biemont Proc. Biol. Sci. **265**: 1161–1165 (1998).
- [14] F. Belloni, D. Doria, A. Lorusso, V. Nassisi, L. Velardi, P. Alifano, C. Monaco, A. Talà, M. Tredici and A. Rainò, J. Phys. D: Appl. Phys. **39**, 2856-2861(2006)
- [15] F. Belloni, et al. J. Phys. D: Appl. Phys. **39**, 2856-2861(2006)
- [16] V Specchia, L Giordano, MP Bozzetti, V Nassisi, D Delle Side 2nd Workshop-Plasmi, Sorgenti, Biofisica ed Applicazioni 2010 (1), 112-115
- [17] M.P. Bozzetti, S. Massari, P. Finelli, F. Meggio, L.A. Pinna, B. Boldyreff. O.G. Issinger, G. Palumbo, C. Ciriaco, S. Bonaccorsi and S. Pimpinelli PNAS **92**: 6067-6071 (1995)
- [18] K.J. Livak and T.D. Schmittingen Methods **25**: 402 (2001).

Bactericide effect of powerful Ultrasonic Bone Surgery device (piezo-surgery) : Oral surgery application in BRONJ treatment: (Biphosphonate Related osteonecrosis of the jaws)

Cornelio Blus¹, Giulio Giannelli^{2*}, Serge Szmukler-Moncler¹

¹ *Professore a. c. Master Nazionale di Il livello in implantologia Università degli studi di Cagliari, Istituto di Scienze Chirurgiche Odontostomatologiche Università degli Studi di Cagliari – Cagliari (Italy)*

² *Unità Operativa Dipartimentale di Odontostomatologia P.O. Sacro Cuore di Gesù ASL LECCE – Gallipoli (Le) Italy*

**Corresponding author. Tel.: +39 0833 506995,
Fax: +39 0833 506166, E-mail: studio.giannelli@teletu.it*

Abstract

I farmaci Bifosfonati sono composti chimici analoghi del pirofosfato e sono in grado di determinare un rallentamento del riassorbimento osseo agendo sul metabolismo degli osteoclasti. L'Osteonecrosi dei mascellari(8-9-10) è stata classificata come una potenziale reazione avversa legata all'uso di farmaci Amino-Bifosfonati ed è da lungo tempo considerata una condizione di difficile risoluzione a causa del rallentato turn-over del metabolismo osseo. L'obiettivo di questo lavoro è stato quello di identificare eventuali presidi chirurgici in grado di risolvere il problema dell'osteonecrosi(11) ed eventualmente impedirne la recidiva, riportata in letteratura come una evenienza frequente. Nel presente studio sono stati trattati 16 pazienti (11 donne e 5 maschi) di età compresa tra 59 e 82 anni,(69aa media). Di questi: 10 pazienti erano stati sottoposti a terapia con bifosfonati a causa di neoplasie metastatizzate, di cui 9 con Acido Zoledronico e 1 con Acido Pamidronico; invece, 6 pz. erano stati trattati per osteoporosi con Acido Alendronico. Undici pazienti riportavano lesioni osteonecrotiche a carico dell'osso mandibolare (10 nella regione anteriore e 1 in quella posteriore); quattro pazienti avevano lesioni a carico del mascellare superiore; un paziente ha avuto una osteonecrosi a carico della mandibola prima ed a distanza di 4 mesi a carico del mascellare superiore; due sul mascellare anteriore, ed altri due sul mascellare posteriore. Per il trattamento chirurgico delle lesioni necrotiche sono state utilizzate attrezzature per la chirurgia ossea ad ultrasuoni ad alta potenza (90 Watt) e bassa frequenza (24-32Kz) (Ultrasonic-Bone Surgery -U.B.S.). I risultati ottenuti hanno dimostrato che tutti i pazienti trattati avevano avuto una remissione dei sintomi ed una chiusura completa per prima o per seconda intenzione delle ferite entro le prime due settimane dall'intervento. Durante il follow-up (che va da un minimo di 6 mesi fino a 12 mesi) cui sono stati sottoposti tutti i pazienti, non si è manifestata ad oggi alcuna recidiva. Dovrebbero essere presi in considerazione altri pazienti ma gli attuali risultati incoraggiano ulteriori esperimenti in vivo/in vitro in merito all'uso della chirurgia ad ultrasuoni nel trattamento delle osteonecrosi.

Introduzione

Da quando nel 2000 il termine chirurgia ultrasonica (o piezoelettrica) è entrato nel dizionario clinico odontoiatrico e maxillo-facciale si è avuto un'evoluzione continua e ininterrotta delle tecniche di osteotomia e osteoplastica correlate .

A fronte dell'enorme diffusione che le tecniche chirurgiche ultrasoniche hanno dimostrato avere nella comune pratica clinica, sono ancora pochissimi i lavori in letteratura che consentono un'analisi chiara degli effetti che tali procedure possano avere nel lungo termine (Blus et al., 2008).

Oltre al mondo clinico anche il mondo della ricerca continua a sviluppare nuove conoscenze inerenti tali

strumenti e tecniche, cercando di raggiungere la comprensione di aspetti ancora oggi non del tutto chiari quali per esempio gli effetti della chirurgia ultrasonica sui batteri o ancora il suo utilizzo per casi fino ad oggi di difficilissimo trattamento come i pazienti affetti da osteonecrosi da bisfosfonati (ONJ).

Oggi le tecniche di chirurgia ultrasonica dimostrano essere più agevoli di quelle con strumenti tradizionali, rotanti o manuali, grazie alla maggiore precisione di taglio, alla possibilità di creare accessi chirurgici più conservativi venendo a mancare il rischio di danneggiamento dei tessuti molli, al minore affaticamento dell'operatore ed ad un rischio minimo di sviluppare termonecrosi ossee, (Barone et al., 2010; Lea et al., 2003; Romeo et al., 2009).

Il vantaggio primario degli strumenti ad ultrasuoni in chirurgia ossea è quello di ottenere, in corrispondenza dei confini della zona sottoposta al taglio chirurgico, un'area di osso altamente vitale e reattivo, ricca di osteociti fondamentale al fine di ottenere una guarigione dei tessuti ottimale. (Berengo et al., 2006; Chiriac et al., 2005; Preti et al., 2007).

BRONJ

Ormai l'osteonecrosi dei mascellari correlata all'utilizzo dei BF è una realtà patologica che negli ultimi anni ha aumentato la sua visibilità(5-6-9).

Dal 2003 sono apparse in letteratura numerose segnalazioni su una possibile relazione tra terapia endovenosa con bifosfonati ,sia con acido pamidronico che con acido zoledronico i quali causavano quadri di osteonecrosi avascolare a carico delle ossa mascellari, dovuti principalmente a manovre odontoiatriche e traumi accidentali; tuttavia in alcuni casi non era evidenziabile alcuna causa scatenante(4-5). L'effetto anti-angiogenico probabilmente dovuto alla loro capacità di ridurre il livello circolatorio del fattore di crescita vascolo-endoteliale sommato a microtraumi e successivi fenomeni di natura infiammatoria , potrebbe giocare un ruolo importante nel determinare i cambiamenti ischemici responsabili di tale fenomeno osteo-necrotico(9-10), sul quale vanno a sommarsi fenomeni di infezione batterica, che tendono a complicare ulteriormente il quadro clinico generale. (11)

La BRONJ (Biphosphonate Related Osteonecrosis of the jaw) si presenta come un focolaio osteomieltico, singolo o multiplo, che appare nelle fasi iniziali come una banale patologia infiammatoria alveolare, refrattaria alle comuni terapie sia locali che sistemiche. Tale focolaio tende ad estendersi alle zone limitrofe fino a manifestarsi con vaste aree di necrosi; l'osso esposto si presenta di colore giallo-biancastro, circondato da aree mucose fortemente edematose ed arrossate(11).

I sintomi all'esordio sono: dolore fisso ad insorgenza spontanea o dopo avulsione dentale, inabilità alla masticazione e all'utilizzo di protesi mobili, ascessi orali e/o cutanei, secrezione di materiale sieropurulento, parestesia, alitosi, malessere, tumefazione, trisma.

I segni clinici caratteristici sono: aree singole o multiple di esposizione ossea, fistola senza esposizione ossea, ascesso cutaneo e/o orale ricoperto da mucosa eritematosa, trisma, comunicazione oroantrale e/o oro-nasali, sinusite mascellare e/o pansinusite, ulcerazione eritematosa cronica della mucosa orale, affioramento di osseo necrotico sottostante, presenza di essudato purulento, possibile sanguinamento spontaneo o provocato, perdita di elementi dentari prima stabili. (9)

Radiologicamente si evidenziano: aspetto tarlato (aree) radiotrasparenti a margini poco definiti), impronta di alveoli post-estrattivi.

Con il tempo tali aree tendono ad essere isolate da un orletto radiotrasparente, formando così un sequestro osseo. Altre volte, invece, tali aree si espandono sino alla frattura patologica.

MATERIALI E METODI

Negli anni si è visto che l'approccio chirurgico⁽¹⁴⁻¹⁶⁻¹⁷⁾, nei casi di BRONJ, non sembra essere elettivo né risolutore, in quanto le lesioni osteonecrotiche che insorgono sono sempre di notevole gravità e vi è un enorme difficoltà a mantenere un margine chirurgico pulito che consenta di non avere recidive. Per questo motivo il più delle volte l'intervento chirurgico risulta essere altamente invalidante.

Abbiamo così applicato un protocollo di chirurgia ossea ad ultrasuoni (piezoelettrica) non estesa , utilizzando il sistema Ultra-Sonic Bone Sugery (Resista srl.Omegna,Italia).

La *tecnica chirurgica ad ultrasuoni* veniva utilizzata principalmente per eseguire: curettage, debridement, sequestrectomia, corticotomia, ospeoplastica, resezione ossea marginale.

Reclutamento dei pazienti

I criteri presi in considerazione nella scelta dei casi sono stati: - diagnosi di ONJ in vari stadi di progressione clinica⁽⁹⁾. Sono stati reclutati solo quei pazienti che presentavano uno stadio di malattia BRONJ 2±3 aventi lesioni non superiori ai 3 cm. [Tab. 1]

I pazienti erano trattati chirurgicamente con punte vibranti connesse ad un apparecchio ad ultrasuoni (piezoelettrico) ad alta potenza, gli stessi i sono stati poi seguiti per almeno 12 mesi dopo l'intervento chirurgico per verificare eventuali recidive.

STADIAZIONE CLINICA DELLE ONJ “ BRONJ STAGE “

- **CATEGORIA A RISCHIO** : non apparente presenza di osso necrotico in pz. in trattamento con BF per via orale o EV
- **STAGE 0** : non segni evidenti di necrosi ossee
- **STAGE 1** : Osso necrotico esposto in assenza di sintomatologia
- **STAGE 2** : Osso necrotico esposto associato a dolore e infezione
- **STAGE 3** : Osso necrotico esposto associato a dolore, infezione e fratture patologiche, fistole extraorali o segni di osteolisi che si estendono fino al bordo corticale inferiore

Ruggiero S., e Altri: J. Oral Maxillofac Surg 67:2-12, 2009 Suppl1: "American Association of Oral and Maxillofacial Surgeons Position Paper on Bisphosphonate-related Osteonecrosis of the Jaws-2009 Update"

Tab.1: Stadiazione BRONJ

I pazienti, che rientravano nei criteri di scelta, 11 donne e 5 uomini con un'età media compresa tra 59-82 anni, sono stati trattati presso l'Ospedale di Gallipoli (Gallipoli, Puglia, Italia) da un unico chirurgo orale.

Di questi: 10 pazienti erano stati sottoposti a terapia con bifosfonati a causa di neoplasie metastatizzate, di cui 9 con Acido Zoledronico e 1 con Acido Pamidronico; invece, 6 pazienti erano stati trattati per osteoporosi con Acido Alendronico.

Undici pazienti riportavano lesioni osteonecrotiche a carico dell'osso mandibolare (10 nella regione anteriore e 1 in quella posteriore); quattro pazienti avevano lesioni a carico del mascellare superiore; un paziente ha avuto una osteonecrosi a carico della mandibola prima ed a distanza di 4 mesi a carico del mascellare superiore; due sul mascellare anteriore, ed altri due sul mascellare posteriore.

Una mandibola presentava una necrosi bilaterale nella regione posteriore; in tutto sono stati trattati 18 siti.

Le cause dell'osteonecrosi erano dovute ad estrazione in 12 pazienti e in tre pazienti ad una protesi incongrua, 1 paziente ha sviluppato Bronj come conseguenza di una grave parodontosi.

Tutti i pazienti affetti da tumore erano stati sottoposti a chemioterapia, terapia ormonale o con immunodepressori. Il trattamento con bifosfonati è durato in media dai 15 ai 94 mesi. L'osteonecrosi è stata diagnosticata in media dai 9 ai 95 mesi successivi all'inizio della terapia a base di bifosfonati. La diagnosi di BRONJ è stata fatta in media da 0 ai 6 mesi dalla sospensione del trattamento. In sei pazienti l'osteonecrosi è stata diagnosticata durante la cura a base di BF.

Protocollo del trattamento

Una volta fatta diagnosi di osteonecrosi, i pazienti sono stati trattati con un ciclo di terapia antibiotica per 2 settimane con un'associazione di Amoxicillina e acido Clavulanico (2g/die) e Metronidazolo (1g/die)

⁽²⁰⁾. Successivamente in caso di mancata guarigione⁽¹²⁾, veniva consigliato il trattamento chirurgico⁽¹⁴⁻¹⁶⁾.

Sintomi e segni clinici

I sintomi e i segni clinici sono stati registrati per ogni paziente prima dell'intervento chirurgico e in seguito durante i successivi controlli. Tutti i pazienti oncologici presentavano esposizione d'osso a differenza di quelli affetti da osteoporosi. [In genere nei pazienti con osteoporosi l'osteonecrosi si manifesta con un sovrapporsi d'infezione, il quadro infiammatorio è quello tipico dell'osteomielite, mentre nei pazienti oncologici l'infezione si manifesta con una evidente esposizione di osso.] Due pazienti presentavano trisma ed un unico paziente riferiva parestesia del labbro inferiore.

Attrezzatura chirurgica ad ultrasuoni

Il trattamento chirurgico è stato effettuato con apparecchio UBS⁽²¹⁻²²⁾ (Resista, Omegna, Italia), un potente strumento chirurgico ad ultrasuoni con punte in lega di titanio e una potenza massima di 90 W⁽²¹⁾ [Fig. 1].



Fig 1. Il dispositivo Ultrasonic Bone Surgery e gli inserti utilizzati: a sinistra: Dispositivo ad ultrasuoni con manopola vibrante. Potenza massima 90 W; a destra: inserti utilizzati. Da sopra: bone scraper, saw tip, orthogonal saw tip, round tip, straight round tip. Tutti gli inserti sono realizzati in lega di titanio.

L'attivazione dell'apparecchio ad ultrasuoni provoca onde cavitazionali che sono in grado di eliminare sia i germi in sospensione che i biofilm batterici⁽²³⁻²⁴⁾. Ciò è stato attribuito alla rottura della membrana cellulare batterica in seguito a ripetuti cicli di potenti implosioni di bolle nelle vicinanze di germi.

Sono state usate tre tipi di punte vibranti (Fig1b) con un apparecchio con potenza di 90 W (livello 5 su 9)⁽²⁴⁾ (Blus et. Al. 2009).

L'inserto "bone scraper" veniva utilizzato per rimuovere l'osso superficiale. Due lame seghettate "saw tips", una verticale e una ortogonale, venivano usate per clivare la zona di osso sequestrata. Le due

punte sferiche, una corta per la zona anteriore e una lunga e dritta, straight round tip, per poter accedere facilmente al vestibolo posteriore e zone linguali, sono state utilizzate per livellare i picchi ossei prima di suturare i tessuti molli.

Protocollo medico

Si è usata terapia antibiotica (Amoxicillina e acido clavulanico 2g/d e Metronidazolo 1g/d) per due settimane a partire dal terzo giorno precedente la chirurgia ad ultrasuoni.

Protocollo chirurgico

Fu utilizzata un'anestesia loco-regionale con Mepivacaina cloridrato *senza vasocostrittore*. Dopo un'incisione muco-periostale il successivo scollamento dei lembi avvenne in modo da avere un pieno accesso alla zona da trattare. A seconda del tipo di trattamento con bifosfonati utilizzato, l'aspetto macroscopico delle lesioni si presentava in modo diverso: nei pazienti con osteoporosi la necrosi ossea non era così estesa come nei pazienti trattati per neoplasie. Era presente osso vitale disseminato di zone necrotiche; in questo caso l'osso necrotico veniva rimosso fino ad ottenere un buon livello di sanguinamento sull'osso sano. Nei pazienti neoplastici l'osso necrotico veniva eliminato creando un piano di clivaggio tra la necrosi e la zona sana circostante per ottenere anche in questo caso un buon livello di sanguinamento. In ogni sito trattato i tessuti venivano successivamente esposti ad una azione di cavitazione intensa per due o tre minuti consecutivi, in modo da eliminare completamente gli eventuali batteri ancora presenti sul sito. Si procedeva quindi suturando i lembi, non prima di aver rimosso dagli stessi l'eventuale tessuto di granulazione residuo. In tutti i casi si è raggiunto lo scopo primario di chiusura. In tutti i casi l'esame istologico ha confermato l'osteonecrosi con infiltrato plasmacellulare; 4 pazienti presentavano inoltre infezione micotica a carico della zona rimossa.

Follow-up e criteri di successo

I pazienti sono stati controllati a distanza di due settimane dall'intervento chirurgico, dopo un mese, sei mesi, un anno e due anni e sono a tutt'oggi inseriti in un programma di richiamo a lungo termine. Sono stati presi in considerazione i sintomi e i segni clinici nei diversi momenti; è stata effettuata radiografia ortopantomica per avere informazioni radiologiche dopo 6 mesi, 1 anno.

I criteri di successo clinico erano:

- la diminuzione del dolore o la completa risoluzione,
- l'osso esposto è stato ricoperto dal tessuto molle,

- guarigione dei tessuti molli nelle zone trattate.

Per questi motivi consideriamo un successo clinico: la riduzione o la scomparsa dei sintomi (dolore, sanguinamento, gonfiore o presenza di pus); guarigione delle ulcere della mucosa e rivestimento tissutale dell'osso esposto; guarigione delle fistole mucose o cutanee.

Risultati

Il post-operatorio ha evidenziato dopo due settimane una buona guarigione dei tessuti, con scomparsa o diminuzione completa dei sintomi.

I controlli successivi a 6 e 12 mesi mettevano in evidenza una chiusura completa della ferita chirurgica con una restituito ad integrum.

Discussione

E' stato piuttosto difficile valutare il successo del trattamento nel lungo periodo in quanto i pazienti affetti da cancro sono soggetti ad elevata mortalità. Per questa ragione il presente studio ha focalizzato la sua attenzione solo su quei pazienti che potevano essere seguiti per almeno 6-12 mesi.

Come detto precedentemente, i pazienti sottoposti a trattamento a base di bifosfonati per motivi oncologici presentavano una necrosi più avanzata rispetto a quelli in trattamento per osteoporosi.⁽²⁵⁻²⁶⁾

In letteratura sono riportati diversi metodi per la risoluzione dei problemi della Onj con alterni successi. Per la prima volta i pazienti affetti da BRONJ sono stati trattati con chirurgia ossea ad ultrasuoni e si sono eseguiti controlli a distanza di 12 mesi.

Questo lavoro è stato eseguito partendo dai risultati ottenuti in vitro sui batteri Gram positivi e Gram negativi⁽²⁷⁾ ed in vivo nella cura del piede diabetico⁽²⁸⁾ e nel posizionamento degli impianti dentali in siti infetti post-estrattivi⁽²⁹⁾.

Un altro elemento a favore è rappresentato dagli studi di Preti et al. , i quali dimostrarono che siti infetti trattati con la chirurgia ad ultrasuoni prima di inserire gli impianti presentavano un incremento localizzato di proteine morfogenetiche⁽³⁰⁾.

Il protocollo medico-chirurgico si basa sull'utilizzo di una terapia antibiotica associata ad un intervento chirurgico con l'utilizzo di un apparecchio per chirurgia ossea ad ultrasuoni. I tessuti infetti e necrotici sono stati sottoposti all'effetto cavitazionale per 2/3 minuti. In esperimenti in vitro condotti dal nostro gruppo, si è evidenziato che l'effetto cavitazionale degli ultrasuoni diminuisce la vitalità batterica (Escherichia coli e B. Subtilis) da 2 a 3 log⁽³¹⁻³²⁾.

Alcuni autori sostengono che i biofilms microbici possono essere coinvolti nel processo del BRONJ⁽³¹⁻³²⁾. In questo contesto, a nostro avviso, il trattamento con la chirurgia ad ultrasuoni potrebbe aver diminuito la

massa critica microbica attorno all'osso e quindi permesso una sinergia con il trattamento medico. Il controllo a due settimane ha evidenziato la chiusura della tessuti molli per prima intenzione. Al follow-up a 30 gg. si poteva osservare la completa chiusura della ferita chirurgica e la scomparsa dell'edema e dei sintomi iniziali.

Conclusioni

L'obiettivo del presente studio era quello di provare un sistema che consentisse di ridurre la progressione dell'osteonecrosi ed evitasse le recidive. Si è introdotto un protocollo combinato medico-chirurgico per la cura di pazienti affetti da BRONJ.

I classici sintomi clinici diagnosticati precocemente in questi soggetti sono risultati scoparsi dopo un mese.

I casi sino ad oggi trattati, anche se necessitano di osservazioni a più lungo termine, ci consentono di affermare, che questa metodica è:

- semplice da usare,
- diminuisce notevolmente i tempi d'intervento,
- garantisce un minimo trauma chirurgico,
- aumenta l'accettazione del trattamento da parte del paziente

E' auspicabile che ricerche a lungo termine vengano eseguite per valorizzare i risultati preliminari fino ad oggi ottenuti.



Prima della chirurgia Onj mascellare spontanea



controllo a 12 mesi

References

1. Hortobagyi GN, Theriault RL, Lipton A, Porter L, Blayney D, Sinoff C, Wheeler H, Simeone JF, Seaman JJ, Knight RD, Heffernan M, Mellars K, Reitsma DJ. Long-term prevention of skeletal complications of metastatic breast cancer with pamidronate. Protocol 19 Aredia Breast Cancer Study Group. *J Clin Oncol* 1998; **16**: 2038-2044.
2. Major P, Lortholary A, Hon J, Abdi E, Mills G, Menssen HD, Yunus F, Bell R, Body J, Quebe-Fehling E, Seaman J. Zoledronic acid is superior to pamidronate in the treatment of hypercalcemia of malignancy: a pooled analysis of two randomized, controlled clinical trials. *J Clin Oncol* 2001; **19**: 558-567.
3. Berenson JR, Hillner BE, Kyle RA, Anderson K, Lipton A, Yee GC, Biermann JS. American Society of Clinical Oncology clinical practice guidelines: the role of bisphosphonates in multiple myeloma. *J Clin Oncol* 2002; **20**: 3719-3736.
4. Rosen LS, Gordon D, Tchekmedyan NS, Yanagihara R, Hirsh V, Krzakowski M, Pawlicki M, De Souza P, Zheng M, Urbanowitz G, Reitsma D, Seaman J. Long-term efficacy and safety of zoledronic acid in the treatment of skeletal metastases in patients with nonsmall cell lung carcinoma and other solid tumors: a randomized, Phase III, double-blind, placebo-controlled trial. *Cancer* 2004; **100**: 2613-2621.
5. Saad F, Gleason DM, Murray R, Tchekmedyan S, Venner P, Lacombe L, Chin JL, Vinholes JJ, Goas JA, Zheng M. Long-term efficacy of zoledronic acid for the prevention of skeletal complications in patients with metastatic hormone-refractory prostate cancer. *J Natl Cancer Inst* 2004; **96**: 879-882.
6. Assael LA. Oral bisphosphonates as a cause of bisphosphonate-related osteonecrosis of the jaws: clinical findings, assessment of risks, and preventive strategies. *J Oral Maxillofac Surg* 2009; **67**: 35-43.
7. Sorensen OH. [Biphosphonates--a new treatment in osteoporosis]. *Ugeskr Laeger* 1991; **153**: 693-694.
8. Van Poznak C, Estilo C. Osteonecrosis of the jaw in cancer patients receiving IV bisphosphonates. *Oncology (Williston Park)* 2006; **20**: 1053-1062; discussion 1065-1056.
9. Ruggiero SL, Dodson TB, Assael LA, Landesberg R, Marx RE, Mehrotra B. American Association of Oral and Maxillofacial Surgeons position paper on bisphosphonate-related osteonecrosis of the

- jaws--2009 update. *J Oral Maxillofac Surg* 2009; **67**: 2-12.
10. Marx RE. Pamidronate (Aredia) and zoledronate (Zometa) induced avascular necrosis of the jaws: a growing epidemic. *J Oral Maxillofac Surg* 2003; **61**: 1115-1117.
 11. Vescovi P, Nammour S. Bisphosphonate-Related Osteonecrosis of the Jaw (BRONJ) therapy. A critical review. *Minerva Stomatol* 2010; **59**: 181-203, 204-113.
 12. Vescovi P, Merigo E, Meleti M, Fornaini C, Nammour S, Manfredi M. Nd:YAG laser biostimulation of bisphosphonate-associated necrosis of the jawbone with and without surgical treatment. *Br J Oral Maxillofac Surg* 2007; **45**: 628-632.
 13. Vescovi P, Manfredi M, Merigo E, Guidotti R, Meleti M, Pedrazzi G, Fornaini C, Bonanini M, Ferri T, Nammour S. Early Surgical Laser-Assisted Management of Bisphosphonate-Related Osteonecrosis of the Jaws (BRONJ): A Retrospective Analysis of 101 Treated Sites with Long-Term Follow-Up. *Photomed Laser Surg.* 2011 Nov 4
 14. Carlson ER, Basile JD. The role of surgical resection in the management of bisphosphonate-related osteonecrosis of the jaws. *J Oral Maxillofac Surg* 2009; **67**: 85-95.
 15. Stanton DC, Balasanian E. Outcome of surgical management of bisphosphonate-related osteonecrosis of the jaws: review of 33 surgical cases. *J Oral Maxillofac Surg* 2009; **67**: 943-950.
 16. Chiu CT, Chiang WF, Chuang CY, Chang SW. Resolution of oral bisphosphonate and steroid-related osteonecrosis of the jaw--a serial case analysis. *J Oral Maxillofac Surg* 2011; **68**: 1055-1063.
 17. Vescovi P, Merigo E, Manfredi M, Meleti M, Fornaini C, Bonanini M, Rocca JP, Nammour S. Nd:YAG laser biostimulation in the treatment of bisphosphonate-associated osteonecrosis of the jaw: clinical experience in 28 cases. *Photomed Laser Surg* 2008; **26**: 37-46.
 18. Curi MM, Cossolin GS, Koga DH, Zardetto C, Christianini S, Feher O, Cardoso CL, dos Santos MO. Bisphosphonate-related osteonecrosis of the jaws--an initial case series report of treatment combining partial bone resection and autologous platelet-rich plasma. *J Oral Maxillofac Surg* 2011; **69**: 2465-2472.
 19. Yoneda T, Hagino H, Sugimoto T, Ohta H, Takahashi S, Soen S, Taguchi A, Toyosawa S, Nagata T, Urade M. Bisphosphonate-related osteonecrosis of the jaw: position paper from the Allied Task Force Committee of Japanese Society for Bone and Mineral Research, Japan Osteoporosis Society, Japanese Society of Periodontology, Japanese Society for Oral and Maxillofacial Radiology, and Japanese Society of Oral and Maxillofacial Surgeons. *J Bone Miner Metab* 2010; **28**: 365-383.
 20. Moretti F, Pelliccioni GA, Montebugnoli L, Marchetti C. A prospective clinical trial for assessing the efficacy of a minimally invasive protocol in patients with bisphosphonate-associated osteonecrosis of the jaws. *Oral Surg Oral Med Oral Pathol Oral Radiol Endod* 2011; **112**: 777-782.
 21. Blus C, Szmukler-Moncler S. Split-crest and immediate implant placement with ultrasonic bone surgery: a 3-year life-table analysis with 230 treated sites. *Clin Oral Implants Res* 2006; **17**: 700-707.
 22. Blus C, Szmukler-Moncler S, Vozza I, Rispoli L, Polastri C. Split-crest and immediate implant placement with ultrasonic bone surgery (piezosurgery): 3-year follow-up of 180 treated implant sites. *Quintessence Int* 2010; **41**: 463-469.
 23. Thacker J. An approach to the mechanism of killing of cells in suspension by ultrasound. *Biochim Biophys Acta* 1973; **304**: 240-248.
 24. Blus C, Szmukler-Moncler S. Atraumatic tooth extraction and immediate implant placement with Piezosurgery: evaluation of 40 sites after at least 1 year of loading. *Int J Periodontics Restorative Dent* 2010; **30**: 355-363.
 25. Merigo E, Manfredi M, Meleti M, Guidotti R, Ripasarti A, Zanzucchi E, D'Aleo P, Corradi D, Corcione L, Sesenna E, Ferrari S, Poli T, Bonanini M, Vescovi P. Bone necrosis of the jaws associated with bisphosphonate treatment: a report of twenty-nine cases. *Acta Biomed* 2006; **77**: 109-117.
 26. Khan N, Licata A, Rogers D. Intravenous bisphosphonate for hypercalcemia accompanying subcutaneous fat necrosis: a novel treatment approach. *Clin Pediatr (Phila)* 2001; **40**: 217-219.
 27. Blus C, Szmukler-Moncler S, Orru G, Denotti G, Piras A, Piras V. Bactericide effect of vibrating ultra-sonic (piezo-surgery) tips. An in vitro study. *Clin Oral Implants Res* 2009; **20**: 905 (abstract).
 28. Blus C, Szmukler-Moncler S, La Rosa A, Moia R. Ultra-sonic debridement. A novel approach of scar debridement. Proceedings of the 2nd Congress of the World Union Wound Healing Societies, 2004, July 8-13, Paris, France, p 184
 29. Blus C, Szmukler-Moncler S, Khoury PM, Piras V, Orrù G, Testori T. Immediate implants placed in infected and non-infected sites after atraumatic tooth extraction and placement with piezo-surgery (ultra-sonic surgery). A 5-

- year Life Table Analysis. Clin Implant Dent Rel Research, submitted.
30. Preti G, Martinasso G, Peirone B, Navone R, Manzella C, Muzio G, Russo C, Canuto RA, Schierano G. Cytokines and growth factors involved in the osseointegration of oral titanium implants positioned using piezoelectric bone surgery versus a drill technique: a pilot study in minipigs. *J Periodontol* 2007; **78**: 716-722.
 31. Sedghizadeh PP, Kumar SK, Gorur A, Schaudinn C, Shuler CF, Costerton JW. Identification of microbial biofilms in osteonecrosis of the jaws secondary to bisphosphonate therapy. *J Oral Maxillofac Surg* 2008; **66**: 767-775.
 32. Ganguli A, Steward C, Butler SL, Philips GJ, Meikle ST, Lloyd AW, Grant MH. Bacterial adhesion to bisphosphonate coated hydroxyapatite. *J Mater Sci Mater Med* 2005; **16**: 283-287.
 33. Sedghizadeh PP, Kumar SK, Gorur A, Schaudinn C, Shuler CF, Costerton JW. Microbial biofilms in osteomyelitis of the jaw and osteonecrosis of the jaw secondary to bisphosphonate therapy. *J Am Dent Assoc* 2009; **140**: 1259-1265.
 34. Bambini F., De Stefano CA, Giannotti L., Meme L., Pellecchia M. "Influence of bisfosfonates on the integration process of endosseous implants evaluated using single photon emission computerized tomography(SPECT)", *Minerva stomatologia* 2003;52:331-338.
 35. Ruggiero SL et al. "Practical Guidelines for the prevention, diagnosis, and treatment of osteonecrosis of the jaw in patients with cancer" *Journal of Oncology Practice*, vol.2,issue1,January 2006.
 36. Ruggiero SL. et al. "Osteonecrosis of the jaws associated with the use of bisphosphonates: a review of 63 cases", *J.oral Maxillofac Surg* 62:527-534, 2004.
 37. Ruggiero SL, Fantasia, Carlson Bisphosphonate-related osteonecrosis of the jaw: background and guidelines for diagnosis, staging and management. *OOO*. Vol. 102 No. 4 October 2006
 38. Ruggiero SL: "Bisphosphonate-Related Osteonecrosis of the Jaw (BRONJ): Initial Discovery and Subsequent Development" 2009 American Association of Oral and Maxillofacial Surgeons *J Oral Maxillofac Surg* 67:13-18, 2009, Suppl 1

A compact spectral camera for VIS-NIR imaging

Andrea Della Patria¹, Claudio Oleari², Fernando Fermi², Angela Piegari³, Anna Sytchkova³

¹ *National Institute of Optics (CNR - INO) U.O.S. di Lecce, Arnesano, Italy*

² *Parma University, Physics Department, Parma, Italy*

³ *ENEA – Optical Coatings Laboratory, Rome, Italy*

Abstract

This paper describes the design of a spectro-photo/radio-metric camera, that can be used in both portable and in-situ applications, whose compactness is made possible by a suitable image spectral scanning scheme based on a Linearly Variable Filter (LVF). Such filter is able to operate continuously from 400 nm to 2500 nm, allowing the hyper-spectral imaging from visible to near infrared.

In traditional scanners the whole apparatus is moved along a path as long as the scene, whereas in this instrument the camera body is still and the LVF it is the only moving part. This solution allows a compact design and an easily portable instrument.

Introduction

Many fields take advantage of multispectral and hyper-spectral imaging (e.g. art conservation, bio-imaging, remote sensing), and several techniques have been proposed over the time [1-6]. In particular, the color of objects measured by multispectral cameras and hyper-spectral scanners is lacking the limits of trichromatic cameras because it is calculated from the spectral reflectance factor; however, it must be pointed out that such types of scanners and cameras are frequently only laboratory instruments, due to their size [1].

In some of instruments the spectral attribute is implemented through a set of filters, with efforts either to find the minimum number of filters needed for the spectral reflectance factor reconstruction or to employ tunable filters. Within this context, the use of Linearly Variable Filters (LVF) has been considered in publications [7-8] and patents [9-11]. Here is proposed the design of a miniaturized spectrometer for the measurement of the spectral radiance of the objects of a scene

and/or the spectral reflectance factor, combining measurement accuracy with small dimensions of the whole instrument. The reproduction of the image of the observed scene will result from the measurement of the spectral reflectance factor.

The camera

The spectro-photo/radio-metric camera can operate either linked to a laptop or in a standalone mode, because is equipped with a rechargeable battery that supplies a CPU and a physical memory used for the scanning process for the acquisition. The miniaturization is made possible by a suitable image spectral scanning based on a LVF.

The LVF is an interference narrow-band transmission filter, obtained by a thin-film wedge shaped coating with wavelength selective transmittance along one direction. The camera body is still while the LVF translates. Its movement is supplied by a piezo-positioner stage with high accuracy and precision. The instrument layout is shown in Figure 1.

The objective lens of the camera focuses the image of a scene on a plane, named the 1st image plane.

The lens is approximately telecentric image side, so as to have rays crossing the image plane within a narrow solid angle. The LVF on the 1st image plane transmits a spectral light band centered on the wavelength λ , which is continuously variable along a direction on the filter whereas remains constant orthogonally. The wavelength is changed on the image by shifting the LVF along the line where the transmission peak wavelength changes, as in Figure 2. Image strips orthogonal to the shift direction are selected at the wavelength λ , for a particular position of the LVF. A relay lens, working with a 1:1 magnification ratio, transports the filtered images on the 2nd image plane, where are captured by an image-matrix sensor. Subsequent wavelength selections are effected through the displacement of the LVF. So, by iterating this procedure the measurement of the spectral radiance of all the image strips is fully accomplished. This method conveniently allows: a) the use of a standard relay lens; b) a simple alignment of the optical components; c) a simple arrangement of the moving LVF and of its motion supplier; d) the use of a LVF that does not affect significantly the optical aberration budget.

A piezo positioner translates the LVF along the direction of wavelength selection.

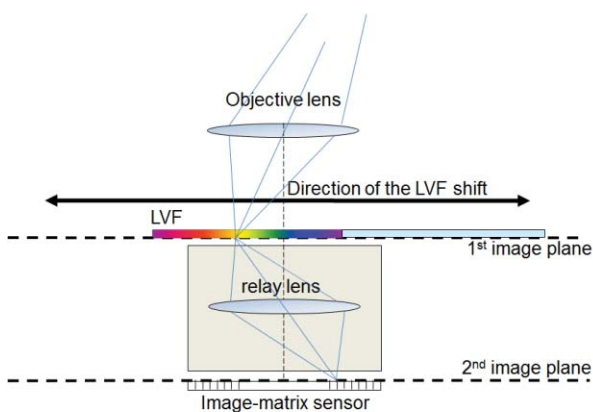


Figure 1 Cross sectional sketch of the proposed camera. Each strip of the image on the 1st image plane is filtered by the LVF. The filtered images are reproduced on the sensor by the relay lens. The whole

spectrum is reconstructed strip by strip as the LVF moves.

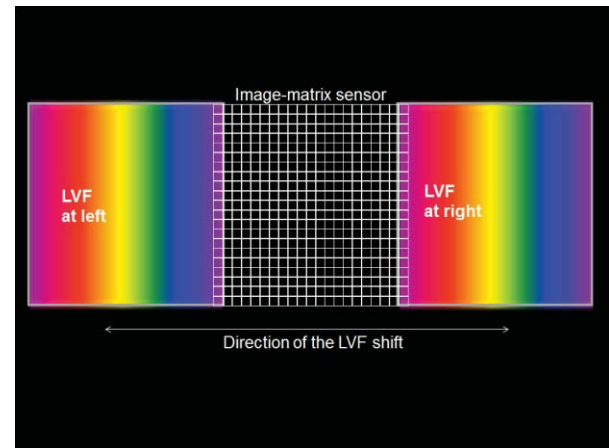


Figure 2 The image-matrix sensor and the two outermost positions of the LVF. Each column of the image sensor colliding on a LVF strip is filtered at a selected wavelength depending on the filter position.

Optical elements

The camera consists of three optical elements, namely an objective lens, a relay lens and a LVF.

Objective and relay lenses

The objective lens creates an image of a scene on the 1st image plane, where it has to provide almost uniform. This is achieved with almost parallel, to the optical axis, off-axis chief ray directions. Besides good correction of aberrations in the visible light, the lens must be well corrected for distortion (< 0.1%), to accomplish pixel correspondence on the image.

The selected objective has five elements, with two external achromatic doublets, Heliar type triplet in crown-out arrangement [2]. It is afocal in the object side, with a back focal length of 47 mm and 20° full Angular Field of View (AFOV). The latter is subtended on the 1st image plane and is approximately 10°, close to diffraction limit due to the nearly symmetric layout. The illumination reduction (relative to on-axis) at field edge is less than 1.5% and if in the case of reflectance factor measurement is unimportant, it is corrected by calibration in the case of radiance measurement.

The symmetry of the layout of the relay lens leaves unaltered the image quality at the 2nd image plane on the image sensor (Figure 3).



Figure 3 Layout of the symmetrical relay system

Linearly Variable Filter

The multi-wavelength linearly variable filter (LVF) is a narrow-band transmission filter with peak wavelength displaced over the surface of the filter itself, along one direction [12]. It is made with a variable thickness interference coating, whose spatial profile depends on the required gradient of the peak wavelength. Here the overall filter length is few millimeters, whereas the spatial gradient is of the order of $100 \div 200$ nm/mm.

It can work in the wavelength range 400-2500 nm, with transmission bandpass of nearly 20 nm. The required in-band (transmitted radiation) and out-band (rejected radiation) absolute values of transmittance should be respectively $T > 0.50$ and $T_{\text{avg}} < 10^{-3}$.

The operating wavelength range will be divided in two parts, 400-1000 nm and 1000-2500 nm, because two different matrix sensors will be necessary to cover the whole spectrum.

Two induced transmission narrow-band filters will be used in these wavelength ranges. Such filters, containing metal and dielectric materials, have a wider rejection range with respect to classical all-dielectric Fabry-Perot filters. An induced transmission filter is made of a stack of metal and dielectric layers and the reflection of the metal layer is suppressed by matching its complex refractive index with the index of surrounding media (glass, air), at a single wavelength, by adding dielectric stacks on its sides. At that wavelength, a transmission peak will appear while the out-band radiation is reflected. The metal layer must be very thin in order to avoid absorption, but a compromise on the value of its thickness is needed to ensure a high out-band rejection,

that is higher for greater thickness. The matching effect, and consequently the transmission peak, will shift to different wavelengths, as the thickness of the dielectric stacks is changed. Figure 4 reports the performance of an induced transmission filter at several transmission windows. The metal layer is silver (60-70 nm) surrounded by two stacks of dielectric materials whose thickness is spatially varied to obtain the reported displacement of the peak wavelength from 450 nm to 2500 nm, over a predefined substrate dimension.

Following the profile of Figure 4, a 21-layer variable filter has been manufactured by radiofrequency sputtering using silicon oxide and tantalum oxide as dielectrics.

Wedge thickness profile has been achieved by moving a properly designed mask inside the vacuum chamber during the thin film deposition [13-14]. The maximum obtained peak transmittance is about 60% and the width of the bandpass is narrower than 20 nm. Induced transmission filters give bandwidths broader than all-dielectric counterparts; moreover, their performance is highly sensitive to variations of the metal thickness. However for such a type of coating, the total number of layers remains quite low and makes the fabrication of the variable filter easier. Although the LVF performance was calculated with incoming plane wavefronts, the beam convergence of 10° cone semi-angle was demonstrated not to introduce significant spectral effects. For this instrument the cone semi-angle is approximately 5.5° , so no significant reduction of the filter transmission is expected.

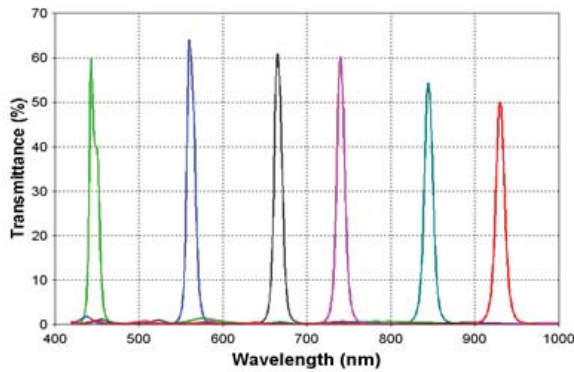


Figure 4 Calculated transmittance of a variable metal-dielectric filter with 21 layers in the visible

Figure 5 is a sketch of the spectral transmittance of the LVF for a slit as wide as the pixel size. The 20 nm bandpass is very frequent in industrial spectrophotometers; however, spectral resolution can be improved by a deconvolution technique [15], specific for colorimetric analysis.

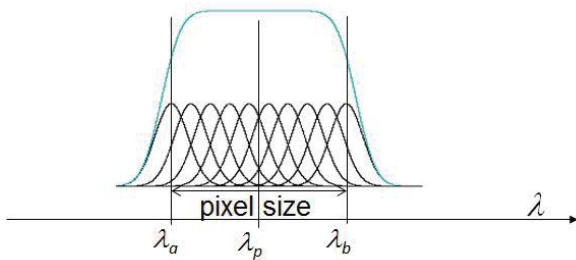


Figure 5 Spectral transmittance of the LVF associated to a slit as large as a pixel. λ_p is the center wavelength, λ_a and λ_b the boundary wavelengths.

Figure 6 shows a view of the LVF as designed for this instrument, with an uncoated area useful for alignment procedures.

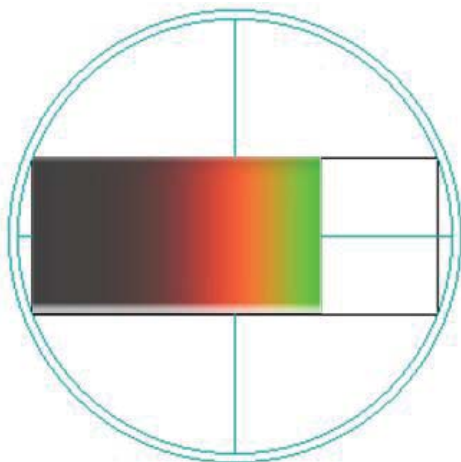


Figure 6 The LVF ($8.8 \times 6.6 \text{ mm}^2$) is deposited on a 1 inch disk of optical glass. A central strip larger than 8.8 mm, is partly covered with the filter and partly

uncovered for framing and for correct setting of the exposure time.

Image reconstruction

From Figure 2 it can be seen that the LVF travels step by step from left to right, while filtering the light that activates the pixels of each matrix column at the wavelength associated with the superimposed column of the filter itself. Any captured image is constituted by pixel columns, filtered at different wavelengths, and is the record of the corresponding raw radiances at the same wavelengths. The collection of all the captured images contains the raw radiance spectra of all the pixels of the scene. The raw radiance spectrum of any pixel is obtained by an ordered selection of the matrix elements of the captured images. These raw spectral data, decreased by the dark current and multiplied by a proper calibration factor, are transformed into correct radiance units.

The radiance spectra relative to a standard reference white surface covering all the scene, measured in the same geometry of vision and illumination of the measured image, allow the measurement of the spectral reflectance factor of all the pixels of the scene.

The wavelength gradient of the LVF and the number of captured images defines the scanning step of the spectra. The scanning step and the bandpass function of the LVF define the quality of the spectral output. The trichromatic image of the scene is obtained from these spectral data by a colorimetric computation for each pixel.

Camera

The use of interline transfer CCD cameras avoids the use of mechanical shutters. With these sensors, each column of pixels is associated with an adjacent column of equal elements. After the exposition process, the charges accumulated in the photosensitive elements are instantly transferred into the vertical registers (before being transferred, line by line, in the horizontal register to read

the output signal of the CCD). The shift of the charges from the pixels to the vertical register reading takes about 1 μ s.

This prototype comes with a 2/3" image sensor. The matrix is 1600x1200 (1.9 MP). The pixels are square with a size of 5.5 μ m.

Conclusions

All parts of the proposed spectrophotometric camera have been optimized [16]. Currently, the construction of a first prototype is in progress with all the optical parts moving for an optimal optical arrangement. This compact instrument, even if designed for application to cultural heritage, will be suitable for all applications in which the hyper-spectral imaging is useful. Furthermore, compactness makes it suitable for remote sensing and in-situ measurements.

References

- [1] G. Antonioli, F. Fermi, C. Oleari, R. Reverberi. "Spectro-photometric Scanner for Imaging of Paintings and Other Works of Art", *CGIV 2004: The Second European Conference on Colour Graphics, Imaging and Vision*, Aachen, pg 219-224 (2004).
- [2] Saunders, D., Cupitt, J. "Image processing at the National Gallery: The VASARI Project", *National Gallery technical bulletin*, 1 4:72 (1993)
- [3] Ribés A., Brettel H., Schmitt F., Liang H., Cupitt J., Saunders D. "Color and Spectral Imaging with the Crisatel Acquisition System", proceedings of *PICS'03 The Digital Photography Conference*, pp. 215-219. Rochester, USA (2003)
- [4] F. H. Imai, R. S. Berns. "Spectral estimation of artist oil paints using multi-filter trichromatic imaging". *9th Congress of the International Color Association*, Proc. of SPIE Vol. 4421 pg. 50-53 (2002)
- [5] C. Fischer, J. Kakoulli. "Multispectral and hyperspectral imaging technologies in conservation: current research and potential

applications". *Reviews in Conservation*, 7, pg 3-16 (2006).

[6] Alexander F.H. Goetz. "Measuring the Earth from Above: 30 years (and Counting) of Hyperspectral Imaging". *photonics.com*: 06/01/2011.

<http://www.photonics.com/Article.aspx?AID=47298>

[7] M. Hauta-Kasari, K. Miyazawa, S. Toyooka, J. Parkkinen, and T. Jaaskelainen. "Spectral Vision System based on Rewritable Broad Band Color Filters", proceedings, *International Symposium on Multispectral Imaging and Color Reproduction for Digital Archives*, MICR'99, Chiba, Japan, October 21-22, pg 155-158 (1999)

[8] K. Miyazawa, M. Hauta-Kasari, and S. Toyooka. "Rewritable Broadband Color Filters for Spectral Image Analysis", *Optical Review*, Vol. 8, No. 2, March / April 2001, pp. 112-119

[9] Chengye Mao, Slidell, L. "Focal plane scanner with reciprocating spatial window", United States Patent number 6,166,373, Dec. 26, 2000.

[10] Lewis Neil E, Haber Kenneth S. "Hybrid imaging spectrometer", World Intellectual Property Organization, Pub. Number WO 02/077587 A2, 03.10.202. / United States Patent number US 2008/0130001 A1, Jun. 5, 2008.

[11] W. J. Smith. "Modern Lens Design: a resource manual", (McGraw-Hill, 1992)

[12] D. Morelli. "Interference Filter Handbook", (OCLI-JDSU, California, 2006), pg 195-200.

[13] A. Piegari, A. Krasilnikova Sytchkova, J. Bulir. "Variable transmission filters for spectrometry", from Space 2. Fabrication process. *Appl. Opt.* Vol 47, C151-C156, pg 13 (2008).

[14] A. Krasilnikova, A. Piegari, M. Dami, L. Abel, F. Lemarquis, M. Lequime. "Spatially resolved spectroscopy for non-uniform thin film coatings: comparison of two dedicated set-up", *SPIE Proc. Optical Fabrication, Testing and Metrology*, Vol 5965, pg 573-580 (2005).

[15] C. Oleari. *“Deconvolution of Spectral Data for Colorimetry by Second Order Local Power Expansion”*, *Color Research and Application*, 35, pg 334-342 (2010).

[16] A. Della Patria., F. Fermi, C. Oleari, A. Piegari, A. Sytchkova. *“A portable Spectro-photo/radio-metric Camera with Spatial Filtering for VIS-NIR Imaging”*, *19th CIC, IS&T: Society for Imaging Science and Technology*. San Jose California Nov. 7-11, 2011. Springfield USA, 285-289, 2011. HSI2012 55

Alternative acceptor materials for organic photovoltaic cells

Troisi L.,¹ Bona F.,¹ Citti C.,¹ Giancane G.,² Granito C.,¹ Liu T.,³ Troisi A.³

¹ *Dipartimento di Scienze e Tecnologie Biologiche ed Ambientali, Organic Chemistry Laboratory, University of Salento, via Monteroni, 73100 Lecce, Italy. Corresponding author: luigino.troisi@unisalento.it*

² *Dipartimento di Beni Culturali, Università del Salento, via Dalmazio Birago, 73100 Lecce, Italy.*

³ *Department of Chemistry and Centre for Scientific Computing University of Warwick, Coventry CV4 7AL, UK.*

Abstract

Synthesis and spectroscopic characterization of perylene derivatives (perylene monoimides and diimides) are reported. The aim of the present work is to investigate the synthesis of these compounds in detail in order to highlight the crucial factors for obtaining a specific class of molecules. The final compounds of the synthetic pathway would be able to mimic the peculiar properties of fullerene derivatives, up to now the best candidates as accepting materials.

Introduction

Organic photovoltaics (OPV) is a young technology that was developed in recent decades[1] and has encouraged scientists to continue their efforts towards new classes of solar cells. Up to now fullerenes have been the best candidate as accepting materials because of their very low lying excited states of their anion[2].

In this work we have designed and synthesized new accepting molecules that mimic the properties of fullerenes and can therefore substitute them in the development of alternative acceptors to be applied in new OPV cells.

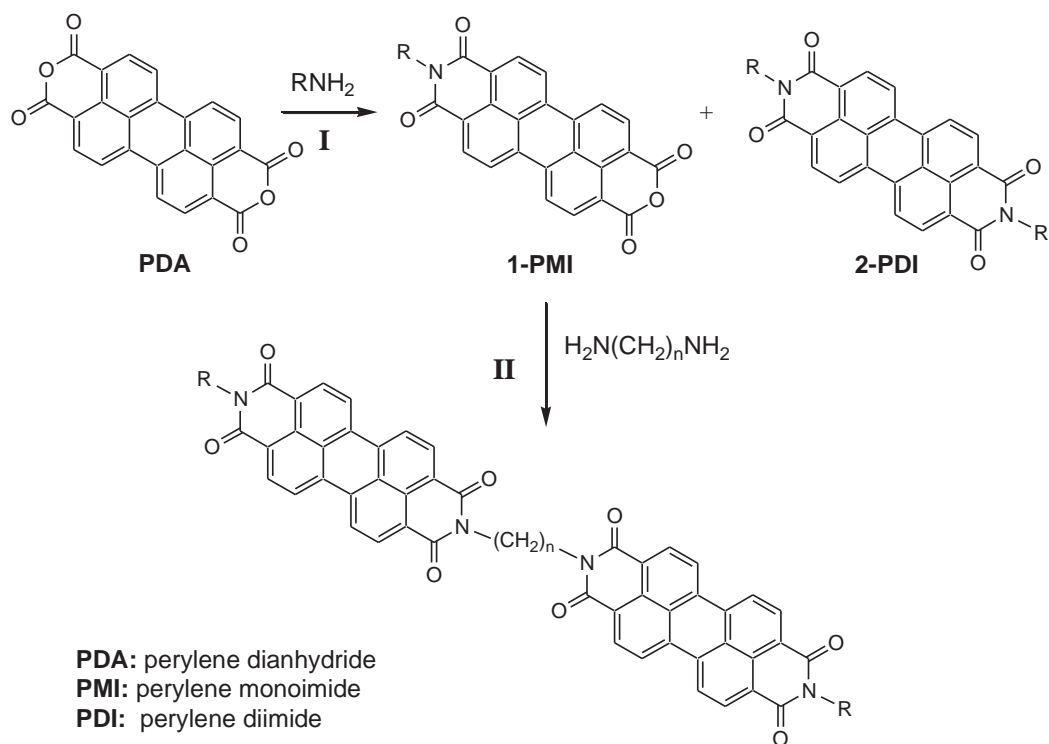
The aim of the present study was to build a class of molecules with a “designed” degeneracy of the LUMO levels. A strategy to generate electron acceptors with quasi degenerate LUMOs may also be to connect identical conjugated electron acceptors

through non-conjugated alkyl links. Changing the acceptor and the link it is possible to modulate the energy levels and their separation.

The new family of proposed acceptors is both easily accessible synthetically and virtually unrelated to any of the current attempts of matching the fullerene properties with different chemistries.

To realize our idea we have limited the synthetic work to a single class of compounds which includes one or more sp^3 carbon or nitrogen-based molecules coordinated to two identical acceptors (P) with the general formula $(CH_2)_n P_2$.

A possible approach to the realization of this synthesis involves perylene as the central core of the acceptor. Scheme 1 illustrates the general synthetic pathway we followed.



Scheme 1

The perylene derivatives are good fullerene mimic candidates showing the following strategic properties:

- large molar adsorption coefficients;
- good electron accepting properties[3];
- possible generation of highly conducting direction along the π - π stacking axis[4];
- robust, thermal stable, inexpensive[5]

Materials and methods

All used reagents were of commercial grade and used without any further purification.

^1H and the ^{13}C NMR spectra were recorded with a Bruker Avance 400 apparatus (400.13 and 100.62 MHz, for ^1H and ^{13}C , respectively) with CDCl_3 as solvent and TMS as internal standard ($\delta = 7.26$ ppm for ^1H spectra; $\delta = 77.0$ ppm for ^{13}C spectra). FT-IR spectra were acquired with a Perkin Elmer Spectrum On spectrophotometer and the analysis were performed on solid samples. UV-Vis spectra

were recorded with an Agilent Cary 5000 spectrophotometer using CH_2Cl_2 as solvent. Fluorescence emission spectra were acquired with a Perkin Elmer LS55 fluorimeter using CH_2Cl_2 as solvent and a polychromatic incident beam.

N-alkyl-perylene-3,4,9,10-tetracarboxylic monoimide (**1-PMI**) and *N,N'*-dialkyl-perylene-3,4,9,10-tetracarboxylic diimide (**2-PDI**) were synthesized following Dincalp's et al. methodology[6], but slightly modified. In a 50 ml flask primary amine (10.0 mmol), $\text{Zn}(\text{AcO})_2$ (1.0 mmol), perylene-3,4,9,10-tetracarboxylic dianhydride (1.0 mmol) and quinoline (8 ml) were poured and stirred at reflux temperature of 210°C over night under a nitrogen atmosphere. The reaction mixture was poured into 160 ml of methanol/10% hydrochloric acid solution (V/V = 2/1) under stirring. The solid precipitate was filtered off and stirred in 40 ml of cold Na_2CO_3 solution (10%) for 2 hours. The precipitate was filtered off again and washed several times with water until the solid was colorless. The crude product was purified by silica gel

column chromatography using methylene chloride as eluent.

Results and Discussion

The stage I (Scheme 1) was carried out according to a modified version of the methodology reported by Dincalp et al[6]. *N*-Alkyl-perylene-3,4,9,10-tetracarboxylic monoimide (**1-PMI**) and *N,N'*-dialkyl-perylene-3,4,9,10-tetracarboxylic diimide (**2-PDI**) were synthesized from perylene 3,4,9,10-tetracarboxylic dianhydride (**PDA**) by reaction with a primary amine in a Zn(OAc)₂ and quinoline (8 mL) solution. The obtained results are reported in Table 1.

Table 1: synthesis of *N*-alkyl-perylene-3,4:9,10-tetracarboxylic monoimide (**1-PMI**) and *N,N'*-bis-alkyl-perylene-3,4:9,10-tetracarboxylic diimide (**2-PDI**).

Entry	R	Products distribution (%) ^a		Total Yield (%) ^a
		PMI	PDI	
1		1a (27)	2a (73)	22
2		1b (33)	2b (67)	9
3		1c (36)	2c (64)	14

^aProducts distribution and total yield calculated on isolated products.

The low PMI yield recovered with this synthetic protocol did not allow us to perform the stage II for preparing the goal compounds (CH₂)_nP₂ (Scheme 1). Zafer et al.[7] reported the preparation of PMI through the PDI hydrolysis with KOH in *tert*-butanol. The hydrolysis of **2a**, using Zafer's

conditions, gave a mixture of products whose separation was difficult. Therefore, we thought to modify Dincalp's methodology slightly changing the reagents stoichiometric ratios. In detail, the reagents used were: primary amine (0.2 mmol), Zn(AcO)₂ (1.0 mmol), perylene-3,4,9,10-tetracarboxylic dianhydride (1.0 mmol), quinoline (20 ml). The reaction mixture was stirred at reflux temperature of 210°C for 15h under a nitrogen atmosphere. The 90% of quinoline was removed by distillation under vacuum and the remained solution was treated with 20 ml of methanol/10% hydrochloric acid solution (V/V = 2/1) under stirring. The solid precipitate was washed with 5 ml of cold Na₂CO₃ solution (10%) and several time with water until the solid was colorless. The crude product was purified by silica gel column chromatography using methylene chloride as eluent. The pure PMI and the pure PDI were isolated with a total yield of 68% in a ratio of PMI/PDI = 62/38.

The pure products were characterized by ¹H, ¹³C NMR and FT-IR spectroscopy. Moreover, UV-Vis absorption and Fluorescence emission measurements were performed (Figures 1 and 2).

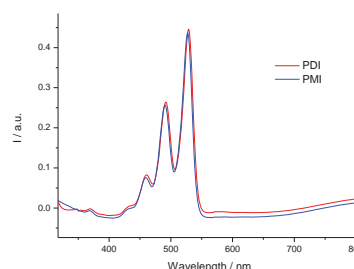


Figure 1. PDI (red) and PMI (blue) UV-Vis absorption spectra at the concentration of 12.5 μM.

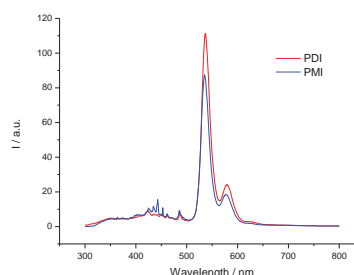


Figure 2. PDI (red) and PMI (blue) fluorescence emission spectra at the concentration of 0.1 μM.

The Fluorescence spectra showed that PDI has a fluorescence quantum yield much higher than PMI.

The bigger fluorescence of PDI due to the presence of two aromatic units compared to the PMI compound give a further contribution to their characterization.

The following step will be the reaction between **1a-PMI** and $\text{H}_2\text{N}(\text{CH}_2)_2\text{NH}_2$ (1,2-ethanediamine) in NMP (N-methylpyrrolidinone) in order to obtain the final compound of the general formula $(\text{CH}_2)_2\text{P}_2$.

Conclusions

An efficient synthesis for PMI has been developed giving an alternative pathway to the known methodology and allowing good yields of the desired product.

The final compound should be tested in combination with a donor in organic solar cells.

Once its activity is evaluated the class of compounds can be extended to many other molecules of similar typology to be applied in organic photovoltaic field.

References

- [1] Tang, C. W. (Eastman Kodak Co., USA). Application: US1980-119328.
- [2] Closs, G.; Miller, J.; *Science* (1988), 240, 440-447.
- [3] Neuteboom, E. E.; Meskers, S. C. J.; Van Hal, P. A.; Van Duren, J. K. J.; Meijer, E. W.; Janssen, R. A. J.; Dupin, H.; Pourtois, G.; Cornil, J.; Lazzaroni, R.; Bredas, J. L.; Beljonne, D.; *J. Am. Chem. Soc.* (2003), 125, 8625.
- [4] Boom, T.; Hayes, R. T.; Zhao, Y.; Bushard, P. J.; Weiss, E. A.; Wasielewski, M. R.; *J. Am. Chem. Soc.* (2002), 124, 9582.
- [5] Liu, S. G.; Sui, G.; Cormier, R. A.; Leblanc, R. M.; Gregg, B. A.; *J. Phys. Chem. B*; (2002), 106, 1307.
- [6] Dincalp, H.; Avcibasi, N.; Icli, S.; *J. Photoch. Photobio. A* (2007), 185, 1-12.
- [7] Zafer, C.; kus, M.; Turkmen, G.; Dincalp; Demic, S.; Kuban, B.; Teoman, Y.; Icli, S.; *Sol. Energ. Mat. Sol. C.* (2007), 91, 427-431.

Production and Extraction of Protons by Solid Hydrogenated Targets via UV Laser Ablation

D. Delle Side^{1,2}, L. Velardi^{1,2}, M. De Marco¹, V. Nassisi^{1,2}

¹ LEAS, Dipartimento di Matematica e Fisica, Università del Salento

² INFN Section of Lecce, Lecce, Italy

domenico.delleside@le.infn.it

Abstract

In this work we present the preliminary investigations about the production of proton beams by pulsed laser ablation of solid disks produced by compressed Titanium dihydride powder. The laser we used was an excimer KrF, operating at low intensity and ns pulse duration. The ion emission was analyzed by the time-of-flight technique using a Faraday cup as ion collector. We performed studies on the produced plasma for different laser fluence values and accelerating voltage. In free expansion mode we obtained protons and titanium ions having kinetic energy of some hundred of eV; by applying a post-accelerating voltage we obtained beams up to 15 keV.

Introduction

In the last years, new techniques to produce proton beams make use of the interaction between high power femtosecond laser pulses and thin metallic foils[1]. In contrast with other techniques, these give the advantage of obtaining highly collimated and energetic protons beams from the rear of the target surface, but require laser systems that, at the time of writing, aren't easy to setup. Depending on the laser parameters, two mechanisms seems to be responsible of this behavior: target normal sheath acceleration (TNSA)[2] and radiation pressure acceleration (RPA)[3]. Despite of the high quality beams obtained through TNSA and RPA systems, older and well known techniques, such as pulsed laser ablation (PLA), still play a fundamental role for applications, since the

former have extremely high total costs of ownership.

It is widely known that the use of the PLA technique allows to easily obtain ions from solid targets, whose energy can be easily increased by applying post acceleration[4, 5]. Today it is possible to easily arrange laser beams at intensities of the order of $10^8 - 10^{10} \text{ W cm}^{-2}$ and ns pulse duration that, interacting with solid matter in vacuum, produces hot plasmas[6] at high temperature and densities, of the order of tens of eV and 10^{17} electrons per cm^3 [7] respectively. Thermal interactions, adiabatic expansion in vacuum and Coulomb interactions are responsible for the primary ions acceleration in plasma. By applying an extraction potential, it is possible to extract specific charged particles. This idea can be applied to plasmas of moderate density owing to their low electric conductivity. The percentage of ionized

material obtained in laser ion sources (LIS) is not very high, with respect to the total ablated material, but sufficient to get ion beams of high intensity.

Nowadays, ion beams of moderate energy have a wide range of applications, from scientific to industrial ones. In this work, we present the preliminary results of a LIS performed for ions acceleration. The resulting protons beams could be utilized in various fields, for example as injector source for hadrontherapy applications [8].

Bearing in mind these considerations, we developed a simple but powerful ion source. In our homemade device we used an excimer laser to get PLA from compressed disks of TiH₂ powder and a vacuum chamber in which we generated plasma and studied the inherent processes. By using a suitable Faraday cup, mounted in front of target, we characterized the collected beams.

Materials and methods

We used a Compex 205 KrF excimer laser operating at $\lambda = 248$ nm, $\tau = 23$ ns and maximum intensity of 600 mJ. Using a 15 cm focal distance lens, the laser beam has been focused on the target in a circular spot with average area of 0.05 mm², obtaining a power irradiance of the order of 10⁸ W cm⁻².

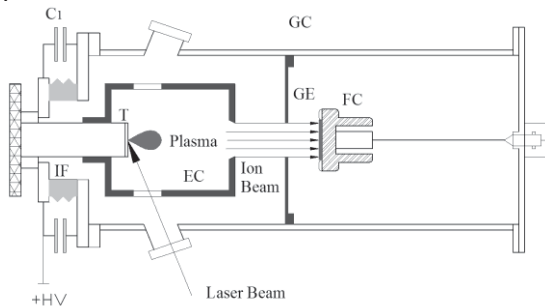


Figure 1: Sketch of the experimental setup

The vacuum compartment (10⁻⁶ mbar) consists of a plasma generation and acceleration chamber (GC) and a removable expansion chamber (EC), which allows an initial free expansion of the plasma before the ion extraction gap, as shown in Fig. 1. The target support (T) was

mounted on the GC by an insulating flange (IF) and kept at a high positive voltage, up to +15 kV in DC mode. Four 1 nF capacitors were connected between the T and the GC to stabilize the accelerating voltage during the fast ions extraction phase. The EC is an almost hermetic cylinder of a length (21 cm) sufficient to let the plasma expand freely and decrease its density. The EC was indispensable to avoid arcs versus ground. Moreover, the EC has an extremity (the one opposite to the target holder) drilled with a 1.5 cm diameter hole, necessary for the ions extraction from the plasma plume.

A grounded electrode (GE), placed in front of the EC at a distance of 3 cm, allows to generate an intense electric field. At the right end of the apparatus, there is a Faraday cup (FC, with a diameter of 7.7 cm) in order to collect and record the ion beams signals by a LeCroy WaveSurfer 422 200 MHz digital oscilloscope, connected to the FC through a 50 Ω characteristic impedance cable. The total fly length available for ions, from the target surface to the FC, is of 28.0 cm (21 cm of free expansion inside EC + 3 cm of acceleration between EC and GE + 4 cm between GE and FC).

The targets used in this work were solid disks obtained by compression of TiH₂ powder. The compression was made at a pressure of 10⁴ kg cm⁻² for 30 minutes. The choice of this particular type of target is justified from the fact that generally hydrogenated materials are good sources of protons and heavy ions [9, 10]; moreover, these powders are relatively cheap and widely available on the international market. Additionally, they could also have a high level of purity, that in our case is reported to be of 99 %.

Results

We irradiated the target with different laser fluence values (respectively 2, 4, 8 and 16 J cm⁻²) and for different accelerating voltages, ranging from 0 V (free expansion) up to +15 kV in steps of 5 kV. The ion time of flight (TOF) signals collected by the FC and

processed by the oscilloscope were analyzed by our team.

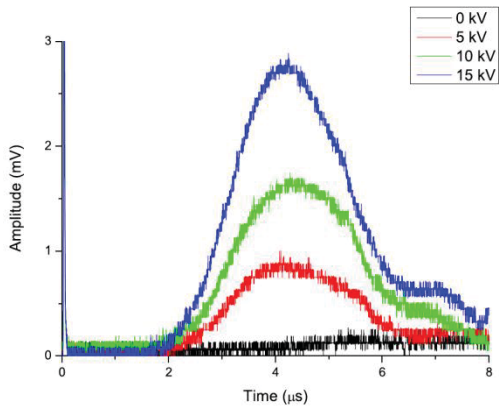


Figure 2: Detail of protons TOF signals at the fluence of 2 J/cm^2 , for different extraction voltages

In the free expansion case, the ions of the plasma plume were accelerated by different processes and the most important are: thermal interactions, photoionization, inverse bremsstrahlung and Coulomb interactions between plasma components. We obtained well defined and separate peaks for protons (Fig. 2) and Ti plasma (a convolution of Ti^{n+} , H^+ and TiH^{n+} , shown in Fig. 3). Applying high positive voltages to the target holder T, these peaks increase in amplitude, denoting a better charge extraction. Protons are faster than any other plasma component since they have a smaller mass.

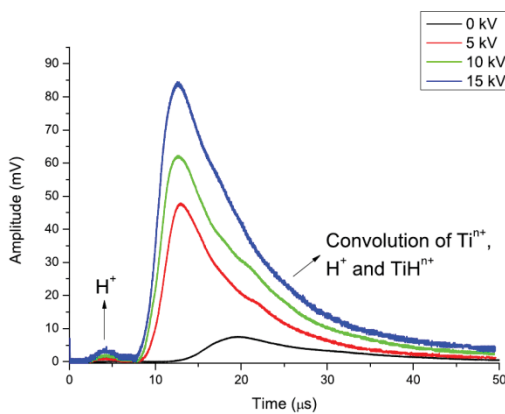


Figure 3: TOF signals at the fluence of 2 J/cm^2 , for different extraction voltages

By TOF analysis, we were able to compute the average kinetic energy both for protons

and Ti ions in free expansion. The results are presented in Fig. 4, where the curves are shown in logarithmic scale.

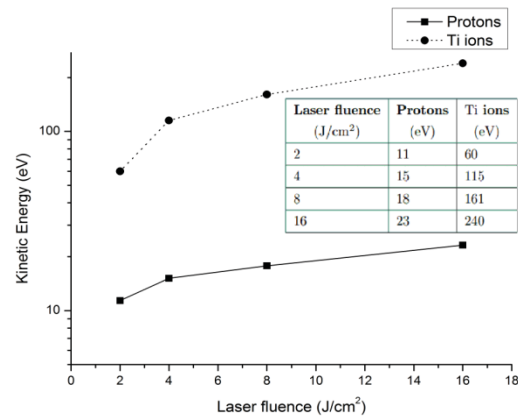


Figure 4: Average protons and titanium ions kinetic energy (in logarithmic scale) as a function of the laser fluence

For what concerns the extracted charge, Fig. 5, we obtained values between 2 and 330 nC per laser shot, depending on the laser fluence and on the applied extracting voltage. Sensibly lower are the results for the charge of protons, Fig. 6. In Table 1 it is shown the number of extracted protons per pulse, depending on the laser fluence and on the extraction voltage.

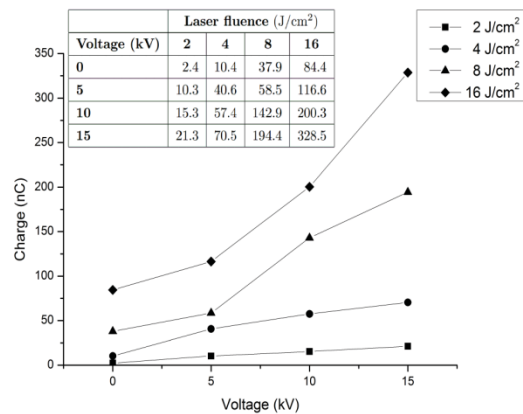


Figure 5: Total extracted charge as a function of the accelerating voltage for different values of the laser fluence

kV	Laser fluence (J/cm ²)			
	2	4	8	16
0	8.4E+07	1.5E+08	4.5E+08	1.9E+09
5	3.4E+08	1.7E+09	2.9E+09	1.0E+10
10	6.4E+08	3.8E+09	5.2E+09	1.5E+10
15	9.0E+08	4.4E+09	7.5E+09	2.6E+10

Table 1: Number of extracted protons per pulse, depending on the laser fluence and on the extraction voltage

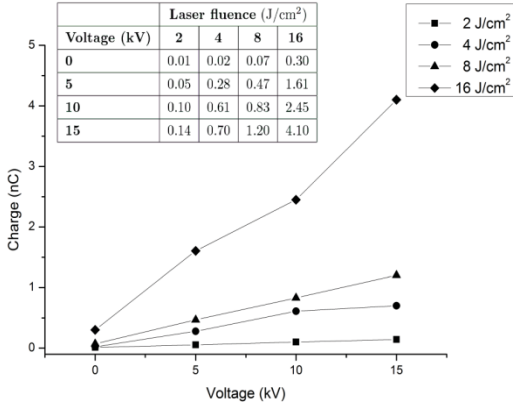


Figure 6: Protons extracted charge as a function of the accelerating voltage for different values of the laser fluence

Looking at Fig. 3, for each value of extraction voltage it is possible to observe the occurrence of plasma peaks. All these slower peaks are the result of the convolution of different charge states of Ti ions present in the plasma plume (in our case, the principal charge state are 1+ [11, 12]) and we suppose also the presence of other components. In fact we expected that the extracted charge for protons and Ti ions should be sharply different from what it was obtained, according to the stoichiometry of the TiH₂ compound. For example, in free expansion at a laser fluence of 2 J cm⁻², the total charge obtained for protons was 0.01 nC, while for Ti plasma was 2.32 nC. This behavior is confirmed also under the effect of accelerating voltages, so we suppose that, after the laser interaction with the target surface, clusters [13], protons and Tiⁿ⁺ ions are induced in the generated plasma. In our case, these clusters could be TiHⁿ⁺ and, due to the

limitations of our diagnostic system, we couldn't appreciate any difference with respect Tiⁿ⁺ ions.

Conclusions

From this preliminary work, it is clear that TiH₂ solid disks are a promising proton source via excimer laser ablation. Accordingly, the use of these targets is very interesting not only using infrared PLA, as already shown in literature [9, 10], but also with the UV one. The study of the TOF signals collected by FC shows that it is possible to increase the proton extraction both increasing the laser fluence and the extraction voltage; but it reveals also a strange behavior for what concerns the extracted charge, if considered with respect to the target stoichiometry. We found a reasonable hypothesis to explain this, but the diagnostics used was not suitable for a proof of its correctness. Nevertheless, we obtained proton bunches with fluxes up to 10¹⁰/pulse which represent a good result [9]. Further work will deserve more attention to the questions still open and the use of mass spectrometry could shed light on them.

References

- [1] Engelich M. et al, Phys. Rev. Lett. 89, 2002, p. 085002.
- [2] Wilks S. C. et al, Phys. Plasmas, 8, 2001, p. 542. [3] Liseykina T. V. et al, Plasma Phys. Control. Fusion, 50 124033 (2008).
- [3] Luches A. et al, Nucl. Instrum. Methods Phys. Res. A, 322, 1992, p. 166.
- [4] Nassisi V. and Pedone V., Rev. Sci. Instrum., 74, 2003, p. 68.
- [5] Belloni F. et al, Rev. Sci. Instrum., 75, 2004, p. 4763.

- [6] Bieleutgeb K. and Proyer S., Appl. Surf. Sci., 110, 1997, p. 331-334.
- [7] Bulanov S. and Khoroshkov V., Plasma Phys. Rep., 28, 2002, p. 453-456.
- [8] Torrisi L. et al, Laser and Particle Beams 29, 210, p. 29-37.
- [9] Sekine M. et al, Rev. Sci. Instrum., 83, 2012, 02B318.
- [10] Velardi L. et al, Rev. Sci. Instrum., 83, 2012, 02B717.
- [11] Belloni F. et al, Rev. Sci. Instrum., 77, 2006, 03B301.
- [12] Proyer S. et al, Physica C 257, 1996, p. 1-15.

Chemical and physical modifications of polyethylene containing nanostructures

A.M. Visco¹, V. Brancato¹, P. Primerano¹, M.F. Milazzo¹,
M. Cutroneo², C. Scolaro², F. Caridi² and L. Torrisi²

¹University of Messina , Dept. of Electronic Engineering, Industrial Chemistry and Engineering, C/da di Dio, vill. S. Agata, 98166 Messina, Italy

²University of Messina, Department of Physics, V.le D'Alcontres 31, 98166 S. Agata, Messina, Italy

Abstract

The polyethylene is an interesting polymer with a good mechanical strength, ductility, biocompatibility and chemical inertia. It finds several applications in many fields, such as chemistry, engineering, bio-medicine and micro-electronics.

The polyethylene chemical and physical properties can be modified embedding different nanostructures in its bulk. Carbon nanotubes, metallic oxides, coloured pigments and other species can be inserted at different concentrations in the polymer material during the preparation phase of thin films and sheets.

Mechanical, optical, thermal and chemical properties can be modified significantly depending on the filler concentration. The absorption coefficient at different radiations can be controlled by the amount of doping structure. In the visible region, for example, the high transparency of pure polyethylene can be strongly reduced by low concentrations of carbon nanotubes.

The colour, the mechanical resistance, the wet ability of the polyethylene and other parameters can be changed by the doping species in order to prepare special devices useful for many applications.

Introduction

Academic and industrial researches are interested in the development of multifunctional materials. In the last decades, great attention was directed to the preparation of advanced composites with suitable synthetic polymers and fillers, with the purpose to obtain the best physical and mechanical features.

For example, the use of filler such as the carbon nanotubes (CNTs) in a polymeric matrix has attracted great attention due to

their highly interesting properties such as the mechanical or electrical ones [1]. They are widely used in the manufacturing of advanced nanocomposites employed in special applications, from microelectronic to aerospace fields. So, in order to improve the mechanical properties of the polymeric matrix, it is necessary a good dispersion of the CNTs in the matrix as well as a strong interaction among the two components [2]. By this way, the matrix can be well bonded to the filler that controls the resulting mechanical strength of all the nanocomposite.

The modification of some physical properties, such as thermal behavior, optical properties (absorption power of laser light), electrical conductivity and thermal stability, is another interesting aspect of the addition of a filler in a matrix. For example, the use of fillers or pigments can be useful in the plastic welding or to make the polymers (generally high insulating materials) electric conductor [3].

The traditional welding of plastic can be made by thermal contact of two counterparts of the same polymeric material; this anyway, is not a thorough method that induces the loss of the starting geometry of the components.

While, laser welding is an accurate technique that permits the retention of the initial geometry of the plastic components that must be jointed. It is well known that a flexible and multipurpose material, such as polyethylene, is an insulating plastic. It has high transparence toward the laser light and a melting temperature of about 130°C. This last property inhibits its use in special applications at high temperatures and pressures [4].

In this paper we studied an high molecular weight polyethylene (the UHMWPE) mixed with CNTs, iron oxide particles and glass containing a pigment, the methylene blue, with the aim to investigate the mechanical and physical changes induced by the presence of different amounts and type of the colored fillers. Several mechanical and physical test were carried out on UHMWPE pure and embedded with the colored fillers at different load (within the range 0.1 wt%-10 wt%).

In particular, we observed changes of both surface and bulk properties, described in the following.

Materials and methods

The polymeric matrix was the Ultra High Molecular Weight Polyethylene, **UHMWPE**, Ticona, GUR 1020, $M_w \approx 3 \times 10^6$ g/mol and average size of particle powder = 150 micron. The fillers were: multi wall carbon nanotubes (**CNT**) obtained by Chemical Vapor Deposition technique have typical outer diameter d_n of CNTs is of 10 nm and length l_n of 10 μ m. The

aspect ratio (l_n/d_n) is of 1000 and the purity >95% [7]. Iron oxide (**Fe₂O₃**), supplied by Across Organics with a purity level of 99.999%, particle size of ten nanometer order. A glass matrix of calcium silicate at high porosity (particle size < 75 μ m and surface area of 70 \div 100 m²/g) was employed to stabilize and retain an organic pigment, the methylene blue hydrate (**BM**), Fluka.

The composites were made by mixing in ethanol the UHMWPE with fillers into an ultrasonic bath for two hours and then heating at 80°C the mix under magnetic stirring to evaporate the solvent. The composites were moulded in a hot press at 200°C/20 min, P=20MPa , obtaining sheets of 60mm \times 60mm and 1mm of thickness colored as blue, black and red, with BM, CNTs and Fe₂O₃ , respectively.

SHORE D hardness mechanical tests were performed by means of a PCE-HT 210, according to the ASTM D 2240 international protocol. The resolution is of 0,1 degrees of hardness and precision of ± 1 degrees, in scale range from 0 to 100.

Contact angle(θ) measurements were carried out by a micro-syringe that deposited a 1 μ l drop of pure distilled water, at 20°C, on the polymer surfaces [5] .

Tensile stresses were applied to the dog bone samples, cutted by a Ray Ran cutting machine (ASTM D638 M3, geometry: 60 mm x 2.5 mm and 1 mm of thickness) by an universal testing machine LLOYD LR 10K and crosshead speed=10 mm. Generally, 10 specimens were tested in order to give the average value.

The melting temperature was determined by a Differential Scanning Calorimeter (Q100 TA Instruments) from 25 °C up to + 180 °C, with a heating rate of 10°C/min.

The Absorption Percentage of the laser light (Optical Spectroscopy) were carried out on polymeric sheets 90 μ m thickness at 240nm, 600 nm and 1080 nm of wavelengths. The absorption percentage was calculated by the following formula:

$$A = 100 - T \quad (1)$$

where A = absorption percentage, $T = I_T/I_0$ transmittance percentage, where I_0 = incident laser intensity and I_T = transmitted laser intensity.

The electrical conductivity, σ (S/cm), was determined as $1/\rho$ (electrical resistivity, Ω cm). The electrical measurements were performed using a HP3457a multimeter and a voltage supply, at temperature within the range of 350-425 K (four probe method) on samples cylindrically shaped (diameter=12 mm, high of 1 mm, gold layer coated to ensure good contact with the electrodes).

Results

The surface relative hardness is plotted in fig.1 considering the ratio D/D_0 , where D is the hardness of each sample with different filler load and D_0 is hardness of pure UHMWPE. The plot shows that the surface hardness improves only when CNTs are added to the polymeric matrix, especially at high percentages. The beginning D/D_0 value (referred to the UHMWPE + 0.3% of CNTs) is 1,007. It improves until 1,035 when the 10 wt % of CNTs is present. In this last case, high loads improve the hardness probably due to the high tendency of the CNTs to agglomerate themselves in bundles.

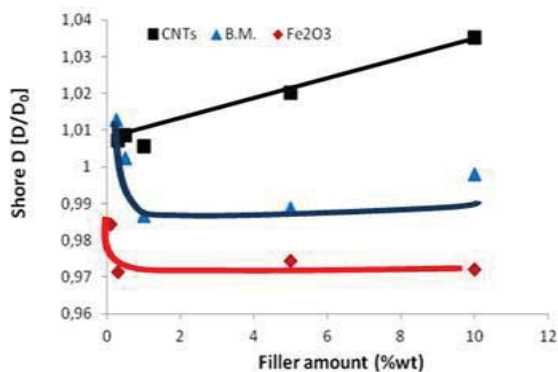


Figure 1 – Relative hardness Shore D of UHMWPE pure and with the three fillers with growing loads.

This effect is highly probable with great concentrations of CNTs. Instead the surface

hardness of UHMWPE decreases in presence of the other two fillers: low amounts of BM and Fe₂O₃ are enough to lower the beginning surface hardness of the polyethylene.

The graph of **figure 2** shows the contact angle measurements performed on the UHMWPE pure and embedded with CNTs in growing amount. The contact angle improves after low load additions of CNTs filler (0.1- 1.0 wt %) from the starting value of about 84° to 105°, which represents the maximum value. High CNT loads decrease the contact angle value, that become similar to the pure UHMWPE. This result shows that the wet ability of UHMWPE decreases with low filler loads but then it re-improves with high CNT contents.

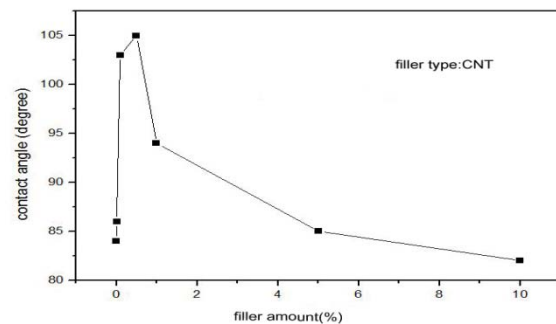


Figure 2 Wet ability of UHMWPE pure and with CNTs with growing loads.

The presence of low amounts of CNTs, well dispersed in the polymeric matrix during the chemical mixing probably, lowers the hydrophilic character of the pure polyethylene. As consequence, the polymer become more hydrophobic. As already discussed, high loads produces bundles of CNTs for their natural tendency to agglomerate. So, the hydrophilic character of the pure polyethylene improves again. The natural tendency of CNTs to agglomerate themselves in bundles was observed in the hardness measurements with high amounts of CNTs, previously discussed: so the wet ability results are in agreement with the hardness ones. The other fillers (Fe₂O₃ and BM) exhibited a behavior similar to the CNTs, although less pronounced due to the lower

agglomerating tendency compared to the CNTs.

In order to study the bulk properties change after the addition of filler in growing amount (within the range 0.1-10 wt %), were performed tensile, calorimetric, optical and electrical tests on UHMWPE both pure as filled.

The effect of filler amount on the ductility of UHMWPE is compared in **figure 3**. As shown, the progressive addition of BM decreases not much the material deformability. The material stiffness improves while the elongation at break decreases.

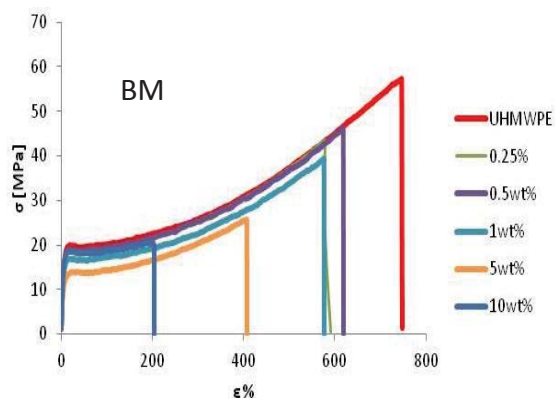


Figure 3 – Average stress-strain curves of UHMWPE pure and with BM as filler at growing loads.

This behavior can be explained considering that the filler presence inhibits the macromolecular chains sliding so they lose their mobility and their characteristic high ductility. This occurs especially in presence of high filler loads. The behavior obtained in presence of BM is representative of the other fillers (Fe_2O_3 and CNTs).

The addition of the filler changes also the polyethylene calorimetric behavior. The T_m/T_{m0} ratio (where T_m is the melting temperature of filled UHMWPE, at the different loads, and T_{m0} is the melting temperature of pure UHMWPE, $\approx 133^\circ\text{C}$) vs filler amount are plotted in the graphs of **figure 4**. This graph clearly indicates that the addition of BM induces an appreciable enhancement of the T_m/T_{m0} ratio while it decreases in presence of either carbon nanotubes or iron oxide. The result above

discussed suggests that only the presence of high percentages of BM enhance the thermal behavior of the polyethylene. Instead the addition of carbon nanotubes or iron oxide worsen it.

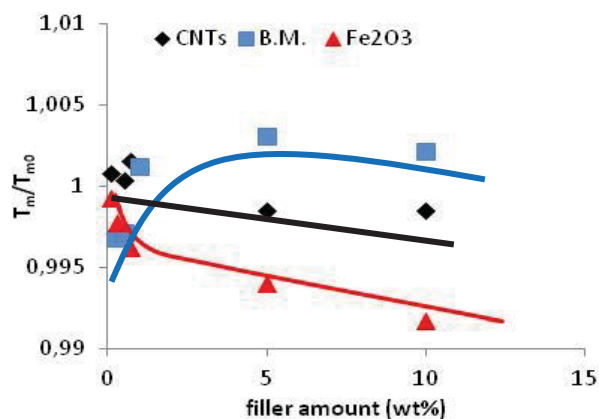


Figure 4 – Change of the melting temperature (T_m/T_{m0} ratio) after the filler addition in different amount.

The light absorption percentage values of five samples (pure PE, PE with 1 wt% of B.M., PE with 5 wt% of B.M., PE with 1 wt% of Fe_2O_3 and PE with 1 wt% of CNTs) are shown in **figure 5**. We investigated three wavelengths in ultraviolet, visible and infrared part of the spectrum. The UHMWPE is transparent to the laser light but it became highly absorbing in presence of CNTs and Fe_2O_3 at all the wavelength investigated. Instead the BM presence makes the material highly absorbent only at the lowest wavelengths, in the UV region, and less in the visible or in IR region. The optical measurement results suggest also that a higher filler load should be preferable to have a greater absorbent material.

The electrical conductivity of the UHMWPE samples containing 0.5 wt% of CNTs at 350K is of $2.7 \mu\text{S}/\text{cm}$; it decreases with increasing the temperature, changing at 393K due to the melting process of the polymer. The conductivity grows with the CNT load, since with 1.0 wt % it become of $55 \mu\text{S}/\text{cm}$ [6]. This result highlights s that the conductivity is due to the presence of CNTs along the polymeric matrix.

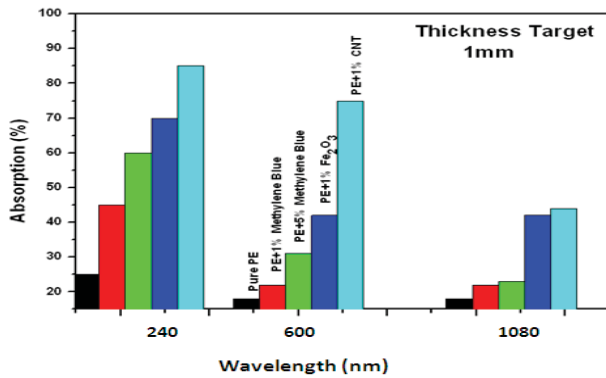


Figure 5 – Optical spectroscopy measurements of UHMWPE pure and with filler at different wavelengths

The melting of UHMWPE favors the mobility of the macromolecular chains where the CNTs are deposited. So they lose their initial network distribution over the polymeric matrix and the conductivity, consequently, falls.

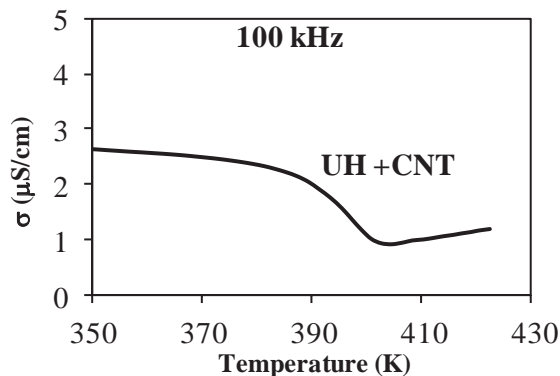


Figure 6 – Electrical conductivity of UHMWPE pure and with the 0.5 wt% CNT at different temperatures

Conclusions

The polyethylene UHMWPE is a multipurpose polymer with high molecular weight, employed for especial uses, like in the biomedical field for its high mechanical performance, or in the chemical industry, for its chemical inertia, or in the electronic field, for its insulating features.

Its main properties are: good deformability, high yielding strength and good stiffness; besides it has also a high transparency, low hardness and low use temperature. The addition of filler changes the polyethylene properties dependently on the filler amount and type. Just regulating these parameters, different physical and mechanical

modification can be induced in the material, as above described by the experimental results. In particular, the surface as well as the bulk properties can be changed. Low filler amounts (generally within the range 0.1-1.0 weight percentages) give a different effect compared to the higher (up to 10 wt%).

The high filler loads, if on the one hand improves the plastic material stiffness, the electrical conductivity (with carbon nanotubes filler) and the optical properties, on the other hand change the melting temperature. The surface properties are instead changed by low filler amounts that improve the hydrophobic character of UHMWPE and decrease its hardness. Vice versa with high filler loads. The behavior is strictly depending on the filler type. Among the fillers studied, the BM induces the best thermal stability while CNTs the best optical absorption properties. The UHMWPE embedded with the iron oxide generally exhibits intermediate features between the UHMWPE with BM and UHMWPE with CNTs.

References

- [1] Z. Spitalsky, D. Tasis, K. Papagelis, C. Galiotis, Prog. in Polym. Sci,35,357–401, 2010.
- [2] Z. Yaping, Z. Aibo, C. Qinghua, Z. Jiaoxia Mat. Sci.& Eng.A 435 – 436(2006)145 – 149
- [3] L. Torrisi, F. Caridi, A.M. Visco, N. Campo Appl. Surf. Sci.257 (2011) 2567-2575
- [4] L. Dosser, K. Hix, K. Hartke, R. Vaia, M. Li, Photon Processing in Microelectronics and Photonics III. Proceedings of the SPIE, vol. 5339, 465-474 (2004).
- [5] L. Torrisi, C. Gentile, A.M. Visco, N. Campo. 2003. Rad. Eff. and Def. in Solids. 158:731-741.
- [6] N. Campo, A.M. Visco. Inter.J. of Polym. Anal. and Charac.,15 (7),438 –449, 2010

Applications of laser welding for the joint of plastic materials

A.M. Visco¹, V. Brancato¹, M. Cutroneo², C. Scolaro², F. Caridi² and L. Torrisi²

¹University of Messina , Dept. of Electronic Engineering, Industrial Chemistry and Engineering, C/da di Dio, vill. S. Agata, 98166 Messina, Italy

²University of Messina, Department of Physics, V.le D'Alcontres 31, 98166 S. Agata, Messina, Italy

Abstract

A pulsed infrared laser source, like the Nd:YAG, welds the irradiated plastic materials by means of a thermal process that gives a direct chemical bond between two layers in close contact each other. The intense photon radiation, of the order of 10^{10} W/cm², is capable to modify the polymeric materials inducing a melting process that seals two sheets at their interface. The sealing action occurs between the polymeric layers if one of them, placed in second plane, can absorb the laser light while the other, placed in first plane, is radiation transparent. The polymer filler presence (like carbon nano-structures, iron oxide, silicate,...) is required in order to absorb the laser light and to obtain the joint at the interface with other polymers through an accurate control the filler concentration. The penetration depth of the laser light and the mechanical resistance can be regulated by the absorption power of the polymeric layer. With this aim, the filler amount must be accurately chosen in order to produce a strong joint. In this work we investigated the applications of Nd:YAG laser welding for the polyethylene biomedical joint devices. In particular, we examined the possibility to define the optimal depth of the sealing action by regulating the filler type and amount in different joint geometries.

Introduction

Laser technology offers many advantages in the welding of plastics. The Through Transmission Visible Laser Welding (TTVLW) process involves localized heating at the interface of two pieces of plastic that will be joined. This method produces strong and hermetically sealed welds with low thermal and mechanical stress, without particulates. Only some materials and combinations of materials are suitable for transmission laser welding because this method needs an optically transparent plastic layer and another absorbent.

There are various methods to make the plastic able to absorb the laser energy, such as the use of nanostructures embedded in the polymer which have high absorption at the used laser wavelength. Additives such as carbon nanotubes (CNTs) nanostructures of Fe₂O₃ or methylene blue for example, can be used to color with black, red or blue respectively, the polymer sample and to increase the visible laser absorption in the first sample layers [1].

Laser light penetrates the upper layer and it is absorbed by the lower material. The melting of the latter transfers the heat to the upper layer. The mutual melting pool solidifies under

external pressure to a high-quality weld [2]. For this reason the pulsed laser welding of polymers depends strongly on the optical characteristics of the coupled polymers [3].

Different laser sources are commonly employed for the welding of polymers, such as continuous CO₂ high-power infrared lasers at 9.4 and 10.6 μm wavelengths, ns pulsed Nd:Yag lasers, generally employed at the second harmonic of 532-nm wavelength, and high-power semiconductor diode lasers, with small dimensions and generally employed in the visible emission range [4].

Many thermoplastic polymers can be joined by laser sources, such as polyethylene, polyvinylchloride, polyethylene terephthalate, polymethylmethacrylate and acrylonitrile butadiene styrene. Often these polymers must be coated or filled with nanostructures, in order to control their absorption coefficient with respect to the used laser wavelength.

The main process parameters that affect the bond quality are: the laser power, the welding speed and time, the laser beam size and uniformity, the adsorption properties of the polymeric materials at the interface of the two polymers and the pressure of clamping.

In this work we studied blends made by polyethylene, a versatile thermoplastic material, doped with different fillers (iron oxide, carbon nanotubes and methylene blue).

We presented some preliminary comparative results about the physical analyses and the mechanical characterization performed on the laser welded joints, with the aim to study the effects of the kind of filler on the welding features. Different geometries available through TTLW and some applications are presented and discussed in the paper.

Materials and methods

Materials

The polymeric matrix was an Ultra High Molecular Weight Polyethylene (UHMWPE resin, Ticona-GUR 1020: $M_w \approx 3 \times 10^6$ g/mol and particle powder size of 150 micron, code "UHMWPE". The fillers were:

- Multi walled carbon nanotubes (MWCNTs): obtained by Chemical Vapor Deposition (CVD) technique, with an aspect ratio (l_n/d_n) of 1000 and purity >95% (code: "CNT");
- Iron oxide, supplied by Across Organics with a purity level of 99.999%, particle size of ten nanometer order (code: "Fe₂O₃");
- A glass matrix of calcium silicate with high porosity (particle size < 75 μm and surface area = 70-100 m²/g) where the organic pigment of methylene blue hydrate (supplied by Fluka) is entrapped, (code: "BM").

The composites were made by following the schema in fig. 1:



Figure 1 – Flow sheet of the preparation steps of the filled polymer.

Some features of the studied samples, like the appearance, the density, ρ , and absorption coefficient (at 532nm and with 1wt% in weight of filler), μ , are resumed in Table I.

MATERIALS	COLOR	ρ (g/cm ³)	μ (cm ⁻¹)
UHMWPE	Semi-transparent 	0.930	5.0
UH/BM.	blue 	0.938	5.6
UH/Fe ₂ O ₃	Red 	0.9340	184
UH/CNTs	Black 	0.944	380

Table I- Materials features

Laser irradiation process

The polymeric targets were irradiated in air at room temperature (25°C) for 2 minutes by a

3-ns Nd:Yag laser operating at 532 nm (second harmonics) or at 1064 nm, in a single pulse or at 10-Hz repetition rate, with an intensity of $1.8 \times 10^8 \text{ W/cm}^2$, a maximum pulse energy of 150 mJ and a laser spot of 28 mm^2 (no focusing lenses were employed). The laser pulse energy has a Gaussian shape with a diametric FWHM of about 3 mm. The incident angle of the laser beam was 0° .

The welded joints were obtained by coupling two rectangular polymeric sheets, partially overlapped for a length of 15 mm. In particular, the UHMWPE sheet, highly laser transparent, was placed on the top (irradiated face) while the highly laser absorbent sheet (UHMWPE + colored filler) was placed on the bottom (un-irradiated face) and pressed each other with pressure of $\approx 180 \text{ kPa}$.

Characterization analyses

The Absorption Percentage of the laser light was measured through the Optical carried out on thin polymeric sheets ($90 \mu\text{m}$ thickness), filled and un-filled, at different wavelength, from 240 nm to 1060 nm.

The absorption percentage was calculated by the following formula:

$$A = 100 - T \quad (1)$$

where A = absorption percentage, $T = I_T/I_0$ transmittance percentage, where I_0 = incident laser intensity and I_T = transmitted laser intensity.

The mass quadrupole spectrometry (Balzer MQS 300) operating between 1 and 300 amu range with sensitivity higher than 1 ppm was employed. The MQS measurements were obtained by irradiating the different polymers in high vacuum conditions (10^{-6} mbar).

The shear test was carried out on the joints at 25°C by a LLOYD LR 10K universal testing machine with a crosshead speed of 5 mm/min. The specimens had a rectangular geometry, 20mm x 30 mm and 1 mm of thickness. For each kind of filler 10 specimens were tested in order to give the average value.

Results

Optical spectroscopy measurements: the absorption power of the pure PE changes after the filler addition in the order:

$$\text{PE} < \text{PE/BM} < \text{PE/Fe}_2\text{O}_3 < \text{PE/CNTs}$$

and it decreases from the lowest wavelengths (UV region) to the highest one (IR region) as plotted in the graph of fig.2.

The knowledge of the absorption power of the materials in a wide spectral range, from UV to IR wavelengths, is important to optimize the interaction between radiation light and targets and to generate hot laser plasma. The plasma properties are strongly dependent on the laser intensity and wavelength.

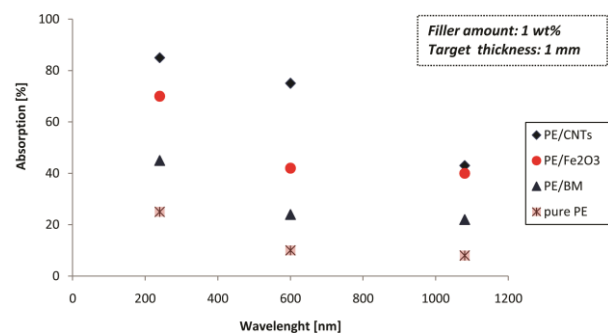


Fig. 2 - Absorption percentage of pure and filled UHMWPE at 240, 600 and 1080 nm.

The effects that the laser light can produce on a generic target are the following:

- long wavelengths, such as infrared radiation, generally induce thermal effects. Heating, vaporization, thermal diffusion and sublimation occur in the target;
- short wavelengths, such as ultraviolet radiation, generally induces chemical effects: breaking of bonding (scission), molecular dissociation, radical formation, molecular cross-linking and chemical reactions;
- visible radiation could induce both thermal and photochemical effects depending on the wavelength and target composition [5].

The filler presence in a polymeric material, like polyethylene, greatly increases the laser light absorption.

CNT filler is the most capable to absorb the UV, Visible and IR light, while the BM is the worst among the tested fillers.

MQS spectra were recorded during the laser irradiation process of a UH/CNT (1wt%) sheet at 532 nm (visible light). The MQS spectroscopy detects the gas species emitted from the polymer during the laser irradiation.

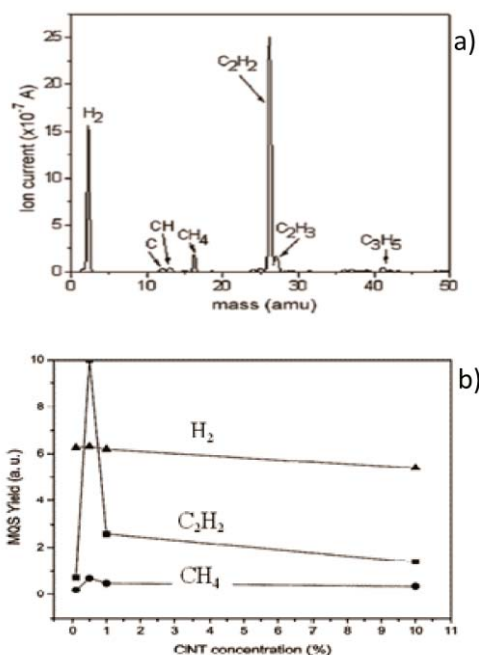


Fig.3 - MQS spectrum of a UH/CNT (1wt%) sheet at 532 nm(a); MQS yield of H₂, C₂H₂ and CH₄ species in the UH-CNT samples vs filler concentration (b)

As example, MQS spectrum of UHMWPE + 1% CNTs is shown in fig. 3a.

The MQS results show that the H₂ and C₂H₂ are the main desorption gasses emitted during the laser ablation. The presence of different C_xH_y groups (CH₄ groups, for example) in the MQS spectra indicates that a complex chemistry contributes to the macroscopic welding because a molecular reorganization, due to C-C and C-H bond breaking, occurs.

The height of the peaks is a complex function of the CNTs concentration, as reported in the measurements plotted in fig. 3b. So, we can suppose that the polymer welding is partially associated with the thermal processes, that occurs at the interface of the sheets, but photo-chemical and ion implantation effects

carry out an important role, too. So, the MQS result has confirmed the optical spectroscopy results above discussed. The Nd:Yag laser source modifies the polymer and generates an energetic process that develops heat, ions, radical species and new chemical rearrangements. These processes involve mainly thermal melting, and other processes, such as chemical processes, which promote the polymeric chain adhesion.

The typical force/deformation curve obtained during a shear test is shown in fig. 4.

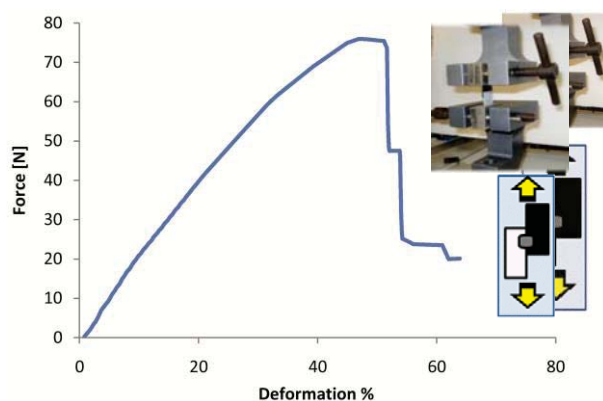


Fig. 4 - Typical force/deformation curve of a joint UH-UH/B.M. In the frames: magnification of a joint during a shear test (above) and force directions applied to the welded sheets (below).

The choice of the best amount of filler in the polymeric matrix and the best wavelength of the laser beam is important to the strength of the joint. In fact the deepness of the welding can be regulated modifying the filler amount: low filler amount generate strong seal, while weak seal occurs with high filler quantity.

In our case, UH/UH-CNTs and UH/UH-Fe₂O₃ are realized with a laser beam operating at 532 nm and with 5wt% of filler. While, UH/UH-BM is realized with a laser beam at 1064 nm and with 10wt% of filler. A higher amount of BM is essential because it has the lower coefficient absorption than the other fillers. Preliminary results of the shear test (fig.5) show that, on the equal irradiation time (5 minutes), the force necessary to break a UH/UH-CNTs joint (\approx 145N) is slightly more than the break force of a UH/UH-Fe₂O₃ joint (\approx 142 N). On the contrary, the UH/UH-BM

shows a weak break strength and the shear force become $\approx 80\text{N}$.

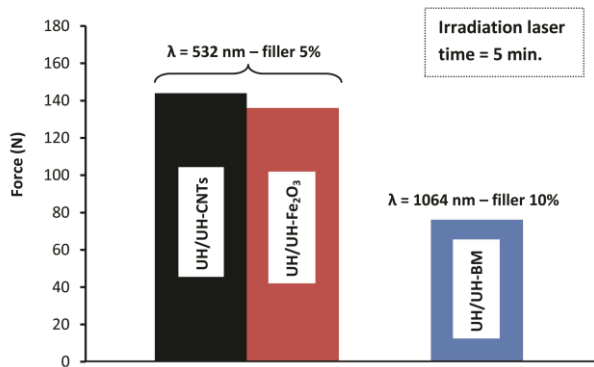


Fig. 5 – Comparison of the shear force at the same irradiation time (5 minutes) of the joint realized with different fillers and at different λ .

In order to improve the adhesion force, the welding of sheets with B.M. should be made in the visible or UV region, according to the result of fig. 2.

Laser welding of polymers is becoming an alternative to conventional technologies and it can be applied to different geometries and in several fields (fig. 6), including: biomedical devices, textiles, food and medical packaging, etc.

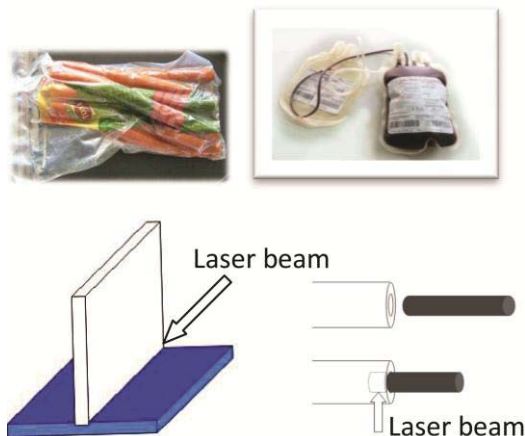


Fig. 6 – Examples of industrial application of laser joints (above) and possible geometries of plastic joints (below)

Different geometries, like tubular or “T joint”, can be represent some examples of application of the laser welding in which the precision of the seal and the absence of particulate are appreciated. In these cases, we can observe that the thickness of the joint can

be very different. Anyway, all these examples highlight the different geometries require different sealing features with different deepness of modification of the materials.

Conclusions

The Nd:Yag laser source modifies the polymer in the contact area, generating an energetic process that develops heat, ions, radical species and new chemical rearrangements. These processes improves with increasing the absorption power of the filler. They involve mainly thermal melting, but there is experimental evidence of other processes, such as chemical ones, which promote the polymeric chain adhesion. Work in progress in order to investigate more deeply on :

- the joints UH/UH-BM by changing the filler load , irradiation time, wavelength;
- new joint realized with other materials (for example PMMA, PP, PEEK, Teflon, PS, etc.);
- the different mechanism (physical and chemical) that are occurring during the laser irradiation.

References

- [1] S.T. Amancio-Filho, J.F. dos Santos. *Polymer Engineering and Science*, 49 (2009) 1461-1476.
- [2] V.V. Semak, R.J. Steele, P.W. Fuerschbach, *J. of Physics D: Applied Physics*, 33 (2000), 1179-1185.
- [3] F. Caridi, L. Torrisi, A.M. Visco; *Optics Communications* 285 (2012) 1199–1205.
- [4] L. Torrisi, F. Caridi, A.M. Visco, N. Campo, *Appl. Surf. Sci.* (2010) Volume 103, Issue 2 (2011), Page 439-445.
- [5] L. Torrisi, F. Caridi, A.M. Visco, N. Campo, *Applied Surface Science* 257 (2011) 2567

Proton emission by TiH₂ laser ablation at different wavelengths

F. Caridi^{1,2}, M. Cutroneo^{1,2}, C. Scolaro^{1,2}, L. Torrisi^{1,3}

¹Dip.to di Fisica e Scienze della Terra, Viale F. Stagno d'Alcontres, 31, 98166, Messina, Italy

²INFN-Sez. CT, Gruppo coll. di Messina, Viale F. Stagno d'Alcontres, 31, 98166, Messina, Italy

³INFN-Laboratori Nazionali del Sud, Via S. Sofia 44, Catania, Italy

Abstract

Ns-pulsed lasers operating in the electromagnetic regions from infrared to visible and to ultraviolet, with single pulse or repetition rate mode, were employed to produce non-equilibrium plasmas by ablating titanium hydrate targets.

The ion emission from the plasma was monitored through time-of-flight (TOF) measurements of emitted species, performed by using an ion collector (IC) placed along the normal to the target surface and a mass quadrupole spectrometer (MQS). Measurements demonstrated that for laser intensity ranging from 10^8 to 10^{11} W/cm² the ion kinetic energy and the ion yield are proportional to the pulse intensity and to the laser wavelength square.

Obtained results at three different wavelengths are compared and discussed.

Introduction

Laser ion source (LIS) is an interesting method to generate ions at high energy, high current and high charge states, on the basis of the laser generated plasma properties [1]. The high ion beam emission directionality along the target normal, high current density, high average charge state and ionization fraction are promising for a possible use as LIS. A special interest is devoted to the possible use of proton beams in nuclear physics, astrophysics, bio- medicine.

At low laser intensity the accelerated proton beams have maximum energies of about 100 eV but they can be post-accelerated by external electrical fields up to energies of the order of 100 keV and a total number of about 10^{10} protons/pulse [2].

At high laser intensities, a proton flux of about 10^9 protons/pulse can be accelerated

at energies above 1MeV or more, without any post-acceleration [3]. To maximize the proton beam current, the choice of the best H-enriched material is challenging. Polymers, polymer foils (C_xH_y bonds) coupled to metal targets and metallic hydrides could be used to take advantage of the high hydrogen concentration.

In this work we focused on the ablation of a TiH₂ target, chosen for its stoichiometry and for the high electron density, that leads to a hot non-equilibrium plasma and consequently to energetic proton beams emission. Obtained results at three laser wavelengths are presented and discussed.

Materials and methods

A Compex 205 KrF excimer laser operating at a wavelength of 248 nm, with 23 ns pulse duration and maximum energy of 600 mJ,

was employed at LEAS, Department of Physics and Mathematics, University of Salento. Using a 15 cm focal distance lens, a power irradiance of the order of 10^8 W/cm^2 was obtained on a TiH_2 solid target mounted in a vacuum chamber at a pressure of 10^{-6} mbar.

A Q-switched Nd:YAG pulsed laser operating at 1064 nm and 532 nm (second harmonic) wavelengths, with 3 ns pulse duration, 1–150 mJ pulse energy, single shot or repetition rate (1–10 Hz) mode, was employed at the “Laboratory of plasma physics” at the University of Messina. The laser beam was focused, through a 35 cm focal lens placed in air, on the surface of the TiH_2 target placed inside a vacuum chamber at 10^{-6} mbar. The laser light passed through a thin window to the target, on which it produced a spot of about 1 mm^2 size. The target was mounted on a holder (externally vertically and angularly mobile) at an incidence angle of 45° . Fig. 1 shows a scheme of the experimental setup.

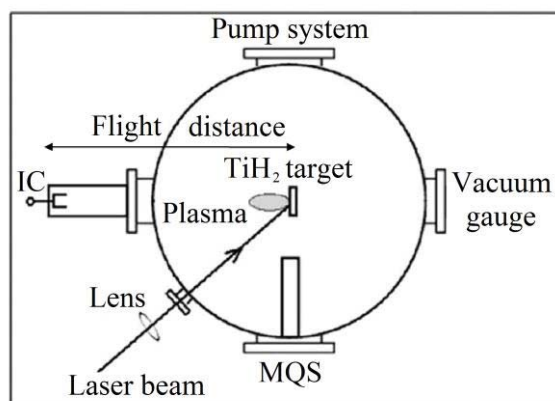


Fig. 1. A scheme of the experimental setup.

A Q-switched Nd:Yag pulsed laser operating at 1064 nm and 532 nm (second harmonic) wavelengths, with 9 ns pulse duration and 900 mJ maximum pulse energy, in single pulse or at a variable repetition rate from 1 up to 30 Hz, was employed at the INFN-LNS of Catania. The laser beam was focused, through a 50 cm focal lens placed in air, on the surface of the TiH_2 target placed inside a

vacuum chamber at 10^{-6} mbar, with a spot size of 1 mm^2 .

The employed target was a TiH_2 thick pill produced with Specac’s Atlas Manual Hydraulic Press. It is available at maximum in 10 ton load configuration. By a digital balance, 200 mg of TiH_2 , in powder has been introduced inside a steel dies and covered with a pellet capsule. Successively, a protective safety shield has been closed in order to maintain constant the temperature and the pressure near a vessel. The upper bolster has been moved down and then, manually, the load has been adjusted. With the aim to manufacture metallic target 1 mm in thick, and 1 cm in diameter have been applied 8 ton of pressure for 18 minutes at room temperature and at environmental conditions of pressure and humidity.

An ion collector (IC), placed along the normal to the target surface, at 0° detection angle and 45° incidence angle, was used in time-of-flight (TOF) approach [4] at the three wavelengths.

A Pfeiffer Vacuum Prisma 200 mass quadrupole spectrometer (MQS), placed at 45° incidence angle, with a high sensitivity in the mass range 1-200 amu, mass resolution below 1 amu, was employed to detect plasma neutrals for several different targets as a function of the irradiation time.

Results

Fig. 2 reports a comparison between IC spectra obtained by irradiating TiH_2 at three different laser intensities, 10^8 W/cm^2 , $3 \times 10^9 \text{ W/cm}^2$ and 10^{10} W/cm^2 at laser wavelengths 248, 532 and 1064 nm, respectively.

The proton energy increases from about 15 eV at 248 nm wavelength and 10^8 W/cm^2 laser intensity (a), to about 105 eV at 532 nm wavelength and $3 \times 10^9 \text{ W/cm}^2$ intensity (b), up to about 195 eV at 1064 nm wavelength and 10^{10} W/cm^2 intensity (c).

The proton peak, in fact, becomes faster increasing the laser intensity. Spectra obtained at 248 nm reports the IC detection of ions as emitted from plasma (0 kV) and as emitted submitting plasma ions to a post-acceleration produced by 15 kV. Of course in this case protons assume a kinetic energy of 15 keV.

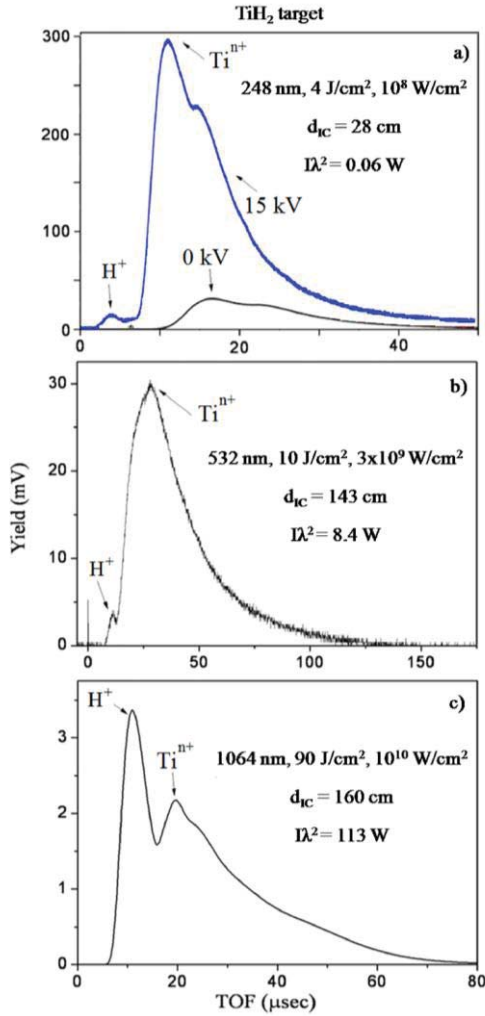


Fig. 2. A comparison between IC spectra obtained by irradiating TiH₂ at three different laser intensities.

The H⁺/Tiⁿ⁺ yield ratio increases from about 1.9x10⁻³ at 248 nm wavelength and 10⁸ W/cm² laser intensity (a), to about 0.13 at 532 nm wavelength and 3x10⁹ W/cm² intensity (b), up to about 1.62 at 1064 nm wavelength and 10¹⁰ W/cm² intensity (c). The proton-to-titanium yield ratio, in fact, becomes higher increasing the laser intensity and the wavelength.

By using different laser intensities and by comparing the detected IC spectra, results indicate that the proton energy and the H⁺/Tiⁿ⁺ yield ratio both increase with the laser intensity and the laser wavelength, by using similar conditions of TiH₂ irradiation.

Fig. 3 indicates that the proton energy (a) and the H⁺/Tiⁿ⁺ yield ratio (b) are linearly proportional to Iλ², where I is the laser intensity and λ the laser wavelength, in agreement with Ref. [5], i.e. the relative yield is proportional to the laser pulse power.

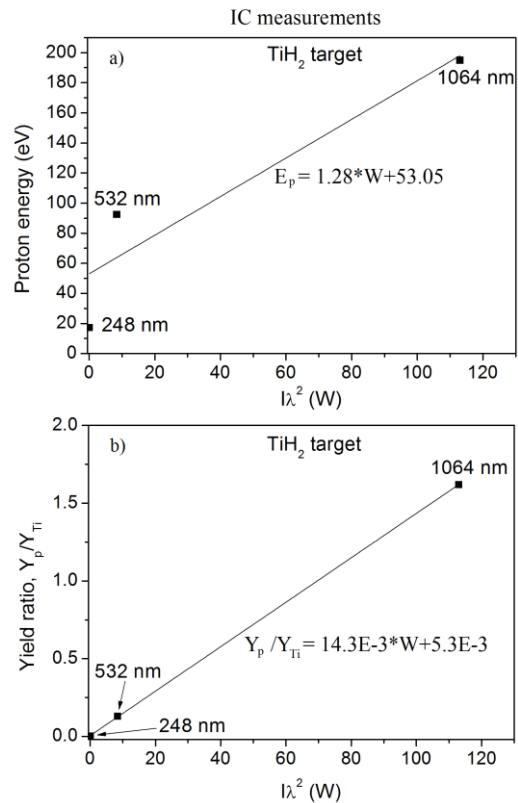


Fig. 3. The proton energy (a) and the H⁺/Tiⁿ⁺ yield ratio (b) as a function of Iλ².

Experimental data can be fitted by an empirical linear relation between the proton energy E_p and the laser pulse power, W, according to the equation:

$$E_p = 1.28 W + 53.05 \quad (1)$$

Similarly, data relative to the yield ratio Y_p/Y_{Ti} and the laser pulse power are correlated by the linear equation:

$$Y_p/Y_{Ti} = 14.3 \times 10^{-3} W + 5.3 \times 10^{-3} \quad (2)$$

Fig. 4 shows MQS mass spectra comparison for titanium detection without and with laser ablation at 1064 nm, 180 mJ and 5 Hz repetition rate (a). The production of Ti, TiH, TiH₂, TiH₃, TiH₄ and TiH₅ was experimentally observed during the ablation process.

Fig. 4b reports a MQS time spectrum obtained during the laser ablation at 1064 nm, 180 mJ and 1 Hz repetition rate, confirming the formation of TiH_x chemical groups (x variable from 0 up to about 5).

The plasma produces different Ti-H molecules with high intensity of TiH₂ and TiH₃ species.

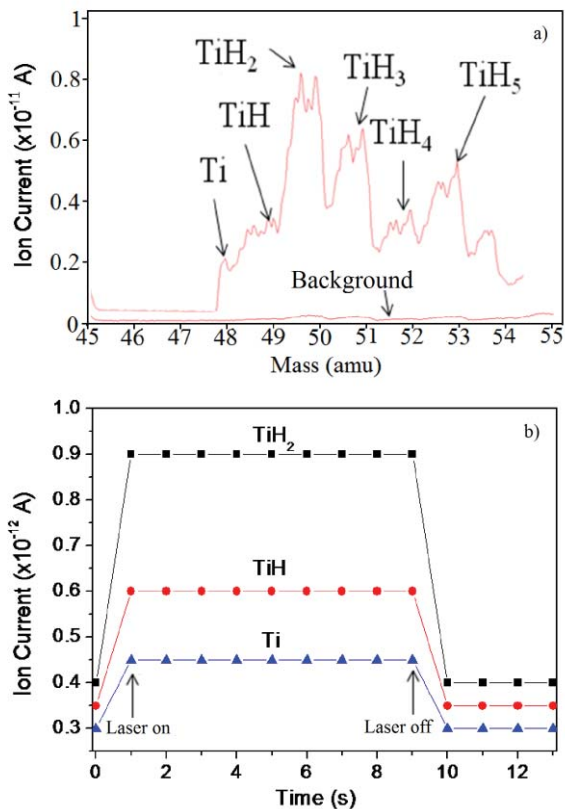


Fig. 4. MQS mass and time spectra for titanium detection.

Fig. 5 shows MQS spectra comparison for hydrogen detection without and with laser ablation at 1064 nm, 180 mJ and 5 Hz repetition rate (a).

An high production of H₂ was obtained with the ablation, as confirmed by the MQS time

spectrum acquired at 1064 nm, 180 mJ and 1 Hz repetition rate and reported in Fig. 5b.

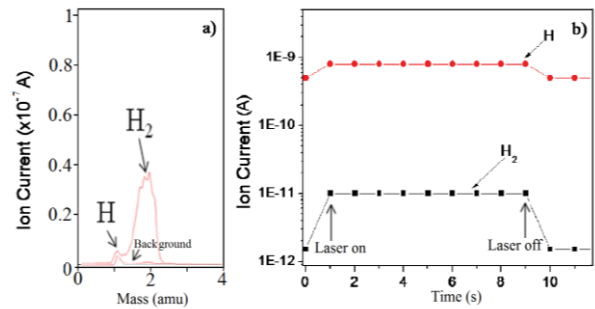


Fig. 5. MQS mass and time spectra for hydrogen detection.

This last result puts in evidence that the TiH₂ target could be employed as a very good hydrogen and proton source in a LIS system.

Discussion and conclusions

At the relatively low laser intensity employed in these experiments was possible to investigate the low energy proton beams generated by the laser matter interaction.

A special hydrogenated target such as TiH₂ allows the generation of plasma with peculiar properties, such as the temperature, density, fractional ionization and equivalent acceleration voltage responsible for the ion acceleration in the plasma. In this work a special interest is devoted to the dependence of the proton energy and yield from the laser parameter $I\lambda^2$. In fact from the literature [6-8] is known that the plasma electrons ponderomotive energy is dependent on this parameter. In this work a dependence also of the proton energy and yield from $I\lambda^2$ is shown.

In order to generate a proton beam from laser-generated plasmas, the use of hydrated titanium targets appears particularly interesting. In order to maximize the proton yield is possible to act on the laser parameters, such as intensity and wavelength, on the target hydrogen

concentration, on the target structural composition (i.e. presence of nanostructures, which can control the laser light absorption coefficient) and on the target geometry. Various targets with proper geometries can allow to increase the proton energy, directivity and yield. Work in this direction is in progress and will be discussed in next papers.

Acknowledgments

Authors thank the research group of LEAS of Lecce, coordinated by prof. V. Nassisi, for the useful support given to this article.

References

- [1] S. Gammino, L. Torrasi, L. Celona, G. Ciavola, F. Consoli, D. Margarone, F. Caridi, *Radiat. Eff. Def. Solids* 163 (4–6) (2008) 277.
- [2] L. Torrasi, L. Giuffrida, M. Rosinski, C. Schallhorn, *Nucl. Instr. and Meth. B* 268 (2010) 2808.
- [3] H. Schwoerer, S. Pfoth, O. Jackel, K.U. Amthor, B. Liesfeld, W. Ziegler, R. Sauerbrey, K.W.D. Ledingham, T. Esirkepov, *Nature* 439 (2006) 445.
- [4] E. Woryna, P. Parys, J. Wolowski, W. Mroz, *Laser Part. Beams* 14 (1996) 293.
- [5] E.L. Clark, K. Krushelnick, M. Zepf, F.N. Beg, M. Tatarakis, A. Machacek, M.I.K. Santala, I. Watts, P.A. Norreys, A.E. Dangor, *Phys. Rev. Lett.* 85 (8) (2000) 1654.
- [6] Torrasi, L., Caridi, F., Giuffrida, L., *Laser and Particle Beams* 29 (1) , pp. 29-37, 2011
- [7] F. Caridi, L. Torrasi, D. Margarone, A. Borrielli, *Laser and Particle Beams*, 26 265-271 (2008).
- [8] M. Cutroneo, L. Torrasi, F. Caridi, R. Sayed, C. Gentile, G. Mondio, T. Serafino, E.D. Castrizio, *Applied Surface Science*, 272 pp. 25-29 (2012).

Enhancing UHMWPE Antibacterial Properties Through Ion Implantation

D. Delle Side¹, P. Alifano², V. Nassisi¹, A. Talà², S. M.Tredici² and L. Velardi¹

¹LEAS, Dipartimento di Matematica e Fisica, Università del Salento and INFN Sez. di Lecce

²Laboratorio di Microbiologia, Di.S.Te.B.A. Università del Salento
domenico.delleside@le.infn.it

Abstract

We propose a new technique for the surface modification of biomedical polymers in order to strongly enhance its antimicrobial quality via ion implantation, in alternative to the well known ones that use chemical reactions or films deposition. We present the experimental results of implantation of ultra high molecular weight polyethylene (UHMWPE) samples by Ag, Cu and Ti ions. As accelerator we used "Platone", a homemade laser ion source accelerator device. The ions were extracted from the plasma generated by a KrF excimer laser operating at 248 nm. A laser beam of 12 mJ/pulse was focused on a solid target mounted in a vacuum chamber in order to obtain plasma. The laser spot was estimated to be of 0.005 cm². This device has an accelerating system composed by two different stages. Using pure Ag, Cu and Ti disks as laser targets and applying voltages of 40 kV to the first accelerating stage and 20 kV to the second one, we produced ion beams containing about 10¹¹ ions/cm² per pulse. The penetration depth of ions was estimated by the Srim code and the largest depth was achieved with Ti ions. Operating 22000 laser shots we implanted our samples with doses of about 10¹⁵ ions/cm². Next we analyzed the effects of ion implantation on the bacterial adherence to UHMWPE samples. To test their antimicrobial quality, a Staphylococcus aureus strain isolated from a catheter-related bloodstream infection was used in these assays. The results demonstrate that the adherence of bacteria is reduced of 21%, 7% and 90% for Ag, Cu and Ti ions-implanted samples with respect to the control ones, confirming the effectiveness of our approach.

Introduction

In the past years, the growing demand for biomaterials of antimicrobial quality gave rise to a new and fruitful research area for material science. For example, UHMWPE is used to make components of prosthetic knee, hip and

shoulder[1], while other materials are used for surgical and dental tools, sanitary equipment, parts of prosthesis type screws[2-4], etc. The essential properties of these materials must be the biocompatibility, wettability and durability. The antibacterial properties are no less essential[5]. Apart from medical applications

many other fields have demonstrated much interest in the antibacterial properties of material including the packing industry of food[6] and the mechanic industry operating in the construction of alimentary machines[7]. These properties together with surface hardness and corrosion resistance can be further improved applying the ion implantation technique[8, 9].

Ag atoms are well known as antibacterial particles while copper and its alloys are known as natural antimicrobial materials. Molecular mechanisms responsible for the antibacterial action of these atoms are today a subject of intensive research and ranges from poisoning on bacteria's respiratory enzymes and electron transport components to interfere with DNA functions and even to an induced toxicity due to the generation of reactive oxygen species. In general, the overall antibacterial effect induced by both metals seems to be the result of a combination of various causes [10-12].

Titanium dioxide is no less important as antimicrobial material, his efficiency is very high but somewhat limited by the necessity of UV light to activate its action[13]. Using ion implantation, energetic Ti ions could exploit surface impurities containing oxygen, inducing the formation of a carbon (from the substrate) doped TiO₂.

We propose to use ion implantation onto the surface of Ag, Cu and Ti metals instead of the application by chemical reactions that can potentially invalidate the biocompatibility, due to a possible formation of undesired by-products that have to be removed with complex techniques. Additionally, the application of thin film deposition could be effective only if the adherence with the bulk is guaranteed and the proprieties of the material surface are preserved. In fact, a successful film deposition needs strong chemical bounds between film and bulk. Besides, the chemical processes involve procedures that use potentially undesired solvents[14, 15]. The

proposed technique, which is able to overcome the previous limitations, consists in the application of a dose of antibacterial ions inside the first surface layers of UHMWPE samples to be treated. The goal can be achieved if the ions are preventively and suitably accelerated.

Material and methods

The UHMWPE is used in many fields and particularly in the medical one due to its extreme versatility, high chemical inertness and its good biocompatibility. The samples used in this work have an average molecular weight of 4×10^6 g/mol, with a density of 0.93 g/cm³. Their dimensions are 20x20mm² for a thickness of 1 mm. Instead, as target for the ion source we used thin discs with a diameter of 2 cm of silver, copper and titanium (99.99% pure).

The accelerator "Platone", installed at the LEAS laboratory at the Dipartimento di Matematica e Fisica, Università del Salento, is a homemade device[16]. It is a laser ion source (LIS) that utilizes a KrF excimer laser (Lambda Physik, Mod. COMPEX) and a stainless steel vacuum chamber as accelerating chamber (AC), Fig. 1. The laser generates a pulsed beam of 248 nm wavelength (5 eV photon energy) and a width (FWHM) variable from 23 to 30 ns. The laser beam, guided by a 15 cm focal length lens, enters the AC through a thin quartz window with an angle of 70 °C with respect to the main axis perpendicular to the target (T). The accelerating chamber has inside a second chamber called expansion chamber (EC) that enables the hydrodynamic expansion of the plasma before the ion extraction. The EC forms a hermetic contact with the support of the target in order to not allow plasma leaks. A base of the EC, together with the support T, is fixed to the AC by an insulating flange (IF) that allows the application of a positive high voltage to the EC. At the opposite EC side there is a hole of 1.5 cm in diameter in order to extract

ions. At a distance of 3 cm from EC, it is placed a grounded electrode (GE), having the central part drilled by a hole of the same diameter of the EC one. After the GE, at a distance of 2 cm, it is placed a further third electrode, connected to a power supply of negative polarity. This electrode was utilized either as Faraday cup (FC) or sample support. The vacuum was obtained through the use of two turbo-molecular pumps, reaching a pressure of the order of 10^{-6} mbar.

It is worth noticing that T and AC are connected through an high voltage fast capacitor (C_1) of 4 nF to ensure the stabilization of the accelerating voltage. Moreover, thanks to the presence of another high voltage capacitor (C_2) of 2 nF and a load resistor of 100 k Ω , the FC could be safely connected to an oscilloscope for diagnostic purposes.

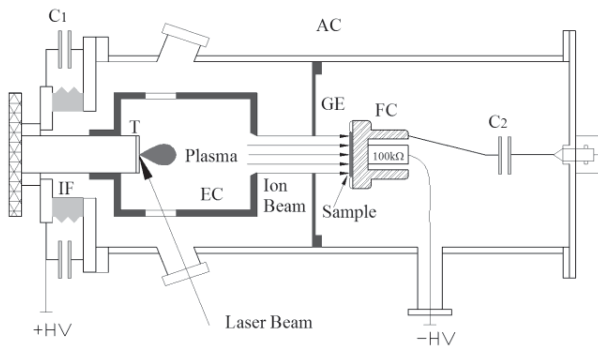


Fig. 1: Cross section of Platone accelerator. IF: insulation flange; AC: accelerating chamber; GE: ground electrode; EC: expansion chamber; FC: Faraday cup.

This device is able to accelerate the plasma ionic component up to 160 keV for charge state. Instead, to preserve the equipment from breakdown risks, during the experiments the accelerating voltages of the first and second stage were fixed at 40 and -20 kV respectively, providing a total ion beam energy of 60 keV per charge state.

Using the Srim code[17], we obtained from a simulation that the maximum implantation depth (reached in the case of +2 ions) is about

250 nm for copper and about 160 nm for silver. Fig. 2 shows the simulation results.

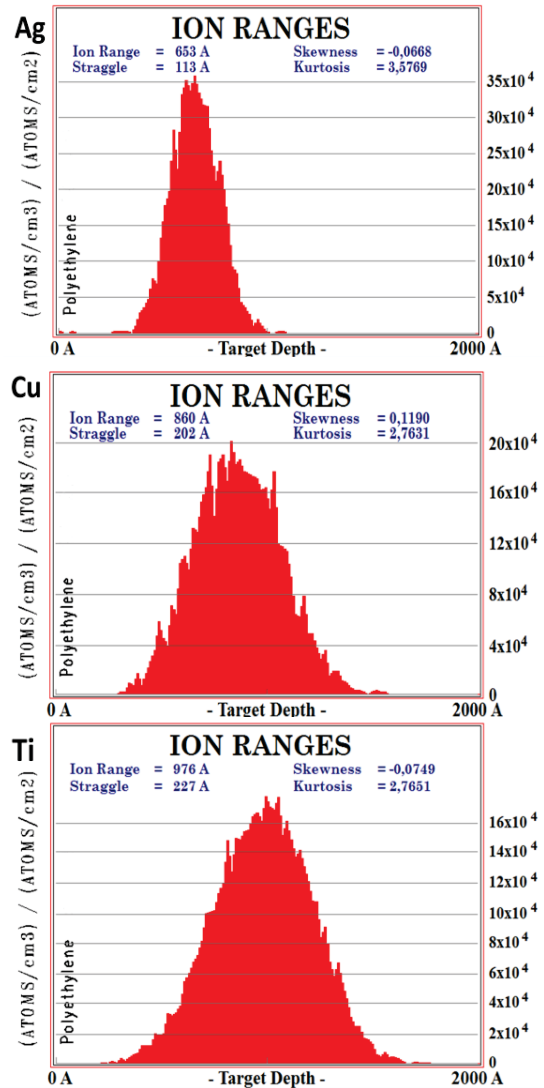


Fig. 2: Simulation results of the penetration depth for Ag, Cu and Ti 1+ ions ; abscissas and ordinates are in linear scale.

Samples implantation

The samples were fixed on the FC collector and implanted with 22000 laser shots, both in the case of silver and copper. Fig. 3 shows a photo of a sample mounted on the FC support. The total dose obtained is roughly the same[18] corresponding to 10^{15} ions/cm².

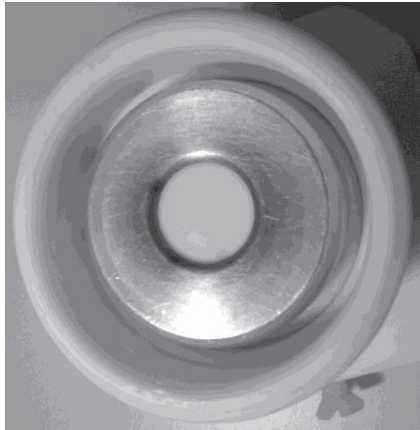


Fig. 3: Photo of the UHMWPE sample mounted on the FC support; the support consists of an inner body of stainless steel to which is applied a negative high voltage and an external insulating cover made of PVC.

Antibacterial experiments

After this treatment the UHMWPE samples were challenged with 10^4 CFU of *Staphylococcus aureus* in micro-wells filled with 4 ml of Nutrient Broth at 37 °C, under moderate shaking; this high concentration was chosen in order to assay the samples under extreme conditions. The *S. aureus* strain was isolated from a catheter-related bloodstream infection. We chose these bacteria since they are among the first causes of infections in humans and in food related pathologies.

Treated and untreated UHMWPE samples were placed in the same tank. After a week of incubation on daylight exposure, when the concentration of *S. aureus* should have reached a value of about 10^{10} CFU, the biofilm matured on the samples surfaces was stained using green-fluorescent nucleic acid stain (SYTO9; Molecular Probes, USA). After 15 min of dark incubation, the biofilm development was viewed with a Nikon Optiphot-2 microscope with an episcopic-fluorescence attachment (EFD-3, Nikon). The images are shown in Figs 4 and 5.

Results

In order to test the antimicrobial effectiveness of our technique, we conducted a fluorescence

microscopy analysis on all the samples. This revealed a sensible reduction of bacterial adhesion on Cu- and Ag-treated UHMWPE samples (Fig. 5a) and an even stronger one on Ti-treated ones (Fig. 5b), with respect to the control. Quantitative analysis, performed by counting the bacterial cells observed in 50 microscopic fields randomly selected, revealed that the mean values of percentages of adherence to the substrate were 93%, 79% and 10% with Cu, Ag and Ti implanted samples respectively. Fig. 6 shows the histogram of results with the relative standard deviation.

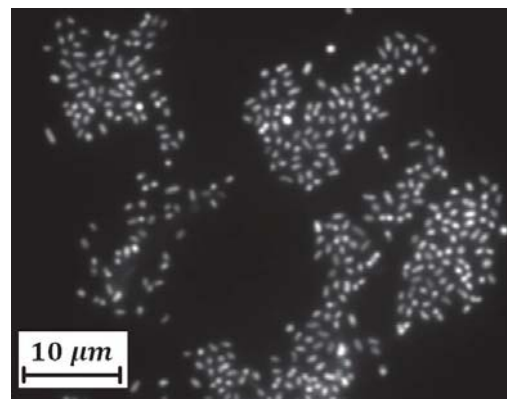
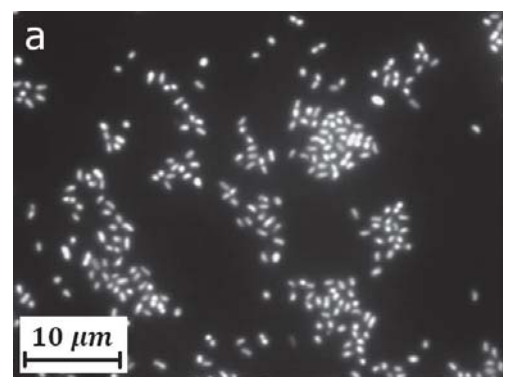


Fig. 4: Representative images showing adherence of *Staphylococcus aureus* to UHMWPE untreated (control) samples.



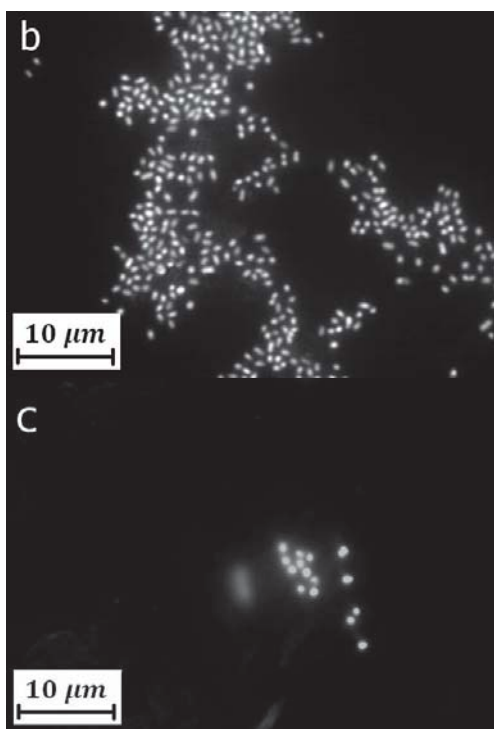


Fig. 5: Representative images showing adherence of *Staphylococcus aureus* to Cu- (a), Ag- (b) and Ti-implanted (c) UHMWPE samples.

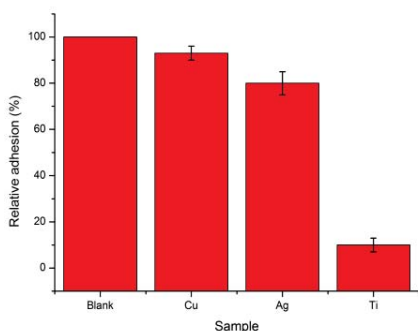


Fig. 6: Relative adhesion (%) of *Staphylococcus aureus* on the sample surfaces. The graph shows the reduction of bacteria on treated samples with respect to the untreated one.

The higher efficiency of the Ti-treated samples in preventing *Staphylococcus aureus* adhesion is very interesting. This behaviour should be ascribed to the fact that the titanium dioxide is formed directly on the surface of the sample, in direct contact with the site that hospited bacteria. Therefore next experiments will be devoted to clarify these aspects.

Moreover, we performed some morphological analysis to understand if the implantation process altered the roughness and wettability of the samples surface.

Using a commercial PCE-RT1200 tester, we measured the arithmetic roughness R_A , given by the arithmetic mean of the absolute value of the vertical distance y_i from the mean line to the i_{th} data point

$$R_A = \frac{1}{N} \sum_{i=1}^N |y_i|;$$

the values obtained are shown in table I.

	Blank	Ag	Cu	Ti
R_A (μm)	1.176	1.435	1.474	1.211

Table I: arithmetic roughness of the samples

As could be seen from the values, the implantation process increases the roughness of the surface.

The wettability of the surfaces has been estimated through the method of the contact angle.

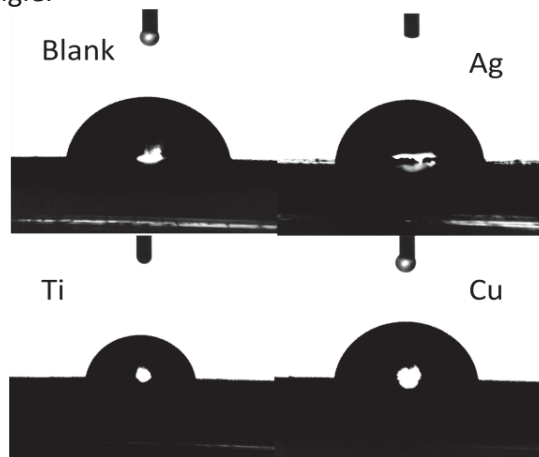


Fig. 7: Water drops used for the estimation of the wettability through the contact angle method

The measurements, whose values are reported in Table II, show that the process does not significantly alter the hydrophilic nature of the UHMWPE surface.

	Blank	Ag	Cu	Ti
θ (deg)	81.7	81.2	79.6	81.4

Table II: contact angles on the samples

Conclusions

In this work we used ion implantation technique to improve the antibacterial properties of the biocompatible UHMWPE. The ion beams utilised for this goal were made respectively of Ag, Cu and Ti ions, accelerated up to a maximum of 60 kV. After this treatment, the UHMWPE samples were challenged with *Staphylococcus aureus* in bacterial adhesion assays. The results demonstrated that the adherence of bacteria showed a reduction of 90%, 21% and 7% for Ti, Ag and Cu implanted samples with respect to non-implanted control one. The technique presented in this work seems to be interesting, since it can open the way to an easier realization of antibacterial biofilms. Higher ion doses could improve the results presented here.

References

- [1] Lee, H. B. (1989). Application of synthetic polymers in implants. In T. Seagusa, T. Higashimura, & A. Abe (Edited by), *Frontiers of Macromolecular Science*. Oxford: Blackwell Scientific Publications.
- [2] Li, B. Z., Zhang, W., & Yan, Q. (1997). *Plastic Sci. Technol.* (6), 16.
- [3] Huang, Z. J. (1999). *J. Mater. Rev.* (13), 35.
- [4] Nakamura, S., Ookubo, N., & Miyakusu, K. (1997). *Nisshin Steel Tech. Rep.* (76), 48.
- [5] Zhang, W., Chu, P. K., Ji, J., Zhang, Y., Liu, X., Fu, R. K., et al. (2006). *Biomaterials* (27), 44.
- [6] Kenaway, E. R., Abdel-Hay, F. I., El-Shanshoury, A. E., & El-Newehy, M. H. (2002). *J. Polym. Sci. Part. A: Polym. Chem* (40), 2384.
- [7] Quintavalla, S., & Vicini, L. (2002). *Meat. Sci.* (62), 373.
- [8] Lorusso, A., Velardi, L., Nassisi, V., Paladini, F., Visco, A. M., Campo, N., et al. (2008). *Nucl. Instrum. Methods B* (266), 2490.
- [9] Noli, F., Lagoyannis, A., & Misaelides, P. (2008). *Nucl. Instrum. Methods Phys. Res. B* (266), 2437.
- [10] Roe, D., Karandikar, B., Bonn-Savage, N., Gibbins, B., & Roullet, J. B. (2008). *J. Antimicrob. Chemother.* (61), 869-76.
- [11] Li, X. Z., Nikaido, H., & Williams, K. (1997). *J. Bacteriol.* (179), 6127-32.
- [12] Baker, J., Sitthisak, S., Sengupta, M., Johnson, M., Jayaswal, R. K., & Morrissey, J. A. (2010). *Appl Environ Microbiol.* (76), 150-60.
- [13] Z. Huang, P. – C. Maness, D. M. Blake, E. J. Wolfrum, S. L. Smolinski and W. A. Jacoby, *J. Photochem. Photobiol. A* 130, 163-170 (2000).
- [14] Allongue, P., Delamar, M., Desbat, B., Fagebaume, O., Hitmi, R., Pinson, J., et al. (1997). *J. Am. Chem. Soc.* (119), 201-207.
- [15] Vittorino, E., Giancane, G., Manno, D., Serra, A., & Valli, L. (2012). *J. Colloid Interface Sci.* (368), 191-196.
- [16] Lorusso, A., Siciliano, M. V., Velardi, L., & Nassisi, V. (2010). *Nucl. Instrum. Methods A* (614), 169.
- [17] Ziegler, J. F. SRIM. Available at <http://www.srim.org>
- [18] Nassisi V., Velardi L. and Delle Side D., *App. Surf. Sci.* 272, p. 114-118 (2013).

The LILIA project: ion beams for hadrontherapy

S. Agosteo¹, M.P. Anania², M. Caresana¹, G. Cirrone³, C. De Martinis⁴, D. Delle Side⁵, A. Fazzi¹, G. Gatti², D. Giove⁴, D. Giulietti⁶, L. Gizzi⁷, L. Labate⁷, P. Londrillo⁸, M. Maggiore⁹, V. Nassisi⁵, A. Pola¹, S. Sinigardi⁸, A. Tramontana³, F. Schillaci³, G. Turchetti⁸, V. Varoli¹, L. Velardi⁵

¹ INFN and Polytechnic of Milan - I

² INFN - LNF Frascati - I

³ INFN - LNS Catania - I

⁴ INFN and University of Milan - I

⁵ INFN-LEAS and University of Salento - I

⁶ INFN and University of Pisa - I

⁷ INFN and CNR Pisa - I

⁸ INFN and University of Bologna - I

⁹ INFN-LNL Legnaro - I

Abstract

The LILIA (Laser Induced Light Ions Acceleration) experiment is now running at the SPARCLAB facility of the Frascati INFN laboratories. The aim of LILIA is to study, design and verify a scheme which foresees the production, the characterization and the transport of a proton beam toward a stage of post acceleration (high frequency compact linac). A description of the experimental set up is given in this paper together with the first evidence of proton acceleration with the laser FLAME.

Introduction

In the past few years, various interesting experiments have been started in order to study the interaction of ultrahigh-power laser pulses (with intensities beyond 10^{18} W/cm² and duration time ranging between 40-1000 fs) with thin solid films (thickness of the order of 0.5-100 μ m) of different elements both metallic (Au, Cu, Pd, Al) and dielectric (polymers). These experiments have shown that, as a result of the laser-target interaction, protons and ions with energies up to 60 MeV are emitted. These protons, mostly originated by contaminated hydrocarbon surface used as target, are accelerated due to their higher charge-mass

ratio with respect to other ions. Nevertheless, it is possible even to accelerate various species of ions by etching the target utilizing different methods. The total number of accelerated particles is strongly correlated to the specific target conditions and the experimental set-up: typical values are in the range from 10^9 to 10^{12} particles for laser pulse.

Laser driven acceleration is characterized by specific interesting properties, which mark a strong difference with respect to the traditional accelerating techniques. The most relevant features may be summarized in the following points: a) the possibility to accelerate ions at tens of MeV in very

compact structures (of the order of a few tens of microns) due to the very high electric fields available with respect to the size of classic accelerators; b) an excellent beam quality with a transverse emittance less than $10^{-3} \text{ mm}\cdot\text{mrad}$; c) a very short duration of the proton bunch (of the order of a few ps); d) the possibility to synchronize the proton beam with the laser beam up to a scale of a few fs to obtain multiple, synchronized sources of different particles (electrons, protons) and radiation (monochromatic X rays).

Due to these considerations laser driven acceleration holds the promise of compact accelerating structures which may be useful in different applications such as medicine (radioisotope production for PET, hadrontherapy), nuclear physics, inertial fusion (proton induced fast ignition), advanced diagnostic (proton imaging of fast electromagnetic fields) or material properties analysis and advanced imaging applications. LILIA is an experiment of light ions acceleration through laser interaction with thin metal targets to be done at the FLAME facility, which is now running in Frascati [1,2]. LILIA, in particular, is finalized to study, design and verify a scheme which foresees the production, the characterization and the transport of a proton beam toward a stage of post acceleration (high frequency compact linacs). Up to now the maximum operating laser intensity is limited to 10^{19} W/cm^2 due to the lack of a parabola with a focal length shorter than the current used. In this configuration, according to the interaction theory by short pulse laser and to performed numerical simulations, we expect a proton beam with maximum energy of a few MeV and a number of proton/shot up to 10^{10} - 10^{12} . When FLAME phase II performances will be available (Short focal length OA Parabola: waist $\approx 2.5\mu$, $I \approx 10^{21} \text{ W/cm}^2$), we might select a bunch at $E = 30 \text{ MeV}$ with a narrow spread ΔE and still have a reasonable number of protons (10^7 - 10^8). This opens a very interesting

perspective for applications such as hadrontherapy in connection with a post-acceleration stage in order to reach energies up and beyond 100 MeV.

Theory

In the majority of experiments for proton accelerations, the regime occurring is the so called TNSA (Target Normal Sheath Acceleration). The laser pulse heats the electrons and ionizes the medium. Next the electrons diffuse around the target building an intense electric field. This field accelerates the free protons present on the target surfaces, both in the forward direction (from the rear side) and in the backward direction (from the front surface). The protons energy depends on the electrons temperature and it has an exponential spectrum due to the thermal distribution of the electron energy. For a given laser, the intensity is

$$I = \frac{2P}{\pi w^2} [W/cm^2] \quad (1)$$

where P is the laser peak power and w is the pulse waist value. It is convenient to introduce the dimensionless parameter:

$$a = \frac{eA}{mc^2} = 0.85 \times 10^{-9} I^{1/2} [W^{1/2}/cm] \cdot \lambda [\mu m] \quad (2)$$

where A is the maximum value of the vector potential. If $a > 1$, the electron quivering motion in the laser fields is relativistic. Let us consider a 1D laser pulse moving on the z direction, the electron temperature (expressed in eV) can be estimated from the kinetic energy as $T = mc^2(\gamma - 1)$ where $\gamma = [1 + (Pz/mc)^2 + a^2]^{1/2}$ and P_z is the longitudinal momentum. If $a \gg 1$ we obtain that $T/mc^2 \sim a$. In 1D geometry, the electrostatic potential can be computed by solving the Poisson equation for a Maxwellian electron distribution. The protons maximum energy can be obtained estimating the maximum value of the electrostatic potential at the target-vacuum interface. After some simplification, the proton maximum energy results approximately proportional to:

$$E_{max}(MeV) = \xi_0 a \quad (3)$$

where $\xi_0 \sim 2$ for a simple one dimensional model. For very short pulses, the scaling found theoretically and in recent experiments (Dresden), keeping the waist fixed, is

$$E_{max} \propto I^{0.8}$$

with a proportionality constant depending on the power, focal spot and target thickness. As a consequence, eq. (3) should be replaced with

$$E_{max}(MeV) = \xi a^{1.6} \quad (4)$$

where the ξ depends on the wavelength and strongly on the thickness. The constant value is $\xi \sim 0.16, 0.085, 0.02$ for a target of thickness $h = 0.5, 5, 20 \mu m$, respectively according to the dependence found in the Dresden experiments. For the highest power $P = 100 TW$ and a waist of $2.5 \mu m$ corresponding to $I = 10^{21} W/cm^2$ and $a = 22$, the maximum energy obtained with a target of $5 \mu m$ thickness is $E_{max} = 12 MeV$ whereas the average energy is $E_0 = 1.7 MeV$. Dresden experiments and numerical investigations (see Fig. 1) show how the proton maximum energy drops significantly increasing with the target thickness.

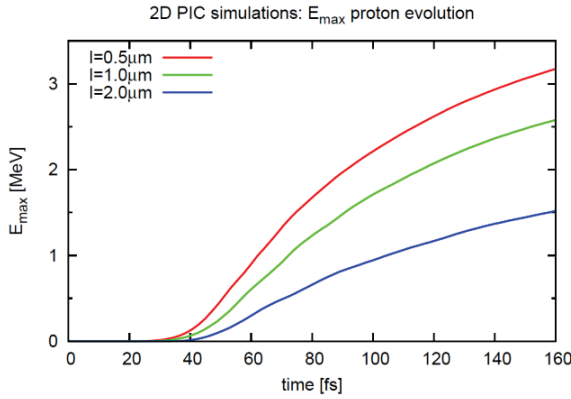


Fig. 1 Energy growth with time for a 2D simulation with $P = 85 TW$ and $a = 5$ for a solid target with $n = 80n_c$ and a thin hydrogen layer. The 3D result can be expected to be one half of the present one

One of the limits of the proton energy achievable in the TNSA regime is related to the fraction of the initial laser energy, absorbed by the electrons of the target. If a large enough layer of plasma near its critical density can be added in front of the solid

target, the energy coupling between the laser pulse and the target is strongly enhanced resulting in higher energy protons. Recent numerical investigations considered solid targets with a foam layer added on the front surface, showing that these targets allow to double the value of the highest proton energy reachable.

The highest energy value $E_{max} = 6 MeV$ for the bare metal target agrees with the scaling (4) of Dresden experiments. The proton energy spectrum in the TNSA regime is exponential with a cut-off

$$\rho(E) = \frac{dN}{dE} = \frac{N_0}{E_0} e^{-E/E_0} \cdot \theta(E_{max} - E) \quad (5)$$

where N_0 is the total number of protons while $\langle E \rangle = E_0$ is the average energy. The number of protons in a given small energy interval is

$$n(E, E + \Delta E) = \int E \left(\frac{dN}{dE} \right) dE \approx N_0 \left(\frac{\Delta E}{E_0} \right) e^{-E/E_0} \quad (6)$$

The average energy is related to the electron temperature and $E_0 \propto a$, but it is considerably smaller than the maximum energy. As a consequence, if a quasi monochromatic bunch has to be selected close to the maximum energy, the corresponding number of protons is a small fraction of the total. In the case of the Dresden experiment it has been shown that for $E_{max} = 12 MeV$ and $N_0 = 10^{12}$ with $E_0 = 1.7 MeV$, the fraction of particle with $E = 10 MeV$ and $\Delta E = 0.1 MeV$ would have only 1.6×10^8 protons

The experiment

The FLAME facility has been fully operational in the middle of 2012 for the first test experiments of electron Laser Wakefield Acceleration (LWFA). In October 2012 it has been possible to install the components for the proton acceleration experiment (LILIA).

As of now the maximum laser intensity is limited to $10^{19} W/cm^2$ due to the lack of a parabola with focal length shorter than the present one. In this configuration, according to performed numerical simulations, we expect a proton beam with maximum energy

of few MeV (10 MeV is as of now the maximum energy allowed by the local authorities for the place where the experiment is located) and total intensities up to 10^{10} - 10^{12} protons/shot. Although these values are modest compared to the present state of art, nevertheless their scientific relevance is very important due to the fact that we will have, with a reasonable effort, a real laser driven source that will play the role of a test facility as far as emission process control and repeatability and post acceleration studies will be involved. In LILIA phase I we plan to perform a parametric study of the correlation of the maximum TNSA accelerated proton energy, with respect to the following parameters:

- Laser pulse intensity (in the range $10^{18} - 5 \cdot 10^{19} \text{ W/cm}^2$)
- Laser pulse energy (in the range 0.1-5 J)
- Laser pulse length (in the range 25 fs-1ps)
- Metallic target thickness (in the range 1-100 μ).

In such a frame we would like to deeply investigate the experimental scale rules within the possibilities offered by the FLAME facility. Moreover, this will provide the opportunity to get experience in the development of diagnostic techniques and in target optimization. The possibility to produce a real proton beam able to be driven for significant distances (50-75 cm) away from the interaction point and which will act as a source for further accelerating structures will be also investigated.

When FLAME phase II performances will be available (Short focal length OA Parabola: waist $\approx 2.5 \mu\text{m}$, $I \approx 10^{21} \text{ W/cm}^2$), we might select a bunch at $E = 30 \text{ MeV}$ with a narrow spread ΔE and still have a reasonable number of protons ($10^7 \sim 10^8$). This opens a very interesting perspective for applications such as hadrontherapy in connection with a post-acceleration stage in order to reach energies up and beyond 100 MeV. Indeed if

a sufficient current intensity can be reached at 30 MeV with a narrow spread $\Delta E/E \sim 1\%$ and a good beam quality after transport, energy selection and collimation, the protons bunch might be post-accelerated after injection in a high field linac (Fig.2), as the one developed for the INFN ACLIP project (suitable for medical applications) [3].

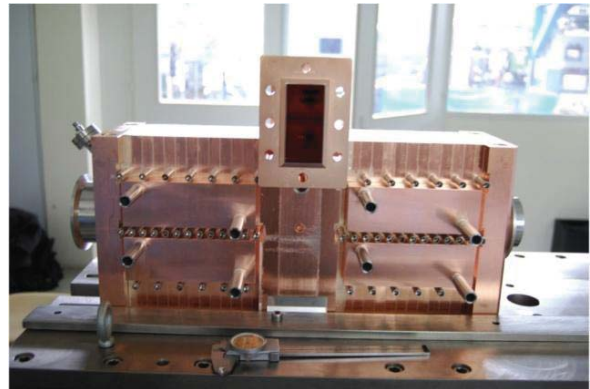


Fig. 2 The INFN ACLIP Linac

The mechanical setup

The SL-LILIA experiment has been designed to be housed in the interaction chamber available at the exit of the laser compressor in the FLAME bunker. The layout of the first phase of the experiment is shown in Fig. 3 and it foresees:

- a special designed optical breadboard, with standard metric holes format, to allow the definition of a common reference plane level and the assembly of components within the chamber;
- a multi shot target holder able to be remotely moved in x-y-z directions and rotated along the z-axis with respect to the laser beam. This will allow a very accurate positioning of the targets with respect to the laser beam and the possibility to perform multi shot experiments without having to open the vent of the chamber to replace the already used targets. The target holder has been designed for the use of aluminum foils

(pure up to 99.0%) with thickness as low as $1 \mu\text{m}$ and the possibility to provide up to 20 usable shots. The position accuracy of the targets with respect to the laser beam is of the order of $20 \mu\text{m}$ for the translation stages and of 0.1 degrees for the rotation stage. The alignment of the targets with respect to the power laser beam will be accomplished using alignment lasers and devoted optical windows in the chamber;

- a remotely movable multi-detector holder able to house 6 stacks of radio-chromic detectors to be used close (50 mm) to the interaction point. A fixed lead foil (3 mm thick) is used to avoid the damage of stacks adjacent to the one of interest for a specific laser shot;
- the availability of multiple detectors copes with the possibility to perform multiple experiments on different targets in a very short time, minimizing the fluctuations in the laser beam characteristics;
- a more accurate analysis of the energy distribution of the produced ions will be carried out at a fixed emission angle with a Thomson parabola (TP) spectrometer with its related detectors. A 150 mm diameter vacuum window in the interaction chamber at an angle of 120 degree with respect to the laser beam will allow the positioning of the TP.

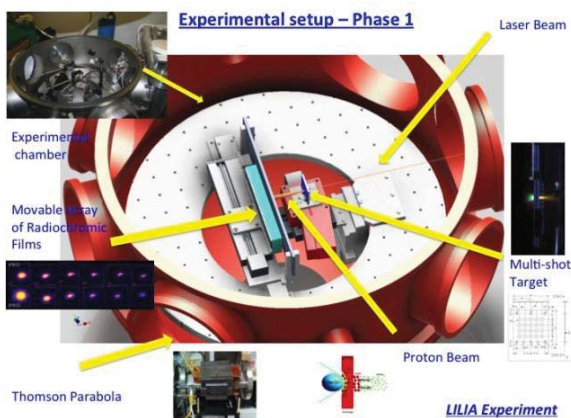


Fig. 3 Sketch of the LILIA mechanical setup

The ion detectors

Radio-chromic films

Radio-chromic detectors involve the direct impression of a material by the absorption of energetic radiation, without requiring latent chemical, optical, or thermal development or amplification. Detectors based on this phenomenon are available as films of different shape and build. They are obtainable as stacks of one or more subtle layer of sensitive material (usually a few microns thick) with intermediate polyester and adhesive layers to act as mechanical support. A radio-chromic film changes its optical density as a function of the absorbed dose. This property, along with the relative ease of use, led to adopt these detectors as simple ion beam transverse properties diagnostic tools. More sophisticated analysis procedures and more complex configuration of these detectors (usually stacks of many films) may give an estimation of energy distribution of the ions in the beam. Two specific commercially available detectors have been considered for the first measurements we are going to do: they are provided by Gafchromic company and named HD-810 and MD-55. The first type is a single layer film with a dynamic range from 0 to 250 Gy while the second one is a double layer film with a 60 Gy maximum dose value.

An analysis procedure based on the reading of the exposed films using a commercial scanner (Epson V750 Pro, maximum optical density 0-4), a calibration correlation with a ISO21550 reference target, along with the conversion curves optical density-dose provided by Gafchromic, lead us to an evaluation of the maximum error in the determination of the true dose of the order of 20%. This value is rather large and it is due both to intrinsic fluctuations in the film sensitivity in the production process and to errors in the image measurements.

A model has been developed for the reconstruction of the ion beam energy spectrum from readings of films arranged in a

stack. For a maximum energy of 10 MeV and a stack of 10 films, test cases give up energy distribution characterized by errors of the order of 25-30%.

The above considerations lead us to the idea to use radio-chromic films just in the first stages of the measurements, in order to provide us a rough idea of the emission process and of the dynamic range of energies and intensities we'll have to deal with.

Thomson Parabola spectrometer

A Thomson spectrometer has been designed and realized within the LILIA collaboration by the LNS group. The main characteristics may be so summarized:

- Analysis of proton and carbon beams ($Q= +1$ to $+6$) from 0.1 to 10 MeV;
- very compact design [160x144x150 mm^3];
- high magnetic field (tunable) up to 1850 gauss;
- high electric field (tunable) up to 20 kV/cm.

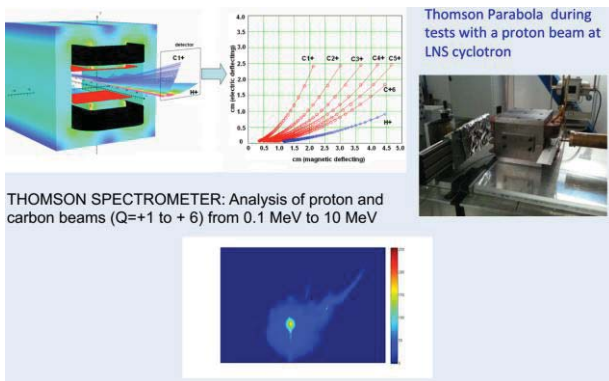


Fig. 4 Thomson Spectrometer for laser plasma facility

Solid state detectors

In addition to the more traditional passive radio-chromic films, or MCP detectors, active solid-state detectors have been studied and tested. They would give a real time information which of course is extremely important to control and change the experiment parameters.

Our basic aim has been the possibility to study and develop a silicon based detector, position sensitive and based on a matrix of simple PIN diodes. These detectors are

thought for the focal plane of the Thomson Parabola Spectrometer, being possible to arrange a 2D array with proper spatial resolution. After a laser shot, a pulse of ions reaches a single pixel of this matrix after being deflected by the TP. The pixel identifies ions with the same Z/A ratio and the same energy. The measure from the pixel is done by integration, with a delayed coincidence with respect to the laser pulse.

The main advantages of this sort of detectors with respect to a scheme that foresees a MCP and a CCD camera, may be pointed out in the following:

- the lower sensitivity of the detector is as low as a single proton charge;
- the capability to work in a rough vacuum environment;
- the availability of low-medium cost detectors;
- the flexibility to design specific geometric configurations able to suit the experimental requirements.

Different materials and structures have been considered and partly characterised: silicon photodiodes (PD), monolithic silicon telescope (MST) and SiC diodes.

Commercial silicon photodiodes (Hamamatsu) are relatively cheap and available in linear array, monolithic silicon telescopes (STm) offer two fully depleted diodes for optimum particle discrimination and large energy range, SiC diodes are radiation hard.

Tests have been performed on the two silicon structures at INFN-LNS and INFN-LNL with 30 MeV proton beam for the first (PD) and 1-5 MeV proton beam and 60 MeV/u carbon beam for the second (MST). The results show that charge collection is optimal in the fully depleted structure (MST), being the other affected by long tails and partial collection. SiC diodes are built on a low doped epitaxial layer and their response to high energy ions passing through will be verified soon.

We plan to further develop and test some of these detectors, but we still have to face the problems which arise from their use in an

extremely high noise environment, as the one present in the surroundings of the laser-target interaction.

Beam Focusing and Transport

The problem to immediately focus the emitted protons in order to obtain a useful beam and to transport it from the interaction region toward external measurement or post-acceleration facilities will be faced both from the numerical computation and experimental point of view. The following general considerations must be taken into account to deal with this item. The excellent emittance is the result of very short initial burst duration and very small "virtual" source size. However, proton beams emerging from a laser-driven target have typically a broad energy spectrum and large, energy dependent, divergence angle (typically 40-60 degrees depending on laser and target parameters). The inherent large divergence and the energy spread can make it hard to utilize the full flux of the proton beam for applications and indeed for further transport and beam manipulation. The manipulation of proton beams gives new challenges due to the high bunch charge and nature of the beams. This means it requires innovative approaches to enable beam control. The possibility to drive a laser emitted proton beam using a scheme based on a pulsed solenoid has been reported in literature [4]. We considered this approach really interesting and we carried out very preliminary simulation runs to define the main features of the components involved.

In our research we will focus on a scheme that foresees a pulsed high field solenoid to collimate the beam directly behind the target foil. This method will provide a first formation of the proton beam very close to the target. Then, it would be necessary to add a second stage to accomplish the final formation of the beam and its transport to a reasonable distance from the source (500-700 mm). This goal may be reached using a

magnetic chicane to filter the unwanted beam component and a conventional beam transport scheme based on high gradient permanent quadrupoles. Elements characterized by gradient values up to 200 T/m with small sizes (8 mm internal bore and 30 mm external diameter), are commercially available.

A start-to-end simulation from laser interaction to a post acceleration stage has been performed according to the scheme of Fig.5. It has been shown by 3D simulations that various acceleration mechanisms may allow to reach 60 MeV for the cutoff energy of protons.

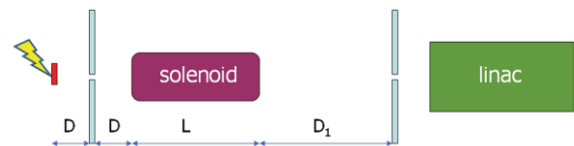


Fig. 5 Scheme of the transport line

A 30 MeV bunch with 2 ~ 3 % spread with over 10^8 protons can be selected with a simple transport line and over 10^7 can be post-accelerated up to 60 MeV with a compact linac [5, 6]. The LILIA experiment is intended to prove that the proposed scheme is applicable and to provide a possible candidate for medical applications.

Preliminary experimental results

During autumn 2012 the mechanical set up has been installed and aligned in the interaction chamber (Fig.6). The FLAME beam has been focused on the target and preliminary test have been carried out. During these tests we were limited for technical problems in the laser power that was of the order of 2 joules. Nevertheless, we have obtained the first experimental evidence of proton acceleration at the FLAME facility.

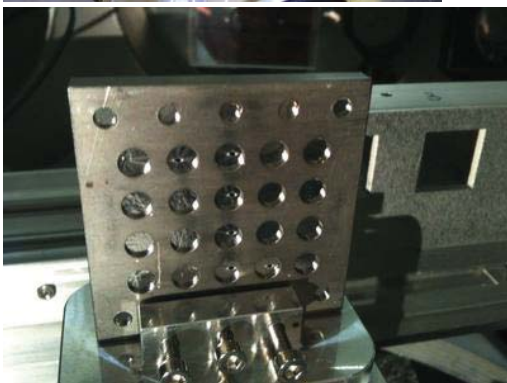
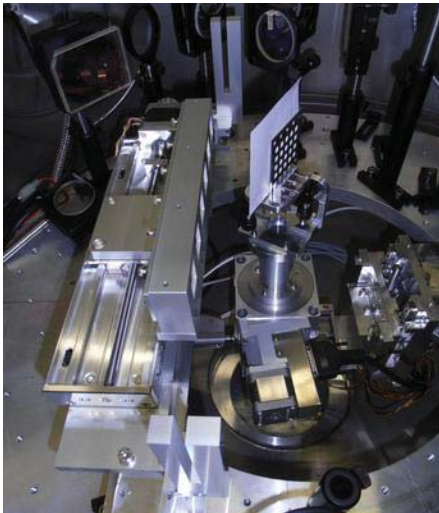


Fig. 6 The remotely movable radio-chromic detectors and the multi-shot target holder

Behind the multi-shot target two different detectors are placed: an EBT3 radio-chromic film by Gafchromic films or a CR-39 plastic polymer. The Figures 7 and 8 show the first pictures of the EBT3 and CR-39 impressed by protons emitted from a 3 μm Al target with a 1.5 Joule laser shot.

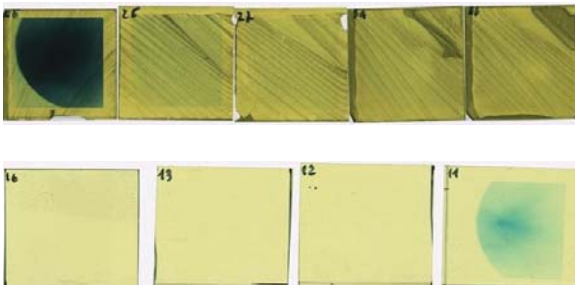


Fig. 7 Impressed EBT3 radio-chromic films

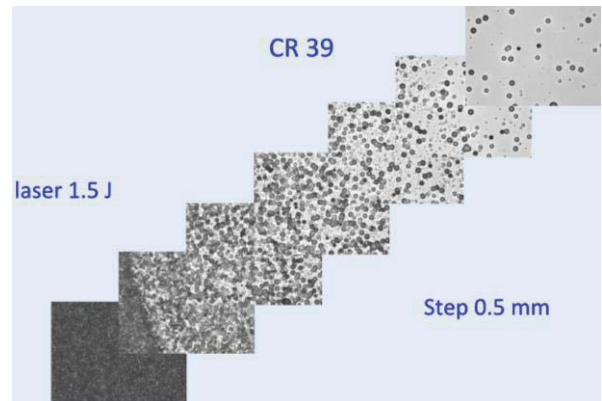


Fig. 8 CR39 film. The pictures are taken in different position of the exposed film with 0.5 mm steps. The CR39 film, also shielded to stop debris, shows a damaged black region in correspondence of the collimated emitted particles and the evidence of scattered protons in the surrounding area

The radio-chromic detector was shielded by a 6 μm thick aluminum foil in order to protect it by the light emission during the laser interaction. From the obtained results we can derive a lower limit for the maximum energy of the emitted protons of at least 1.6 MeV.

Acknowledgements

Luigi Gini from the INFN Milan, has given a continuous and decisive help for the preparation of the experimental set-up. Alvin Sashala Naik from the INFN and Polytechnic of Milan has contributed to the preparation and analysis of the CR39. To all of these people go our deepest thanks.

References

- [1] M. Ferrario et al. "Recent Results at the SPARC_LAB Facility" Proceedings of IPAC2012, New Orleans, Louisiana, USA.
- [2] A. Bacci, D. Batani, G.P. Cirrone, C. De Martinis, D. Delle Side, A. Fazzi, D. Giove, D. Giulietti, L. Gizzi, L. Labate, T. Levato, P. Londrillo, M. Maggiore, L. Martina, V. Nassisi, M. Passoni, A. Sgattoni, L. Serafini, S. Sinigardi, G. Turchetti, L. Velardi, "Laser induced proton acceleration at the FLAME facility in Frascati: LILIA experiment", Atti del II

Workshop Plasmi, Sorgenti Biofisica ed Applicazioni, Lecce, 26 Ottobre 2010, Edizione Coordinamento SIBA, ISBN 978-88-8305-087-9 (print version), (2012).

- [3] V. G. Vaccaro, M. R. Masullo, C. De Martinis, L. Gini, D. Giove, A. Rainò, V. Variale, L. Calabretta, A. Rovelli, S. Lanzone, S. Barone, "A Side Coupled Proton Linac Module 30-35 MeV: First Acceleration Tests. Proceedings of Linear Accelerator Conference LINAC2010, Tsukuba, Japan.
- [4] D. Shuman, E. Henestrokza, G. Ritchie, W. Waldron, D. Vanacek, S.S. Yu, "A pulsed solenoid for intense ion beam transport"

proceedings of 2005 Particle Accelerator Conference, 3798-80 (2005)

- [5] Giorgio Turchetti, Stefano Sinigardi, Pasquale Londrillo, Francesco Rossi, Marco Sumini, Dario Giove, Carlo De Martinis, "The LILIA experiment: Energy selection and post-acceleration of laser generated protons. AIP Conf. Proc. 1507, 820 (2012); doi: 10.1063/1.4773804.
- [6] G. Turchetti, S. Sinigardi, P. Londrillo, F. Rossi, D. Giove, C. De Martinis, "Transport and energy selection of laser generated protons for postacceleration with a compact linac". Physical Review Special Topics-Accelerators and Beams 16 (3), 031301

High voltage pulse of short duration to feed solenoids for intense ion beam transport

Nassisi V¹, Delle Side D¹, Velardi L¹, Buccolieri G¹, Paladini F¹, Giove D², De Martinis C², Fazzi A³

¹ Department of Mathematics and Physics, University of Salento, LEAS Laboratory and INFN, Lecce, Italy

² Department of Physics, University of Milan and INFN, Milan, Italy

³ Polytechnic of Milan and INFN, Milan, Italy

Abstract

A high voltage pulser up to 50 kV, with a main pulse of 2 μs time duration, was realized using a fast high voltage capacitor of 150 nF (50 kV) connected to the ground by a homemade spark-gap. The circuit, contained in a metallic box, had short electric connections in order to reduce any stray inductances. The diagnostics was performed by two systems: an auto-integrating Rogowski coil and an integrator connected to a current transformer, both suitable for pulses longer than 1 μs . In order to get the above characteristic the Rogowski coil circuit must have a ratio L/R higher than 1 μs , while the integrator, formed by a resistance and a capacitance, must get the product RC higher than 1 μs . In the first system, the load resistance can be easily reduced, instead it is very difficult to reduce the coil resistance. The Rogowski coil we build exhibited a ratio $L/R=2 \mu\text{s}$, while the integrator circuit connected to the transformer exhibited a value $RC=5 \mu\text{s}$. We made a solenoid with an inductance of 2.8 μH (11 rings, length 14 cm) which was fed by the current generated by the pulser up to 4 kA, 1 μs at 24 kV of charging voltage. Under the above conditions, we estimate a magnetic field of 0.4 T applying the Ampere law. Actually, the magnetic field was measured in dc mode by means of a Hirst GM07 gauss-meter having a conversion coefficient of 0.08 mT/A which determined a magnetic field at the center of 320 mT. Potentially, at the maximum voltage of 50 kV we can get a magnetic field up to of 0.7 T.

Introduction

To focus hadron beams of cylindrical symmetry, a magnetic field provided by a solenoid is used[1]. At moment the magnetic field structure is not well known since depends on the development of the Flame facility in Frascati. Flame is a high power Laser with an intensity up to 10^{21} W/cm^2 [2]. An experiment is in progress named LILIA. The aim of LILIA is to study, design and verify a scheme which foresees the production, the characterization and the transport of a proton beam toward a stage of post acceleration. To improve the transport or to enhance the beam

emittance, a magnetic field of suitable gradient is necessary. We challenge to get a short solenoid to be fitted inside the interaction chamber of Flame with a maximum field of 0.7 T.

Theory

In this phase we wanted to make a solenoid utilizing the material available in the LEAS laboratory. We used as conducting wire a common 10 mm diameter copper tube. It formed a solenoid composed of 11 rings of 3 cm radius and 14 cm length. By the Ampere law

$$B = \mu_0 \frac{iN}{l} k$$

where k is the factor of correction, we can estimate the magnetic field. To get fields of the order of Tesla, high currents in the range of tens kA are necessary.

The value of the inductance of the above solenoid is computed by the ratio Φ_B/i obtaining $L = 2.8 \mu H$.

Fig. 1 reports a working scheme of the solenoid.

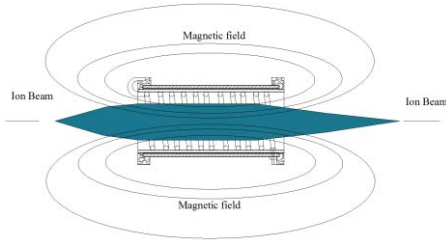


Fig. 1: Schematic distribution of the magnetic field

Materials and methods I

To get the above value a high voltage must be applied to solenoid. So we made a pulser composed by a capacitor (150 nF, 50 kV) closed on the solenoid by a home-made spark gap, Fig. 2

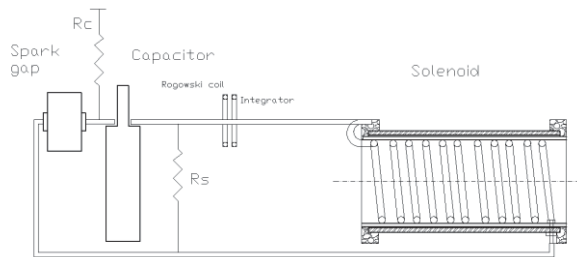


Fig. 2: Scheme

A high voltage power supply charges the capacitor by the charging resistor R_c and R_s , discharging resistor. The supply current was measured by two diagnostic systems. Under 24 kV charging voltage, both systems provided a pulse current of about 4 kA as maximum value, with a damped sinusoidal waveform of frequency 230 kHz. The main pulse duration was $1 \mu s$, while the total duration was of $20 \mu s$. Fig. 3. shows the output signals recorded by two different diagnostic systems: upper trace by an integrator connected to a current transformer; bottom trace by a Rogowski coil.

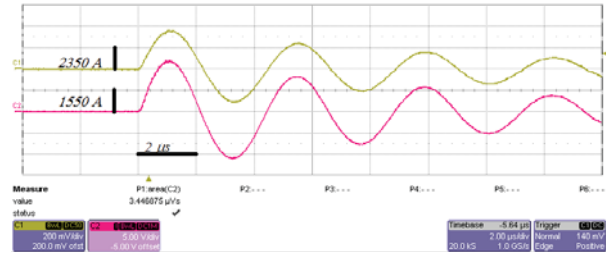


Fig. 3: Output current waveform: Upper by an integrator; bottom by a Rogowski coil.

Materials and methods II

The Rogowski coil[3] utilized was composed of 140 rings realized by a conductive wire of 0.8 mm in diameter. The diameter of the rings was 2 cm, while the one of the coil was 3.5 cm. Its inductance was $11 \mu H$ while its resistance 0.4Ω . To get the properties of an integrator, the coil was closed on a load resistor of 0.5Ω . In this conditions the integrating time $L/R = 12 \mu s$. Therefore, by the theory, the longest pulse that the system can diagnose is less than $12 \mu s$, 1 or $2 \mu s$. Diminishing the R value, the integrator time increases only up to $4 \mu s$ and the response tends to zero.

The second diagnostic system, the integrator connected to a current transformer, was composed of a coil with 60 rings connected to an integrator composed of a resistor of 331Ω and an capacitor of 15 nF connected to ground. The small number of rings allows to diminish the stray capacitance between the coil and the case, avoiding the oscillations and allowing the application of the integrator of high input impedance.

The calibration of both systems was performed by means of a fast exponential pulse. It was obtained by a pulser containing a 110 nF capacitor connected by a fast switch to a 50Ω coaxial structure as shown in Fig 4.

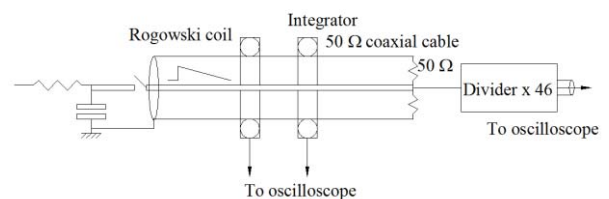


Fig. 4: Experimental setup for calibration.

The input current is calculated by the signal of the divider multiplying for 46/50, bottom trace Fig.5. The upper trace is the Rogowski coil response. The attenuator coefficient is $A=310 \text{ A/V}$.

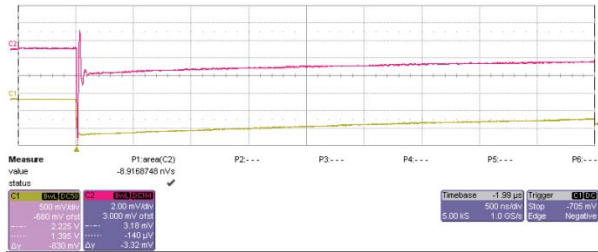


Fig. 5: Rogowski coil calibration. Attenuation $A= 310 \text{ A/V}$.

Fig. 6 shows the waveform of the input current (upper trace) and the response of the integrator/transformer (bottom trace). The attenuator coefficient is $A=260 \text{ A/V}$

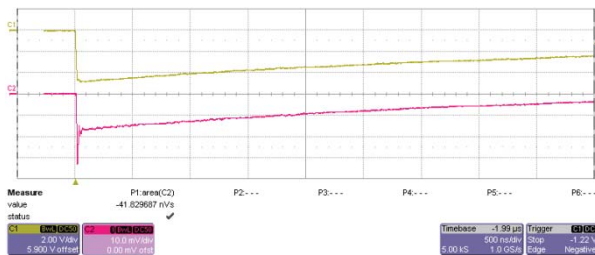


Fig. 6: Integrator/transformer calibration. Attenuation $A= 260 \text{ A/V}$.

Results

The magnetic field provided by the solenoid can be evaluated by the theory utilizing the current intensity value. By Fig. 3 the maximum current is about 4 kA and the corresponding field is 0.4 T. Due to the experimental conditions this value is oversized. The high voltage does not allow to get a direct measurement of the field, so we fed the solenoid with a low voltage in order to get a modest current value, 10 A. In these conditions we measured the magnetic field inside the solenoid utilizing the gaussmeter GM07. Under the above current condition, the magnetic field was very modest and the correlation between field and current was 0.08 mT/A. By this value we determined the

magnetic field at 4 kA current, which was 320 mT.

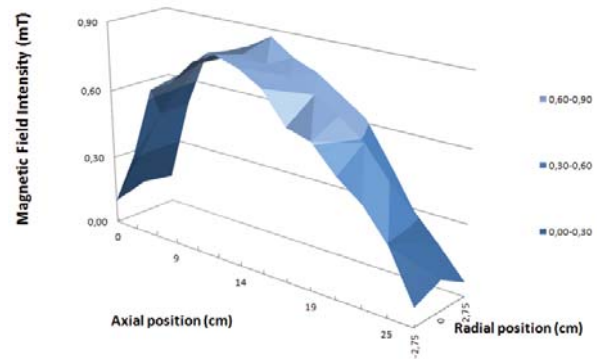


Fig. 7: Magnetic field inside the solenoid @ 4 kA.

Conclusions

We have realized magnetic field pulse with the main duration of $2 \mu\text{s}$, 320 mT at 24 kV power supply. The pulse waveform was a damped sinusoid for a duration of $20 \mu\text{s}$. At the maximum voltage of 50 kV we can get a magnetic field of 0.7 T of the same duration.

References

- [1] D. Shuman, E. Henestroza, G. Ritchie, W. Waldron, D. Vanacek, S.S.Yu, LBNL, Proceedings of 2005 Particle Accelerator Conference, pag. 3798-800, 2005.
- [2] A. Bacci, D. Batani, G.P. Cirrone, C. De Martinis, D. Delle Side, A. Fazzi, D. Giove, D. Giulietti, L. Gizzi, L. Labate, T. Levato, P. Londrillo, M. Maggiore, L. Martina, V. Nassisi, M. Passoni, A. Sgattoni, L. Serafini, S. Sinigardi, G. Turchetti, L. Velardi, "Laser induced proton acceleration at the FLAME facility in Frascati: LILIA experiment", Atti del II Workshop Plasm, Sorgenti Biofisica ed Applicazioni, Lecce, 26 Ottobre 2010, Edizione Coordinamento SIBA, ISBN 978-88-8305-087-9, pag. 136-143 (print version), (2012).
- [3] V. Nassisi and A. Luches, "Rogowski coil: Theory and Experimental Results", Rev. Sci. Instrum., 50, 900-02 (1979).

Advances in the SPES Project and its ion source systems

D. Scarpa¹, M. Manzolaro¹, J. Vasquez¹, L. Biasetto¹, A. Cavazza¹, S. Corradetti¹, J. Montano¹, M. Manente², D. Curreli³, G. Meneghetti³, D. Pavarin^{2,3}, A. Tomaselli⁵, D. Grassi⁴, P. Benetti⁵, A. Andrighetto¹, G. Prete¹

¹ INFN - Legnaro National Laboratories, Legnaro, Padova, ITALY

² CISAS (Centro Interdipartimentale Studi Attività Spaziali), University of Padova, Via Venezia 1, Padova, ITALY

³ Department of Mechanical Engineering, University of Padova, Via Venezia 1, Padova, ITALY

⁴ Università di Pavia, Dipartimento di Chimica Generale, Via Taramelli 12, Pavia, Italy

⁵ Università di Pavia, Dipartimento di Ingegneria Elettronica, Via Ferrata 1, Pavia, Italy

Abstract

SPES (Selective Production of Exotic Species) is an INFN project to develop a Radioactive Ion Beam facility as an intermediate step toward the future generation European ISOL facility EURISOL.

The aim of the SPES project is to provide high intensity and high-quality beams of neutron-rich nuclei to perform forefront research in nuclear structure, reaction dynamics and in interdisciplinary fields like medical, biological and material sciences.

It is based on the ISOL method with an UCx Direct Target able to produce 10¹³ fission/s by proton induced fission in the UCx target. The development of new target ion source systems for the SPES facility is currently in progress at Legnaro National Laboratories. In this context the study of ion sources and their performance in terms of ionization efficiency and transversal emittance is a crucial point in order to maximize the available yields, particularly for short-lived isotopes. In this work preliminary off-line measurements for the SPES surface, plasma and laser ion sources are presented.

The SPES project

SPES is a new mid-term ISOL facility dedicated to the production of neutron-rich beams. It is an INFN project involving the two national laboratories, LNL and LNS and other INFN sites in Italy. The project consists of a proton driver, a 70 MeV cyclotron with two exit ports for a total current of 750 μ A, an UCx ISOL target and ion-source, a beam transport system with a high resolution mass selection and the superconductive PIAVE-ALPI accelerator complex in operation at LNL that will be used as radioactive beam re-accelerator.

A 40 MeV 200 μ A proton beam, delivered by the cyclotron, impinges on the uranium carbide

target, the neutron rich isotopes produced as fission fragments with a rate of 10¹³ fission/sec, are extracted by the ion source, mass separated and sent via proper beam lines to the PIAVE-ALPI re-accelerator. The re-acceleration stage with the superconductive linac ALPI qualifies the project in terms of good quality of beams (intensity and energy spread) and in the final energy which is sufficient to perform nuclear reactions close to the Coulomb barrier between medium-heavy mass ions. The uranium carbide targets have been already developed and represent an innovation in terms of capability to sustain the primary beam power.

The ions, extracted in a 1+ state with different ion sources, depending on the kind of

isotope, will be transported in ALPI, with a benefit from the experience gained in LNS (Catania) with the EXCYT project, which will be taken as a reference for the optimization of the various magnetic elements and diagnostics. To fit the proper entrance parameters for beam re-acceleration with the linac, an RFQ-cooler and a Charge Breeder are planned. The design and construction of the Charge Breeder will be made in collaboration with SPIRAL2.

With the high intensity beams delivered by SPES, a challenging and broader range of studies in nuclear spectroscopy and reaction mechanism will be performed. Interesting areas where new data will be collected are those in the very neutron rich regions, where shell evolution is an issue. Effects of how the pairing interaction is modified in the nuclear medium will receive significant inputs by measurements of multi-nucleon transfer reactions to specific nuclear states. Effects of rotational damping in the decay of high energy levels, for instance the dynamical dipole emission, will be studied by changing the N/Z of projectile and target. Sub-barrier fusion processes will make use of proper neutron rich to investigate the tunneling process in presence of very positive Q-values, an issue interesting also for astrophysics.

As the cyclotron can supply two beams at the same time, a second independent facility can be operated. Interest has been already shown up by other communities. In particular, the high intensity proton beam could be used to produce innovative radioisotopes for nuclear medicine as well as neutrons in a wide energy spectrum, which, in turn, is interesting for measurements of neutron capture reactions of astrophysical interest.

The SPES layout is shown in figure 1; the ISOL facility is located in the white area, housing the cyclotron proton driver, the two RIB targets, the High Resolution Mass Spectrometer (HRMS) and the transfer lines. Two laboratories for applied

physics and other applications are planned, which makes use of the Cyclotron proton beam.

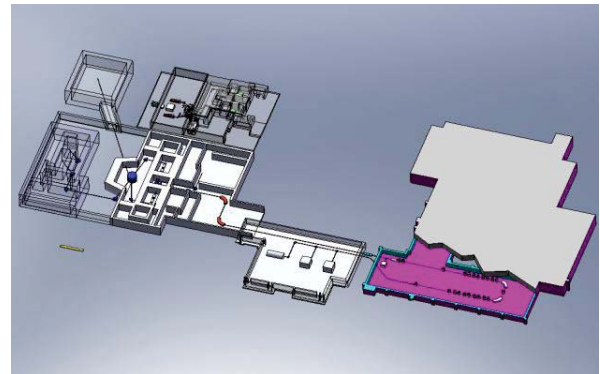


Fig. 1 The lay out of the SPES ISOL facility and connection to the re-accelerator.

The Target Ion-Source system

The interaction of the proton beam with the UCx target will produce fission fragments of neutron-rich isotopes that will be extracted by thermal motion and ionized at 1^+ charge state by a source directly connected with the production target.

The hot-cavity ion source chosen for the SPES project was designed at CERN (ISOLDE) [9]. The conceptual design is shown in figure 2.

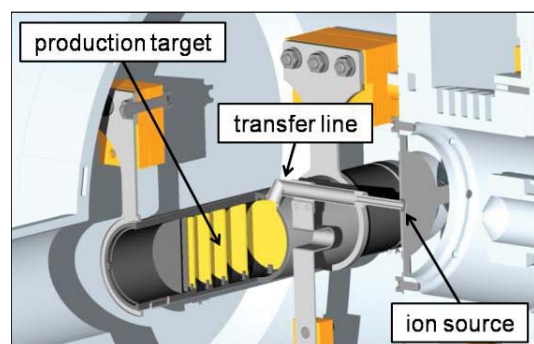


Fig. 2 Conceptual design of the SPES production target system.

The source has the basic structure of the standard high temperature RIB ion sources employed for on-line operation. The ionizer cavity is a W tube (34 mm length, 3 mm inner

diameter and 1 mm wall thickness) resistively heated to near 2000°C. The isotopes produced in the target diffuse in the target material and after that will effuse through the transfer tube (its length is approximately equal to 100 mm) into the ionizer cavity where they undergo surface, plasma or laser ionization. Ideally those atoms should be ionized +1, then extracted and accelerated to 30-60 keV of energy and after that injected in the transport system. For alkalis and some rare earth elements high ionization efficiencies can be achieved using the surface ionization technique. The halogens have too high ionization levels and must be ionized by plasma ionization source. For most part of the others elements, the laser resonant photo-ionization, using the same hot cavity cell, is a powerful method to achieve a sufficient selective exotic beams. This technique is under study in collaboration with the INFN section of Pavia. To produce the large part of the possible beams three class of ion sources are under development at SPES: the Spes Surface Ion Source (SSIS), the Spes Plasma Ion Source (SPIS), the Spes Laser Ion Source (SLIS). In Figure 5 the areas of application of the different sources are shown.

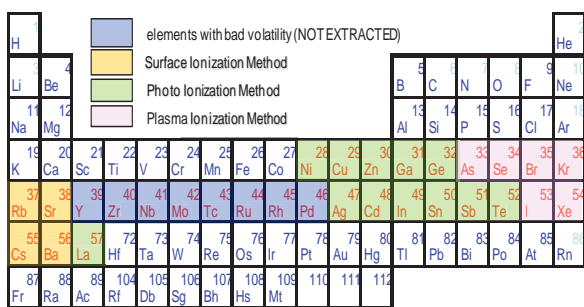


Fig. 5 The main isotopes that will be ionized and extracted in the SPES project.

An extensive simulation of the target behaviour for thermal and release properties is at the bases of the target-ion-source design. Experimental work to bench mark the simulations was carried out in collaboration with HRIBF, the Oak Ridge National Laboratory ISOL facility (USA).

Surface and Plasma ion sources

With the aim to characterize both SSIS and SPIS, a dedicated test bench delivering stable ion beams has been manufactured at LNL². It is composed of three functional subsystems: the ion source complex, the beam optics subsystem and the diagnostic subsystem. In the first one 25 kV of potential difference between the ion source and the extraction electrode allows the ion beam generation. The aforementioned ion sources and the main accessories needed for their functioning and testing are shown in figure 1. During the tests both the ion sources were accurately positioned inside a vacuum chamber able to guarantee pressure levels between 10⁻⁵ and 10⁻⁶ mbar.

The SSIS is the first ion source tested at LNL for the SPES project: it is able to produce efficiently +1 ions for the elements with ionization potential smaller than 7 eV, mainly for the alkali and the alkaline earth metals (such as Rb, Cs, Sr, Ba). Efficiency values higher than 50% can be reached with this device. The SSIS is at present similar to the ISOLDE/CERN MK1 surface ion source. It is composed of a W tubular ionizing cavity (length, external diameter and internal diameter equal to 34, 5 and 3.1 mm, respectively) connected on one side to a Ta support and on the other one to the Ta transfer line³. The oven device represented in figure 1 is constituted by a 250 mm long Ta tube, with external and internal diameters of 2 and 1 mm, respectively; at one end a calibrated solution of the requested element is placed and hermetically sealed in, whereas the other end is connected to the transfer line and thus to the ion source. During operation the SSIS and the transfer line are resistively heated at temperature levels close to 2000°C. An independent power supply heats in a similar way the oven, allowing the atoms of interest (introduced with the calibrated solution) to effuse towards the ion source.

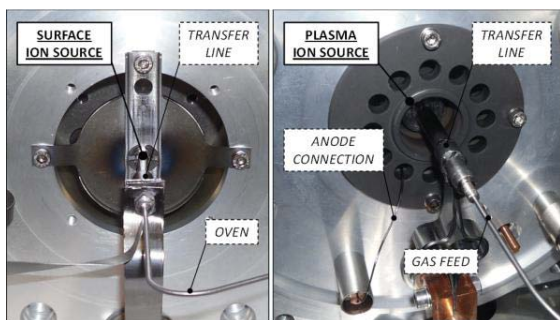


Fig. 3. The SPES Surface Ion Source (SSIS) and the SPES Plasma Ion Source (SPIS).

The SPIS (based on the principle of the FEBIAD ion source⁶) is the second source tested at the LNL test bench. It is a particular version of the ISOLDE/CERN MK5 source⁴, a non selective device able to ionize a large spectra of elements, in particular noble gases. The main differences of the SPIS respect to the MK5 source are the following: the discharge chamber and the anode cylinder are made of tantalum instead of molybdenum, and the anode is electrically insulated thanks to three small cylinders made of Al_2O_3 , avoiding the usage of BeO_2 . In addition the SPIS is not thermally insulated by external molybdenum screens and the parts composing the cathode are connected by TIG welding instead of electron beam welding. A Ta wire connects the anode to the power supply used to increase its electrical potential respect to the rest of the source. The Ar beams provided for the preliminary study of the SPIS were produced thanks to a constant and regular Ar gas flow. It enters the vacuum chamber by means of a calibrated leak and then flows through a thin Ta tube in the direction of the Ta transfer line.

Ionization efficiency test

The test bench described in the previous paragraph is still under development. In particular the mass separator is not installed yet and it is not possible, at present, to select a particular mass and an ion charge state. In this context accurate ionization efficiency

measurements cannot be performed. Waiting for more detailed sets of measurements to perform in the next future, some preliminary ionization efficiency estimations were done for Cs using the SSIS. Taking advantage of SSIS's selectivity and capability to produce exclusively singly charged ions, beam contaminants could be reduced to negligible quantities and the beam current monitored by the Faraday cup could be rapidly converted into an ion flux. Ionization efficiency for Cs was measured using calibrated Cs samples housed inside the oven (see figure 3). To perform this kind of measurement the SSIS's temperature was rapidly increased up to 2100°C. Then the oven was heated, allowing the Cs sample to vaporize, while the ion current was continuously recorded until the sample completely evaporated out of the source. The ionization efficiency was calculated as the ratio of the integrated number of detected ions to the total number of atoms in the calibrated sample. Some background tests (performed installing the oven without Cs sample and integrating the ion current) showed that contaminants can be considered negligible. An ionization efficiency value of about 51% was obtained, by far lower than the theoretical value of 95% calculated using the well known Saha-Langmuir equation⁷. This discrepancy (reported in other similar works⁷) seems to be strictly linked to the high volatility of Cs. In fact a considerable fraction of the Cs atoms could be lost during the positioning of the sample inside the oven and during the heating procedure, before the tungsten cavity is hot enough to ionize the atoms. During the tests the ion beam current was always kept between 1 and 3 μA . The extraction voltage ($V_{\text{extraction}}$) was fixed at 25 kV. Accurate ionization efficiency measurements (using the new Wien filter) for both SSIS and SPIS, will be performed in the next future.

Emittance measurements

Emittance measurements for the SSIS and the SPIS were made following the same approach proposed in ². In particular the root-mean-square (RMS) emittance for both SSIS and SPIS was monitored varying the extraction electrode position. Results are reported in figures 4 and 5. For both ion sources the minimum RMS emittance value was detected at about 75 mm of distance between the extraction electrode and the source extraction hole. The aforementioned results confirm data reported in ² and ⁸.

During the SSIS emittance measurements a Cs beam of intensities between 350 and 400 nA was provided. A current of 360 A was set to heat the transfer line and the ion source. For the SPIS emittance tests a 1 μ A Ar beam was kept stable for all the measurement time. The cathode current and the anode voltage (V_{anode}) were set to 330 A and 150 V, respectively. A current of 5 A was adopted to feed the anode magnet. For all the emittance measurements $V_{extraction}$ was fixed at 25 kV.

Numerical simulation of the ion beam extraction and emittance calculation for the Spes Plasma Ion Source

With the aim to study the SPIS beam extraction system, a set of numerical simulations has been done using the 3D Particle-in-Cell code named "F3MPIC": it is a brand new

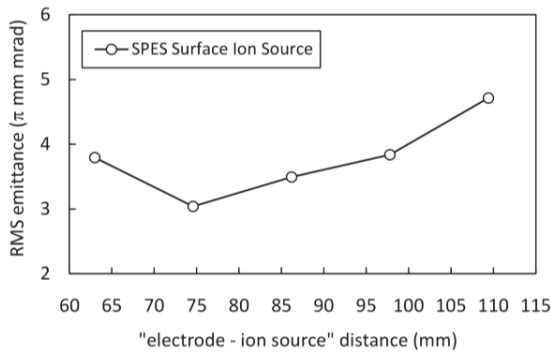


Fig. 4. Measured RMS emittance for the SPES Surface Ion Source.

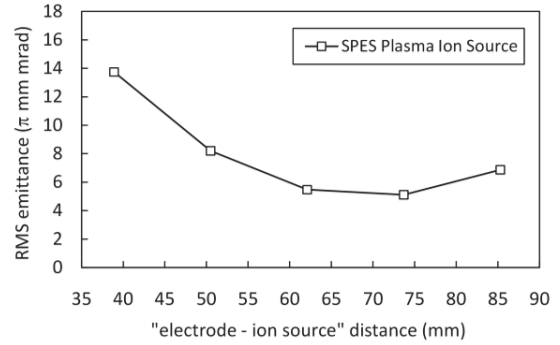


Fig. 5. Measured RMS emittance for the SPES Plasma Ion Source.

electrostatic and electromagnetic code recently developed at CISAS for plasma simulations in complex geometries ⁵. F3MPIC works in time domain, moving particles inside a volumetric mesh composed by tetrahedra. The tracking of particles inside the tetrahedra is done using a fast priority-sorting algorithm. Both charged and not-charged species can be simulated. Static and dynamic electromagnetic interactions among charged particles are treated consistently. At each time step the charge and the current densities obtained from particle motion is weighted on the vertex of the tetrahedra, and then the Poisson equation of Electrostatics, or the full set of Maxwell equations, are solved by means of the finite element method. The interaction of charged particles with neutral species is treated using the Monte-Carlo-Collision method.

The SPIS has been numerically simulated with F3MPIC, using a two-species plasma of single-ionized Ar ions plus electrons. Both plasma species are treated in kinetic conditions, with typical time scales regulated by the fastest electrons species, corresponding to time-steps below the nano-second time scale. The equilibrium of the extracted Ar beam is then reached on time scales greater than 600 nano-seconds. Ions and electrons are generated inside the volume of the anode, with initial temperatures of $T_i = 300$ K and $T_e = 1.0$ eV. Ions are extracted by the potential difference of 25150 V ($V_{extraction} + V_{anode}$) between the anode

and the extraction electrode. Figure 6 shows the simulation of the extracted ion beam in stationary conditions. Particle numerical diagnostic has been placed on a control surface after the electrode, where the electric field is small and the ion beam has already formed. Here the positions and velocities of particles have been recorded in order to obtain the beam properties of interest, in particular the RMS emittance.

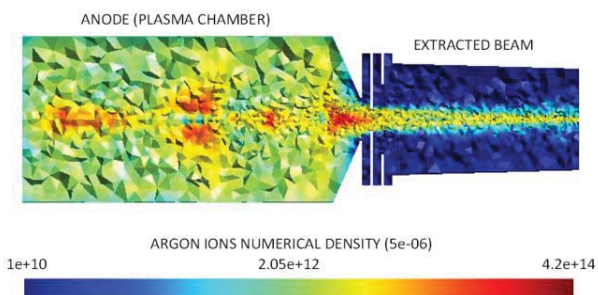


Fig. 6. Simulation of the SPIS extracted ion beam.

With the purpose to validate the code with experimental data, the RMS emittance for an “electrode – ion source” distance ($d_{\text{extraction}}$) of 38 mm was calculated; a value of 16.8π mm mrad was obtained, in good agreement with the correspondent experimental value (13.7π mm mrad, see figure 3). New simulations are in progress at CISAS to scan more values of $d_{\text{extraction}}$. Once the SPIS F3MPIC model will be validated in a more complete way, it will be used to optimize the beam extraction of the SPES ion sources.

Laser ion-source studies

At Spectroscopy Laser Laboratory of Chimica Generale in Pavia University studies about Aluminum laser photoionization were made using Optogalvanic Signal (OGE) in Hollow Cathode Lamp (HCL). We investigated two kinds of OGE signals: the slow or thermal and fast one, both obtained with a commercial Aluminum HCL manufactured by ISTC. The laser ionization path for Aluminum is the one color,

two steps selective photoionization arising from laser wavelengths closed to 308 nm [10].

Pavia experimental setup

The Pavia experiment (figure 7) involves one Lambda Physik LPD 3002E dye laser pumped by 10 Hz Quanta System flash lamp frequency doubled Nd:YAG laser .



Fig. 7. Pavia Experimental setup.

The tunable dye laser radiation, once duplicated with a second harmonic generator Potassium Dihydrogen Phosphate crystal (KDP) in order to achieve the proper wavelength, is focused into the HCL through a 10 cm focal lens. Both optogalvanic signals are picked-up from the lamp power supply circuit. In these particular kind of set-up the HCL is used as atomic source. The atoms of Aluminum loaded into the cathode are sputtered by the atoms of the plasma which sustain the lamp discharge. Once sputtered, Aluminum atoms are available for spectroscopic investigations, while the power supply electric field separates charges when created and allows to collect OGE signals. In order to record the signals we use a boxcar averager and a USB6009 National Instruments datalogger to digitalize and store data on pc.

Pavia signals and results

Two kinds of signal are collected from these measurements.

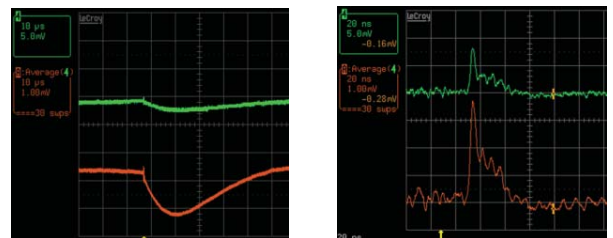


Fig. 8. Left: slow (10 $\mu\text{sec}/\text{div}$; 5 mV/div) OGE Right: fast (20 nsec/div; 5 mV/div) OGE.

1) Thermal or “slow” optogalvanic signal:

The laser resonant radiation is absorbed by the Aluminum atoms, modifying the Boltzmann distribution of electronic levels and in tens of microseconds a new momentary Boltzmann equilibrium holds up, including the ionization one. A change of discharge impedance occurs, indeed. If laser radiation wavelength is off resonance its energy is not absorbed and the collected signal is zero. Temporal behavior of the signal is reported in figure 2, left.

2) “fast” optogalvanic signal:

In the particular case of Aluminum, two steps absorption of the laser radiation near 308 nm wavelength brings atoms to ionization. The first resonant absorbed photon excites the atom while the second one, with the same energy, ionizes the excited atom. In this phenomenon, electrons are immediately available as carriers instantaneously modifying the lamp impedance, hence producing a signal. Ionization process persists tens of nanosecond following the laser pulse duration. Example of this signal is reported in figure 2, right. The “fast” OGE signal[4] is observable not only with Aluminum. The same process can also take place in other elements, with different colors and steps ionization schemes, as spectroscopic investigations suggest.

Photo-ionization in LNL hot cavity

The Aluminum ionization path verified in the HCL System can be used also in the framework of the SPES project in order to provide Aluminum ionization in a hot cavity.

In Legnaro we performed Aluminum ionization using the LPX200 excimer laser by Lambda Physik, charged with XeCl gas, lasing around 308 nm wavelength. The spectrally inhomogeneous laser radiation overlaps the absorption line of aluminum and tests are going on to control is selective photoionization

occurs. The Legnaro set-up (figure 9) involves the SPES front end apparatus. A small tantalum tube (oven) is charged by a calibrated amount of Aluminum and it is directly connected to the hot cavity of SPES system.

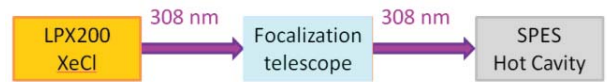


Fig 9. Legnaro Experimental Setup

Once heated the oven to 2000 °C it evaporates atoms of Aluminum which reach the hot cavity and are ready for ionization. Laser radiation, delivered by a focusing telescope 6 meter far away, enters in the 3 mm diameter hot cavity producing ionization. Ionized atoms are extracted by means of the 25 kV high voltage extractor and they are collected by a faraday cup.

Legnaro signals and results

The Faraday Cup (FC) current is the result of the ionization process in the hot cavity. In the normal operation of the front end system, the FC is inserted directly in front of the extractor, collinear to the ion beam after a quadrupole and an electrostatic lenses system.

In order to allow laser radiation to reach the hot cavity, it is mandatory to displace the FC from the laser beam propagation axes. The quadrupole and electrostatic lenses allow to collect anyway a signal. Figure 10 represents this setup: the red arrow symbolizes the laser beam path straight to the ion source, the green arrow indicates the ion beam path towards the faraday cup. Variations in the laser pulse energy or in the laser repetition rate directly affect the faraday cup current. These variations are proof of laser photoionization. The figure 11 represents the variation of the faraday cup current produced by the sweep in the frequency of the of the laser pulses (a) and the variation produced by two energy pulses set (b).

At the Pavia Spectroscopic Lab., we investigated atomic Aluminum absorption lines

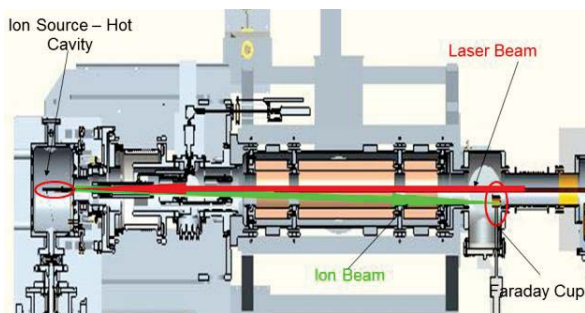


Fig. 10. Laser beam path (red) toward hot cavity vs Ion beam path (green) toward off center FC.

using tunable laser. Thanks to OGE signals a simple way in view of better understanding the spectral properties of photoionization on Aluminum atoms was pursued with success. In Legnaro INFN National Lab, first laser photoionization was obtained with excimer XeCl laser, covering a possible ionization path for Aluminum. The results in the measured ion beam current allows to conclude that under laser action a ionization process takes place in the SPES hot cavity even if a complete system characterization is nowadays not possible. Further investigations using a mass separator will certify the selectivity of laser photoionization on Aluminum despite others atomic species present in the hot cavity, permitting ionization and transport efficiency measurements.

Acknowledgments

The authors wish to thank L. Biassetto, A. Galatà, M. Lollo, A. Cavazza, L. Costa, G. Bassato, M. Giacchini, M. Poggi and L. Boscagli from INFN-LNL for their precious scientific and technological support. Special thanks also to the ISOLDE group (CERN). Numerical simulations have been conducted using F3MPIC plasma code developed in the Helicon Plasma Hydrazine COMbined Micro (HPH.com grant agreement n° 218862) research program funded in the 7th Framework Programme (FP7/2007-2013) by REA. A special thank to D. Rondini from CISAS for the development of F3MPIC.

References

- [1] A. Andrighetto, C.M. Antonucci, S. Cevolani, C. Petrovich, M. Santana Leitner, Eur. Phys. J. A **30**, 591 (2006).
- [2] J. Montano, J. Vasquez, A. Andrighetto, G. Bassato, L. Calabretta, M. Poggi, G. Prete, Nucl. Instrum. and Meth. Phys. Res. A **648**, 238 (2011).
- [3] M. Manziolaro, G. Meneghetti, A. Andrighetto, Nucl. Instrum. and Meth. Phys. Res. A **623**, 1061 (2010).
- [4] S. Sundell, H. Ravn, The ISOLDE Collaboration, Nucl. Instrum. and Meth. Phys. Res. B **70**, 160 (1992).
- [5] D. Pavarin, F. Ferri, M. Manente, D. Curreli, D. Melazzi, D. Rondini, A. Cardinali, Proceedings of the 32th International Electric Propulsion Conference, Wiesbaden (Germany), 11-15 September 2011.

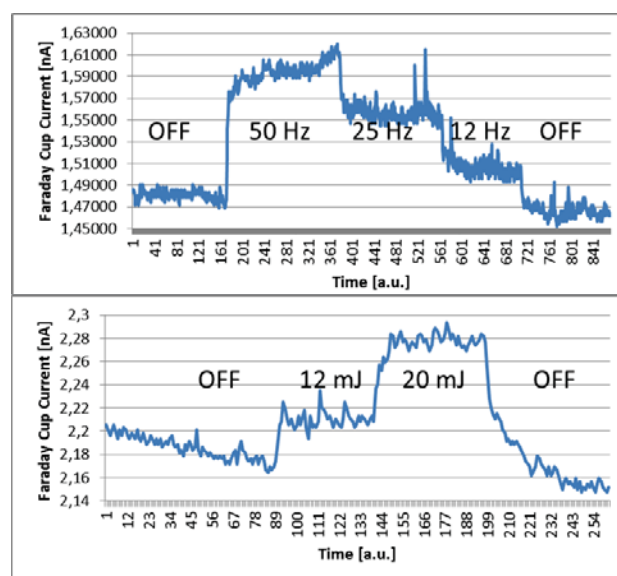


Fig. 11. Faraday cup current signal of ion collected under laser action in a) proportional to several repetition rate value, b) proportional to several energy pulse value.

- [6] R. Kirchner, E. Roeckl, Nucl. Instrum. and Meth. Phys. Res. **133**, 187 (1976).
- [7] Y. Liu, Y. Kawai, H. Z. Bilheux, Proceedings of 2005 Particle Accelerator Conference, Knoxville (Tennessee), 16-20 May 2005.
- [8] F. Wenander, J. Lettry, M. Lindroos, Nucl. Instrum. and Meth. Phys. Res. B **204**, 261 (2003).
- [9] J. Lettry, Proceedings of the 1999 Particle Accelerator Conference, New York, 1999
- [10] Tomita, Mattolat, Kessler, Raeder, SchwelInus, Wendt, Watanabe, Iguichi, J. of Nucl. Sci. and Tech., Suppl. 6, 37 (2008).

Indice Autori

Autore	Pagine
Accoto G	1
Agnello N	68
Agosteo S	151
Alemanno E	29
Alifano P	145
Anania M P	151
Andrighetto A	161
Argentiero A	68
Batzella S	53
Bello L	53
Benetti P	161
Benvenuto M	68
Biasetto L	161
Blus C	106
Bona F	119
Bortone I	68
Bozzetti M P	101
Brancato V	5, 128, 135
Buccolieri A	17
Buccolieri G	1, 17, 160
Buccolieri R	53

Caiaffa V	68
Capomolla M	73, 80, 84, 91
Caresana M	151
Caricato A P	29
Caridi F	38, 128, 135, 140
Carlà A	53
Castellano A	17, 53
Cataldo R	17, 53
Cavalera E	73, 80, 84
Cavazza A	161
Cazzato M	91
Chiodini G	29
Chitano G	68
Cicala G	43
Ciccarese G	91
Ciccarese N	17
Cirrone G	151
Citti C	119
Congedo A	17
Corradetti S	161
Corrado M	29
Currelli D	161
Cutroneo M	5, 23, 38, 128, 135, 140
De Benedittis A	1
De Marco M	11, 123

De Martinis C	151, 160
De Mitri I	53
De Nunzio G	53
Della Patria A	113
Delle Side D	1, 11, 17, 101, 123, 145, 151, 160
Dell'Isola D	101
Demitri R	53
Di Paola G	73, 84
Di Paolo Emilio M	34
Di Rosa S	68
Di Sabatino S	53
Distante A	68
Donativi M	53
Falini A	53
Fazzi A	151, 160
Fermi F	113
Ferrarese A	68
Festuccia R	34
Fiore G	29
Friscini A	101
Galuccio G	53
Gatti G	151
Gaudino G	68
Gentile C	23
Gerardi R	1

Giancane G	49, 119
Giannelli G	106
Giove D	151, 160
Giulietti D	151
Gizzi L	151
Giuffreda E	1
Gorgoglione M A	17
Granito C	119
Grassi D	161
Grimaldi M	53
Imperio E	49
Italiano A	23
Klír D	60
Krása J	1, 60
Labate L	151
Leone A	73, 80,84
Limongi T	34
Liu T	119
Londrillo G	151
Magaletti V	43
Maggiore M	151
Manca A D	53
Manente M	161
Manzolaro M	161
Margarone D	60

Martino M	29
Massafra A	53
Meneghetti G	161
Milazzo M F	128
Montano J	161
Nassisi V	1, 11, 17, 101, 123, 145, 151, 160
Natali M	73, 80, 84, 91
Neglia C	68
Oleari C	113
Paladini F	160
Palatella L	96
Palladino L	34
Papaleo A	73, 84, 91
Pastore G	53
Pastore G	73, 80
Pavarin D	161
Peccarisi M	53
Pedullà E	38
Peluso A	68
Pennetta C	96
Perrino R	29
Pfeifer M	60
Piegari A	113
Pimpinelli S	101
Pinto C	29

Piscitelli P	68
Pola A	151
Prete G	161
Primerano P	128
Quarta R	53
Quarta S	91
Řezáč K	60
Ricci F P	73, 84
Roszkowska A M	38
Rucco M	53
Russo D	73, 80, 84, 91
Santantonio M	73, 80, 84
Scarpa D	161
Schillaci F	151
Scolaro C	38, 128, 135, 140
Sinigardi S	151
Soffietti R	53
Spagnolo S	29
Specchia V	101
Sytchkova A	113
Szmukler-Moncler S	106
Talà A	145
Tomaselli A	161
Torrise A	23
Torrise L	5, 23, 38, 128, 135, 140

Torsello M	53
Tramontana A	151
Tredici S M	145
Troisi A	119
Troisi L	119
Turchetti G	151
Ullschmied J	60
Valli L	49
Varoli V	151
Vasquez J	161
Velardi L	1, 11, 17, 101, 123, 145, 151, 160
Velyhan A	60
Visco A M	5, 128, 135
Vitale S	64
Zagari A	80, 91
Zecca I	53

© 2013 Università del Salento – Coordinamento SIBA
ISBN 978-88-8305-101-2 (print version)



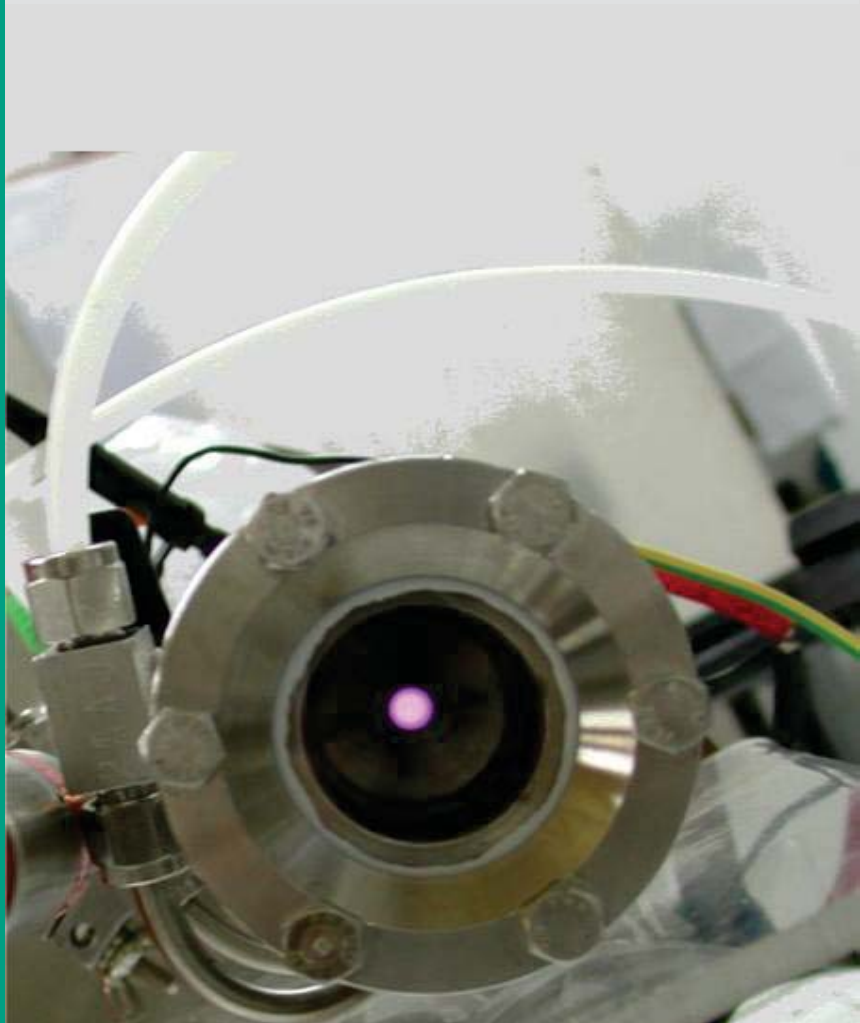
eISBN 978-88-8305-102-9 (electronic version)
<http://siba-ese.unisalento.it>

Finito di stampare nel mese di Luglio 2013 presso AGM per conto dell'Università del Salento



COMITATO SCIENTIFICO

- Prof. Vincenzo Nassisi
(Università del Salento)
- Prof. Pietro Alifano
(Università del Salento)
- Prof. Josef Krása
(ASCR, Prague, CZ)
- Prof. Luigino Troisi
(Università del Salento)
- Prof. Lorenzo Torrisi
(Università di Messina)
- Dr Fabio Belloni
(European Commission, Research & Innovation)
- Dott. Prof. Giuseppe Rollo
(Ospedale "F. Miulli" - Ortopedia – Acquaviva d.F.)
- Prof. Carlo De Martinis
(Università degli Studi di Milano)
- Dott. Mario Santantonio
(U.O.C. Radioterapia Oncologica - Ospedale V. Fazzi Lecce)
- Prof. Guglielmo Mondio
(Università di Messina)
- Prof. Danilo Giulietti
(Università di Pisa)
- Prof. Alessandro Distante
(Università di Pisa - IFC)
- Prof. Libero Palladino
(Università dell'Aquila, INFN)
- Dr. Giovanni Buccolieri
(Università del Salento)
- Prof. Alessandro Sannino
(Università del Salento)
- Dr.ssa Grazia Cicala
(IMIP - CNR, Bari)



COMITATO ORGANIZZATORE

- Prof. Vincenzo Nassisi
(LEAS - Dip.to di Matematica e Fisica - Lecce)
- Dr. Fabio Paladini
(LEAS - Dip.to di Matematica e Fisica - Lecce)
- Dr. Domenico Delle Side
(LEAS - Dip.to di Matematica e Fisica - Lecce)
- Dr. Luciano Velardi
(LEAS - Dip.to di Matematica e Fisica - Lecce)
- Sig. Salvatore Mega
(Dip.to di Matematica e Fisica - Lecce)

SEGRETERIA SCIENTIFICA

- Dott.ssa Daniela Dell'Anna
(Dip.to di Matematica e Fisica - Lecce)